

Investigation of the Dye-Anatase Interface in Dye Sensitized Solar Cells

Kee Eun Lee



Department of Mining and Materials Engineering

McGill University

Montreal, QC, Canada

February, 2012

A thesis submitted to McGill University in partial fulfillment of
the requirements of the degree of Doctor of Philosophy

© Kee Eun Lee, 2012

Abstract

The scope of this thesis is the study of the dye (N719) - TiO₂ (anatase) interface in dye sensitized solar cell (DSSC). The study of the TiO₂ semiconductor/Ru complex [*cis* - (2,2'-bipyridyl - 4,4'-dicarboxylate)₂(NCS)₂ ruthenium(II): N719] interface is important in order to understand the sensitization event as the dye and semiconductor are key factors for high conversion efficiency in DSSC. In spite of several studies of the interaction of the N719 dye/TiO₂ films, the anchoring mechanism has been debated for a decade because it has not been fully revealed. Thus, this thesis aims at unifying the previous different views on the binding mechanism and the type of groups involved in the N719-TiO₂ system as well as further elucidate new spectral information via vibrational spectroscopy (ATR-FTIR and SERRS), imaging techniques (Confocal Raman mapping and ATR-FTIR imaging) and electron spectroscopy (XAS and XPS). The combination of vibrational and electronic spectroscopic results allows for all the operating binding modes on the interface from molecular structure to interfacial electronic structure to be determined.

We focused on the spectral change in our Raman and ATR-FTIR spectra rather than depend on $\Delta\nu$ values (frequency difference) as the only method for differentiating binding modes. Furthermore, the hydroxyl vibrations of the N719 and two distinct nanocrystalline anatase surfaces (Dyesol and our own aqueous-synthesized variety) that occur before / after adsorption and their relation to the binding mechanism were explored using ATR-FTIR, SERRS, Confocal Raman mapping and ATR-FTIR imaging. As a result of this analysis the binding of the N719 dye to TiO₂ was proposed to occur through two neighboring carboxylic acid/carboxylate groups via a combination of bidentate-bridging and H-bonding involving a donating group from the N719 (and/or Ti-OH) units and acceptor from the Ti-OH (and/or N719) groups. This binding mechanism was further elucidated by investigating the electronic interactions of TiO₂ substrates and the N719 molecules via surface sensitive techniques (XAS and XPS) and probing methods (electron yield) before and after the sensitization event. This allowed us to propose that additional electronic interactions occur through the aromatic electron density of the

bipyridine groups and the d states found in TiO_2 and that there is extra H-bonding interaction of the NCS ligand of the dye with the TiO_2 surface groups ($\text{OH}/\text{H}_2\text{O}$).

From the application standpoint, TiO_2 nanocrystalline films were prepared from commercial and aqueous-synthesized precursors by screen printing with the purpose of correlating physical properties and in particular surface TiO_2 groups ($\text{Ti-OH}/\text{Ti-OH}_2$) to DSSC performance. Their morphological features were characterized in terms of particle size, shape, BET surface area, pore size, Raman and AFM analysis. This work showed the distribution of surface $\text{Ti-OH}/\text{Ti-OH}_2$ groups in Aqueous TiO_2 to be qualitatively richer than in Dyesol TiO_2 . The current–voltage characteristics ($I-V$), electrical impedance spectroscopy (EIS) and open circuit voltage decay (OCVD) were also investigated in relation to the TiO_2 film physical properties. It was found that photoelectrodes composed of surface hydroxyl-rich TiO_2 nanocrystalline material exhibits longer electron lifetime attributed to enhanced surface-dye binding that suppresses interfacial recombination. The relations between the film’s morphology, adsorption properties, and electrochemical behavior are comprehensively discussed.

Résumé

L'objectif de cette thèse est l'étude de l'interface colorant (N719) – TiO₂ (anatase) dans la cellule solaire sensibilisée par un colorant (DSSC). L'étude de l'interface du semiconducteur TiO₂/complexe Ru [*cis* - (2,2'- bipyridyl - 4,4'- dicarboxylate)₂ (NCS)₂ ruthenium(II): N719] est importante pour comprendre l'évènement de sensibilisation étant donné que le colorant et le semiconducteur sont des facteurs clés pour une conversion à haute efficacité dans la DSSC. En dépit de plusieurs études sur l'interaction au niveau des films colorant N719/TiO₂, le mécanisme d'ancrage a été débattu pendant une décennie, et est toujours non complètement connu. Ainsi, cette thèse vise à unifier les différents points de vue antérieurs sur le mécanisme de fixation et le type de groupements impliqués dans le système N719-TiO₂ ainsi que d'élucider de nouvelles informations spectrales moyennant la spectroscopie vibrationnelle (ATR-FTIR et SERRS), Les techniques d'imagerie (la cartographie Raman à confocale et l'imagerie ATR-FTIR) et la spectroscopie électronique (XAS et XPS). La combinaison des résultats de la spectroscopie vibrationnel et électronique permet de déterminer tous les modes de fixation fonctionnels à l'interface de la structure moléculaire et la structure électronique. Nous nous sommes concentrés sur le changement spectral dans les spectres Raman et FTIR-ATR et non seulement aux variations de fréquence $\Delta\nu$, comme étant la seule méthode qui différencie entre les différents modes de fixation. Par ailleurs, les vibrations de l'hydroxyle de N719 et les surfaces de deux distinctes anatase nano-cristalline (Dyesol et nos propres variétés aqueuses synthétisés) qui se produisent avant / après l'adsorption et leur relation avec le mécanisme de fixation ont été explorés par ATR-FTIR, SERRS, cartographie à confocale Raman et l'imagerie ATR-FTIR. En conséquence à cette analyse, la fixation du colorant N719 avec TiO₂ a été proposée. Elle se produise à travers deux groupements carboxylique / carboxylate voisins via une combinaison de pontage bidentés et liaisons-H. Ces derniers impliquent un groupement donneur des unités de N719 (et / ou Ti-OH) et accepteur des groupements Ti-OH (et / ou N719). Ce mécanisme de fixation a été ensuite élucidé en étudiant les interactions des substrats de TiO₂ et les molécules N719 via les techniques sensibles de surface (XAS and XPS) et les méthodes à sonde (rendement d'électron) avant et après l'évènement de sensibilisation. Cela nous a permis

de proposer que les interactions électroniques supplémentaires se produisant à travers la densité des électrons aromatiques des groupes bipyridine et les états *d* trouvés dans TiO₂ et qu'il y a des interactions supplémentaires de liaisons hydrogènes des ligands de NCS du colorant avec les groupements (OH/H₂O) de la surface de TiO₂.

Du point de vue application, les films TiO₂ nanocristallins ont été préparés à partir de précurseurs commerciaux et aqueuse synthétisés par sérigraphie dans le but de corrélérer les propriétés physiques et en particulier les groupements (Ti-OH/Ti-OH₂) à la surface de TiO₂ par rapport à la performance de la DSSC. Les caractéristiques de leurs morphologies ont été discutés en fonction de la taille des particules, leur forme, leur surface BET, la taille des pores, l'analyse AFM et la spectroscopie Raman. Les caractéristiques courant-tension (I-V), la spectroscopie d'impédance électrique (SIE), le déclin de tension en circuit ouvert (OCVD), ont également été étudiés en relation avec les propriétés physiques du film de TiO₂.

Acknowledgements

There are many people who, in many ways, have contributed to the work presented in this thesis and to whom I would like to express my gratitude.

First of all, I really want to appreciate professor Demopoulos for trusting me and giving me the opportunity to do this PhD in Materials Engineering, for scientific support and always taking time to discuss results. I also thank him to give me several opportunities to learn such as sending me CLS (Canadian Light Source) summer school, many international conferences and Prof. Bisquert's lab in Spain.

Special thanks to Mario, now he is Dr. Gomez. He helped me with all the publications and taught me vibrational and electron spectroscopy from the theory to experimental, which cost him lots of time and effort to guide my research and solve problems. Although it was strict when he trained me, I learned a lot from all the works with him. Also I highly appreciated the fruitful collaborations with several researchers; Dr. Samir Elouatik at University of Montreal for helping me to learn Raman mapping and IR imaging; Dr. Youngfeng Hu and Tom Regier in Canadian Light Source for their measurements in SXRMB/SGM line and discussions for interpreting results. I'm also thankful to the current and previous members of "Aqueous processing group" (Levente, Guobin, Hassan, Cecile, Karl, Renaud, Derek and Nima) for helping me in the lab and class.

I would also like to express my appreciation to my friend, Marja Koivumaki, for giving me strength to continue my PhD study in Canada when I came here to improve my English. It was grateful to attend all the bible studies and church meetings with her. Staying with her family and learning life lessons from her are one of the most valuable times in my life. The beautiful beach, parks and forests in B.C where I used to walk with her made me fall in love with the nature of this country, Canada.

Finally, I should thank my parents for bringing me up, giving me all of their love and support. Especially, I'm grateful to my father to encourage me to continue my PhD study abroad. He showed me endurance and persistent efforts toward his work for entire his life,

which has affected me a lot to become a scientist. Without the pray from my mother and father, I could not overcome hardship nor accomplish this PhD study. To my parents, I dedicate this work.

Contributions of Author and Co-Authors of Published Works Presented in This Thesis

Kee Eun Lee, Mario A. Gomez, Samir Elouatik, and George P. Demopoulos, Further Understanding of the Adsorption Mechanism of N719 Sensitizer on Anatase TiO₂ Films for DSSC Applications Using Vibrational Spectroscopy and Confocal Raman Imaging. *Langmuir* **2010**, 26(12), 9575–9583

Kee Eun Lee, Mario A. Gomez, Tom Regier, Yongfeng Hu, and George P. Demopoulos, Further Understanding of the Electronic Interactions between N719 Sensitizer and Anatase TiO₂ Films: A Combined X-ray Absorption and X-ray Photoelectron Spectroscopic Study. *Journal of Physical Chemistry C*. **2011**, 115, 5692–5707

K. E. Lee, M. A. Gomez, S. Elouatik, G. B. Shan, and G. P. Demopoulos, Vibrational Spectroscopic Imaging of N719-TiO₂ Films in the High Wavenumber Region Coupled to EIS Analysis. *Journal of Electrochemical Society* **2011**, 158 (7) H708-H714

Kee Eun Lee, Mario A. Gomez, Cecile Charbonneau, George P. Demopoulos, Enhanced surface hydroxylation of nanocrystalline anatase films improves photocurrent output and electron lifetime in DSSC photoanodes. Submitted to *Electrochimica Acta* **2012**, accepted

In all these works, the author has produced the materials under investigation, performed all analysis, in addition to their detailed characterization. Aqueous TiO₂ is the only instance which was not synthesized by the current author; rather this was conducted by Cecile Charbonneau, a fellow PhD student in our group, who provided the synthetic material.

The comprehensive supervisory role was conducted by the official supervisor (Prof. Demopoulos). The guidance and direction on issues of vibrational spectroscopy and X-ray absorption spectroscopy were given to the current author by Mario Gomez (fellow PhD student).

Data pre-processing and map generation of confocal Raman/ATR-FTIR imaging was provided by Dr. Samir Elouatik at Department of Chemistry of University of Montreal; however, the measurements, analysis and writing the manuscript were conducted by the first author.

In addition, the data collection of X-ray absorption spectroscopy was taken by Tom Regier (Ti L-edge, O K-edge, C K-edge and N K-edge) and Dr. Yongfeng Hu (Ti K-edge and EXAFS) in Canadian Light Source. The interpretation of spectra and data processing were also guided by them.

Dr. Guobin Shan (a PhD with our group) provided the cells for the EIS analysis (*J. Electrochem. Soc.* paper) and Cecile Charbonneau performed BET analysis for the last paper submitted to *Electrochim. Acta*.

The accuracy of the above statements is attested by the student's supervisor.

George P. Demopoulos _____

Mario A. Gomez _____

Samir Elouatik _____

Tom Regier _____

Yongfeng Hu _____

Guobin Shan _____

Cecile Charbonneau _____

Table of contents

Abstract	i
Résumé	iii
Acknowledgements	v
Contributions of Author and Co-Authors of Published Works Presented in This Thesis	vii
Table of contents	ix
List of figures	xiv
List of tables	xix
1. Introduction	1
1.1 Motivation	1
1.2. Objectives and contribution of this work	2
1.3. References	3
2. Literature review	4
2.1 Overview	4
2.2 Dye-sensitized Solar Cell	4
2.2.1 Introduction	4
2.2.2 Basic principles of dye-sensitized solar cells	5
2.2.3 Semiconductor-TiO ₂	8
2.2.2.1 TiO ₂ surface	10
2.2.4 Dye	12
2.2.4.1 Ru complex	13
2.2.4.1.1 Different protonation level of N3	14
2.2.4.1.2 Extending the π -system	15
2.2.4.1.3 Amphiphilic dyes with alkyl chains	16
2.2.4.2 Porphyrine dyes	16
2.2.4.3 Metal free organic dyes	17
2.2.4.3.1 Coumarin dyes	17

2.2.4.3.2 Indoline dyes -----	18
2.2.4.3.3 Triarylamine dyes -----	19
2.2.5 Electrolyte -----	20
2.2.5.1 Iodine based electrolyte -----	20
2.2.5.1.1 Ionic liquids -----	21
2.2.5.1.2 Additives -----	21
2.2.5.2 Hole conducting materials - -----	22
2.2.5.3 Recent developments of electrolytes in DSSC -----	23
2.2.6 Counter electrode -----	23
2.3 Spectroscopic techniques -----	24
2.3.1 Vibrational spectroscopy -----	24
2.3.1.1 ATR-FTIR spectroscopy -----	24
2.3.1.2 micro Raman Spectroscopy -----	27
2.3.2 Core-hole electron spectroscopy -----	28
2.3.2.1 X-ray Photoelectron Spectroscopy -----	29
2.3.2.2 X-ray Absorption Spectroscopy -----	32
2.3.3 Electrochemical impedance spectroscopy (EIS) -----	38
2.4 Application of these techniques in DSSC -----	41
2.5 References -----	42
3. Adsorption Mechanism of N719 Sensitizer on Anatase TiO₂ Films for DSSC Applications Using Vibrational Spectroscopy and Confocal Raman Imaging -----	51
3.1 Abstract -----	52
3.2 Introduction -----	52
3.3 Experimental section -----	56
3.3.1. TiO ₂ film preparation -----	56
3.3.2 Methods -----	56
3.3.3 Raman imaging data processing -----	57
3.3.3.1 Raman imaging Data pre-processing -----	57
3.3.3.2 Spectral curve-fitting and map generation -----	57
3.4 Result and Discussion -----	58

3.4.1 ATR-FTIR -----	58
3.4.1.1 N719-TiO ₂ dye region -----	58
3.4.1.2 N719-TiO ₂ high wavenumber region -----	64
3.4.2 Resonance-Raman @ 514 nm -----	69
3.4.2.1 N719-TiO ₂ dye region @ 514 nm -----	69
3.4.2.2 Stearic acid-TiO ₂ dye region @ 514 nm -----	73
3.4.2.3 Confocal Raman Imaging -----	75
3.4.2.4 N719-TiO ₂ high wave-number region @ 514 nm -----	78
3.4.2.5 Stearic acid-TiO ₂ high wave-number region @ 514 nm -----	79
3.4.3 Proposed binding Scheme -----	80
3.5 Conclusions -----	81
3.6 Acknowledgements -----	82
3.7 References -----	82

4. Vibrational Spectroscopic Imaging of N719-TiO₂ Films in the High Wavenumber Region Coupled to EIS Analysis -----	88
4.1 Abstract -----	89
4.2 Introduction -----	89
4.3 Experimental Section -----	93
4.3.1 TiO ₂ film preparation and cell fabrication -----	93
4.3.2 Raman imaging -----	93
4.3.3 ATR-FTIR imaging -----	94
4.3.3.1. Data preprocessing and map generation on IR imaging -----	94
4.3.4 Photo-electrochemical measurements -----	95
4.4 Results and Discussion -----	95
4.4.1 Confocal Raman imaging -----	95
4.4.2 Micro ATR-IR imaging -----	100
4.4.3. Electrochemical impedance spectroscopy -----	102
4.5 Conclusions -----	106
4.6 Acknowledgements -----	107
4.7 References -----	107

5. Electronic Interactions between N719 Sensitizer and Anatase TiO₂ Films: A Combined XAS and XPS study	110
5.1 Abstract	111
5.2 Introduction	112
5.3 Experimental Section	115
5.3.1 Sample preparation	115
5.3.2 XANES	116
5.3.3 XPS	117
5.3.4 Cell fabrication and photovoltaic measurements	117
5.4 Results and Discussions	117
5.4.1 XANES	117
5.4.1.1 Ti L-edge	117
5.4.1.2 Ti K-edge	122
5.4.1.3 O K-edge	126
5.4.1.4 C K-edge	128
5.4.1.5 N K-edge	132
5.4.2 XPS	134
5.4.2.1 Ti 2p	135
5.4.2.2 O 1s	136
5.4.2.3 N 1s	139
5.4.2.4 S 2p	144
5.4.2.5 C1s/Ru 3d	146
5.4.3 Photovoltaic characteristics	148
5.4.4. Proposed binding scheme	149
5.5 Conclusions	149
5.6 Acknowledgements	152
5.7 References	152
6. Enhanced surface hydroxylation of nanocrystalline anatase films improves photocurrent output and electron lifetime in DSSC photoanodes	159

6.1 Abstract	159
6.2 Introduction	160
6.3 Experimental Section	163
6.3.1 TiO ₂ film preparation and cell fabrication	163
6.3.2 TiO ₂ films characterization	164
6.3.3 Photo-electrochemical measurements	164
6.4 Results and Discussions	165
6.4.1 TiO ₂ films properties	165
6.4.2 EIS and OCVD	176
6.5 Conclusions	181
6.6 References	182
7. Global conclusion and claims to originality	186
7.1 Global conclusion	186
7.2 Claims to originality	189
7.3 Suggestions to future work	191
7.4 References	191
Appendix – Experimental details	192
A.1 Materials and Reagents	192
A.1.1 Conductive glass	192
A.1.2 Preparation of meso-porous TiO ₂ pastes	192
A.1.3 Preparation of mesoscopic TiO ₂ electrodes	193
A.1.4 Sensitizers	194
A.1.5 Counter electrode	195
A.1.6 Device assembly	195
A.2 Current-voltage curves	195
A.3 References	197

List of Figures

- Figure 2.1 Device structure of the dye sensitized solar cell (left) and actual DSSC
- Figure 2.2 Energy band diagram of a conventional p-n junction solar cell in case of thermal equilibrium (above); under illumination (below)
- Figure 2.3 Schematic energy diagram and operating principle of DSSC
- Figure 2.4 Dynamics of the processes involved in the conversion of light into electricity in a dye sensitized solar cell
- Figure 2.5 Surface Ti-OH and Ti-OH₂ groups on TiO₂ anatase (red: titanium, gray: oxygen and white: hydrogen)
- Figure 2.6 Chemical structures of Zn-porphyrine dyes
- Figure 2.7 Chemical structures of coumarin derivatives
- Figure 2.8 Chemical structures of indoline derivatives
- Figure 2.9 Chemical structures of triarylamine dyes
- Figure 2.10 Molecular structures of imidazolium iodides. DMPImI: 1,2-dimethyl-3-n-propylimidazolium iodide, EMImI: 1-ethyl-3-methylimidazolium iodide and MPImI: 1-methyl-3-n-propylimidazolium iodide
- Figure 2.11 Structure of spiro-OMeTAD
- Figure 2.12 Simplified schematic instrumentation of FTIR
- Figure 2.13 A pictorial representation of internal reflections through a high refractive index medium, for example, ZnSe, used as the internal reflection element (IRE). At each reflection, an evanescent wave is produced that decays exponentially into the medium above
- Figure 2.14 Photo-electric process in XPS (left) and Auger relation to core hole (right)
- Figure 2.15 Chemical shifts in XPS
- Figure 2.16 X-ray photoelectron spectroscopy-small area detection
- Figure 2.17 XPS of Cu-Ni alloy

Figure 2.18 Schematic of the photo-absorption and relaxation processes occurring in a XAS experiment

Figure 2.19 Schematic of the possible measurement techniques for NEXAFS spectroscopy

Figure 2.20 XAS spectrum of Molybdenum metal including XANES and EXAFS

Figure 2.21 Scheme of interaction of a photoelectron with the atoms of the nearest environment

Figure 2.22 Crystal field splitting diagram for different symmetry and coordination (a) and Ti-L edge spectra of rutile TiO_2 , Ba_2TiO_4 and frenosite showing the effect of coordination change to the XANES spectra (b)

Figure 2.23 EXAFS data processing: spline function (A), k^3 -space (B) and R space (B) plots

Figure 2.24 General transmission line mode of DSSC

Figure 2.25 Typical Nyquist plots of a N719 sensitized DSSC: Nyquist plot (above) and Bode plot (below)

Figure 3.1 Possible anchoring modes for the N719 molecule

Figure 3.2 The molecular structures of various Ru sensitizer complexes: (a) N3: (cis-di(thiocyanato)-bis(2,2'-bipyridyl-4,4'-dicarboxylic acid)-ruthenium(II)), (b) N712: (tetra(tetrabutylammonium)[cis-di(thiocyanato)-bis(2,2'-bipyridyl-4,4'-dicarboxylate)-ruthenium(II)]) and (c) N719: (bis(tetrabutylammonium)[cis-di(thiocyanato)-bis(2,2'-bipyridyl-4-carboxylate-4'-carboxylic acid)-ruthenium(II)])

Figure 3.3 Binding mechanisms that have been proposed by previous authors

Figure 3.4 ATR-FTIR spectra of N719 dye and N719- TiO_2 in (a) low wave number region and (b) high wave number region

Figure 3.5 ATR-FTIR spectra of Stearic acid and Stearic acid- TiO_2 in (a) low wave number region and (b) high wave number region

Figure 3.6 ATR-FTIR spectra of TiO_2 film (Aqueous and Dyesol) in (a) low wave number region, (b) high wave number region.

Figure 3.7 ATR-FTIR spectra of (a) N719, 2,2'-bipyridine and 2,2'-bipyridine-4,4'-dicarboxylic acid, ATR-FTIR and Raman spectra of (b) 2,2'-bipyridine and (c) 2,2'-bipyridine-4,4'-dicarboxylic acid

Figure 3.8 Raman spectra of (a) TiO₂, N719 and N719 –TiO₂ in low wave number region, (b) TiO₂ film in high wave number region and (c) N719 and N719-TiO₂ in high wave number region

Figure 3.9 Raman spectrum of N719-TiO₂ at 632 nm

Figure 3.10 Raman spectra of Stearic acid and Stearic acid- TiO₂ in (a) low wave number region and (b) high wave number region

Figure 3.11 Confocal Raman images showing the N719 distribution on TiO₂ film (Dyesol and Aqueous), 70 x 70 μm wide, 10 μm step size, monitoring the intensity at (a),(e) 640 cm⁻¹, (b),(f) 1376 cm⁻¹ (c),(g) 1542 cm⁻¹ and (d),(h) 1725 cm⁻¹

Figure 3.12 Confocal Raman images showing the N719 distribution on TiO₂ film (Dyesol and Aqueous), 10 x 10 μm wide, 2 μm step size, monitoring the intensity at (a),(e) 640 cm⁻¹, (b),(f) 1376 cm⁻¹ (c),(g) 1542 cm⁻¹ and (d),(h) 1725 cm⁻¹

Figure 4.1 Schematic of Raman instrumentation

Figure 4.2 Schematic of micro-ATR-FTIR instrumentation and geometries of IR beam

Figure 4.3 Real microscope images of Aqueous (left) and Dyesol (right) TiO₂ films

Figure 4.4 Raman spectra of (a) TiO₂, N719 and N719 –TiO₂ in low wave number region, (b) TiO₂ film in high wave number region and (c) N719 and N719-TiO₂ in high wave number region (adopted from Figure 3.8)

Figure 4.5 AFM images of Dyesol (a) and Aqueous TiO₂ (b)

Figure 4.6 Confocal Raman images of the naked TiO₂ film at 640 cm⁻¹ (a) Dyesol TiO₂ (b) Aqueous TiO₂

Figure 4.7 IR spectra of the naked TiO₂ films showing the water groups ~1600 cm⁻¹ (adopted from Figure 3.6)

Figure 4.8 Confocal Raman images for the naked TiO₂ films showing surface OH/OH₂ groups at 3076 cm⁻¹ (a) Dyesol and (b) Aqueous

Figure 4.9 Confocal Raman images for the N719 adsorbed TiO₂ showing surface OH/OH₂ groups at 3086 cm⁻¹ (a) Dyesol and (b) Aqueous

Figure 4.10 ATR-FTIR spectra of naked TiO₂ and N719 adsorbed TiO₂ in the range of 2600-4000 cm⁻¹ (adopted from Figure 3.6(b) and Figure 3.4(b), respectively)

Figure 4.11 ATR-IR images for the naked TiO₂ showing surface OH/H₂O groups at ~3200 cm⁻¹ (a) Dyesol and (b) Aqueous

Figure 4.12 ATR-IR images for the N719 adsorbed TiO₂ showing surface OH/H₂O groups at ~3100 cm⁻¹ (a) Dyesol and (b) Aqueous

Figure 4.13 Electrochemical impedance spectra of the DSSCs based on two different TiO₂ films (Dyesol and Aqueous) measured at open circuit voltage under 100 mW/cm² (top) Nyquist plot (bottom) Bode phase plot

Figure 5.1 TEM image of TiO₂ particulate

Figure 5.2 Titanium L-edge XANES spectra of the TiO₂ and N719-adsorbed TiO₂ film

Figure 5.3 Ti L-edge of TEY and FY for the pure TiO₂ (a) (c) and N719-TiO₂ (b) (d)

Figure 5.4 Ti K-edge XANES of TiO₂ and N719-TiO₂ (a) Solaronix and (b) Aqueous

Figure 5.5 Derivatives of Ti K-edge XANES for TiO₂ and N719-TiO₂

Figure 5.6 EXAFS spectra of TiO₂ and N719-TiO₂

Figure 5.7 EXAFS spectra of TiO₂ and N719-TiO₂ (a) Solaronix and (b) Aqueous

Figure 5.8 Oxygen K-edge XANES spectra of the TiO₂, neat N719 and N719-adsorbed TiO₂ films (a) Solaronix (b) Aqueous

Figure 5.9 Carbon K-edge XANES spectra of (a) neat N719 and N719-Solaronix TiO₂ (b) comparison of N719-adsorbed Solaronix and Aqueous; and naked TiO₂ film (c) Solaronix (d) Aqueous

Figure 5.10 C K-edge XANES of the bare aqueous TiO₂ (organic contaminant) and the dyed adsorbed TiO₂

Figure 5.11 C K-edge spectra recorded at normal (90°) and grazing photon incidence angle (30°) for neat N719 and N719-Solaronix samples

Figure 5.12 Nitrogen K-edge XANES spectra of (a) the neat N719 and N719-adsorbed TiO₂ films (Solaronix and Aqueous) at normal incidence and (b) the neat N719 and N719-TiO₂ (Solaronix) at normal (90°) incidence and 30 degree

Figure 5.13 Ti 2p XPS spectra of TiO₂ and dye-adsorbed TiO₂; (a) Solaronix (b) Aqueous TiO₂

Figure 5.14 O 1s XPS spectra of TiO₂ and dye-adsorbed TiO₂; (a) Solaronix (b) Aqueous TiO₂

Figure 5.15 Peak fitting of the O 1s XPS spectra for pure (a) Solaronix and (b) Aqueous TiO₂; and dye-coated (c) Solaronix and (d) Aqueous N719-TiO₂ systems

Figure 5.16 N 1s XPS spectra of N719 and N719-adsorbed TiO₂; (a) Solaronix and (b) Aqueous TiO₂

Figure 5.17 Peak fitting of N 1s XPS spectra for (a) N719 and dye-adsorbed TiO₂; (b) Solaronix and (c) Aqueous TiO₂

Figure 5.18 XPS spectra for comparison of 8hrs and 1week sample for N719-TiO₂

Figure 5.19 S 2p XPS spectra of N719 and N719-adsorbed TiO₂; (a) Solaronix and (b) Aqueous TiO₂

Figure 5.20 Peak fitting of S 1s XPS spectra for (a) N719 and dye-adsorbed TiO₂; (b) Solaronix and (c) Aqueous TiO₂

Figure 5.21 C 1s XPS of the bare TiO₂ (organic contaminant) for Solaronix and Aqueous TiO₂

Figure 5.22 C 1s XPS spectra of N719 and N719-adsorbed TiO₂; (a) Solaronix and (b) Aqueous TiO₂

Figure 5.23 I-V curves of DSSCs fabricated with two different TiO₂ electrodes

Figure 6.1 TEM images of TiO₂ particles (a) Aqueous (b) Alfa Aesar 5 nm (c) Alfa Aesar 10 nm

Figure 6.2 Raman spectra of TiO₂ films

Figure 6.3 Tapping mode AFM three-dimensional height images of TiO₂ films

Figure 6.4 Surface profiles of TiO₂ films

Figure 6.5 Pore size distributions of TiO₂ films

Figure 6.6 O 1s XPS spectra of TiO₂ films

Figure 6.7 TGA results of TiO₂ films

Figure 6.8 Nyquist plot (above) and Bode phase plot (below)

Figure 6.9 Open circuit voltage decay (a) and life time (b)

List of tables

Table 2.1 Structure of Ru-complex photo-sensitizers

Table 3.1 Summary of $\Delta\nu$ values for different carboxylate/carboxylic acid group-TiO₂ systems compounds

Table 3.2 Assignment of the bands observed in ATR-FTIR of N719, N719-TiO₂ (Dyesol), stearic acid, and stearic acid-TiO₂ (Dyesol)

Table 3.3 Raman assignment for N719 and N719 adsorbed TiO₂ films

Table 3.4 Raman assignment for stearic acid and stearic acid adsorbed TiO₂ film

Table 4.1 Photovoltaic performance and impedance data of the DSSCs fabricated with two different TiO₂ electrodes

Table 5.1 N 1s Intensity Ratios

Table 6.1 Dye adsorption on TiO₂ films

Table 6.2 Properties of TiO₂ films determined from adsorption-desorption curves

Chapter 1. Introduction

1. 1 Motivation

With a growing demand for energy combined with the prospect of global warming and climate change, research and development efforts intensify for the development of renewable energy sources such as photovoltaic, tidal power or wind energy. Considering the abundance of solar radiation reaching the Earth (some 120,000 TW compared to a current global consumption of ~13 TW), solar energy constitutes a strategic energy source, if cost effective solar cell technologies are widely developed and implemented. Solar cells can be classified according to their type into three groups: Si bulk heterojunction cells (first-generation technology); thin film (CuInGaSe₂ (CIGS), CdTe) solar cells (second-generation); or organic photovoltaic (OPV) and Dye Sensitized Solar Cells (DSSC) (third-generation). Among these the first type (silicon-based) dominates currently the solar energy market. However, the high cost of solar grade silicon production and processing including its significant environmental footprint (1.5 tones of CO₂ produced per tone of Si) limits its wider proliferation, but intensive research and development efforts are directed to overcome these obstacles. Thin film-based solar cells have broken into the commercial scene in part because of their advantage of using only a small fraction of semiconducting materials in comparison to the Si-based solar cells and their lower production cost in the case particularly of CdTe. However, over the longterm concerns are expressed either because of the use of toxic elements like Cd or rare elements like In. The third generation cells are not yet a commercial reality but they are the focus of intensive research studies. One of these types of cells is the DSSC that is based on electrochemistry at the interface between a dye adsorbed onto a porous network of nanometer-sized titanium dioxide particles and a redox electrolyte. Since Gratzel and co-workers [1-3] first reported on the DSSC, its overall energy conversion efficiency has been raised to 12 %, which makes it a serious contender for commercial application. However, a number of issues remain to be addressed hence the great R&D attention the

DSSC attracts [4]. This thesis constitutes part of this R&D effort having as focus the understanding of the dye/TiO₂ interface.

1.2 Objective of the present work

In this work, dye/semiconductor interfaces have been investigated by means of vibrational spectroscopy (IR and Raman), electron spectroscopy (XPS and XANES) and imaging techniques (confocal Raman mapping and ATR-FTIR imaging). The studies have mainly focused on all possible bonding features relevant to electron transfer processes between adsorbed dye molecules and semiconducting substrates. The dye used in these studies is N719 [5], a ruthenium bipyridine complex adsorbed via carboxyl linker groups to the semiconductor, titanium dioxide (TiO₂). Furthermore, the electrochemical properties of the complete DSSC using commercial TiO₂ sources and our in-house aqueous-synthesized variety (Aqueous TiO₂) were characterized by I-V curves, EIS (electrochemical impedance spectroscopy) and OCVD (open circuit voltage decay) methods as well as the bonding between adsorbate and substrate.

The thesis is divided into seven chapters: Following this initial chapter, the literature review of DSSC system is described in chapter 2. Chapters 3, 4 and 5 focus at the molecular level on the interface of dye-TiO₂ using vibrational spectroscopy, core-level electron spectroscopy and imaging techniques. Chapter 6 describes the electrochemical techniques of complete solar cells via the use of commercial and synthetic TiO₂ sources as a photo-anode to perform a systematic study of the relations between the film's morphology, adsorption properties, and electrochemical behavior with the purpose of correlating physical properties to DSSC performance. Finally, Chapter 7 summarizes the results obtained in the previous chapters-papers included in this thesis. The experimental methods used in the thesis are described in the appendix.

1.3 References

- [1] B. O'Regan, M. Graetzel, *Nature* 353 (1991), pp 737-740
- [2] Anders. Hagfeldt, Michael. Graetzel, 95 (1995), pp 49-68
- [3] Michael Gratzel, *Nature* 414, (2001), pp 338-344
- [4] Hagfeldt, A.; Boschloo, G.; Sun, L.; Kloo, L.; Pettersson, H. *Chem. Rev.* **2010**, *110*, 6595–6663
- [5] Nazeeruddin, M. K.; De Angelis, F.; Fantacci, S.; Selloni, A.; Viscardi, G.; Liska, P.; Ito, S.; Takeru, B.; Gratzel, M. *J. Am. chem. Soc.* 127 (2005) 16835

Chapter 2. Literature Review

2.1 Overview

This chapter reviews the theoretical background necessary for understanding the generated experimental results. In the first part, the operating principle and the key components (semiconductor, dye and electrolyte) of the dye sensitized solar cell (DSSC) are discussed in detail. The second part of this review provides the general theory of some key characterization techniques (vibrational spectroscopy, core-level electronic spectroscopy and electrochemical impedance spectroscopy) employed in this study.

2.2 Dye sensitized solar cell

2.2.1 Introduction

The dye sensitized nanocrystalline solar cell was developed by Gratzel and co-workers in 1991[1]. Record efficiencies of up to 12 % for small cells [2] and about 9 % for minimodules [3], promising stability data, for example, the critical 1000 h stability test at 80 °C with a durable efficiency of 8-9 %, and pre-commercial fabrication methods have been accomplished. A schematic of a typical DSSC device (left) and a transparent dye sensitized solar cell running a small motor under a diffuse day-light (right) are shown in Figure 2.1.

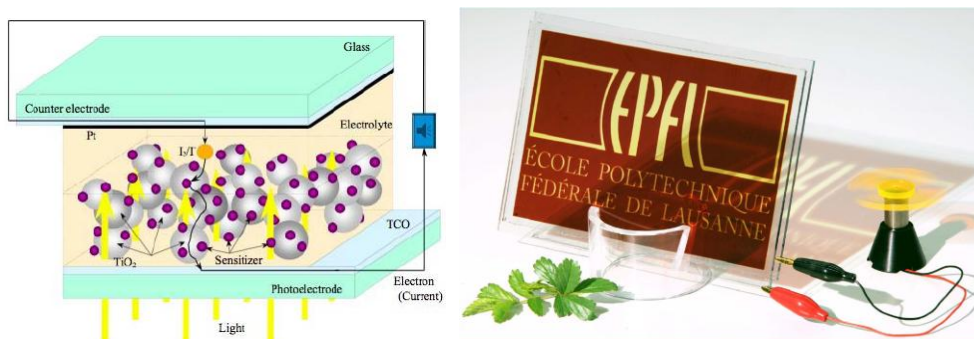


Figure 2.1 Device structure of the dye sensitized solar cell (left) and actual DSSC (right) [3]

The prospect of low-cost investments and fabrication are key features of DSSC in comparison to silicon-based solar cells. DSSC performs also relatively better compared with other solar cell technologies under diffuse light conditions and at higher temperatures. DSSC offers the possibilities to design solar cells with a large flexibility in shape, color, and transparency, which in turn opens up new commercial opportunities [4]. For these reasons, DSSC was emerged as a new generation photovoltaic device that is being studied extensively. Current R&D efforts focus mainly on the design of new dyes, development of electrolytes and investigating various semiconductor materials. A review of the most significant recent studies [5] in DSSC is presented in the following section.

2.2.2 Basic principles of dye sensitized solar cell

Conventional solar cells convert light into electricity by exploiting the photovoltaic effect that exists at semiconductor junctions. These photovoltaic devices are based on the concept of charge separation at an interface of two materials of different conduction mechanism, normally between solid-state materials, either n- or p-type regions with electron and hole majority carriers in a single semiconductor material, heterojunctions between different semiconductors or semiconductor-metal junction (Schottky) [6-9].

When the two halves are brought together, the Fermi levels (E_F) on either side are forced to coincide, causing the valence and conduction bands to bend. These bent bands represent a built-in electric field over the space referred to as the depletion region (Figure 2.2). In the case of illumination as shown in Figure 2.2(below), a photon which is absorbed by the material passes through the solar cell. This absorption takes the form of a band-to-band electronic transition, so an electron/hole pair is produced. If these carriers can diffuse to the depletion region before they recombine, then they are separated by the electric field, causing one quantum of charge to flow through an external load.

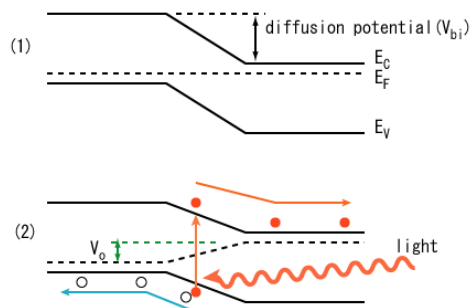


Figure 2.2 Energy band diagram of a conventional p-n junction solar cell in case of thermal equilibrium (above); under illumination (below) [6]

In contrast, the photo-electrochemical cells (as is the case of DSSC) work on a different principle, whereby the processes of light absorption and charge separation are differentiated. The schematic structure of the DSSC invented by the Gratzel group [4, 10-12] is shown in Figure 2.3. Its operation involves the following steps [13].

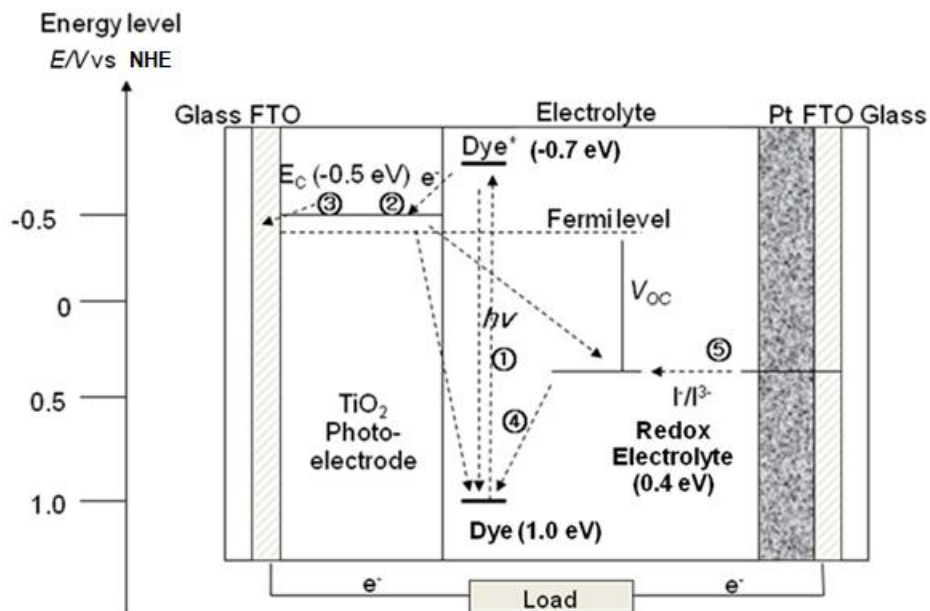


Figure 2.3 Schematic energy diagram and operating principle of DSSC [12]

- 1) Ru complex photosensitizers (Dye^+) adsorbed on the TiO_2 surface absorb incident photon flux. The sensitizers are excited from the ground state (Dye) to the excited state (Dye^*).
- 2) The excited electrons are injected into the conduction band of the TiO_2 electrode, resulting in the oxidation of the sensitizer.

- 3) Injected electrons in the conduction band of TiO_2 are transported by diffusion along the TiO_2 nanoparticle network towards the external conducting glass made of fluorine-doped tin oxide (FTO) and subsequently reach the Pt counter electrode through the external load.
- 4) The oxidized sensitizer (Dye^*) accepts electrons from the I^- ion redox electrolyte, regenerating the ground state (Dye), and I^- is oxidized to I_3^- state.
- 5) The oxidized redox mediator, I_3^- , diffuses toward the counter electrode where is re-reduced to I^- ions.

As in natural photosynthesis, in the artificial analog sunlight sets in action a molecular electron pump. The sensitizer (S) is bound as a monomolecular coating on the surface of a semiconductor oxide, such as TiO_2 . It absorbs the incident solar rays, and is thereby raised to the electronically excited state S^* . From this state it injects an electron into the conduction band of the mesoporous oxide semiconductor. The conduction band electrons then cross the film and are directed through a charge collector into the external current circuit where electrical work is done. The electrons are then returned to the cell through a counter electrode. Between this counter electrode and the oxide is an electrolyte containing a redox couple, i.e., triiodide and iodide (I_3^-/I^-). This redox electrolyte allows for the transport of electrical charge between the two electrodes. The electrons reduce triiodide to iodide ions which diffuse from the counter electrode to the nanocrystalline film surface where they regenerate the sensitizer by electron transfer to the sensitizer cations, while simultaneously the iodide is oxidized back to iodine or triiodide. The redox catalytic cycle leading to the conversion of light into electrical current is thereby closed [13].

The dye sensitized solar cell is working on the basis of differential kinetics (Figure 2.4). The performance of DSSC can be understood in regard of the kinetic competition of the various redox processes involved in the conversion of light into electricity. Ultrafast electron injection has been observed in the femtosecond-picosecond (10^{-15} - 10^{-12} s) time domain [14]. Regeneration of the oxidized dye is typically characterized by rate constants of 10^5 - 10^7 s^{-1} [15]. This is more than 100 times faster than recombination of injected electrons with the oxidized redox species (e.g. triiodide) and orders of magnitude faster

than back transfer to the dye cation in the absence of a redox mediator. As electron transport in the semiconductor electrode is generally one order of magnitude faster than recombination, the charge collection efficiency is near unit for optimized cells [16,17].

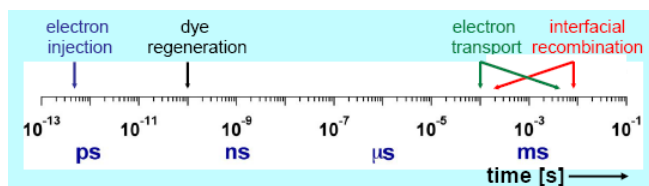


Figure 2.4 Dynamics of the processes involved in the conversion of light into electricity in a dye sensitized solar cell [18]

2.2.3 Semiconductor - TiO_2

The key to the breakthrough for DSSC in 1991[1] was the use of a mesoporous TiO_2 electrode, with a high internal surface area, to support the monolayer of a sensitizer. Typically, the increase of surface area by using mesoporous electrodes is about a factor 1000 in DSSC. TiO_2 still gives the highest efficiencies, but many other semiconductor metal oxide systems have been tested, such as ZnO , SnO_2 , and Al_2O_3 [19-21]. Besides these simple oxides, ternary oxides, such as SrTiO_3 [22] and Zn_2SnO_4 [23] have been investigated, as well as core-shell structures, such as ZnO -coated SnO_2 [24]. In this work, TiO_2 was only applied to make our solar cell. Thus the characteristics of TiO_2 are mainly described here.

TiO_2 is a stable, nontoxic oxide, which has a high refractive index ($n = 2.4$ - 2.5) and is widely used as a white pigment in paint, toothpaste, sunscreen and self-cleaning materials. Several crystal forms of TiO_2 occur naturally: rutile, anatase, and brookite. Rutile is the thermodynamically most stable form. Anatase is, however, the preferred structure in DSSC, because it has a larger bandgap (3.2 vs 3.0 eV for rutile) and higher conduction band edge energy, E_c . This leads to a higher Fermi level and V_{oc} (open circuit voltage) in DSSC for the same conduction band electron concentration [4].

For dye sensitized solar cells, the most common technique for preparation of TiO_2 nanoparticles is sol-gel techniques by hydrolysis of a titanium precursor such as titanium (IV) alkoxide with excess water catalyzed by acid or base, followed by hydrothermal growth and crystallization. Acid or base hydrolysis gives materials of different shapes and properties, and the rate of hydrolysis, temperature, and water content can be tuned to

produce particles of different sizes. Transmission electron microscopy (TEM) measurements revealed that for TiO₂ nanoparticles prepared under acidic conditions, crystalline anatase particles are formed exposing mainly the $\langle 101 \rangle$ surface [25,26]. Preparation in acetic acid compared with nitric acid increased the proportion of the $\langle 101 \rangle$ face about 3-fold [26]. The differences can be explained by different growth rates: in acetic acid crystal growth was enhanced in the $\langle 001 \rangle$ direction compared with the growth in the presence of nitric acid [27]. On the other hand, Hore et al. found that base catalyzed conditions led to mesoporous TiO₂ that gave slower recombination in DSSC and higher V_{oc} but a reduced dye adsorption compared with the acid-catalyzed TiO₂ [28]. The produced particles are formulated in a paste with polymer additives (such as ethyl cellulose, polyethylene glycol or hydroxypropyl cellulose) and deposited onto conductive glass substrates using doctor blading or screen printing techniques. Finally, the film is calcined at 450 °C in air to remove organic components and to make electrical connection between the nanoparticles. The porosity of the resulting mesoporous film can be controlled by changing the amount of polymer in the paste and is ideally about 50-60 wt % [4]. Higher porosity causes less interconnection between the particles and a decrease in charge collection efficiency [29].

Several improvements to the TiO₂ electrode in the DSSC have been made since 1991 in terms of light absorption, light scattering, charge transport, suppression of charge recombination, and improvement of the interfacial energetic. The employed architecture of the mesoporous TiO₂ electrode is as follows:

- (a) A TiO₂ blocking layer which coats the FTO plate to prevent contact between the redox mediator in the electrolyte and the FTO, prepared by chemical bath deposition, spray pyrolysis, or sputtering [30]. In this study, the blocking layer was prepared by dipping into 0.2 M TiCl₄ aqueous solution (chemical bath deposition) at 60 °C for 30 min.
- (b) A transparent (light absorption) layer consisting of a 10~12 μm thick film of mesoporous TiO₂ with ~20 nm particle size that provides a large surface area for sensitizer adsorption and good electron transport to the substrate.
- (c) A light scattering (anti-reflective) layer on the top of the mesoporous film, consisting of a ~3 μm porous layer containing ~400 nm sized TiO₂ particles [31]. Similar sized spherical voids in the nanocrystalline films are effective for light scattering [32].

(d) An ultrathin overcoating of TiO₂ on the whole structure, deposited by means of chemical bath deposition (using 0.2 M TiCl₄ aqueous solution), followed by heat treatment. The TiCl₄ treatment leads to the deposition of an ultrapure TiO₂ shell (~1 nm) on the mesoporous TiO₂ [33] (which may contain impurities or have carbon residues at the surface). The procedure leads to increased dye adsorption due to increased roughness despite a decrease in BET area (in m²/g) [25,30,33]. It lowers the acceptor levels in TiO₂ in energy,[33,34] which can improve the injection efficiency. It also improves electron lifetime significantly, leading to an increase in the electron diffusion length [34,35].

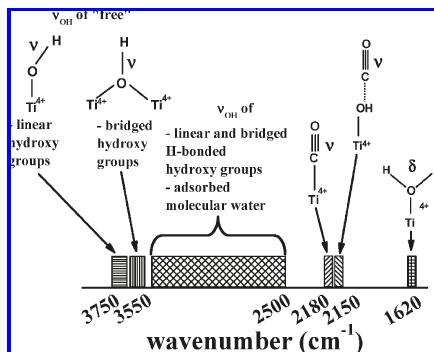
2.2.3.1 TiO₂ surface

Since the binding between dye and TiO₂ occurs on the surface of TiO₂, it is important to consider the surface groups on TiO₂. Thus this section reviews several reports related to TiO₂ surface groups and how these affect the DSSC system.

Among the physical properties and chemical structure of the TiO₂ surface, the surface OH groups on the TiO₂ surface have been assumed to play important roles in photocatalytic reactions[36] in which the surface OH groups and adsorbed water react with photogenerated holes and transform into hydroxyl radicals (•OH) with strong oxidation power. Regarding the mechanism of photoinduced hydrophilicity, it has been proposed that UV irradiation leads to an increase in the number of surface OH groups, which in turn increases the hydrophilicity of the TiO₂ surface [37]. For this reason, Kuribayashi et al. conducted a study on UV radiation onto their TiO₂ film before dye adsorption. They suggested that the generation of OH sites by UV irradiation on the TiO₂ electrodes prior to N719 dye adsorption is effective in increasing the short-circuit current density (J_{sc}) of the dye sensitized solar cells [38].

Prior to Kuribayashi et al.'s study, Finnie et al. also noted the effect of various surface treatments on the extent of dye uptake by the films in the course of optimizing the film dyeing procedure in DSSC, which suggested that attachment of the dye molecules involves interaction with hydroxyl groups on the surface of the TiO₂ [39]. They mentioned that the surface properties of TiO₂ depend strongly on how it is prepared. In particular, particle size and the presence of surface impurities (e.g., chloride, sulfate, etc.) from the various synthetic procedures used are important factors giving rise to such variability.

For the extensive study of TiO₂ surface, Minella et al. carried out IR spectroscopy in a controlled atmosphere and investigated the effect of fluorination on the surface properties of TiO₂. In their study, a series of quite narrow, partly resolved components between 3750 and 3550 cm⁻¹, a broad absorption spread over the 3550-2500 cm⁻¹ range, and a band at ca. 1620 cm⁻¹ were observed (Scheme 2.1) [40]. The last two sets of signals are simple in nature, as they are due to the $\delta_{\text{H}_2\text{O}}$ of adsorbed water molecules and to carbonate-like species, respectively. Conversely, both components at higher frequency are due to the -OH stretching modes of surface hydroxy groups [in both the linear (Ti-OH) and bridged (Ti-OH-Ti) forms] and adsorbed H₂O, which depending on their behavior as “free” or “H-bonded” oscillators, can contribute to the 3750-3550 cm⁻¹ pattern (free ν_{OH} oscillators) or to the 3550-2500 cm⁻¹ broad absorption (H-bonded ν_{OH} oscillators) [41-45].



Scheme 2.1 Schematic diagram showing the location/range, on a wavenumber axis, of the IR signals related to surface hydroxy groups and adsorbed H₂O and CO [40]

Selloni conducted computer simulation of TiO₂ single crystal to understand the reactivity and other surface physico-chemical properties [46]. The first-principles calculations showed that water molecules undergo spontaneous dissociative adsorption on clean anatase (001). On the other hand, the majority (101) facets in anatase TiO₂ adsorb water without dissociation. It is assumed that anatase TiO₂ crystals containing in the large size (001) facets are expected to have higher reactivity, compared with those crystals dominated by the (101) facets. The atomic structures of anatase (001) and (101) surface are shown below.

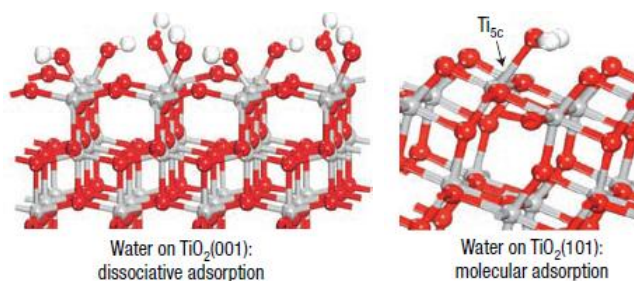


Figure 2.5 Surface Ti-OH and Ti-OH₂ groups on TiO₂ anatase (red: titanium, gray: oxygen and white: hydrogen) [46]

2.2.4 Dye

The dye is the photoactive element of the photovoltaic device, harvesting the incident light for the photon-to-electron conversion. To be used as sensitizer in DSSC, the photosensitizer should fulfill some essential characteristics [4].

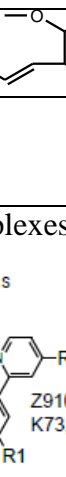
- (1) The sensitizer should be panchromatic. In this case, the absorption spectrum of the sensitizer covers the whole visible region and even the part of the near-infrared.
- (2) The sensitizer should contain anchoring groups such as -COOH, -H₂PO₃ or -SO₃H in order to strongly bind the dye onto the semiconductor surface.
- (3) The LUMO (lowest unoccupied molecular orbital, excited state) level of the sensitizer should be higher in energy than the conduction band edge of the semiconductor, so that an efficient electron transfer process between the excited dye and conduction band (CB) of the semiconductor can happen.
- (4) For dye regeneration, the oxidized state level of the sensitizer must be more positive than the redox potential of electrolyte.
- (5) The aggregation of dye molecules on the semiconductor surface is unfavorable so that it should be avoided through optimization of the molecular structure of the dye or by addition of coadsorbents that prevent aggregation. Dye aggregates (H- and J-aggregates) can, however, be controlled which in turn lead to an improved performance compared with a monomer dye layer as described by Mann et al.[47].
- (6) The photosensitizer should be photostable as well as exhibit good electrochemical and thermal stability.

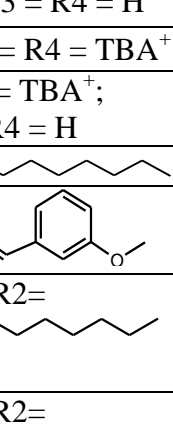
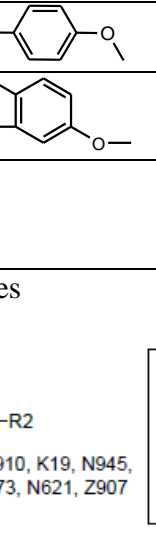
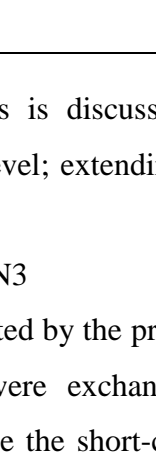
Based on these requirements, many different photosensitizers including metal complexes, porphyrins and metal-free organic dyes have been designed and applied to DSSC in the past two decades.

2.2.4.1 Ru-complexes

Among the metal complexes, Ru complexes [12] have shown the best photovoltaic properties due to a broad absorption spectrum, suitable excited (LUMO) and ground state (HOMO) energy levels, relatively long lifetime in the excited state, and good stability [4]. Several Ru complexes used in DSSC have reached more than 10 % solar cell efficiency under standard measurement conditions. Some representative Ru-complex photosensitizers are listed in Table 2.1.

Table 2.1 Structure of Ru-complex photo-sensitizers [48]

Dye	Extinction coefficient ($M^{-1}cm^{-1}$)	Substituent groups	η (%)	Year	Ref.
N3	13,000 _{538 nm}	R1 = R2 = R3 = R4 = H	10.0	1993	[49]
N712	N/A _{518nm}	R1 = R2 = R3 = R4 = TBA ⁺	8.2	2003	[50]
N719	13,500 _{535 nm}	R1 = R2 = TBA ⁺ ; R3 = R4 = H	11.2	2005	[51]
Z907	12,200 _{522 nm}	R1 = R2 = 	7.3	2003	[52]
Z910	16,900 _{543 nm}	R1=R2= 	10.2	2004	[53]
K19	18,200 _{543 nm}	R1=R2= 	7.0	2005	[54]
N621	7,830 _{530 nm}	R1=R2= 	9.6	2005	[51]
K73	18,000 _{545 nm}	R1=R2= 	9.0	2006	[55]
N945	18,600 _{545 nm}	R1=R2= 	10.8	2007	[56]
Black dye (N749)	7,000 _{~600 nm}		10.4	2001	[57]

Ru-complexes		
 <p>N3, N712, N719</p>	 <p>Z910, K19, N945, K73, N621, Z907</p>	 <p>black dye</p>

The evolutionary development of Ru-complexes is discussed on the basis of three molecular features: trying different protonation level; extending π system; and adopting alkyl chains for amphiphilic dyes.

2.2.4.1.1 Different protonation level of N3

Nazeeruddin et al.[50] investigated the effect exerted by the proton content of the N3 dye on the performance of DSSC. The protons were exchanged for a bulky tetra-n-butylammonium (TBA⁺) group. As a consequence the short-circuit photocurrent (I_{sc}) is 17.5-18.5 mA/cm² for N3 (all protons), while it is only about 12-13 mA/cm² for N712 (all TBA⁺ groups). Although the photovoltage of N712 is 200 mV higher than the one of

N3, this is insufficient to compensate for the current loss. For the incident monochromatic photon-to-current conversion efficiency (IPCE), the value in the plateau region is 80 % for N3 while for N712 it is only about 66 %. At 700 nm (red region), the IPCE value is twice as high for the fully protonated N3 as compared to the deprotonated N712. However, the photovoltaic performance of N719 carrying two protons and two TBA⁺ groups was found to be superior to that of N3 and N712 that contain four and no protons, respectively. Hence the doubly protonated form of the complex (N719) became the benchmark sensitizer.

2.2.4.1.2 Extending the π -system

One strategy for increasing the light-harvesting efficiency is to increase the conjugation length of the ligand. To further extend the π -conjugated system of the bipyridine and enhance the harvesting of solar light, Gratzel et al. incorporated the 3-methoxystyryl group into the ancillary ligand to obtain a novel Ru dye, Z910, which exhibited prominent efficiency (10.2 %). The study demonstrated that enhancing the molar extinction coefficient is a good strategy to improve the photovoltaic performance of Ru dyes [53].

The performance of these novel sensitizers on thick electrodes (10~12 μm) and with volatile electrolytes is similar as for the N3 (e.g. Z910 10.2 % [53] and N945 10.8 % [58]). But almost equivalent efficiency is obtained when applied on thin electrodes (2~5 μm) and with non-volatile electrolytes (e.g. K73 with 3-methoxypropionitrile 9.0 %). At the same time, they exhibit remarkable stability at 80 °C in darkness and at 60 °C under AM 1.5 illuminated. The excited state of these dyes is between -0.71 V and -0.79 V vs. NHE [58], which is sufficiently more negative than the conduction band of TiO₂ (ca. -0.1 V vs. NHE) hence complete charge injection is ensured.

Furthermore, Gratzel group designed the N749 dye, also called the “black dye” in which the Ru center has carboxylated terpyridyl and three thiocyanate groups as ligands. Based on this dye, an IPCE spectrum was obtained over the whole visible range extending into the near IR region up to 920 nm [57]. However its extinction coefficient is rather low, requiring thicker films for sufficient light absorption having as result an unfavorable series resistance [10].

Recently Berlinguette and coworkers reported a series of asymmetric cyclometalated Ru(II) complexes (the similar structure of “black dye”) bearing a TPA (triphenylamine) unit bridged by a thiophene in order to further enhance light absorption [59]. The new cyclometalated dyes devoid of NCS ligands generated high η (>8 %) in DSSC. Their studies showed that the tridentate ligand proximate to the TPA unit maximizes light harvesting in the visible region, maintains sufficient electron transfer toward the semiconductor surface, and ensures that the LUMO (lowest unoccupied molecular orbital) is situated on the anchoring ligand to enable facile charge injection into the TiO₂ [60].

2.2.4.1.3 Amphiphilic dyes with alkyl chains

Amphiphilic molecules contain a polar, water-soluble group as well as a non-polar, water-insoluble hydrocarbon chain. In order to suppress the susceptibility of dye (such as N3) toward water, N3-based Ru-complexes were modified by replacing two of the four carboxylic groups into long alkyl chains (detailed structures given in Table 2.1). In these sensitizers, the conjugated π -system of the bipyridil-ligand is smaller and thus, the absorption coefficient is typically lower. Yet, the initial conversion efficiencies are still reasonably good, ranging from 7.3 % for Z907 (with 9 carbon atoms) [52] to 9.6 % for N621 (with 13 carbon atoms) [51]. The main advantage of these dyes is their extraordinary stability. For example, Z907 sensitized DSSCs passed 1000 h at 80 °C in darkness and at 55 °C under illumination without any degradation [52].

2.2.4.2 Porphyrin dyes

One of the drawbacks of ruthenium complexes is the limited absorption in the near-infrared region of the solar spectrum. Porphyrins exhibit intense spectral response bands in the near-IR region and possess good chemical, photo and thermal stability, providing good potential candidates for photovoltaic applications.

The introduction of porphyrins as photosensitizers in DSSC is particularly interesting given their primary role in photosynthesis. Owing to appropriate LUMO (lowest unoccupied molecular orbital) and HOMO (highest occupied molecular orbital) energy levels and very strong absorption of the Soret band in the 400-450 nm region, as well as the Q-band in the 500-700 nm region [61], porphyrin derivatives can be suited as panchromatic photosensitizers for DSSC. Several studies have demonstrated that

porphyrin dyes can show efficient photoinduced electron injection into the conduction band of TiO_2 [62,63].

The best initial efficiencies were achieved with differently substituted Zn-tetraphenylporphyrins (ZnTTP). The cells based on Zn-3 yielded close to 85 % IPCE with a corresponding overall efficiency of 5.6 % under AM 1.5 irradiation [64]. Recently, Campbell et al. further extended the π system in the β -position with functional group and obtained a more efficient porphyrin sensitizer, Dye 2 [65,66]. Dye 2 exhibited an IPCE value of up to 75 % and an impressive efficiency of 7.1 % in DSSC with a liquid electrolyte and achieved a conversion efficiency of 2.4 % in solid-state DSSC [4].

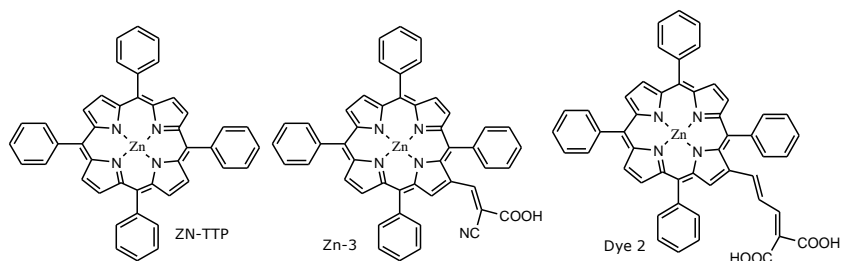


Figure 2.6 Chemical structures of Zn-porphyrin dyes [64,65]

2.2.4.3 Metal free organic dyes

Organic dyes as an alternative to the noble Ru complexes exhibit many advantages: (1) The molecular structures of organic dyes are in many forms and can be easily designed and synthesized. (2) Concerning the cost and environment issues, organic dyes are superior to noble metal complexes. (3) The molar extinction coefficients of organic dyes are usually higher than those of Ru complexes, making them attractive for thin film and solid-state DSSC [4]. Here, the most distinctive metal organic dyes such as coumarin dyes, indoline dyes and triarylamine derivatives are introduced.

2.2.4.3.1 Coumarin dyes

A class of organic dyes consisting of a coumarin unit and a cyanoacrylic acid unit linked by vinylene, isophorone, or thienyl was developed by Arakawa et al. [67,68]. C343, recognized as the original coumarin sensitizer, exhibited an effective electron injection process [69]. However, when this dye was used in DSSC, it showed a lower efficiency than Ru complex-based DSSC due to the narrow light response range in the visible region. Later, they introduced vinylene ($-\text{CH}=\text{CH}-$) groups to coumarin derivatives to exhibit

wide absorption. NKX-2311 dye exhibits red-shift in the absorption spectra and improved efficiencies. Yet, the lengthening of the dye with the vinylene units also enhances dye aggregation on the TiO₂ surface resulting in a decrease of electron injection yield owing to the intermolecular charge transfer. Under optimized conditions, the NKX-2311 based DSSC gave 6.0 % efficiency under AM 1.5 [67]. In subsequent experiments, they found that there were two problems associated with the introduction of vinylene units: the complicated synthesis procedure and possible isomerization. In view of this, NKX-2677 was introduced to include thienyl and isophorone units employed to expand the conjugated system. Their experimental work showed that the number of thiophene units affect the photovoltaic properties due to different aggregation issues on the TiO₂ surface. As a result, the NKX-2677 based DSSC gave 6.1-8.1 % overall efficiency under AM 1.5 [68].

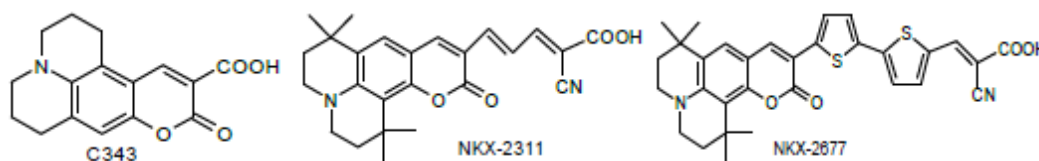


Figure 2.7 Chemical structures of coumarin derivatives [68]

2.2.4.3.2 Indoline dyes

Horiuchi, Uchida and co-workers first reported this type of organic dye with simple synthesis procedures, low costs, and good efficiencies obtaining 6.1 % power conversion efficiency of the D102 in 2003 [70]. To further improve the DSSC performance, an additional rhodanine framework was introduced to the molecular structure of D102 to extend the absorption spectrum, giving a series of novel indoline dyes [71]. Among these dyes, D149 showed most prominent efficiency, 8.0 %, under AM 1.5 irradiation. Gratzel et al. achieved 9.0 % efficiency based on D149 through optimizing the TiO₂ electrode thickness [72]. In 2008, Ito and co-workers developed D205 with a rhodanine framework substituted with n-octyl to suppress the dye π -stacked aggregation on the semiconductor surface and obtained a 9.5 % efficiency [73]. This is one of the best efficiencies for organic dye sensitized solar cells. Moreover, endowing the sensitizer with an octyl chain can effectively suppress electron recombination between electrons in the conduction band of TiO₂ and electrolyte, resulting in higher open-circuit voltage and short-circuit current.

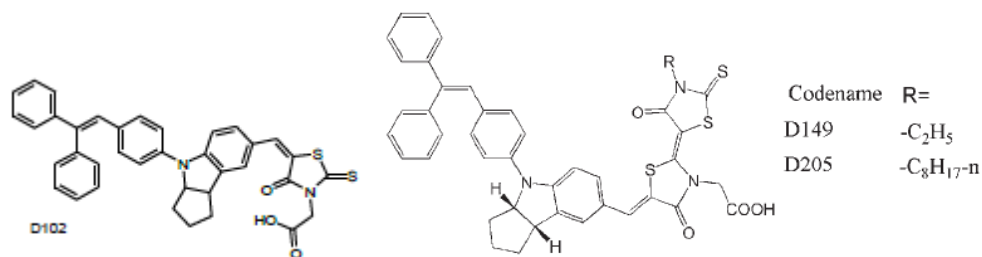


Figure 2.8 Chemical structures of indoline derivatives [73]

2.2.4.3.3 Triarylamine dyes

This class of organic sensitizers has been investigated widely due to prominent electron-donating ability and hole-transport properties of the triarylamine unit. To date, a very large number of triarylamine dyes have been developed and most of them have shown good power conversion efficiencies in DSSC [4]. In this section, only prominent dyes containing triarylamine moieties are introduced.

Lin et al. reported a series of efficient triarylamine type organic dyes. D5 with simple structure and short synthesis route showed over 5.1 % efficiency. Later on, they replaced the thiophene unit of D5 with furan and achieved 7.4 % overall efficiency [74].

Great efforts in developing dimethylfluorenylamino-based organic dyes have been made by Ko and co-workers [75]. The tailored dimethylfluorenylamino moiety can ensure greater resistance to degradation when exposed to light or high temperature, because it possesses a bipolar character that allows the formation of both stable cation and anion radicals [75]. Under AM 1.5 illumination, JK-1 gave efficiencies of 8.0 %. More structural modifications of fluorine-based organic dyes have been performed through changing the π bridge or electron acceptor and introducing the alkyl chains into fluorene or π -bridge. JK-45 and JK-46 are two successful examples of the molecular optimization with alkyl chains [75]. The introduction of long alkyl chains into thiophene π -bridge of JK-46 can enhance the tolerance toward water in the electrolytes. A JK-45 and JK-46 based DSSC with volatile electrolyte yielded overall conversion efficiency of 7.42 and 8.60 %, respectively while the N719 based DSSC showed 10.31 %.

In 2009, Wang and co-workers made great progress in developing efficient triarylamine organic dyes [76]. By using the alkoxy-substituted triphenylamine as electron donors and changing different π -bridges, they developed the triphenylamine dye, C217 [76]. The

C217 containing both EDOT (3,4-ethylenedioxythiophene) and TT (thienothiophene) π -bridges showed an absorption band with a peak at 552 nm, exceeding 90 % IPCE values from 440 to 590 nm [76]. Efficiencies of 9.8 % and 8.1 % with liquid electrolyte and solvent-free ionic electrolyte under AM 1.5 were obtained, respectively. The two efficiency values are the records of DSSC based on organic dyes so far. Furthermore, the high performance cell based on C217 with ionic electrolyte still retained >96 % of its initial efficiency after 1000 h under full sunlight soaking at 60 °C.

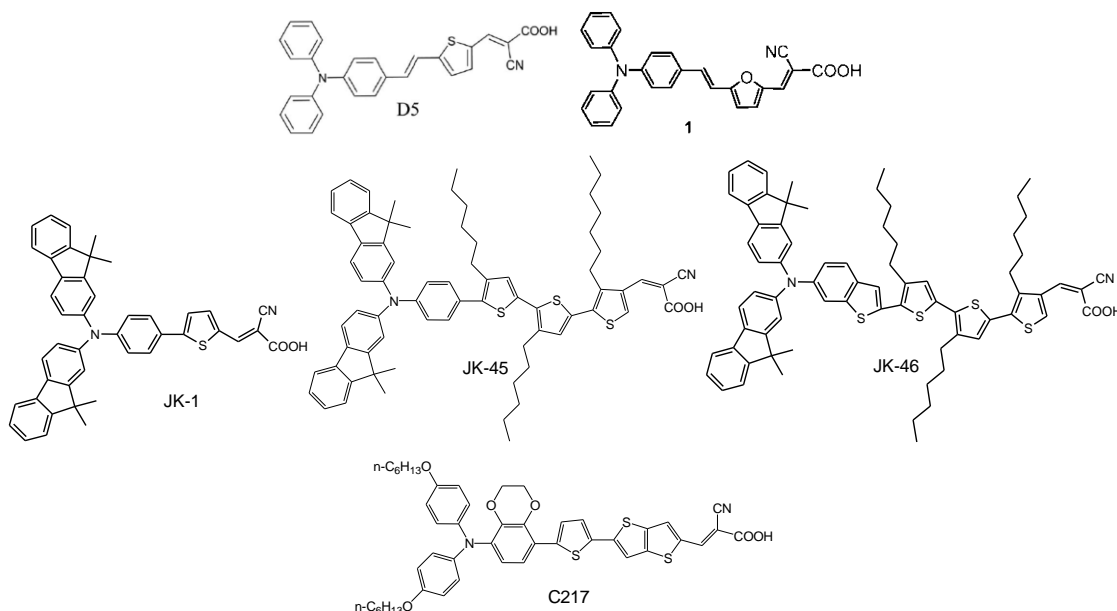


Figure 2.9 Chemical structures of triarylamine dyes [74-76]

2.2.5 Electrolyte

2.2.5.1 Iodine based electrolyte

The redox couple in the electrolyte is used to regenerate the oxidized dye. It should have a high diffusion coefficient and be able to penetrate the nanostructured film. These requirements are best matched by a liquid electrolyte. A common electrolyte is the triiodide/iodide (I_3^-/I^-) couple in an organic solvent. The typical electrolyte has the following composition: 0.6 M 1,2-dimethyl-3-n-propylimidazolium iodide (ionic liquid), 0.1M LiI, and 0.05 M I_2 in methoxyacetonitrile or acetonitrile (solvent) with tert-butyl pyridine (additive) [4,12]. Organic solvents are used instead of water, since the dye usually is unstable in water. The problem with liquid electrolytes is generally that they

are very difficult to encapsulate for long time. For commercial use, it is necessary to overcome this problem in an efficient manner. By far, the most significant advances towards electrolytes with negligible vapor pressure were achieved with ionic liquids, which are introduced in the following section.

2.2.5.1.1 Ionic liquids

The first ionic liquids tested belong to the imidazolium family (Figure 2.10), and these are the most commonly used in electrochemical applications, also in solar cells. Both good photoelectrochemical performance and stability were observed. The area of ionic liquids is vastly dominated by imidazolium-based electrolytes, and some of the main conclusions were that the combination of photochemical stability and low viscosity, and thus ion mobility, remains a challenge [77].

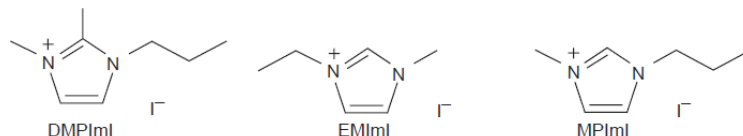


Figure 2.10 Molecular structures of imidazolium iodides. DMPImI: 1,2-dimethyl-3-n-propylimidazolium iodide, EMImI: 1-ethyl-3-methylimidazolium iodide and MPImI: 1-methyl-3-n-propylimidazolium iodide [78]

2.2.5.1.2 Additives

4-*tert*-Butylpyridine (TBP) was first applied in DSSC by Gratzel and co-workers in 1993, demonstrating a remarkable increase in V_{oc} of these cells in combination with LiI-based electrolytes [49]. On the basis of intensity-modulated photovoltage spectroscopy (IMVS) measurements; it was shown that TBP shifts the titania band edge toward higher energies [79]. Haque et al. studied the effects of TBP and lithium cations on shifts of TiO_2 conduction band and trap levels, as well as on recombination kinetics between electrons in TiO_2 and oxidized dye molecules [80]. The change in the kinetics was attributed to the change in TiO_2 energy levels. The effects of TBP were studied in more detail in DSSC showing that both band edge shift and increased electron lifetime play a role [81].

Although TBP and Li^+ ions have opposite effects on the conduction band and trap states, and thus on the kinetics of electron injection and recombination, it is a very common combination of additives in solar cell electrolytes. The reason for the good overall performance of this combination is not fully understood. Adding to the complexity results

from ionic liquids with varying amounts of water, in which the interplay among lithium cations, TBP, and water appeared to be essential but not clearly understood [82].

2.2.5.2 Hole conducting materials

Due to the disadvantage of triiodide/iodide (I_3^-/I^-) based electrolytes that they are chemically very aggressive, hole conducting materials (HTM) have been developed for DSSC. Most HTMs are inorganic solids, organic polymers or p-conducting molecules [48]. In organic hole conductor, positive charge moves by a hopping mechanism between neighboring molecules or moieties, as opposed to I_3^-/I^- electrolytes where charge transport is due to movement of redox molecules [4]. Though most HTMs are chemically less aggressive, a number of problems are encountered, which is the reason why the triiodide/iodide redox couple is still superior to HTM in terms of efficiency.

A general problems with solid hole conductors in DSSC is the pore filling. For efficient cells, it is necessary for all dye molecules to be in contact with both TiO_2 and the hole conductor. Also, no (or very few) interruption in the hole-conducting path are an essential requirement. However most efficient DSSC with HTM to have a TiO_2 film thickness of about 2 μm only, which is not sufficient for complete light harvesting with the current sensitizers. In case of organic polymer hole conductors, the hole mobility is significantly lower than in a liquid electrolyte, which increases the series resistance of the cell [4].

Triarylamine-based compound, such as the 2,2',7,7'-tetrakis(N,N-di-p-methoxyphenylamine)-9,9'-spirobifluorene (spiro-MeOTAD) in Figure 2.11, is the most popular hole conductor in solid-state DSSC. It was first introduced by Bach et al. in 1998 [83]. The main advantage of this material is its high glass transition temperature (T_g) of ~ 120 °C. Thus, it forms amorphous layers to fill the pore. The device has been optimized and the current state of the art is at 4 % efficiency with an ambiphillic sensitizer Z907 [52].

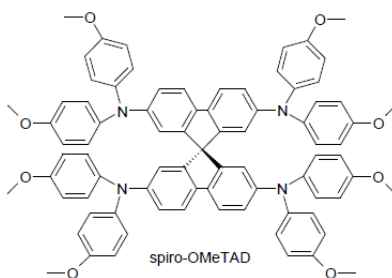


Figure 2.11 Structure of spiro-OMeTAD [83]

Rau and coworkers made a comparison between liquid and solid electrolytes, and concluded that recombination is a larger problem in the solid cells than in the liquid ones [84]. The FTO-interface can be shielded with a compact TiO₂ layer to avoid short-circuiting of the cell, but the recombination with conduction band electrons is inherent and is difficult to suppress.

2.2.5.3 Recent developments of electrolytes in DSSC

In 2008, an article published by Bai et al. in *Nature Materials* demonstrated cell efficiencies of 8.2 % using a new solvent-free liquid redox electrolyte consisting of a melt of three salts, as an alternative to using organic solvents as an electrolyte solution. Although the efficiency with this electrolyte is less than the 11 % being delivered using the existing iodine-based solutions, the efficiency appears to be improved further [85].

In 2010, cooperative research between Grätzel's group at the École Polytechnique Fédérale de Lausanne and Marsan's group at the Université du Québec à Montréal led to the development of a new electrolyte based on the disulfide/thiolate T₂/T⁻ couple, where T⁻ represents 5-mercapto-1- methyltetrazole ion and T₂ stands for its dimer. It is known that the triiodide/iodide redox couple has two main disadvantages: it is corrosive and partially absorbs visible light. The new disulfide/thiolate redox couple overcomes these disadvantages making it very attractive for flexible DSSC that use transparent conductors as current collectors. An efficiency of 6.4 % under full sunlight was achieved using their iodide-free electrolyte [86].

2.2.6 Counter electrode

Counter electrodes for DSSC with triiodide/iodide (I₃⁻/I⁻) electrolytes can be rather easily prepared by deposition of a thin catalytic layer of platinum onto a conducting glass substrate. Without platinum, fluorine doped tin oxide (SnO₂:F-FTO) glass is a very poor counter electrode and has a very high charge transfer resistance (more than 10⁶ Ω cm²) in a standard triiodide/iodide electrolyte [87]. Pt can be deposited using a range of methods such as electrodeposition, spray pyrolysis, sputtering, and vapor deposition. Best performance and long-term stability has been achieved with nanoscale Pt clusters

prepared by thermal decomposition of platinum chloride compounds [88]. In this study, Pt counter electrode is prepared by dropping 5 mM H_2PtCl_4 solution on the FTO glass. Other materials for the counter electrode (graphite/carbon black and CoS) have been developed. Kay and Grazel developed a counter electrode from a mixture of graphite and carbon black for use in DSSC with the monolithic cell geometry because carbon materials are suited as catalysts for the reduction of triiodide [89]. Very recently, electrodeposited CoS has been identified as a suitable catalyst for the triiodide/iodide redox couple [90], which is far less expensive, more efficient, more stable and easier to produce in the laboratory.

2.3 Spectroscopic techniques

2.3.1 Vibrational spectroscopy

Vibrational spectroscopy methods are used to experimentally identify the surface species generated upon molecular adsorption and the species generated by surface reactions. The vibrational spectroscopy techniques used in this thesis are shortly presented below.

2.3.1.1 ATR-FTIR spectroscopy

Infrared (IR) spectroscopy deals with the infrared region of the electromagnetic spectrum, that is light with a longer wavelength and lower frequency than visible light. Infrared spectroscopy exploits the fact that molecules absorb specific frequencies that are characteristic of their structure. These absorptions are resonant frequencies, i.e. the frequency of the absorbed radiation matches the frequency of the bond or group that vibrates. The energies are determined by the shape of the molecular potential energy surfaces, the masses of the atoms, and the associated vibronic coupling [91].

In order for a vibrational mode in a molecule to be "IR active," it must be associated with changes in the permanent dipole. A molecule can vibrate in many ways, and each way is called a *vibrational mode*. For molecules with Number of atoms (N) have $3N - 5$ degrees of vibrational modes if they are linear, whereas nonlinear molecules have $3N - 6$ degrees of vibrational modes (also called vibrational degrees of freedom). As an example H_2O , a non-linear molecule, has $3 \times 3 - 6 = 3$ degrees of vibrational modes. More complex molecules have many bonds, and their vibrational spectra are correspondingly more complex, i.e. big molecules have many peaks in their IR spectra [91].

Fourier transform infrared (FTIR) spectroscopy is a measurement technique that allows one to record infrared spectra. Infrared light is guided through an interferometer and then through the sample (or vice versa). (Figure 2.12) A moving mirror (MM) inside the apparatus alters the distribution of infrared light that passes through the interferometer. The signal directly recorded, called an "interferogram", represents light output as a function of mirror position. A data-processing technique called Fourier transform turns this raw data into the sample's spectrum: Light output as a function of infrared wavenumber. With reference to Fig. 2.12, FM1 is the fixed mirror; BS1 is the beamsplitter; MM is the moving mirror; and D1 is the infrared detector producing the infrared interferogram that is then transformed into the spectrum. D2 is a photodiode that serves as a detector of laser [92].

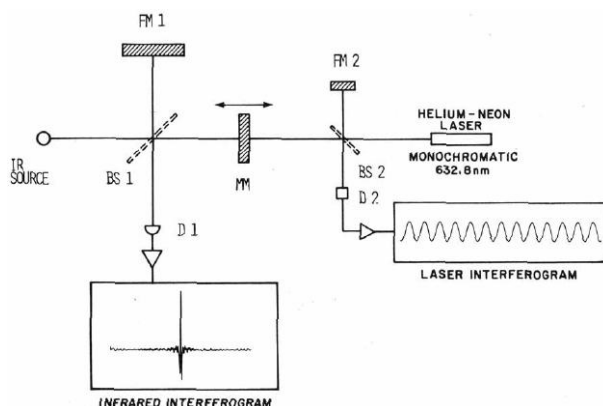


Figure 2.12 Simplified schematic instrumentation of FTIR [92]

Attenuated total reflectance–Fourier transform infrared (ATR–FTIR) spectroscopy is a versatile tool for measuring infrared spectra of solids and liquids. ATR–FTIR spectroscopy of solids and liquids requires that the sample of interest be placed onto an internal reflection element (IRE). The IR beam from the spectrometer is directed onto the element at an angle, θ , greater than the critical angle, θ_c , so that the infrared light undergoes internal reflection. At each point of internal reflection an evanescent wave is produced, from which, the radiation can be absorbed by a sample that is placed in direct contact with the IRE. The evanescent wave of the infrared radiation has a limited

penetration depth on the order of 1 μm [9,94]. A pictorial representation is shown in Figure 2.13.

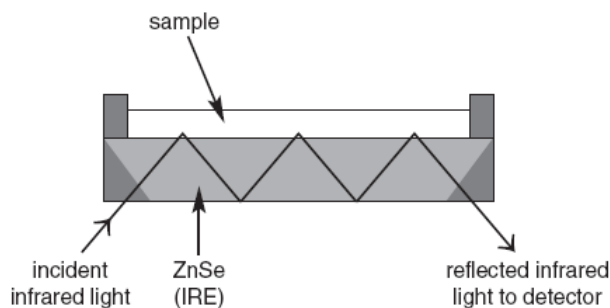


Figure 2.13 A pictorial representation of internal reflections through a high refractive index medium, for example, ZnSe, used as the internal reflection element (IRE). At each reflection, an evanescent wave is produced that decays exponentially into the medium above [95].

The absorption of the infrared light by the solid or liquid sample in direct contact with the IRE can be measured in this way. The absorbance is proportional to the path length, which is similar to transmission infrared spectroscopy. However, in the case of ATR-FTIR spectroscopy, the effective path length, b' , is equal to the number of reflections of the IR beam times the penetration depth,

$$b' = N d_p \quad (\text{eq. 2.1})$$

where N is the number of reflections and d_p is the penetration depth per reflection. The penetration depth, d_p , is

$$d_p = \frac{\lambda_1}{2\pi n_1 [\sin^2 \theta - n_{21}^2]^{1/2}} \quad (\text{eq. 2.2})$$

where n_1 is the index of refraction of the IRE, n_2 is the index of refraction of the sample medium in contact with the crystal, n_{21} is equal to n_2/n_1 and $\lambda_1 = \lambda_{\text{vacuum}} \cdot n_1$ [96-98]. The small penetration depth and short path length allow for infrared absorption measurements of a strongly adsorbing medium such as those for infrared measurements of aqueous solutions or polymers [93].

In the experiment presented in this thesis, a horizontal ATR internal reflection element, diamond, was chosen for the compatibility, refractive index, and transmission range as

well as durability and lower cost that still produced quality spectra. In addition, since d_p is wavelength dependent, the relative intensities of the absorption bands measured with different internal reflection elements can differ and these may also differ from a transmission FTIR spectrum of the sample [93].

2.3.1.2 Micro Raman Spectroscopy

Raman spectroscopy as a technique providing microscopic (vibrational) information on organic adsorbates at the semiconductor/solution interface was used in the present work. A brief description of the Raman effect is necessary in order to understand the theory behind surface-enhanced Raman. The Raman effect, originally observed by Lord Raman in 1928, is also a light-scattering effect. When an incident electromagnetic field, E_i , interacts with a molecule, an electric dipole is induced in the molecule [100-102], given by:

$$p = \alpha E_i \quad (\text{eq. 2.3})$$

where α is referred to as the polarizability of the molecule and p is the induced dipole. The incident field is a time-varying quantity of the form

$$E_i = E_o \cos(2\pi\nu_i t) \quad (\text{eq. 2.4})$$

For a vibrating molecule, the polarizability is also a time varying term with the frequency of vibration, ν_{vib} :

$$\alpha = \alpha_o + \alpha_{\text{vib}} \cos(2\pi\nu_{\text{vib}} t) \quad (\text{eq. 2.5})$$

Multiplication of the two time-varying terms, E_i and α , gives a cross term of the form:

$$\frac{\alpha_{\text{vib}} E_o}{2} \left[\cos 2\pi t(\nu_i + \nu_{\text{vib}}) + \cos 2\pi t(\nu_i - \nu_{\text{vib}}) \right] \quad (\text{eq. 2.6})$$

This cross term in the induced dipole represents light that can be scattered at both higher and lower energy than the Rayleigh (elastic) scattering of the incident radiation. The increments are given by the vibrational frequencies of the molecule, ν_{vib} . These lines are referred to as the “anti-Stokes” and “Stokes” lines, respectively. The Stokes lines are generally stronger. Since the Stokes and anti-Stokes lines contain the same type of information, generally only the stronger Stokes lines are scanned. When Lord Raman initially observed this effect, it was very difficult to discern owing to an extremely faint signal. However, use of a laser as the illumination source produces enough intensity that

current detection systems using either photomultiplier tubes or charge-coupled device (CCD) detectors can be used to observe the Raman effect relatively easily [99].

Raman spectra of molecules adsorbed onto metal colloids have been observed to exhibit a considerable signal enhancement [101,103-105]. This effect has been studied repeatedly since its discovery in 1974 and is known as surface-enhanced Raman spectroscopy (SERS). SERS is similar to resonance Raman scattering except that the resonances involved are not exclusively intramolecular. Nanoscale surface roughness supports the electromagnetic resonance which is the dominant mechanism of enhancement [106].

When electromagnetic radiation is incident on the particles of a metal colloid, a resonant field is induced. This resonance effect can be understood in terms of the bonding structure of metals. The electrons in metals behave as a sea of free negative charges, or plasma, bound by stationary cations. Excitation by an electromagnetic wave at a particular frequency can induce a resonant vibration of these free electrons. These vibrations are known as plasmons. The vibrating electrons will generate an additional electric field near the particle's surface at their vibrational frequency [103].

The enhancements in Raman signals observed in SERS are encountered when Raman-active molecules are adsorbed onto the surface of small metal particles. Since the Raman intensity is proportional to the square of the induced dipole moment [100], an enhancement of the signal can arise from a change in either the polarizability, α , or the exciting electromagnetic field, E_i (see eq. 2.3). Although both effects can contribute to the observed enhancement, the dominant contribution in this case is the electromagnetic field effect. Because of the resonance effect between colloidal metals and incident radiation, the field that actually induces Raman scattering on adsorbed molecules is a sum of the incident field, E_i , and the resonantly induced field near the surface, E_{ind} [99].

2.3.2 Core-hole electron spectroscopy

Electron spectroscopy methods are used to experimentally study the electronic structure of materials. The electronic structure can, for example, give information about what elements are present in the sample and their chemical state. By exciting an atom using an X-ray source, the electron configuration of the atom is changed; one (usually a core-shell) electron or more electrons populate unoccupied bound or continuum states. The success

of this spectrometry lies in the fact that the photoelectrons act as very sensitive probes that can “feel” the charge distribution and the arrangement of the neighboring atoms around the absorbing atom, or, in other words, they can feel the arrangement of the neighboring atoms (*chemical environment*). The electron spectroscopy techniques used in this thesis are shortly presented below.

2.3.2.1 X-ray Photoelectron Spectroscopy

X-ray Photoelectron spectroscopy, based on the photoelectric effect [107,106], was developed in the mid-1960’s by Kai Siegbahn and his research group at the University of Uppsala, Sweden [109].

X-ray photoelectron spectroscopy (XPS), also known as ESCA (Electron Spectroscopy for Chemical Analysis) is a powerful surface analysis technique, which provides elemental information about a surface as well as chemical state information. A sample material is bombarded by “monoenergetic” soft X-rays, causing electrons to be ejected. XPS spectral lines are identified by the shell from which the electron was ejected (1s, 2s, 2p, etc.) [110,111].

The ejected photoelectrons are collected as a function of their energy from which binding energies can be obtained using the Einstein equation:

$$BE = h\nu - KE - \Phi_{spec} \quad (\text{eq. 2.7})$$

where BE is the binding energy of the electron, KE is kinetic energy and Φ_{spec} the work function of the spectrometer. On a finer scale, it is also possible to identify the chemical state of the elements present from small variations in the determined kinetic energies.

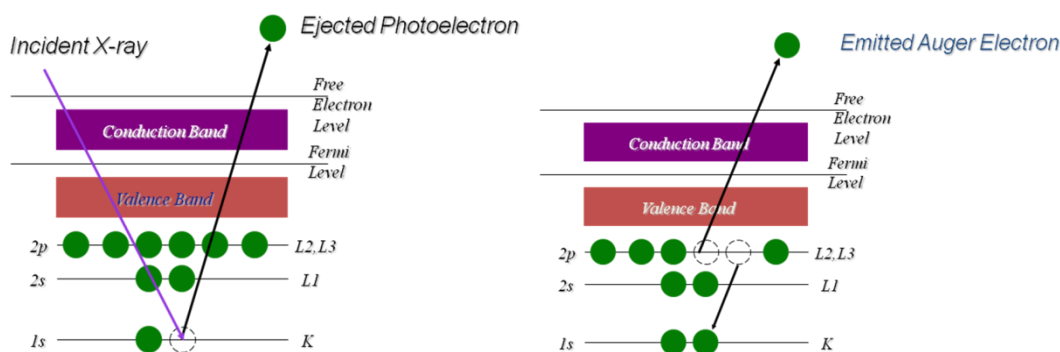


Figure 2.14 Photo-electric process in XPS (left) and Auger relation to core hole (right) [112]

Following the XPS process (Figure 2.14 left), the atom will release energy (relax back to ground state) by the emission of an Auger Electron. The L electron falls to fill core level vacancy (step 1). Then, a KLL Auger electron emitted to conserve energy is released in step 1. The kinetic energy of the emitted Auger electron is:

$$KE = E(K) - E(L_2) - E(L_3) \quad (\text{eq. 2.8})$$

The XPS instrument measures the kinetic energy of all collected electrons. Thus, the electron signal includes contributions from both photoelectron and Auger electron lines. For the kinetic energy scale in XPS ($KE = h\nu - BE - \Phi_{spec}$), photoelectron line energies are dependent on photon energy. However, Auger electron line energies are not dependent on photon energy. In case of binding energy in XPS ($BE = h\nu - KE - \Phi_{spec} - E_{ch}$), photoelectron line energies are not dependent on photon energy. But, Auger electron line energies are dependent on photon energy. E_{ch} is Surface Charge Energy. E_{ch} can be determined by electrically calibrating the instrument to a spectral feature such as C1s at 285.0 eV or Au4f_{7/2} at 84.0 eV [113].

Chemical shift values in XPS depend on the degree of electron bond polarization between nearest neighbor atoms. A specific chemical shift is the difference in BE values of one specific chemical state versus the BE of the pure element [114]. Figure 2.15 shows chemical shifts in XPS.

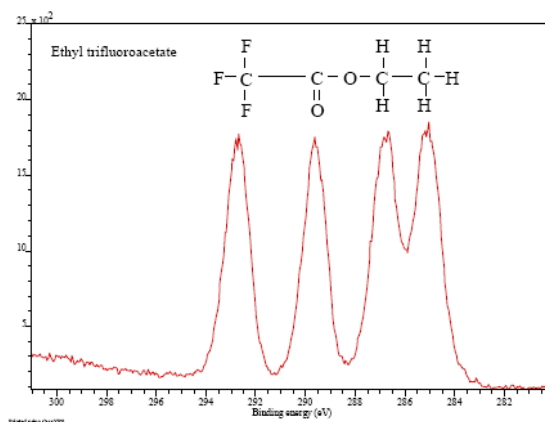


Figure 2.15 Chemical shifts in XPS [111]

Peaks derived from peak-fitting a raw chemical state spectrum are due to the presence of different chemical states. The chemical state of a group of elements, can be similar to, but is different from the chemical state of another very similar group of elements because the

two groups have different ratios of the same elements and exhibit different chemical, electronic, and physical properties that can be detected by various spectroscopic techniques [115]. In addition to the identity of the element and the orbital (s, p, d, f) electron binding energies depend on the formal oxidation state of the atom and the local chemical environment. Both cases cause small binding energy shifts (< 5 eV). An increase in oxidation state causes the binding energy to increase due to a decrease in the screening of the bound electron from the ion core. Thus, the ability of XPS to determine oxidation states is used extensively in catalysis research [116].

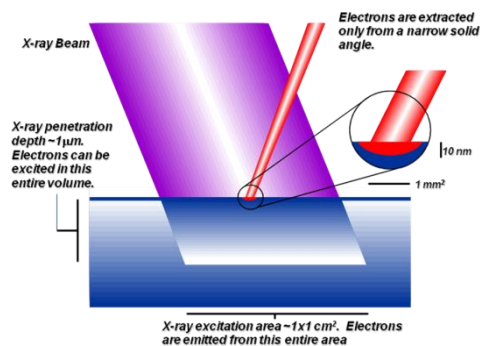


Figure 2.16 X-ray photoelectron spectroscopy-small area detection [112]

XPS probes 2-20 atomic layers (3-10 nm) deep for a solid sample as shown in Figure 2.16. The energy of the photoelectron depends on the angle (with respect to the surface) of the measurement. The escape depth Z of the photoelectron depends on its inelastic mean free path length λ as well as on its emission angle α with respect to the surface. The sampling depth can therefore be varied by making use of the equation:

$$Z = \lambda \cdot \sin\alpha \quad (\text{eq. 2.9})$$

The lateral resolution of this technique is around 2-10 μm. The particular strengths of XPS are semi-quantitative elemental analysis of surfaces, as well as chemical state analysis for vacuum-compatible materials as diverse as biological to metallurgical samples.

One more important characteristic of XPS is that XPS can be used for semi-quantitative analysis. Figure 2.17 (below) shows the quantitative analysis of Ni-Cu alloy from the XPS survey scan.

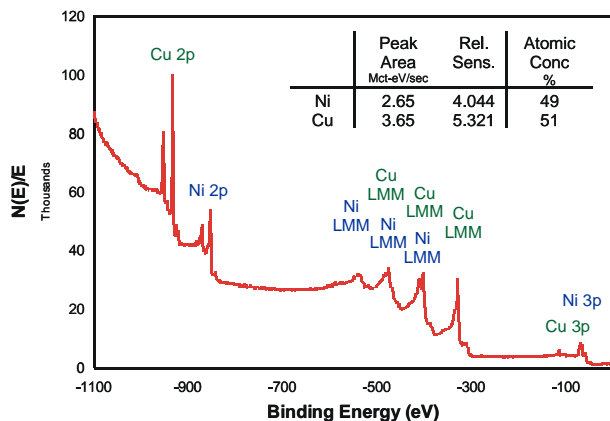


Figure 2.17 XPS of Cu-Ni alloy [112]

Quantitative accuracy depends on several parameters such as: signal-to-noise ratio, peak intensity, accuracy of relative sensitivity factors, and correction for electron transmission function, surface volume homogeneity, and correction for energy dependency of electron mean free path, and degree of sample degradation due to analysis. Under optimum conditions, the quantitative accuracy of the atomic percent (at %) values calculated from the major XPS peaks is 90-95 % for each major peak. If a high level quality control protocol is used, the accuracy can be further improved. Under routine work conditions, where the surface is a mixture of contamination and expected material, the accuracy ranges from 80-90 % of the value reported in atomic percent values. The quantitative accuracy for the weaker XPS signals, that have peak intensities 10-20 % of the strongest signal, are 60-80 % of the true value [117,118].

2.3.2.2 X-ray Absorption Spectroscopy

X-ray absorption spectroscopy (XAS) is a technique that measures the absorption, μ , by a sample as a function of photon energy, E (usually in units of electron volts). At the appropriate energies, core level electrons are promoted to empty or partially-empty bound states; at higher energies, the electrons are completely ionized to the continuum of unbound states [119]. As shown in Figure 2.18, there are several distinct processes that can occur during the generation of the XAS spectrum. The incident photon beam excites an electron from a core state into an unoccupied electronic state and the subsequent relaxation of the excited molecule results in the ejection of either an Auger electron or an

energetic photon with the cross-section of each process being atomic number dependent [120]. Indeed, it is generally possible to monitor each of these processes, as illustrated in Figure 2.19.

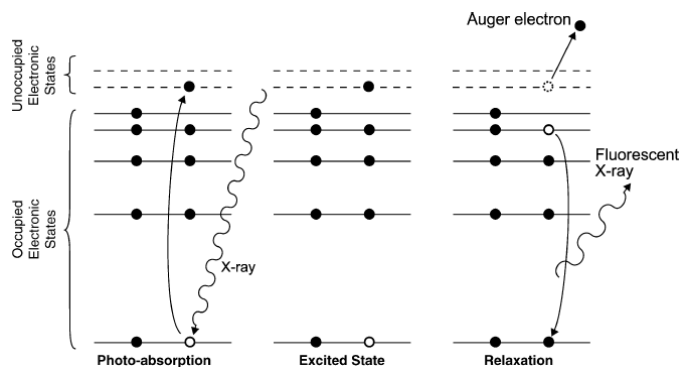


Figure 2.18 Schematic of the photo-absorption and relaxation processes occurring in a XAS experiment [121]

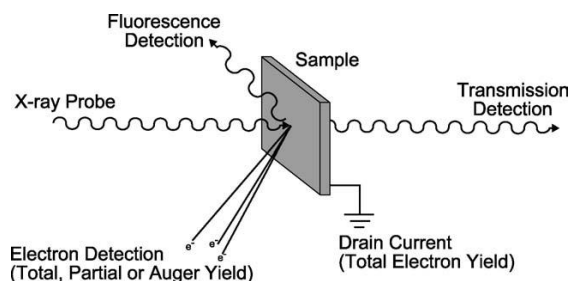


Figure 2.19 Schematic of the possible measurement techniques for NEXAFS spectroscopy [121]

The absorption process depicted in Figure 2.18 cannot be detected directly and so the XAS signal must be detected through either the absence of the absorbed photons in the transmitted X-rays (transmission detection) or through the particles ejected during the relaxation process that follows (fluorescence detection or electron detection). Energy discrimination allows the electron detection technique to be broken down into total (TEY), partial (PEY) and Auger (AEY) electron yield detection schemes [121].

XAS transitions are named according to the initial state with the principal quantum number as an uppercase letter and the specific absorption line (when more than one line is possible) as a subscript number. For example, $1s = K$; $2s = L_1$; $2p_{1/2} = L_2$; $2p_{3/2} = L_3$; $3s$

= M_1 ; and so on; thus, a K-edge spectrum spans the photon energy for the ionization of electrons from the 1s orbital whereas an $L_{2,3}$ -edge spectrum corresponds to the 2p electron ionization region [122,123].

XAS is an element-specific technique because the ionization energies of core electrons are generally well-separated from their nearest neighbor. For example, the C K-edge occurs at approximately 285 eV whereas the N K-edges are at ~ 400 eV. XAS is also versatile because it can be applied to almost any element and is sensitive to oxidation state, coordination number, or geometry. A key benefit of XAS is that it can be used for dilute, non-crystalline samples [119].

XAS (X-ray Absorption Spectroscopy) includes both XANES (X-ray Absorption Near Edge Structure) and EXAFS (Extended X-ray Absorption Fine Structure) regions of the XAS spectrum as shown in the Figure 2.20. Both of these are distinct but at the same time complementary methods which can be used to determine chemical, electronic and symmetry-coordination information for an element of interest [124,125].

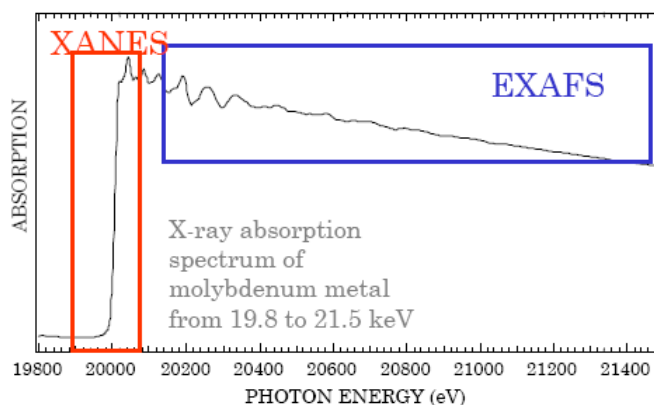


Figure 2.20 XAS spectrum of Molybdenum metal including XANES and EXAFS [126]

The limiting energy that divides XANES from EXAFS is not exactly defined since the transition from the one regime to the other is smooth: as energy is increased, the transition starts happening gradually. As a rule of thumb, near-edge structure ends approximately where the electron wavelength equals the distance from the absorbing atom to its nearest neighbors [127], which usually means about 40–50 eV above the edge. In the XANES regime, the electron's kinetic energy is small and the scattering on the neighboring atoms tends to be strong for this reason, while the effect of the scatterers

becomes smaller at higher energies; in EXAFS region, the photoelectrons are only weakly scattered.

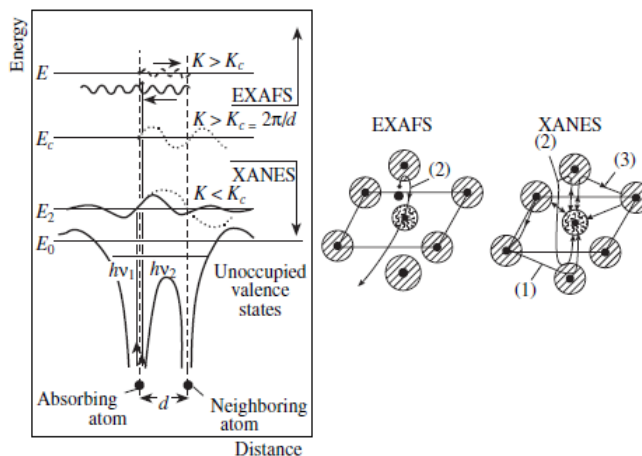


Figure 2.21 Scheme of interaction of a photoelectron with the atoms of the nearest environment [128]

In Figure 2.21, schematic diagrams illustrate the process of photon absorption by an atom in a solid. At photon energies exceeding the electron binding energy in an atom, an electron with an energy E and a wave vector k become excited. This electron is scattered by the potentials of the neighboring atoms (including the potential of the absorbing atom itself). At low photoelectron energies and, accordingly, large wavelengths, which are comparable with the interatomic distances R_0 in the crystal lattice, the contribution of multiple scattering generally significantly exceeds that of single scattering events. At high photoelectron energies, the de Broglie wavelength ($\lambda = h/p$, h is plank constant and p is momentum) is very small, and the processes of single scattering generally dominate [128].

XANES can be used to investigate the local coordination chemistry (octahedral, tetrahedral), molecular orbitals (p-d hybridization, crystal field theory), band structure (the density of available occupied electronic states) and spin state (high or low spin) of materials at the bulk and at interfaces [124,129,130]. More specifically, XANES at the $L_{2,3}$ -edge of transition metal cations (such as Ti^{4+}) are dominated by exchange

interactions, spin-orbit splitting and crystal field effects; all of which makes it a perfect probing tool to study coordination states. Thus the $L_{2,3}$ -edge XANES probes the electronic structure and crystal field details within the first coordination sphere (surface) and bulk depending upon which decay channel is used for detection (TEY, FY, PEY) [124,131,132]. In transition metal systems, the crystal field is related to their coordination and symmetry (Figure 2.22(a)) which in turn directly affects the XANES L-edge spectra of all transition metals including Ti^{4+} as shown very nicely by the spectra in Figure 2.22(b) and theoretically described by de Groot [132].

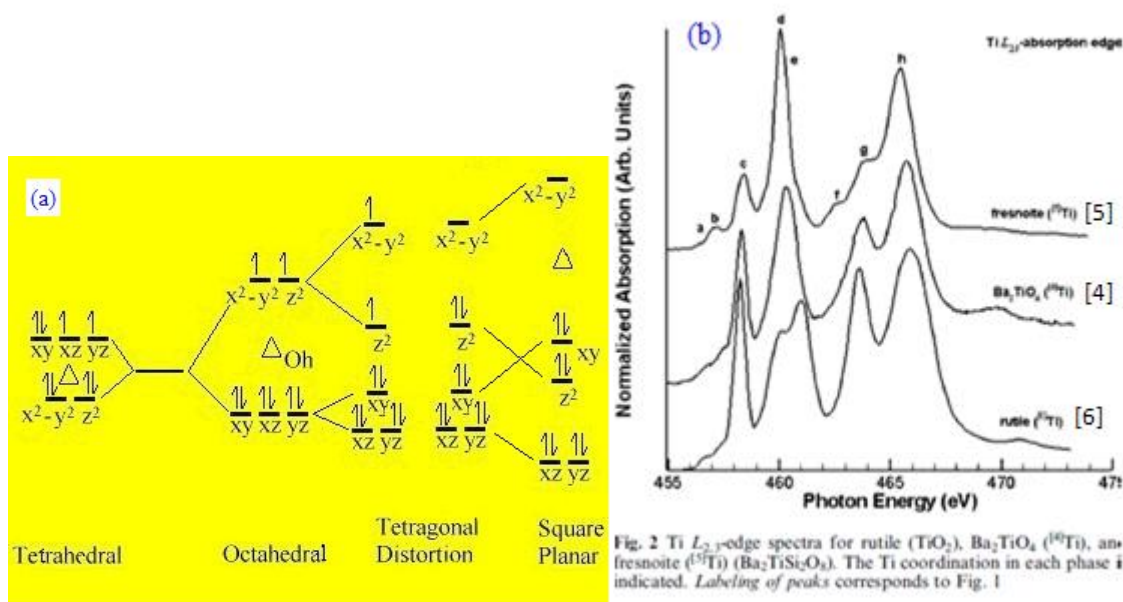


Figure 2.22 Crystal field splitting diagram for different symmetry and coordination (a) and Ti -L edge spectra of rutile TiO_2 , Ba_2TiO_4 and frenosite showing the effect of coordination change to the XANES spectra (b) [131]

For example if we take the case where a Ti^{4+} atom is in a coordination of O_h vs D_{4h} , the crystal field that is observed is distinct as shown from Figure 2.22(b). Thus if the coordination (symmetry) changes from O_h (CN = 6) to D_{4h} (CN = 4) around the Ti atoms, not only is the symmetry affected but so is the crystal field that is expressed. The fine structure of transition metal XANES spectra are well known to be governed by the crystal field, which is determined by the local symmetry around the Ti atoms, and as such have a significant impact upon the XANES spectra (Figure 2.22(b)).

EXAFS gives us information about (1) distances between central and neighboring atoms, (2) the number of neighboring atoms, (3) the nature of neighboring atoms (their approximate atomic number) and (4) changes in central-atom coordination with changes in experimental conditions.

In order to analyze EXAFS data, a number of variables must be considered. Some parameters are calculated or determined from model compounds whereas others are refined in the fitting process. Eq. 2.10 is the single-scattering EXAFS equation, which can be separated into the amplitude function and the phase function. Overall, eq. 2.10 describes the sum of all absorber-scatterer interactions, each of which is represented by a damped sine wave [133].

$$\chi(k) = \sum_s \frac{N_s A_s(k) S_0^2}{k R_{as}^2} \exp(-2R_{as}/\lambda(k)) \exp(-2k^2 \sigma_{as}^2) \cdot \sin(2k R_{as} + \phi_{as}(k)) \quad (\text{eq. 2.10})$$

In eq. 2.10, the parameters that are of principal interest for coordination chemistry are the number of scattering atoms, N_s and the absorber–scatterer distance, R_{as} . However, there are a variety of other parameters that must either be determined or be defined in order to extract the chemically relevant information. Chief among these are $A_s(k)$ and $\sigma_{as}(k)$. These represent, respectively, the energy dependence of the photoelectron scattering, and the phase shift that the photoelectron wave undergoes when passing through the potential of the absorbing and scattering atoms. These amplitude and phase parameters contain the information necessary to identify the scattering atom [134]. Once the $\chi(E)$ is isolated, the oscillations can be viewed and fit in k -space (\AA^{-1}), which is usually weighted as k^3 to enhance the dampened high k region (Figure 2.23(B)) [135]. The Fourier-Transform of the k -space plot results in a more conceptually-useful depiction in R -space (\AA) (Figure 2.18(C)) [119].

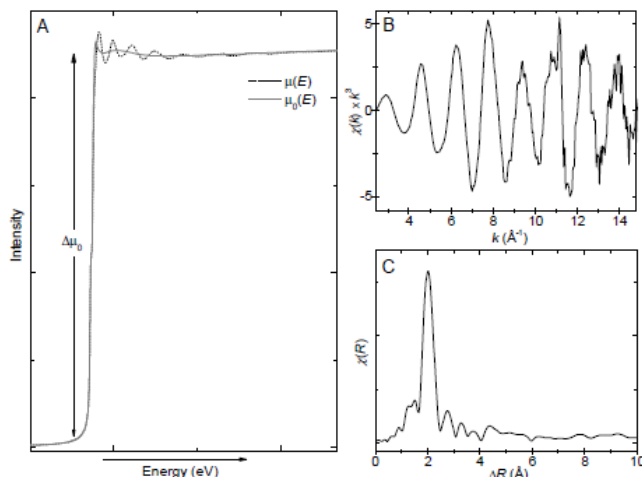


Figure 2.23 EXAFS data processing: spline function (A), k^3 -space (B) and R space (B) plots [133]

Although the R space plot is shifted and does not represent exact bond distances, examination ensures that the processing procedures have been successful and can indicate the relative number and distance of scattering atoms. To extract quantitative information from the EXAFS oscillations, some parameters are determined from model compounds or *ab initio* calculations. Those parameters are used for iterative data fitting [119].

In our studies the XANES region was the major tool of use in this study; however, the EXAFS region of the Ti K-edge was also investigated due to its relevance to previous works. Thus each term is used in the appropriate manner for the relevant section.

2.3.3 Electrochemical impedance spectroscopy (EIS)

Electrochemical impedance spectroscopy (EIS) is a steady state method measuring the current response to the application of an ac voltage as a function of the frequency [135]. An important advantage of EIS over other techniques is the possibility of using tiny ac voltage amplitudes exerting a very small perturbation on the system. EIS has been widely employed to study the kinetics of electrochemical and photoelectrochemical processes including the elucidation of salient electronic and ionic processes occurring in the DSSC [136-139]. The electronic processes in a DSSC are described by a general transmission line model, as shown in Figure 2.24 [141]. The Nyquist diagram (Figure 2.25(above)) features typically three semicircles that in the order of increasing frequency are attributed

to the Nernst diffusion within the electrolyte, the electron transfer at the oxide/electrolyte interface and the TiO_2 film, and the redox reaction at the platinum counter electrode[136]. However, owing to the complexity of the system, the unambiguous assignment of equivalent circuits and the elucidation of processes occurring on dye sensitized mesoscopic TiO_2 electrode is difficult and remains a topic of debate [140].

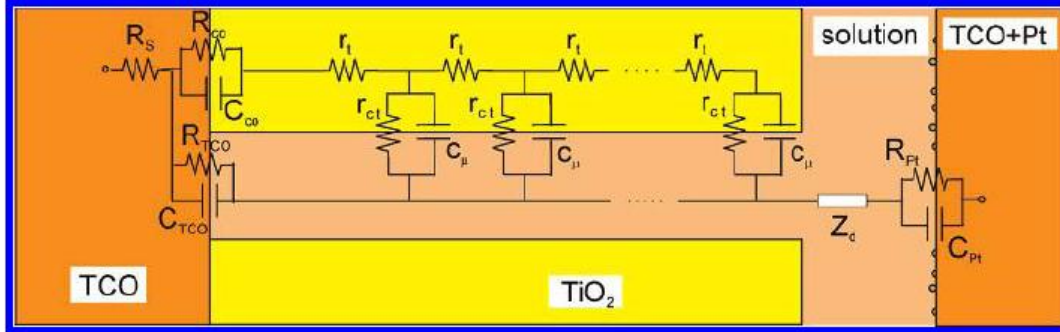


Figure 2.24 General transmission line mode of DSSC [141]

Here, the whole mesoscopic TiO_2 film is treated as an interconnected network. Under a forward bias, electrons are injected from FTO substrate into the TiO_2 and the film is charged by electron propagation through individual particles with a resistance of r_t . Some of the injected electrons recombine with the oxidized species in the electrolyte, characterized by a charge transfer resistance of r_{ct} and a capacitance of c_{ch} , and the rest of the electrons are then recaptured by the FTO current collector during the opposite phase of the sinusoidal voltage modulation. The two channels for electron transportation through TiO_2 and that of the I_3^- through the electrolyte are coupled in series [140-143]. Taking d as the thickness of the mesoscopic TiO_2 film, the electron transport resistance is $R_t = r_t \times d$, the interfacial charge recombination resistance is $R_{ct} = r_{ct} / d$ and the chemical capacitance of the film is $C_{ch} = c_{ch} \times d$, where the lower case letters represent resistances and capacitance that are normalized to the film thickness [142]. $R_{\text{FTO/EL}}$ and $C_{\text{FTO/EL}}$ stand for the charge transfer resistance and the corresponding double layer capacitance at exposed FTO/electrolyte interface and change with surface conditions (blocking layer and cleanliness). Due to the irreversibility of I/I_3^- couple on FTO, $R_{\text{FTO/EL}}$ is usually very large. The diffusion of I_3^- within a thin layer cell is described by a Nernst diffusion impedance Z_d . Regeneration of I_3^- at the counter electrode is characterized by R_{CE} and

C_{CE} , which are the charge transfer resistance and double layer capacitance at the platinized FTO, respectively [143].

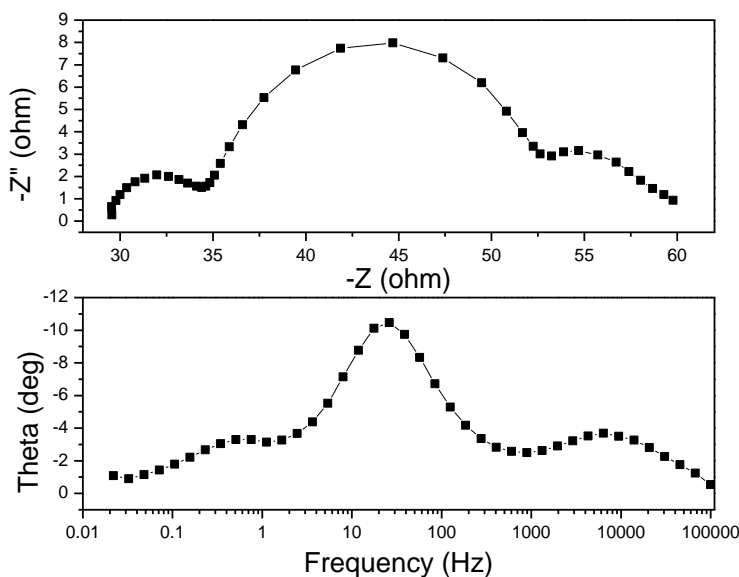


Figure 2.25 Typical EIS plots of a N719 sensitized DSSC: Nyquist plot (above) and Bode plot (below)

Typical impedance spectra are shown in Figure 2.25 and the data are measured using N719 sensitizer and commercial TiO_2 paste. The above curve displays real part (Z') versus the imaginary part (Z'') of the impedance, usually known as the Nyquist plot. The curve in below is the Bode plot where the phase angle θ is plotted against frequency. As shown in Figure 2.25 (above), the Nyquist plot consists of three semicircles. The semicircle occurring at high frequencies represents redox charge transfer at the platinum counter electrode, the large one at intermediate frequencies stands for the electron transport in the TiO_2 layer, and the electron transfer at the oxide/electrolyte interface while the third one at low frequencies is attributed to ion diffusion within the electrolyte. Accordingly, there are three peaks in the Bode plot, corresponding to the RC time constants shown in the Bode plot.

At the proper conditions, electron transport in the mesoscopic TiO₂ film, electron recombination at the TiO₂-electrolyte interface, charge transfer at the counter electrode, and diffusion of the redox species in a electrolyte can be well distinguished according to the spectral shapes of the impedance response as a function of frequency [141].

2.4 Application of these techniques in DSSC

In the subsequent chapters which are based on manuscripts/papers, appropriate reference is made to specific literature sources in relation to the study described. Here, only a brief general reference to the application these techniques in DSSC is discussed.

The use of vibrational spectroscopy in DSSC was described by Finnie et al. [144] in 1998 and Leon et al. [145] in 2006. Finnie et al. [144] reported analysis by IR and Raman spectroscopy of a series of parent dyes (N3, N719 and N712) and performed an in situ IR study of the corresponding sensitized TiO₂ photoelectrodes, to investigate the manner in which the dye molecules interact with the TiO₂ surface. They used $\Delta\nu$ method ($\Delta\nu_{\text{COO-asym}} - \Delta\nu_{\text{COO-sym}}$) in IR spectra to observe the nature of binding between dye and TiO₂ surface. This is because of the low symmetry of the COOH and COO⁻ groups which does not allow distinguishing the type of coordination based on the number of infrared and Raman active bands. In Leon et al.'s work [145], Raman, resonance Raman, and ATR-FTIR spectroscopies were used to investigate the nature of binding of two Ru-bpy complexes N719 and a new Ru complex (Ru(dcbpyH₂)₂(bpy-TPA₂)](PF₆)₂) on mesoporous TiO₂ films.

Core-shell electron spectroscopy for DSSC was described in the works of Ju et al. [146] in 2001, Zubavichus et al. [147] in 2002 and Johansson et al. [148] in 2005. Each groups used different electron spectroscopic technique such as EXAFS, XANES and XPS. Johansson et al. [148] used XPS to obtain element specific information on the electronic structure and molecular surface structure. They compared the molecular and electronic structure of N3 with that of BD (black dye) and N719 in detail when adsorbed on nanostructured TiO₂. In Zu et al.'s work [146], the interfacial structure of N3 dye adsorbed TiO₂ was probed by X-ray absorption spectroscopy and the Ti-O interatomic distance and the coordination number of the O atoms around the Ti central atoms were extracted by EXAFS calculation. Zubavichus et al. [147] characterized N719 and black dye adsorbed TiO₂ films using X-ray photoelectron spectroscopy, and Ti K-edge XAFS

(XANES and EXAFS). The data indicate, within the sensitivity limits of the methods applied, that coating with the dyes leads to a stronger distortion of the local environment of Ti atoms in anatase nanoparticles.

Electrochemical impedance spectroscopy (EIS) has been a useful tool to study the electrochemical performance of the dye sensitized solar cells. Among many DSSC publications including EIS characterization, the work of Wang et al. [140,141] and Bisquert [137,138,142] are mostly referred due to their systematic studies. Wang et al. [140,141] used EIS to investigate electronic and ionic processes in dye sensitized solar cells. They showed a theoretical model to interpret the frequency response of the device. Using EIS, they interpreted DSSC performance variations under prolonged thermal aging, which results mainly from the decrease in the lifetime of the conduction band electrons in the TiO₂ film. Bisquert [137,138] has developed an approach to the impedance of anomalous diffusion mechanisms in electrochemical systems to derive a series of improved models for the analysis of advanced devices.

2.5 References

- [1] Oregan, B.; Gratzel, M. *Nature* **1991**, *353*, 737
- [2] Gao, F.; Wang, Y.; Shi, D.; Zhang, J.; Wang, M.; Jing, X., Humphrhy-Baker, R.; Wang, P.; Zakeeruddine, S.; Gratzel, M. *J. Am. Chem.Soc.* **2008**, *130*, 10720
- [3] www1.eere.energy.gov/solar/review_meeting/pdfs/prm2010_nrel_frank.pdf
- [4] Hagfeldt, A.; Boschloo, G.; Sun, L.; Kloo, L.; Pettersson, H. *Chem. Rev.* **2010**, *110*, 6595
- [5] Fonash, S. J. In *Solar cell application physics*. Elsevier: USA, 2010; Chapter 7
- [6] Solanki, C. S., P-N Junction Diode: An Introduction to Solar Cells. *Solar Photovoltaics: Fundamentals Technologies and Applications*, PHI Learning Private Limited: New Delhi, 2009; pp 73-93
- [7] Zhang, J.; Zhang, L.; Liu, H.; Sun, A.; Liu, R. *Electrochemical Technologies for Energy Storage and Conversion*. Wiley-VCH: Weinheim, Germany, 2012; pp 89
- [8] Gordon, J. *Solar energy: the state of the art : ISES position papers*, James & James (science publisher) Ltd: London, UK; 2001; pp 302
- [9] Kitai, A. *Principles of Solar Cells*,

LEDs and Diodes: The Role of the PN Junction. Wiley & Sons: West Sussex, UK; 2011; pp 160

[10] Hagfeldt, A.; Gratzel, M. *Chem. Rev.* **1995**, *95*, 49

[11] Gratzel, M. *Nature* **2001**, *414*, 338

[12] Hara, K.; Arakawa, H. Dye-sensitized Solar Cells. In *Handbook of Photovoltaic Science and Engineering*; Luque, A.; Hegedus, S.; John Wiley & Sons Ltd.; England, 2003; pp 663-700

[13] Lee, K. E.; Charbonneau, C.; Shan, G.; Demopoulos, G. P.; Gauvin, R. *JOM*, **2009**, April, 52

[14] Anderson, N.; Lian, T. *Annu. Rev. Phys. Chem.* **2005**, *56*, 491

[15] Gratzel, M. *Inorg. Chem.* **2005**, *44*, 6841

[16] Frank, A. J.; Kopidakis, N.; van de Lagemaat, J. *Coord. Chem. Rev.* **2004**, *248*, 1165

[17] Wenger, B., "Effect of electronic and nuclear factors on the dynamics of dye-to-semiconductor electron transfer", PhD dissertation, EPFL, Lausanne, 2006

[18] <http://mageep.wustl.edu/SYMPOSIA/2008/Presentations/Tuesday/Misc/8.15am%20Graetzel.pdf>

[19] Yoshida, T.; Tochimoto, M.; Schlettwein, D.; Wohrle, D.; Sugiura, T.; Minoura, H. *Chem. Mater.* **1999**, *11*, 2657

[20] Tennakone, K.; Kumara, G.; Kottegoda, I. R. M.; Perera, V. P. S. *Chem. Commun.* **1999**, 15

[21] Ito, S.; Makari, Y.; Kitamura, T.; Wada, Y.; Yanagida, S. *J. Mater. Chem.* **2004**, *14*, 385

[22] Guo, P.; Aegerter, M. A. *Thin Solid Films* **1999**, *351*, 290

[23] Tan, B.; Toman, E.; Li, Y. G.; Wu, Y. Y. *J. Am. Chem. Soc.* **2007**, *129*, 4162

[24] Kay, A.; Gratzel, M. *Chem. Mater.* **2002**, *14*, 2930

[25] Barbe, C. J.; Arendse, F.; Comte, P.; Jirousek, M.; Lenzenmann, F.; Shklover, V.; Gratzel, M. *J. Am. Ceram. Soc.* **1997**, *80*, 3157

[26] Zaban, A.; Aruna, S. T.; Tirosh, S.; Gregg, B. A.; Mastai, Y. *J. Phys. Chem. B* **2000**, *104*, 4130

[27] Neale, N. R.; Frank, A. J. *J. Mater. Chem.* **2007**, *17*, 3216

- [28] Hore, S.; Palomares, E.; Smit, H.; Bakker, N. J.; Comte, P.; Thampi, K. R.; Kroon, J. M.; Hinsch, A.; Durrant, J. R. *J. Mater. Chem.* **2005**, *15*, 412
- [29] Benkstein, K. D.; Kopidakis, N.; van de Lagemaat, J.; Frank, A. J. *J. Phys. Chem. B* **2003**, *107*, 7759
- [30] Ito, S.; Liska, P.; Comte, P.; Charvet, R. L.; Pechy, P.; Bach, U.; Schmidt-Mende, L.; Zakeeruddin, S. M.; Kay, A.; Nazeeruddin, M. K.; Gratzel, M. *Chem. Commun.* **2005**, 4351
- [31] Zhang, Z. P.; Ito, S.; O'Regan, B.; Kuang, D. B.; Zakeeruddin, S. M.; Liska, P.; Charvet, R.; Comte, P.; Nazeeruddin, M. K.; Pechy, P.; Humphry-Baker, R.; Koyanagi, T.; Mizuno, T.; Gratzel, M. *Z. Phys. Chem.* **2007**, *221*, 319.
- [32] Hore, S.; Nitz, P.; Vetter, C.; Prahl, C.; Niggemann, M.; Kern, R. *Chem. Commun.* **2005**, 2011
- [33] Sommeling, P. M.; O'Regan, B. C.; Haswell, R. R.; Smit, H. J. P.; Bakker, N. J.; Smits, J. J. T.; Kroon, J. M.; van Roosmalen, J. A. M. *J. Phys. Chem. B* **2006**, *110*, 19191
- [34] O'Regan, B. C.; Durrant, J. R.; Sommeling, P. M.; Bakker, N. J. *J. Phys. Chem. C* **2007**, *111*, 14001
- [35] Barnes, P. R. F.; Anderson, A. Y.; Koops, S. E.; Durrant, J. R.; O'Regan, B. C. *J. Phys. Chem. C* **2008**, *113*, 1126
- [36] Fujishima, A.; Honda, K. *Nature* **1972**, *238*, 37
- [37] Sakai, N.; Fujishima, A.; Watanabe, T.; Hashimoto, K. *J. Phys. Chem. B* **2003**, *107*, 1028
- [38] Kuribayashi, K.; Iwata, H.; Hirose, F. *ECS trans.* **2007**, *6*, 15
- [39] Finnie, K. S.; Cassidy, D. J.; Bartlett, J. R.; Woolfrey, J. L. *Langmuir* **2001**, *17*, 816
- [40] Minella, M.; Giulia, M. F.; Maurino, V.; Minero, C.; Pelizzetti, E.; Coluccia, S.; Martra, G. *Langmuir*, **2010**, *26*, 2521
- [41] Morterra, C. *J. Chem. Soc., Faraday Trans. 1* **1988**, *84*, 1617
- [42] Prinet, M.; Pichat, P. P.; Mathieu, M. V. *J. Phys. Chem.* **1971**, *75*, 1216
- [43] Tsyganenko, A. A.; Filimonov, V. N. *J. Mol. Struct.* **1973**, *19*, 579
- [44] Busca, G.; Sausey, H.; Saur, O.; Lavalley, J. C.; Lorenzelli, V. *Appl. Catal.* **1985**, *14*, 245
- [45] Martra, G. *Appl. Catal., A* **2000**, *200*, 275

- [46] Selloni, A. *Nat. Mater.* **2008**, *7*, 613
- [47] Mann, J. R.; Gannon, M. K.; Fitzgibbons, T. C.; Detty, M. R.; Watson, D. F. *J. Phys. Chem. C* **2008**, *112*, 13057
- [48] Junghänel, M. “Novel aqueous electrolyte films for hole conduction in dye sensitized solar cells and development of an electron transport model”, PhD dissertation, Freie Universität Berlin, Berlin, 2007
- [49] Nazeeruddin, M. K.; Kay, I.; Rodicio, A.; Humphrey-Baker, R.; Müller, E.; Gratzel, M.; *J. Am. Chem. Soc.*, **1993**, *115*, 6382
- [50] Nazeeruddin, M. K.; Humphry-Baker, R.; Liska, P.; Gratzel, M. *J. Phys. Chem. B*, **2003**, *107*, 8981
- [51] Nazeeruddin, M. K.; De Angelis, F.; Fantacci, S.; Selloni, A.; Viscardi, G.; Liska, P.; Ito, S.; Takeru, B.; Gratzel, M. *J. Am. chem. Soc.*, **2005**, *127*, 16835
- [52] Ding, I.; Tetreault, N.; Brilllet, J.; Hardin, B. E.; Smith, E. H.; Rosenthal, S. J.; Sauvage, F.; Grazel, M.; McGehee, M. D. *Adv. Funct. Mater.* **2009**, *19*, 2431–2436
- [53] Wang, P.; Zakeeruddin, S. M.; Moser, J. E.; Humphrey-Baker, R.; Comte, P.; Aranyos, V.; Hagfeldt, A.; Nazeeruddin, M. K.; Gratzel, M. *Adv. Mater.*, **2004**, *16*, 1806
- [54] Wang, P.; Klein, C.; Humphry-Baker, R.; Zakeeruddin, S. M.; Gratzel, M. *J. Am. chem. Soc.*, **2005**, *127*, 808
- [55] Kuang, D.; Ito, S.; Wenger, B.; Klein, C.; Moser, J. E.; Humphry-Baker, R.; Zakeeruddin, S. M.; Gratzel, M. *J. Am. chem. Soc.*, **2006**, *128*, 4146
- [56] Zikalova, M.; Zikal, A.; Kavan, L.; Nazeeruddin, M. K.; Liska, P.; Gratzel, M. *Nano Lett.*, **2005**, *5*, 1789
- [57] Nazeeruddin, M. K.; Pechy, P.; Renouard, T. Zakeeruddin, S. M.; Humphry-Baker, R.; Comte, P.; Liska, P.; Le, C.; Costa, E. Shklover, V.; Spiccia, L.; Deacon, G.B.; Bignozzi, C. A.; Gratzel, M. *J. Am. Chem. Soc.* **2001**, *123*, 1613
- [58] Nazeeruddin, M. K.; Bessho, T.; Cevey, Le.; Ito, S.; Klein, C.; De Angelis, F.; Fantacci, S.; Comte, P.; Liska, P.; Imai, H.; Graetzel, M. *J. Photochem. Photobiol., A*, **2007**, *185*, 331-337
- [59] Robson, K. C. D.; Sporinova, B.; Koivisto, B. D.; Schott, E.; Brown, D. G.; Berlinguette, C. P. *Inorg. Chem.* **2011**, *50*, 6019–6028

- [60] Robson, K. C. D.; Koivisto, B. D.; Yella, A.; Sporinova, B.; Nazeeruddin, M. K.; Baumgartner, T.; Gratzel, M.; Berlinguette, C. P. *Inorg. Chem.* **2011**, *50*, 5494–5508
- [61] Lammi, R. K.; Wagner, R. W.; Ambroise, A.; Diers, J. R.; Bocian, D. F.; Holten, D.; Lindsey, J. S. *J. Phys. Chem. B* **2001**, *105*, 5341.
- [62] Cherian, S.; Wamser, C. C. *J. Phys. Chem. B* **2000**, *104*, 3624.
- [63] Fungo, F.; Otero, L.; Durantini, E. N.; Silber, J. J.; Sereno, L. E. *J. Phys. Chem. B* **2000**, *104*, 7644.
- [64] Campbell, W. M.; Burrell, A. K.; Officer, D. L.; Jolley, K. W. *Coord. Chem. Rev.* **2004**, *248*, 1363.
- [65] Campbell, W. M.; Jolley, K. W.; Wagner, P.; Wagner, K.; Walsh, P. J.; Gordon, K. C.; Schmidt-Mende, L.; Nazeeruddin, M. K.; Wang, Q.; Gratzel, M.; Officer, D. L. *J. Phys. Chem. C* **2007**, *111*, 11760.
- [66] Schmidt-Mende, L.; Campbell, W. M.; Wang, Q.; Jolley, K. W.; Officer, D. L.; Nazeeruddin, M. K.; Gratzel, M. *ChemPhysChem* **2005**, *6*, 1253.
- [67] Hara, K.; Sato, T.; Katoh, R.; Furube, A.; Ohga, Y.; Shinpo, A.; Suga, S.; Sayama, K.; Sugihara, H.; Arakawa, H. *J. Phys. Chem. B* **2003**, *107*, 597.
- [68] Hara, K.; Wang, Z. S.; Sato, T.; Furube, A.; Katoh, R.; Sugihara, H.; Dan-Oh, Y.; Kasada, C.; Shinpo, A.; Suga, S. *J. Phys. Chem. B* **2005**, *109*, 15476.
- [69] Rehm, J. M.; McLendon, G. L.; Nagasawa, Y.; Yoshihara, K.; Moser, J.; Gratzel, M. *J. Phys. Chem.* **1996**, *100*, 9577
- [70] Horiuchi, T.; Miura, H.; Uchida, S. *J. Photochem. Photobiol., A* **2004**, *164*, 29.
- [71] Horiuchi, T.; Miura, H.; Sumioka, K.; Uchida, S. *J. Am. Chem. Soc.* **2004**, *126*, 12218.
- [72] Ito, S.; Zakeeruddin, S. M.; Humphry-Baker, R.; Liska, P.; Charvet, R.; Comte, P.; Nazeeruddin, M. K.; Pechy, P.; Takata, M.; Miura, H.; Uchida, S.; Gratzel, M. *Adv. Mater.* **2006**, *18*, 1202
- [73] Ito, S.; Miura, H.; Uchida, S.; Takata, M.; Sumioka, K.; Liska, P.; Comte, P.; Pechy, P.; Gratzel, M. *Chem. Commun.* **2008**, 5194.
- [74] Lin, J. T.; Chen, P.-C.; Yen, Y.-S.; Hsu, Y.-C.; Chou, H.-H.; Yeh, M.-C. *P. Org. Lett.* **2009**, *11*, 97

- [75] Choi, H.; Baik, C.; Kang, S. O.; Ko, J.; Kang, M. S.; Nazeeruddin, M. K.; Gratzel, M. *Angew. Chem., Int. Ed.* **2008**, *47*, 327.
- [76] Zhang, G. L.; Bala, H.; Cheng, Y. M.; Shi, D.; Lv, X. J.; Yu, Q. J.; Wang, P. *Chem. Commun.* **2009**, 2198.
- [77] Wang, Y. Q.; Sun, Y. M.; Song, B.; Xi, J. T. *Sol. Energy Mater. Sol. Cells* **2008**, *92*, 660.
- [78] Hara, K.; Nishikawa, T.; Kurashige, M.; Kawauchi, H.; Kashima, T.; Sayama, K.; Aika, K.; Arakawa, H. *Sol. Energy Mater. Sol. Cells* **2005**, *85*, 21–30
- [79] Schlichthorl, G.; Huang, S. Y.; Sprague, J.; Frank, A. J. *J. Phys. Chem. B* **1997**, *101*, 8141.
- [80] Haque, S. A.; Tachibana, Y.; Willis, R. L.; Moser, J. E.; Gratzel, M.; Klug, D. R.; Durrant, J. R. *J. Phys. Chem. B* **2000**, *104*, 538.
- [81] Boschloo, G.; Hagman, L.; Hagfeldt, A. *J. Phys. Chem. B* **2006**, *110*, 13144.
- [82] Mikoshiba, S.; Murai, S.; Sumino, H.; Hayase, S. *Chem. Lett.* **2002**, 1156.
- [83] Bach, U.; Lupo, D.; Comte, P.; Moser, J. E.; Weissortel, F.; Salbeck, J.; Spreitzer, H.; Gratzel, M. *Nature* **1998**, *395*, 583.
- [84] Kron, G.; Egarter, T.; Werner, J. H.; Rau, U. *J. Phys. Chem. B* **2003**, *107*, 3556
- [85] Bai, Y.; Cao, Y.; Zhang, J.; Wang, M.; Li, R.; Wang, P.; Zakeeruddin, S. M.; Gratzel, M. *Nat. Mater.* **2008**, *7*, 626
- [86] Wang, M.; Chamberland, N.; Breau, L.; Moser, J. E.; Humphry-Baker, R.; Marsan, B.; Shaik, M.; Zakeeruddin, S. M.; Gratzel, M. *Nat. Chem.* **2010**, *2*, 385
- [87] Hauch, A.; Georg, A. *Electrochim. Acta* **2001**, *46*, 3457.
- [88] Papageorgiou, N.; Maier, W. F.; Gratzel, M. *J. Electrochem. Soc.* **1997**, *144*, 876.
- [89] Kay, A.; Gratzel, M. *Sol. Energy Mater. Sol. Cells* **1996**, *44*, 99
- [90] Wang, M.; Anghel, A. M.; Marsan, B.; Ha, N.C.; Pootrakulchote, N.; Zakeeruddin, S. M.; Gratzel, M. *J. Am. Chem. Soc.*, **2009**, *131*, 15976
- [91] Harris, D. C.; Bertolucci, M. D. *Symmetry and spectroscopy: an introduction to vibrational and electronic spectroscopy*; Courier Dover Publications; Mineola, N.Y.; 1989; pp 93-224
- [92] Perkins, W. D. *J. Chem. Educ.* **1987**, *64*, A269-A271

- [93] Ingle, J. D., Jr.; Crouch, S. R. *Spectrochemical Analysis*; Prentice-Hall: Upper Saddle River, NJ, 1988; pp 34–35.
- [94] Tanaka, T.; Nagao, S.; Ogawa, H. *Anal. Sci.* **2001**, *17*, i1081
- [95] Schuttlefield, J. D.; Grassian, V. H. *J. Chem. Educ.* **2008**, *85*, 279
- [96] Gebel, M. E.; Kaleuati, M. A.; Finlayson-Pitts, B. J. *J. Chem. Educ.* **2003**, *80*, 672
- [97] Harrick, N. J. *Internal Reflection Spectroscopy*; Wiley: New York, 1967; pp 1–327.
- [98] Hug, S. J.; Sulzberger, B. *Langmuir* **1994**, *10*, 3587
- [99] Gabriela C. Weaver and Karen Norrod, *J. Chem. Educ.* **1998**, *75*, 621
- [100] Ferraro, J. R.; Nakamoto, K. *Introductory Raman Spectroscopy*; Academic: Boston, 1994.
- [101] Creighton, J. A. *Surface Enhanced Raman Spectroscopy*; Chang, R. K.; Furtak, T. E., Eds.; Plenum: New York, 1982; pp 315–338.
- [102] Diem, M. *Introduction to Modern Vibrational Spectroscopy*; Wiley: New York, 1993.
- [103] Kerker, M. *Proc. R. Inst. GB* **1989**, *61*, 229
- [104] Kerker, M. *Appl. Opt.* **1991**, *30*, 4699
- [105] Kneipp, K.; Moskovits, M.; Kneipp, H. *Surface-enhanced raman scattering physics and applications*; Springer: Germany, 2006; pp 1-13
- [106] Campion, A.; Kambhampati, P. *Chem. Soc. Rev.* **1998**, *27*, 241
- [107] Hertz, H. *Ann. Physik* **1887**, *31*, 983
- [108] Einstein, A. *Ann. Physik* **1905**, *17*, 132 (1921 Nobel Prize in Physics)
- [109] Siegbahn, K.; Nordling, C.; Fahlman, A.; Nordberg, R.; Hamrin, K.; Hedman, J.; Johansson, G.; Bergmark, T.; Karlsson, S.-E.; Lindgren, I.; Lindberg, B. *ESCA Atomic, Molecular and Solid State Structure Studied by Means of Electron Spectroscopy*; Presented to the Royal Society of Sciences of Uppsala, December 3, 1965; Amqvist & Wiksells: Uppsala, 1967.
- [110] *Electron Spectroscopy of Solids and Surfaces. Faraday Disc. Chem.Soc.*, No. 60; The Faraday Division Chemical Society: London, 1975.
- [111] Siegbahn K.; Svartholm N., *Nature* **1946**, *157*, 872
- [112] groups.mrl.illinois.edu/nusso/0-ppt/XPS%20Class%2099.pps

- [113] ISO 15472: 2001. *Surface Chemical Analysis—X-ray Photoelectron Spectrometers—Calibration of Energy Scales*; International Organization for Standardization: Geneva, 2001.
- [114] Fadley, C.S. *J. Electron. Spectrosc. Relat. Phenom.* **2010**, 178–179, 2
- [115] Powell, C. J. *J. Chem. Educ.* **2004**, 81, 1734
- [116] Patterson, T.A.; Carver, J. C.; Leyden, D. E.; Hercules, D. M. *J. Phys. Chem.* **1976**, 80, 1700.
- [117] Nichols, G. D.; Hercules, D. M. *Applied Spectrosc.* **1974**, 28, 219.
- [118] Wyatt, D. M.; Carver, J. C.; Hercules, D. M. *Anal. Chem.* **1975**,
- [119] Penner-Hahn, J. E. *Coord. Chem. Rev.* 2005, 249, 161-177 47, 1297
- [120] Briggs, D.; Seah M. P.(Eds.), *Practical Surface Analysis: Auger and X-ray photoelectron spectroscopy*, 2nd ed., Wiley, 1990; vol. 1, pp 145-223
- [121] Watts, B.; Thomsen, L.; Dastoor, P. C. *J. Electron. Spectrosc. Relat. Phenom.* **2006**, 151, 105
- [122] Thompson, A.; Vaughan, D., Eds. *X-ray Data Booklet*: Lawrence Berkeley National Laboratory: Berkeley, 2001.
- [123] Wende, H. *Rep. Prog. Phys.* **2004**, 67, 2105
- [124] Stöhr, J. *NEXAFS Spectroscopy*; Springer: Berlin, 1992
- [125] Hayes, T. M.; Boyce, J. B. In *Solid State Physics*; eds. Ehrenreich, H., Seitz, F., Turnbull, D.; Academic: New York, 1982; vol 37, pp 173-351
- [126] Simon R. Bare, EXAFS Data Collection and Analysis Course, NSLS, September 23-25, 2002
(<http://chemistry.st-and.ac.uk/staff/gh/teaching/CH5711/Further%20reading/xanes.pdf>)
- [127] *X-ray Absorption – Principles, Applications, Technologies of EXAFS, SEXAFS and XANES*, ed. by D. C. Koningsberger and R. Prins, John Willey (1998), chapter 2
- [128] Aksenov, V. L.; Koval'chuk, M. V.; Kuz'min, A. Yu.; Purans, Yu.; Tyutyunnikov, S. I. *Crystallogr. Rep.* **2006**, 51, 908
- [129] Nilsson, A. *J. Electron. Spectrosc. Relat. Phenom.* **2002**, 126, 3
- [130] Ade, H.; Stoll, H. *Nat. Mater.* **2009**, 8, 281
- [131] Handerson, G. S.; Liu, X.; Fleet, M. E. *Phys Chem Mineral* **2002**, 29, 32
- [132] de Groot, F. *Coord. Chem. Rev.* **2005**, 249, 31

- [133] Zhang, H. H.; Hedman, B.; Hodgson, K. O. *Inorganic Electronic Structure and Spectroscopy, Volume I: Methodology*; Solomon, E. I., Lever, A. B. P., Eds.; John Wiley & Sons: New York, 1999, p 513-554
- [134] Penner-hahn, J. E. http://www.umich.edu/~jphgroup/XAS_Course/CCC2_XAS.pdf
- [135] Ross, M. J.; William, K. R. *Impedance Spectroscopy: Emphasizing Solid Materials and Systems*; John Wiley & Sons: New York, 1987
- [136] Kern, R.; Sastrawan, R.; Ferber, J.; Stangl, R.; Luther, J. *Electrochim. Acta* **2002**, *47*, 4213
- [137] Bisquert, J. *Phys. Chem. Chem. Phys.* **2003**, *5*, 5360.
- [138] Bisquert, J.; Garcia-Belmonte, G.; Fabregat-Santiago, F.; Ferriols, N. S.; Bogdanoff, P.; Pereira, E. C. *J. Phys. Chem. B* **2000**, *104*, 2287.
- [139] Zaban, A.; Meier, A.; Gregg, B. A. *J. Phys. Chem. B* **1997**, *101*, 7985.
- [140] Wang, Q.; Moser, J. E.; Gratzel, M. *J. Phys. Chem. B* 2005, *109*, 14945
- [141] Wang, Q.; Ito, S.; Gratzel, M.; Fabregat-Santiago, F.; Mora-Sero, I.; Bisquert, J.; Bessho, T.; Imai, H. *J. Phys. Chem. B* 2006, *110*, 25210
- [142] Bisquert, J. *J. Phys. Chem. B* **2002**, *106*, 325
- [143] Zhang, Z. "Enhancing the Open-Circuit Voltage of Dye-Sensitized Solar Cells: Co-adsorbents and Alternative Redox Couples", PhD dissertation, EPFL, 2008
- [144] Finnie, K. S.; Bartlett, J. R.; Woolfrey, J. L. *Langmuir* 1998, *14*, 2744-2849
- [145] Leon, C. P.; Kador, L.; Peng, B.; Thelakkat, M. *J. Phys. Chem. B* 2006, *110*, 8723-8730
- [146] Ju, X.; Wu, K. W.; Hou, Y. J.; Xie, P. H.; Zhang, B. W. *Surf. Interface. Anal.* **2001**, *32*, 95-97
- [147] Zubavichus, Y. V.; Slovokhotov, Yu. L.; Nazeeruddin, M. K.; Zakeeruddin, S. M.; Gratzel, M.; Shklover, V. *Chem. Mater.* **2002**, *14*, 3556-3563
- [148] Johansson, E. M. J.; Hedlund, M.; Siegbahn, H.; Rensmo, H. *J. Phys. Chem. B* 2005, *109*, 22256-22263

Chapter 3. Adsorption Mechanism of N719 Sensitizer on Anatase TiO₂ Films for DSSC Applications Using Vibrational Spectroscopy and Confocal Raman Imaging

In this first of 4 papers-chapters series, the binding mechanism between N719 dye and anatase TiO₂ surface is studied using vibrational spectroscopy (ATR-FTIR and Raman) and Confocal Raman imaging. Raman and IR spectroscopy can show the changes in molecular symmetry due to adsorption (therefore, the molecular orientation at the surface) and changes in chemical bonding associated with surface adsorption hence their application in this work. These two techniques are complementary since according to the spectroscopic selection rule for infrared spectroscopy is only transitions that cause a change in dipole moment that can be observed; on the other hand, for a mode to be Raman active it must involve a change in the polarisability, which means that not all vibrational modes appear in Raman spectra. In fact for centrosymmetric molecules the Raman active modes are IR inactive, and vice versa. Therefore, two vibrational spectroscopic techniques were combined to investigate the nature of binding of the N719 on TiO₂. This spectroscopic study aimed at (1) resolving and unifying the binding mechanism ideas that have been proposed to operate between the N719 complex and nano-crystalline anatase TiO₂ films; and (2) in particular shedding light as to the way in which various molecular groups are involved in the binding mechanism.

3.1 Abstract

Vibrational spectroscopic studies of N719 dye adsorbed-TiO₂ films have been carried out by using Raman SERRS, ATR-FTIR and Confocal Raman imaging. The high wavenumber region (3000~4000 cm⁻¹) of dye adsorbed TiO₂ is analyzed in Raman and IR spectra to investigate the role of TiO₂ surface groups in the anchoring mode. As a complementary technique, Confocal Raman imaging is employed to study the distribution features of key dye groups (COO⁻, bipyridine and C=O) on the anatase surface. Sensitized TiO₂ films made from two different nanocrystalline anatase powders are investigated: a commercial one (Dyesol) and our synthetic variety produced through aqueous synthesis. It is proposed the binding of the N719 dye to TiO₂ to occur through two neighboring carboxylic acid/carboxylate groups via a combination of bidentate-bridging and H-bonding involving a donating group from the N719 (and/or Ti-OH) units and acceptor from the Ti-OH (and/or N719) groups. The Raman imaging distribution of COO⁻_{sym} on TiO₂ was used to show the covalent bonding, while the distribution of C=O mode was applied to observe the electrostatically bonded groups.

3.2 Introduction

Dye-sensitized solar cells (DSSCs) are being intensively investigated due to their application in solar energy conversion and photovoltaic systems[1-4]. The TiO₂ semiconductor/Ru complex [*cis* - (2,2'- bipyridyl - 4,4'- dicarboxylate)₂ (NCS)₂ ruthenium(II): N719] interface has been studied to understand the sensitization event using vibrational spectroscopy[5-8], X-ray absorption spectroscopy[9] and computational modeling studies[10-12]. In spite of several studies of the interaction of the N719 /TiO₂ system, the anchoring mechanism has been debated for a decade. The importance of investigating the type of anchoring between the sensitizer molecules and the TiO₂ surface is emphasized by the fact that the bonding mechanism and electronic coupling between semiconductor and dye, directly impacts onto electron transfer and the performance of the dye-sensitized photoanode[13].

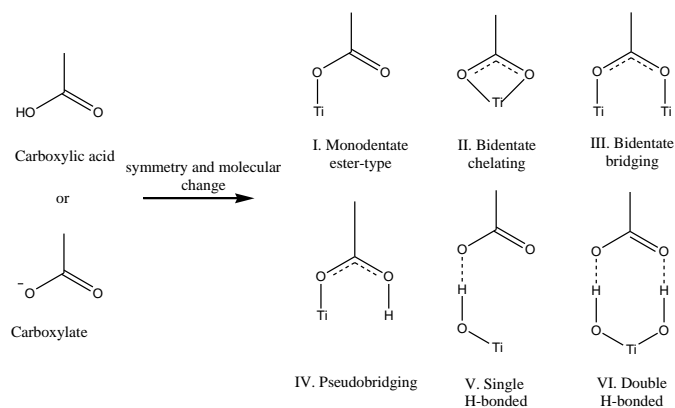


Figure 3.1 Possible anchoring modes for the N719 molecule

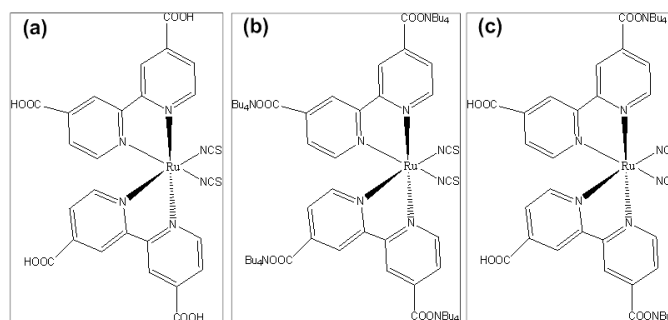


Figure 3.2 The molecular structures of various Ru sensitizer complexes: (a) N3: (cis-di(thiocyanato)-bis(2,2'-bipyridyl-4,4'-dicarboxylic acid)-ruthenium(II)), (b) N712: (tetra(tetrabutylammonium)[cis-di(thiocyanato)-bis(2,2'-bipyridyl-4,4'-dicarboxylate)-ruthenium(II)]) and (c) N719: (bis(tetrabutylammonium)[cis-di(thiocyanato)-bis(2,2'-bipyridyl-4-carboxylate-4'-carboxylic acid)-ruthenium(II)])

Figure 6.1 shows the possible anchoring modes for the carboxylic and carboxylate groups that may participate in the N719 binding to the TiO₂ surface[8,14]. Falaras[5] reported that the N719 sensitizer (Fig. 2) binds to the TiO₂ surface via ester-like bond (mode I, Fig.3.1) deduced from the $\nu(\text{C}=\text{O})$ shift of 20 cm^{-1} relative to the neat dye in the FTIR spectrum. Finnie *et al.*[6] reported that the N3 (Fig. 3.2) sensitizer anchors on the surface of TiO₂ in a bidentate chelating or bridging type of mode (modes II and III, Fig. 3.1). In their case, they used the splitting of carboxylate stretching bands ($\Delta\nu = \nu_{\text{asym}}(\text{COO}^-) - \nu_{\text{sym}}(\text{COO}^-)$) to distinguish possible modes of coordination, which indicated a bridging or bidentate chelating coordination. Shklover *et al.*[10] made further suggestions as to the

possible anchoring modes of the N3 sensitizer on the TiO₂, based on computational studies, and presented two thermodynamically favorable models (Fig. 3.3(A),(B)).

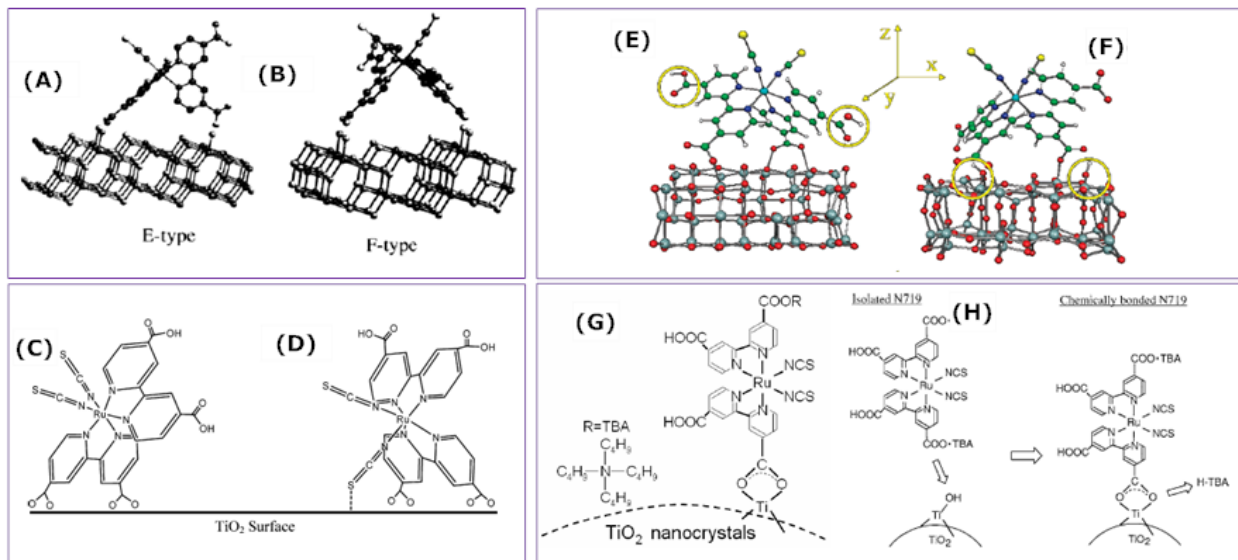


Figure 3.3 Binding mechanisms that have been proposed by previous authors [10,12,16,17,25]

Figure 3.3(A) indicates the N3 molecule bonded to the TiO₂ surface via two of its four carboxylic acid groups coming from two different bipyridine ligands and (B) indicates the N3 molecule bonded to the TiO₂ surface via one carboxylic acid and one carboxylate group coming from two different bipyridine ligands[10]. Figure 3.3(C) and (D) show how the NCS ligand of N3 and N719 molecule may interact with the TiO₂ surface where the former shows a configuration with chemically equivalent NCS groups and the latter shows a configuration where sulfur atoms in NCS interact with the TiO₂ surface[25]. Figure 3.3(E) and (F) show the configurations where the two protons initially carried by the N719 dye are retained on the N719 and when there are transferred from the dye to the TiO₂ particles respectively[12]. Lastly, Figure 3.3(G) and (H) show a binding mechanism where the N719 dye adsorbs to the TiO₂ via one of its carboxylate groups displacing the Ti-OH surface proton to the TBA⁺ molecules[16,17].

Nazeeruddin *et al.*[7] supported Shklover *et al.*'s findings[10] based on their ATR-FTIR spectra; here they investigated three types of Ru complexes (N3, N712 and N719, Fig. 3.2) to determine how many carboxylic groups coordinate and which groups (COOH

or COO⁻) are involved. Binding of all four of the binding groups was deemed for steric reasons to be impossible and thus they proposed the use of only two carboxylic groups in a bridging coordination (mode III, Fig. 3.1). On the basis of carboxylate vibrations present in the FTIR spectra of the N719 complex adsorbed onto TiO₂, they further specified that it was the two carboxylic groups *trans* to the NCS group involved in the bridging mechanism (Figure 3.3). The bidentate chelating mode (mode II, Fig. 3.1) was deemed highly unstable[15]. Later on, Leon *et al.*[8] examined the adsorption of N719 onto TiO₂ using SERRS at 514nm, SERS at 632 nm, normal FTIR and ATR-FTIR spectroscopies; here they suggested based on the $\Delta\nu$ frequency change of COO⁻ (Table 3.1) that the N719 carboxylate groups bind either by the bridging or bidentate chelating modes (III and II respectively, Fig. 3.1). When the 632 nm wavelength was used, the Raman spectra showed the presence of the $\nu(\text{C}=\text{O})$ vibration, which should not be observed if bidentate chelating occurs (mode II, Fig. 3.1). However, this was justified due to the presence of adsorbed and non-adsorbed molecules.

Recently, Hirose *et al.*[16,17] in a departure from previous studies proposed that the N719 adsorption on the TiO₂ surface is facilitated by the presence of surface OH sites that leads to the formation of bidentate chelating linkage (mode II, Fig. 3.1) with one of its four carboxylate groups (Fig. 3.3). Wang and Lin[18] reported surface hydroxyl groups induced on the TiO₂ semiconductor oxide surface by O₂ plasma treatment lead to increased dye adsorption, although no surface characterization or discussion of the binding mechanism was offered[19,20]. On the basis of the literature works reviewed above and our own interest in hydroxyl-rich TiO₂ as photoanode in DSSCs, a greater understanding of the role of the N719 anchoring (COO⁻ and COOH) groups and TiO₂'s surface groups (Ti-O, Ti-OH, Ti-OH₂) is needed[21,22]. To this end, we have undertaken this spectroscopic study with the aim at (a) resolving and unifying the binding mechanism ideas that have been proposed to operate between the N719 complex and nano-crystalline anatase TiO₂ films; and (b) in particular shedding light as to the way in which molecular groups involved in the binding mechanism are distributed. In order to elucidate the latter aspect, TiO₂ films with two different anatase powders are used: a commercial one (Dyesol) and our house variety produced via an aqueous synthesis

route[22]. For comparison, we also examine the stearic acid (C₈H₁₄O₂) as a binding molecule, and analyze the spectra of the stearic acid-adsorbed TiO₂ film.

3.3 Experimental section

3.3.1. TiO₂ film preparation

The Ru complex ((bis(tetrabutylammonium)[cis-di(thiocyanato)-bis(2,2'-bipyridyl-4-carboxylate-4'-carboxylic acid)-ruthenium(II)]): N719) used in this work was obtained from Dyesol. The study of the binding of the Ru complex involved two nanostructured TiO₂ (both anatase; one commercial-Dyesol and our aqueous produced variety-Aqueous[22]) films prepared by paste deposition, annealing and sensitization[23] The TiO₂ paste of the Aqueous product was prepared with Ethyl Cellulose and α -Terpineol as per procedure for screen printing pastes described elsewhere[24]. With the exception of the Aqueous TiO₂ powder, all other chemicals used were purchased from commercial sources (Sigma Aldrich, Fisher Scientific) and used without further purification. TiO₂ electrodes were prepared by screen printing on FTO conductive glass substrates (Nippon Sheet Glass with a sheet resistance of 10 Ω per square). The TiO₂ paste was spread out onto a FTO glass and sintered at 450°C in air for 30 min yielding a 6~10 μ m thick nanostructured anatase film. For ATR-FTIR measurement, TiO₂ paste was deposited onto the cover glass to get better signals. The dye adsorption was experimentally performed by immersing the TiO₂ electrodes for 24 h in a 0.5 mM solution of N719 in ethanol. The coated TiO₂ was rinsed several times with ethanol to remove physisorbed N719 dye molecules and was left to dry in air.

3.3.2 Methods

Infrared spectra were obtained using a Perkin Elmer FTIR spectrometer with a Miracle single bounce diamond ATR cell from PIKE Technologies. Spectra over the 4000 to 550 cm⁻¹ range were obtained by the co-addition of 10 scans with a resolution of 4 cm⁻¹. Raman spectra and images were collected with an InVia Raman microscope from Renishaw using a polarized He-Ne laser operating at 514 nm. Spectra and images were collected with 50x and 100x short distance objectives, respectively. The area of the mapping images was collected with a piezo-motorized stage using two different step sizes:

one at 5 μm x 5 μm with a step size of 2 μm and the other at 70 μm x 70 μm with a step size of 10 μm. Data pre-processing, map generation (via univariate analysis) and further details can be found in Supplementary Information. The energy resolution was 4 cm⁻¹ at the full width half max (FWHM) of the internal Si reference peak. The scans were collected at 10 % of the laser output at the microscope exit (3mW) to avoid radiation damage to the dye molecules.

3.3.3 Raman imaging data processing

3.3.3.1 Raman imaging Data pre-processing

Prior to performing spectral univariate analysis to derive map profiles representing spatial variation of relative concentration of a specific band (correlated to a chemical species or a functional group), data pre-processing is a necessary step to clean up the mapping spectra from cosmic rays that add sharp feature artefacts unrelated to real Raman scattering information. Usually, cosmic rays are automatically removed by the acquisition software (Renishaw's Wire3) by performing additional spectral accumulations, and subsequently taking the median of each recorded pixel spectral data point value. Even if this automatic pre-processing routine guarantees a large part of cosmic ray-free data, however in the case of a large quantity of mapping spectra a residual contribution of cosmic rays still remains and must be removed by manual data treatment. If cosmic ray features are not completely removed they can significantly influence the univariate data analysis method, especially if the cosmic rays overlap with the bands of interest.

3.3.3.2 Spectral curve-fitting and map generation

Spectral curve fitting of all the Raman mapping spectra was performed on the bands located in the spectral regions of interest in order to adequately remove local baseline contribution and efficiently resolve overlapping spectral bands. This curve fitting step ensures a more accurate calculation of the relative areas of the bands used in the univariate analysis method. Further, the curve-fitting calculated areas of specific bands were represented as a function of spatial mapping position to generate the final two dimensional spectral maps (showing the spatial distribution of a chemical component as a

color coded scale for the intensity). For this purpose, an automatic curve fitting routine of the Renishaw Raman instrument software (Wire3) was used for band decomposition and baseline removal. The fitting is based on a least squares iteration model that uses a combination of Gaussian and Lorentzian functions for spectral bands fitting and a polynomial curve for baseline correction.

3.4 Results and Discussion

3.4.1 ATR-FTIR

3.4.1.1 N719-TiO₂ dye region

Band assignment: Figure 3.4 (a) presents the ATR-FTIR spectra of the neat N719 dye and the N719 dye adsorbed onto the two TiO₂ films (Dyesol and Aqueous); the suggested band assignments are summarized in Table 3.2. The IR spectrum of the neat N719 dye (Fig. 3.4(a)) shows the presence of carboxylic acid and carboxylate groups as evident by the $\nu(\text{C}=\text{O})$ at 1708 cm⁻¹, $\nu(\text{C}-\text{O})$ at 1230 cm⁻¹, and $\nu(\text{COO}^-_{\text{asym and sym}})$ at 1605 and 1373 cm⁻¹ [6,7].

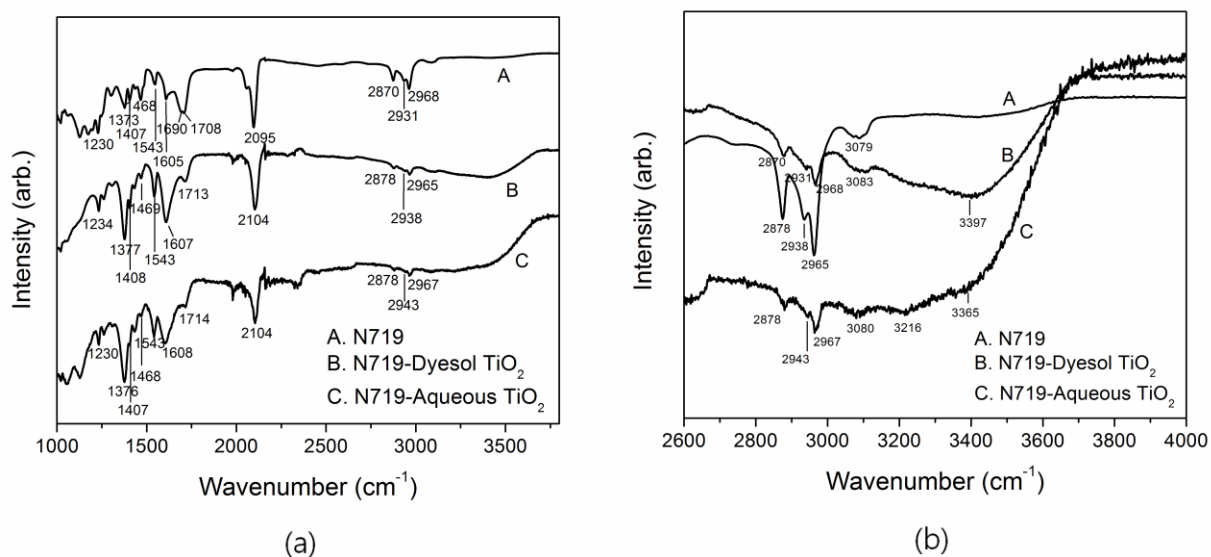


Figure 3.4 ATR-FTIR spectra of N719 dye and N719-TiO₂ in (a) 1000 - 4000 cm⁻¹ region and (b) 2600 - 4000 cm⁻¹ region

The spectrum of N719-adsorbed TiO₂ (Dyesol and Aqueous) similarly shows a carbonyl stretch band at ~ 1713 cm⁻¹ due to carboxylic acid groups and carboxylate vibrations of the $\nu(\text{COO}^-_{\text{asym and sym}})$, $\nu(\text{C}-\text{O})$ modes at ~1607, 1377 and 1234-1230 cm⁻¹, respectively.

The occurrence of ester like bond can be ruled out in our experimental results [insignificant ($\sim 5\text{ cm}^{-1}$) shift of C=O vibration] [6-8]. The band due to $\nu(\text{NC})$ of thiocyanate was found to shift to higher energy ($\sim 9\text{ cm}^{-1}$) in the adsorbed samples (Dyesol and Aqueous), indicating that perhaps these groups participate in the binding interaction between the N719 molecule and TiO₂ in accordance with the XPS study by Johansson *et al.* (D-type, Fig. 3.3) [25]. Finally, it is worth to note that the vibrational modes of the TBA⁺ ions should not be active in the adsorbed samples if the anchoring of both carboxylate anions occurs via covalent bonding, but this is not the case. Hirose *et al.* assumed that in order for the TBA⁺ ion(s) to be dissociated from the N719 molecule [17,18], it must react with a proton from surface Ti-OH/Ti-OH₂ groups (Fig. 3.3 (G) and (H)). In our case, the TBA⁺ ions' vibrational mode ($\sim 1469\text{ cm}^{-1}$) is still observed before and after adsorption (Dyesol and Aqueous) but a decrease in intensity is monitored in the latter case.

Parameter $\Delta\nu$: Many research groups have used the carboxylate difference ($\Delta\nu = \nu_{\text{asym}}(\text{COO}^-) - \nu_{\text{sym}}(\text{COO}^-)$) in the infrared spectra as a criterion to elucidate the type of bonding between the metal oxide surface and adsorbents, such as sensitizer, gas and polymer molecules [6-8,26]. In particular, the neat/solid ($\Delta\nu_{\text{salt}}$) state and the adsorbed state ($\Delta\nu_{\text{ads}}$) have been used to determine bond coordination *in carboxylate and carboxylic acid groups* [6-8,26,27]. Deacon and Phillips made elaborate examinations of infrared spectra of solid acetates and trifluoroacetates (carboxylates) having known crystal structures,[28,29] from which the $\Delta\nu$ parameter was derived as a result of the COO⁻ low symmetry. The nature of the binding mode can be inferred from the following criteria: if $\Delta\nu_{\text{ads}} > \Delta\nu_{\text{salt}}$ = unidentate; if $\Delta\nu_{\text{ads}} < \Delta\nu_{\text{salt}}$ = chelate or bridge; and if $\Delta\nu_{\text{ads}} \ll \Delta\nu_{\text{salt}}$ = chelate [28,29]. In an effort to apply the $\Delta\nu$ criterion to the type of bonding operating between the N719 dye and other reagents with similar binding groups onto TiO₂, the $\Delta\nu$ values from several previous studies were analyzed. These values are summarized in Table 3.1, along with the postulated binding mechanism for each case. Careful examination of all these values for our system reveals quite wide range of variation (ranging from 5 - 25 cm^{-1}) [5,7,16,17,30].

Table 3.1 Summary of $\Delta\nu$ values for different carboxylate/carboxylic acid group-TiO₂ systems compounds

Compound	$\nu_{\text{asym}}(\text{COO})$ (cm ⁻¹)	$\nu_{\text{sym}}(\text{COO})$ (cm ⁻¹)	$\Delta\nu$ (cm ⁻¹)	Binding mode	ref
N719	1618	1376	242	Ester-like unidentate	5
N719-TiO ₂	1617	1382	235		
N3	1609	N/A	N/A	Bridging/ Bidentate chelating	6
N712	1615	1364	244		
N719	1615	1371	251		
N3-TiO ₂	1610	1380	230		
N712-TiO ₂	N/A	N/A	N/A		
N719-TiO ₂	N/A	N/A	N/A		
N3	1613	N/A	N/A	Bridging	7
N712	1616	1352	264		
N719	1608	1365	243		
N3-TiO ₂	1593	1383	211		
N712-TiO ₂	1601	1371	230		
N719-TiO ₂	1602	1373	227		
N719	1606	1354	252	Bridging/ Bidentate chelating	8
N719-TiO ₂	1602	1375	227		
N719	N/A	N/A	N/A	Bidentate chelating	16,17
N719-TiO ₂	1626	1352	274		
N719	1603	1377	235	Bridging	This work
N719-TiO ₂ (Dyesol)	1607	1377	230		
N719-TiO ₂ (Aqueous)	1608	1376	232		
Stearic acid	N/A*		N/A*	Bidentate chelating /Bridging	This work
Stearic acid-TiO ₂	1608/156 [‡]	1403	205/163		
(m-Py-EPE-Ipa)	1603*	1414*	189	Bidentate/Unidentate	32
(m-Py-EPE-Ipa)-TiO ₂	1593/1557 [‡]	1417	176/140		

[Ru(CO) ₂ (C ₂ H ₅ COO)] _n	1548	1410	138	Bridging	57
Ru(OAc)(CO) ₂ (PPh ₃)	1613	1315	298	Unidentate	58
EMAA	N/A	N/A	N/A	N/A	59
EMAA-Cu	1600	1375	227	Unidentate	26
M1	1634	1370	264	Bridging	27
M1-TiO ₂	1587	1382	205		
M3	1645	1373	272		
M3-TiO ₂	1586	1395	191	Bridging	

* The value is not mentioned in the reference and estimated through the figure for this table.

‡ Two Δv_{Ads} values are given because the carboxylate band is split into two and each one was taken.

In the present study, the Δv value is 235 cm⁻¹ in the neat N719 and 230 cm⁻¹ in the adsorbed state, giving a difference of 5 cm⁻¹ between Δv_{salt} and Δv_{Ads} . Our separation value (5 cm⁻¹) may then be taken as evidence of “bidentate bridging” in agreement with previous spectroscopic and computational reports [6-8,16,17]. However, given the observed difference in the Δv separation value for the same system reported by previous authors and our studies, further supporting evidence was collected in our study to investigate the type of bonding between dye’s COO⁻/COOH groups and TiO₂.

Structural changes: In general, the ATR-FTIR spectra in the region 1000-2200 cm⁻¹ of dye adsorbed-TiO₂ films appear to be similar (with some modest variation in intensity for certain bands [31]) with the neat N719 spectrum in terms of spectral structure for the groups of interest (C=O, COO⁻, NCS), before or after adsorption (Fig. 3.4(a)). However, structural changes of molecules in the IR vibrational spectra have been observed for C=O, COOH and COO⁻ modes involved in chemisorption; for example, Taratula *et al.*[32] showed the structural change of the COO⁻ vibrational mode with their bulky *m*-Py-EPE-Ipa molecules on TiO₂ [33]. Similarly, Pal *et al.*[34] investigated the binding mechanism of stearic acid molecules on TiO₂ and reported the disappearance of the C=O stretching band at 1702 cm⁻¹ upon adsorption and the appearance of three new bands owed to bound

carboxylate groups on the TiO₂ nano-surface. This was confirmed by the present authors (Fig. 3.5(a), Table 3.2).

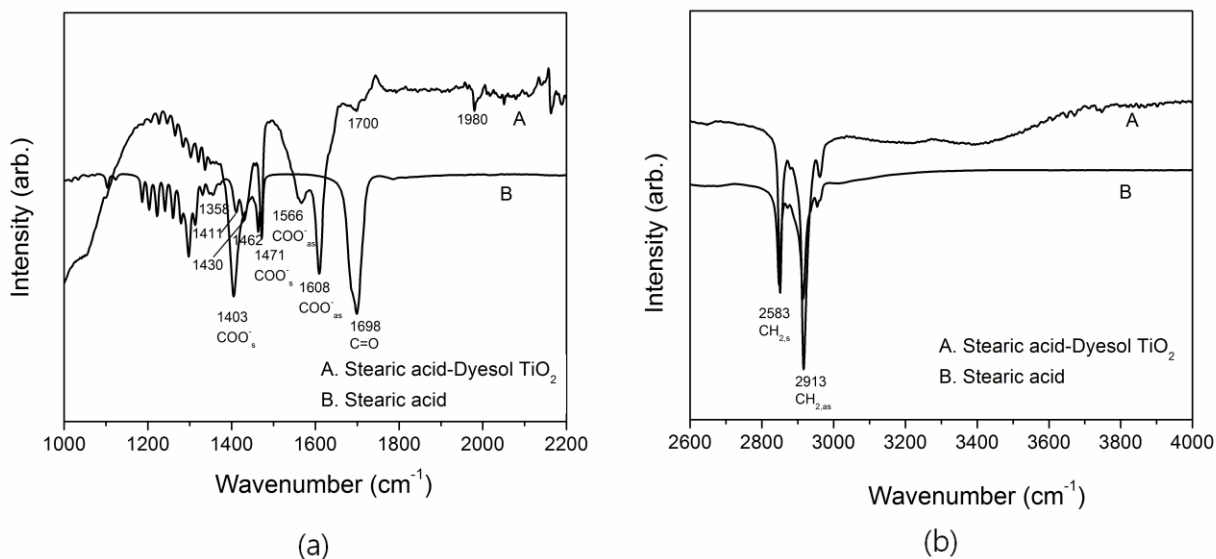


Figure 3.5 ATR-FTIR spectra of Stearic acid and Stearic acid-TiO₂ in (a) low wave number region and (b) high wave number region

Table 3.2 Assignment of the bands observed in ATR-FTIR of N719, N719-TiO₂ (Dyesol), stearic acid, and stearic acid-TiO₂ (Dyesol)

N719 v(cm ⁻¹)	N719- Dyesol TiO ₂ v(cm ⁻¹)	Assignment	Stearic acid v(cm ⁻¹)	Stearic acid- Dyesol TiO ₂ v(cm ⁻¹)	Assignment
1230	1234	C=O	1358	1403	-COO ⁻ _{sym}
1373	1377	COO ⁻ _{sym}	1411		
1407	1408	bpy			
1468	1469	δ(CH ₂) in TBA ⁺	1430		
1543	1543	bpy	1462		
1605	1607	COO ⁻ _{asym}	1471	1471	-COO ⁻ _{sym}
1708	1713	COO ⁻		1566	-COO ⁻ _{asym}
2095	2104	NC		1608	-COO ⁻ _{sym}
2870	2878	CH _{2,asym}	1700	1698	C=O
2931	2938	CH _{2,sym}		1980	
2968	2965	CH ₃	2583	2853	CH ₂ _{sym}
3079	3083	CH/OH [‡]	2913	2913	CH ₂ _{asym}
	3397	OH			

‡ This band is suggested to be a mixture of CH from bpy and OH from COOH (Fig. 3.7)

From Figure 3.5(a), it can be observed that upon adsorption of stearic acid onto TiO₂, there are significant spectral changes to the C=O and COO⁻ vibrations, indicating that there is a loss of symmetry and change of bond order in the binding groups (Figure 3.1) [35]. Upon binding on the TiO₂ surface, the ν(C=O) band is removed and replaced by two carboxylate asymmetric bands at 1608 and 1566 cm⁻¹. Thus, we can demonstrate that stearic acid is covalently bonded on TiO₂ surface and little to no electrostatic interaction is present. In contrast to stearic acid-TiO₂ system, the ν(C=O) near 1700 cm⁻¹ of our spectrum of N719-adsorbed TiO₂ (Figure 3.4(a)) does not split nor disappears (only a decrease in intensity is observed), and ν(COO⁻_{asym} and _{sym}) stretches are still observed indicating that there are carbonyl groups unbound in the N719 molecules. The lack of

structural spectral change (C=O and COO⁻ bands) in the neat/solid and adsorbed dye states may indicate that some of its COOH and/or COO⁻ groups remain unbound [6-8,16] and that complementary electrostatic/H-bonding components in addition to bidentate bridging (mode III, Fig. 3.1) may be present [36].

3.4.1.2 N719-TiO₂ high wavenumber region

In this section, we focus on the hydroxyl vibrations of the N719 and TiO₂ surface groups and their relation to the type of bonding mechanism that occurs upon adsorption. The interaction of N719 with the TiO₂ surface has been largely examined previously in terms of the characteristic vibrational signals of the dye molecules (1000-2200 cm⁻¹) as presented in the previous section. Previous studies have only briefly touched on the role of Ti-OH/Ti-OH₂ groups on the TiO₂ surface [16,17] and that of OH units from the carboxylic acid groups of the dye molecules [11,12]. Finnie et al. focused on examining the dye vibrational region (1000-1800 cm⁻¹); however, they reported that H-bonding could not occur between the dye and the TiO₂ surface, and attributed a sharp $\nu(\text{OH})$ IR vibration at 3582 cm⁻¹ observed in the adsorbed sample as indicative of uncoordinated carboxylic acid groups [6]. They further refuted the possibility of H-bonding (via acid groups), because no broad $\nu(\text{OH})$ features were observed at ~ 3000 cm⁻¹ in their adsorbed samples. Hirose et al. studied the hydroxyl structure of the N719 dye adsorbed onto TiO₂ (UV radiated and non) samples [16,17], but no reference to the OH units on the TiO₂ surface was considered. Here, it was suggested that the N719 dye adsorbed onto the TiO₂ surface by consuming surface OH sites in the UV radiated TiO₂. It was proposed that the N719 dye is adsorbed on the surface via the carboxylate anions and a bidentate chelating complex is formed at the TiO₂ surface via only one carboxylate group per dye molecule (Figure 3.3 (G) and (H)). Interestingly, in that study, the splitting of the $\nu_{\text{sym}}(\text{COO}^-)$ group was observed for the adsorbed sample but was attributed to chemically bonded, isolated and/or physisorbed N719 dye molecules on the TiO₂ surface, without consideration given that the $\nu_{\text{sym}}(\text{COO}^-)$ splitting was due to different symmetry of the binding molecule in the pure versus that of the adsorbed state (anchoring mode V or VI in Fig. 3.1). De Angelis et al. reported a DFT (Density Functional Theory) computational study focusing on the protons carried by the N719 sensitizer's carboxylic acid groups and their role in

binding onto the TiO₂ surface, but not on OH units of the TiO₂ surface [11,12]. In contrast to previous studies [5-8], it was reported that the carboxylic acid groups (and not the carboxylate) were used to anchor the dye onto the TiO₂ surface via proton transfer from the dye to the TiO₂ surface [11,12]. Based on their computational studies the distinction between non-adiabatic (dye with COO⁻ binding groups) or adiabatic (dye with COOH binding groups) electron injection mechanism was made proposing that the high rates of electron injection observed experimentally should suggest an adiabatic mechanism, i.e. dye binding through its COOH groups.

Analysis of the spectra: Figure 3.4(b) presents the ATR-FTIR spectra of the high wavenumber region for N719 dye and the N719-TiO₂ (Dyesol and Aqueous) samples. This region consists of the usual CH stretches as well as important chemical information on the OH stretches from hydroxyl units (free or bound via H-bonding) in chemical groups of interest, such as COOH and Ti-OH/Ti-OH₂.

The spectra of the pure Dyesol and Aqueous TiO₂ films were published recently and reproduced in Figure 3.6 [22].

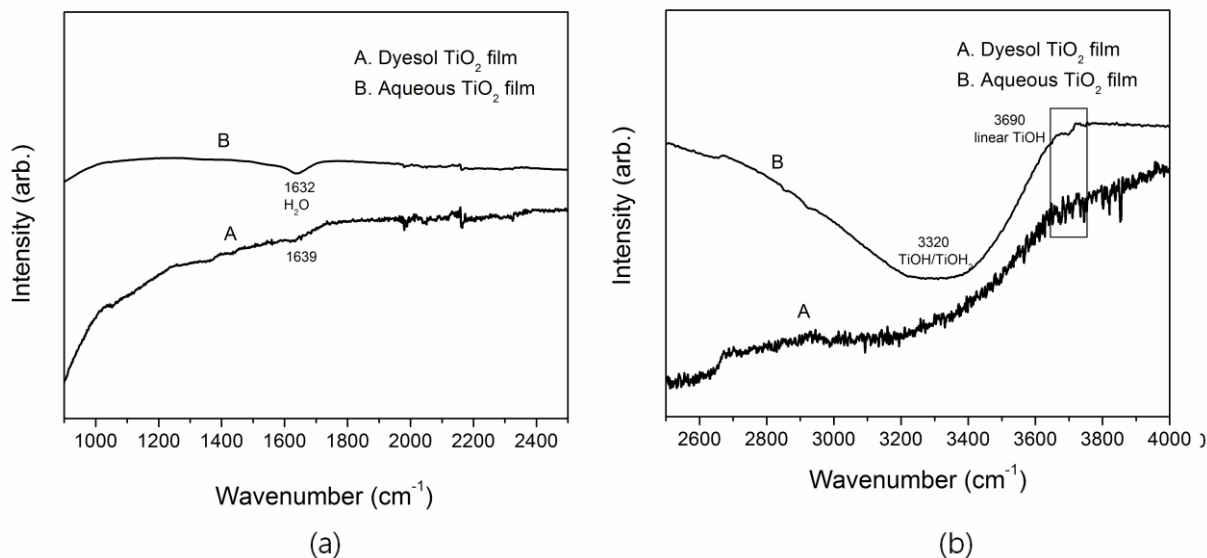


Figure 3.6 ATR-FTIR spectra of TiO₂ film (Aqueous and Dyesol) in (a) low wave number region, (b) high wave number region.

The IR spectra of pure TiO₂ films (Dyesol and Aqueous) show an adsorbed water peak at $\sim 1632\text{ cm}^{-1}$ in Figure 3.6(a). In the high wavenumber region (Fig. 3.6(b)), the broad band is shown at 3320 cm^{-1} indicating the mixture of surface hydroxyl groups and adsorbed molecular water [38,39]. In the case of Aqueous TiO₂, this broad band is strongly represented in comparison to Dyesol TiO₂ moreover the small peak at 3690 cm^{-1} is observed clearly for Aqueous TiO₂ indicative of the isolated hydroxyl groups (linear Ti-OH[38]). The Dyesol TiO₂ film spectrum shows a weak $\nu(\text{OH})$ infrared vibration at 3400 cm^{-1} , while our Aqueous TiO₂ [22] shows a much stronger broad hydroxyl vibration occurring at 3320 cm^{-1} . These bands may be attributed to Ti-OH/Ti-OH₂ [37] groups as also done recently by Minella *et al.*[38]. In addition a small band is seen at 3690 cm^{-1} typical of linear hydroxy groups [38,39]. From the observation of these vibrations, it is evident that the TiO₂ surface groups do not consist only of Ti-O sites, as considered in previous dye-TiO₂ binding studies [10-12] but more importantly of Ti-OH/Ti-OH₂ groups. In previous studies on the binding of the N719 onto TiO₂, the high wavenumber spectra of the pure TiO₂ films was not presented or discussed in relation to the adsorbed samples [6,7,16]. The presence of Ti-OH/Ti-OH₂ units, as those identified in the commercial (Dyesol) and our synthetic (Aqueous) samples, need to be considered in understanding the binding mechanism between the anchoring groups (COOH vs. COO⁻) and the TiO₂ surface. This is especially relevant and important to elucidate in the case of our in-house-made TiO₂ from aqueous media [22].

The high wavenumber structure of the neat N719 dye molecule spectrum (Fig. 3.4(b), Table 3.2) exhibits the usual $\nu(\text{CH})$ stretches from the TBA⁺ occurring between $2874\text{-}2963\text{ cm}^{-1}$ [7]. But in addition, a distinct band at 3079 cm^{-1} is observed which may be attributed to the $\nu(\text{CH})$ from bipyridine and the OH units from the carboxylic acid moiety of the N719 dye molecules[40]. In order to substantiate this assignment in particular with reference to the $\nu(\text{OH})$ of the COOH groups, the high wavenumber region of 2,2' - bipyridyl and 2,2'-bipyridyne-4,4'-dicarboxylic acid were investigated (Figure 3.7).

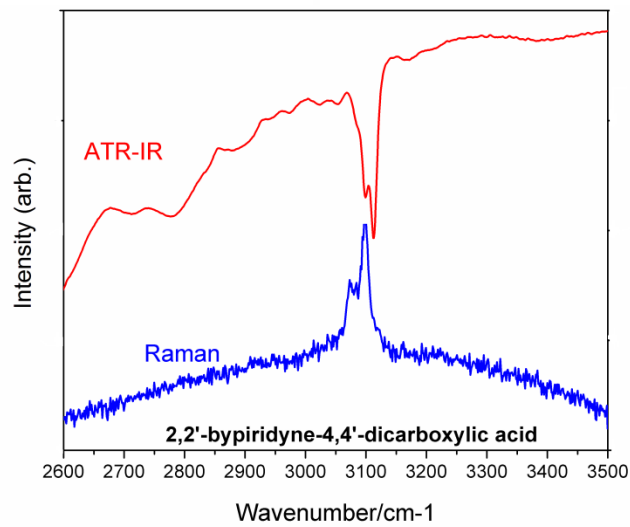
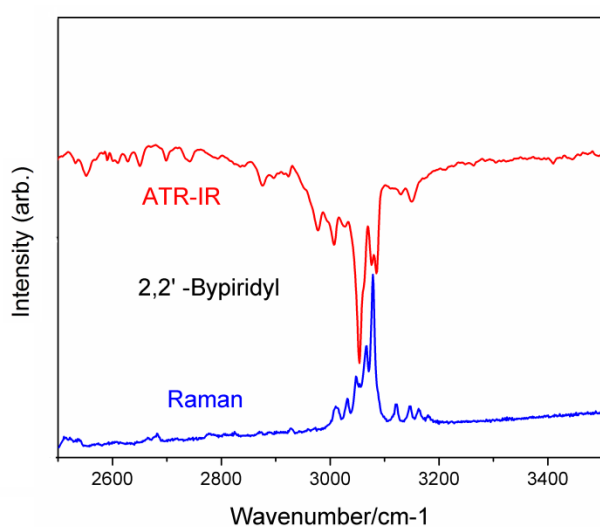
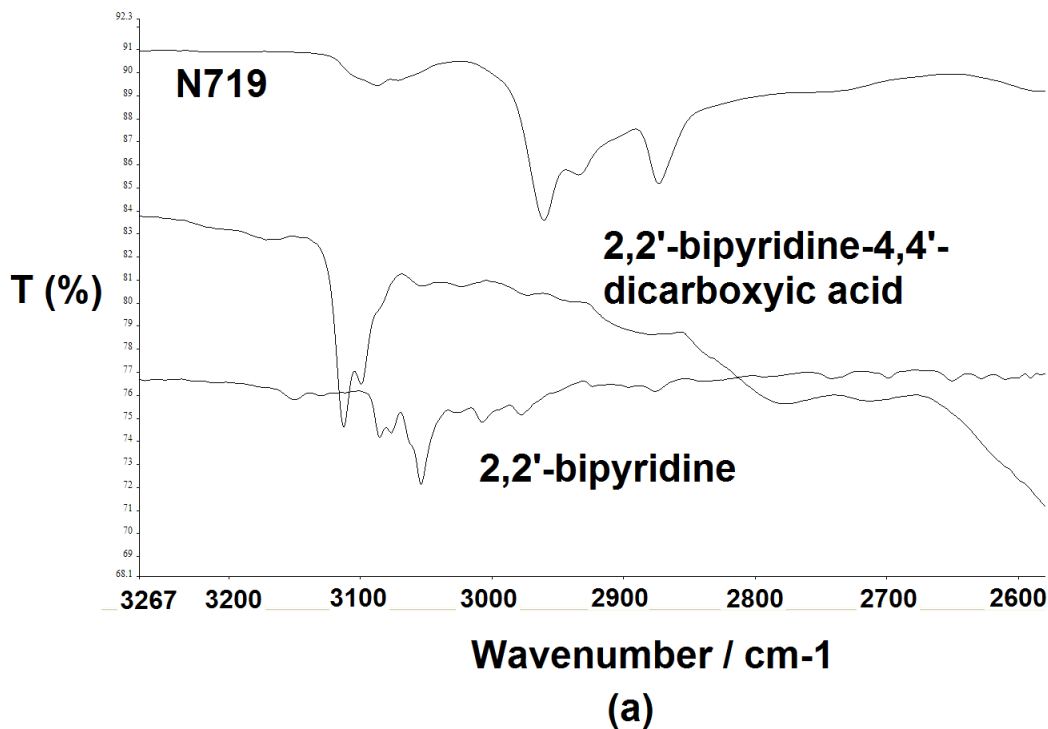


Figure 3.7 ATR-FTIR spectra of (a) N719, 2,2'-bipyridine and 2,2'-bipyridine-4,4'-dicarboxylic acid, ATR-FTIR and Raman spectra of (b) 2,2'-bipyridine and (c) 2,2'-bipyridine-4,4'-dicarboxylic acid

2, 2'-bipyridine and 2, 2'-bipyridine-4,4'-dicarboxylic acid were chosen specifically as they are the ligands of the N719 molecule. In the IR spectrum of 2,2'-bipyridine, the CH stretches from pyridine occurred at $\sim 2874 - 3200 \text{ cm}^{-1}$. On the other hand, in the IR for

the 2,2'-bipyridine-4,4'-dicarboxylic acid, only a strong doublet band at 3090-3100 cm⁻¹ is observed. More interestingly, there is no extra band for OH in 2,2'-bipyridine-4,4'-dicarboxylic acid in the comparison to the spectrum of 2,2'-bipyridine in the IR or Raman spectra as shown in Figure 3.7 (It should be noted that the 2,2'-bipyridine-4,4'-dicarboxylic acid showed the usual C=O stretch at 1700cm⁻¹ expected of a COOH group). In the Raman spectra of 2,2'-bipyridine and 2,2'-bipyridine-4,4'-dicarboxylic acid, the peak due to CH stretches is exist in the same region. However, again there is no extra peak representing the OH in the Raman spectrum of 2,2'-bipyridine-4,4'-dicarboxylic acid. The OH vibration due to COOH groups should be active in either the IR or Raman spectra as these are complementary technique, but as we have shown the OH stretches are not clearly evident. Thus, the peak around 3090-3100 cm⁻¹ for 2,2'-bipyridine-4,4'-dicarboxylic acid (in the IR and Raman) should be a mixture of OH units from COOH and CH stretches from pyridine. By extrapolation, the vibrational peak at 3080 cm⁻¹ in the N719 and N719 dye adsorbed TiO₂ is interpreted to be a mixture from bipyridine $\nu(\text{CH})$ and $\nu(\text{OH})$ stretches from COOH groups.

The spectra of the adsorbed N719 onto the TiO₂ films show the usual vibrations occurring at 2876 - 2966 cm⁻¹ (Fig. 3.4(b)) corresponding to TBA⁺ vibrations[7]. The broad diffuse band observed in the films after adsorption at 3397(Dyesol) and 3365(Aqueous) cm⁻¹ are attributed to the surface Ti-OH/Ti-OH₂ groups [38,39] similar with the assignment made above for the pure TiO₂ (Fig. 3.6(b)) [22]. It is noted that the small band at 3697 cm⁻¹ observed in pure Aqueous TiO₂ (Fig. 3.6(b)) and typical of linear hydroxy groups [38] is removed upon dye adsorption (Fig. 3.4(b)). The preservation of the surface Ti-OH/Ti-OH₂ group broad vibrations upon adsorption of the dye suggests their involvement in the binding mechanism via electrostatic (H-bonding) interaction.

Stearic acid-TiO₂ high wave number region: In an effort to further strengthen the assertion made with reference to the involvement of Ti-OH/Ti-OH₂ surface groups in the binding of the dye, we decided to examine the analogous system of stearic acid-TiO₂, the binding mechanism of which is well established [34,41]. Figure 3.5(b) presents the ATR-FTIR spectra of the high wavenumber region for the pure stearic acid and the Dyesol TiO₂-stearic acid (adsorbed) sample. The IR spectra of the pure stearic acid at this higher

wavenumber region show the usual alkyl chain CH₂ and CH₃ asymmetric and symmetric stretches [34,41,43] at 2600 – 3000 cm⁻¹, but we note the absence of hydroxyl vibrations from the free carboxylic acid groups. From our high wavenumber spectra of Figure 3.5(b), we can see that upon binding of stearic acid on TiO₂, there is no change to the vibrational structure of the alkyl chains, as expected (since they do not participate in the bonding) in agreement with previous works [34,41,43]. But more importantly we do not observe the surface Ti-OH/Ti-OH₂ groups vibrations after adsorption of stearic acid unlike the N719-TiO₂ case (compare Fig. 3.4(b) and 3.5(b)). This implies that most of the Ti-OH/Ti-OH₂ units have been replaced by the carboxylate binding complex involving covalent bonding between stearic acid and TiO₂ surface groups [44].

3.4.2 Resonance-Raman @ 514 nm

3.4.2.1 N719-TiO₂ dye region @ 514 nm

Band assignment: The Raman spectra of commercial (P25 and Dyesol) and our Aqueous TiO₂ have been previously described elsewhere [22] and will not be discussed in detail but are shown for comparison to the adsorbed samples in Figure 3.8(a). The Raman spectra (Fig. 3.8(a)) of the dye adsorbed films (Dyesol and Aqueous) show the normal modes of anatase at 144, 197, 398, 514, and 640 cm⁻¹ assigned to E_g, B_{1g}, A_{1g} or B_{2g} and E_g modes, respectively [42,45]. It should be noted that these bands appear as less resolved in the N719 adsorbed-Aqueous TiO₂ versus those of the N719 adsorbed-Dyesol, as a result of the lower crystallite size in the former [22].

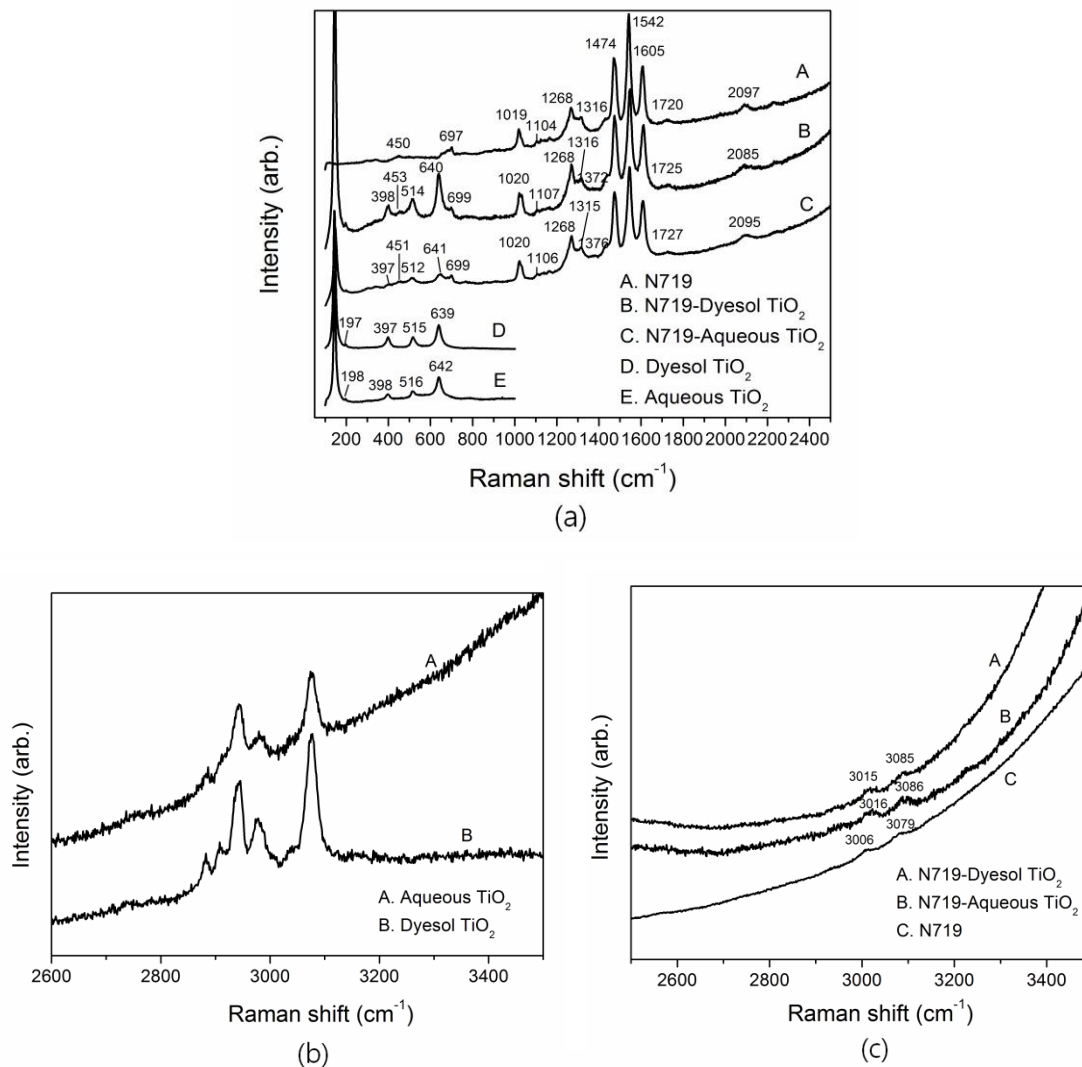


Figure 3.8 Raman spectra of (a) TiO₂, N719 and N719 –TiO₂ in low wave number region, (b) TiO₂ film in high wave number region and (c) N719 and N719-TiO₂ in high wave number region

The peak positions in the 100-2000 cm⁻¹ region of the Raman spectra and their assignment are listed in Table 3.3. The Raman spectrum of the neat N719 dye has been published extensively [6,7,8,46] thus we will not discuss it in any detail but indicate where the important vibrations occur. The Raman spectrum of the neat N719 is composed of strong bipyridine bands (1605, 1542, 1474 cm⁻¹), weak C=O modes (1720 cm⁻¹) arising from COOH groups, C-C and C-O stretches (1268 cm⁻¹) and the CN modes (2097 cm⁻¹) from NCS groups (Table 3.3) [6,8].

Table 3.3 Raman assignment for N719 and N719 adsorbed TiO₂ films

N719 v(cm ⁻¹)	N719-Dyesol TiO ₂ v(cm ⁻¹)	N719- Aqueous TiO ₂ (cm ⁻¹)	Assignment	ref
	145	146	TiO ₂ (E _g)	42,45
	197	198	TiO ₂ (E _g)	42,45
	398	397	TiO ₂ (B _{1g})	42,45
450	453	451	out-of-plane ring deformation	6,8,
	514	515	TiO ₂ (A _{1g} ,B _{1g})	42,45
	639	642	TiO ₂ (E _g)	42,45
697	699	699	in-plane ring deformation	6,8,54
1019	1025	1023	bpy ring breathing	6,8,54
1104	1107	1106	in-plane C-H wagging	6,8,54
1268	1268	1268	C-C inter-ring, C-O stretch	6,8,54
1316	1316	1315	C=N (bpy ring)	6,8,54
	1372	1376	symmetric stretch –COO ⁻	6,8,54
1474	1474	1474	C=N (bpy ring)	6,8,54
1542	1542	1542	C=C (bpy ring)	6,8,54
1605	1605	1605	C=C (bpy ring)	6,8,54
1720	1725	1727	C=O stretch	6,8,54
2097	2085	2095	CN (SCN)	6,8,54
3006	3015	3016	OH	
3079	3085	3085	OH	

In the N719 adsorbed TiO₂ (Dyesol and Aqueous) films, the symmetric stretch COO⁻ band appears as a very weak band at 1372 (and 1376) cm⁻¹ but not in the free N719 [7,8,11,16]. Leon *et al.*[8] mentioned that this band is proof of chemisorption between the dye and TiO₂ surface and is the only Raman spectral evidence of the presence of chemisorption between the N719 and TiO₂ surfaces [47].

The Raman spectra of the N719-TiO₂ films for both Aqueous and Dyesol products are quite similar in terms of vibrational structure to that of free N719 (aside from the weak

COO⁻ band). Umapathy *et al.*[48] also reported a similar phenomenon (no change in spectral structure of the Raman spectra of the non-adsorbed and adsorbed molecules) using Ru-based sensitizers RBDA and RB4H adsorbed on TiO₂. They attributed the lack of change in the Raman spectra of the non-adsorbed and adsorbed samples as indication of physisorption (electrostatic) rather than chemisorption (covalent bonding) mode. Thus, it may be deduced from the similar lack of change in the Raman spectra of N719-TiO₂ (Fig. 3.8(a)) - notwithstanding the weak COO⁻ band - that physisorption is also an important component of the adsorption mechanism in this system as well.

Carbonyl group interaction: In the dye-adsorbed Dyesol and Aqueous TiO₂ samples (Fig. 3.8(a)), a weak band at ~1725 cm⁻¹ is observed and attributed to $\nu(\text{C}=\text{O})$ stretching of COOH groups. This band is observed at slightly higher energy (~5-7 cm⁻¹) in comparison to the neat N719 Raman spectrum (Fig. 3.8(a)). The fact that this band appears in the Raman (and IR spectra-Fig. 3.4(c)) could indicate that some (most likely two) C=O from COOH groups are not bound[49] but also that they are simply involved in electrostatic interaction/H-bonding [7,8,11,12]. Previous authors have justified the occurrence of this Raman band at 532 nm,[8,54] (near the main absorption band of N719 in which adsorbed and non-adsorbed molecules contribute to the signal) as a result of the resonance effect. In analogy, one could also argue that some carbonyl vibrations from unbound groups should then be observed in the IR and Raman at resonant (514, 532 nm) or non-resonant energies (632 nm – Fig. 3.9) since N719 has four carbonyl groups (2COOH and 2COO⁻) of which only two are reported to bind to the surface [7]. Experimentally, the carbonyl band was indeed observed (albeit with reduced intensity) in the IR (Fig. 3.4(a)) as well as at near resonance energy (514 nm) in the Raman (Fig. 3.8(a)). However, this interpretation is in contradiction to the work by Leon *et al.*[8] who stated that the Raman spectra at 632nm (SERS and no resonance) of N719-TiO₂ showed no $\nu(\text{C}=\text{O})$ vibration present and as such they opted for the coordination of the carboxy ligands to TiO₂ via bidentate chelating or bridging bonds (modes II and III, Fig. 3.1).

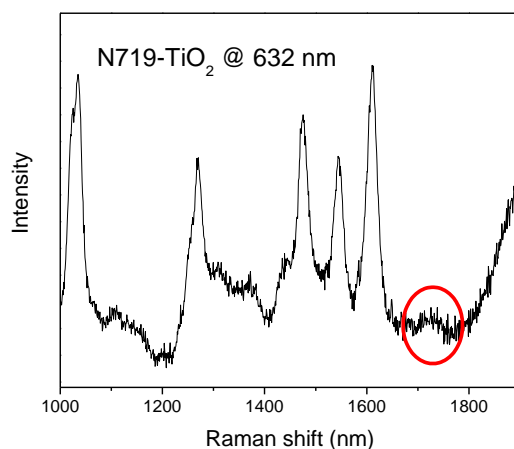


Figure 3.9 Raman spectrum of N719-TiO₂ at 632 nm. The circle around 1700 cm⁻¹ highlighted in red indicates C=O vibration upon adsorption. This band was observed not only at the resonance Raman scattering (514 nm) but also, non resonance Raman scattering spectrum such as at 632 nm.

Thiocyanate group: The vibration occurring at 2085 and 2095cm⁻¹ for the N719-TiO₂ samples, Dyesol and Aqueous respectively, is assigned to the $\nu(\text{CN})$ stretching of the -NCS ligands. This band shows a shift ($\sim 2\text{-}12\text{ cm}^{-1}$) to lower frequency in the Raman spectra (Fig. 3.8, Table 3.3), in comparison to the CN band of the neat N719 [25]. Shifts to lower energies in vibrational spectroscopy are usually indicative of lower force constants of the bonds of interest as a result of lengthening of the bond distance or due to electronic effects (electronegativity, conjugation etc). Thus in our case, there appears to be some interaction of the -NCS ligands with the TiO₂ surface, causing the NC bonds to be slightly longer in the adsorbed samples (versus the neat state) [50]. This is in agreement with previous work by Johansson *et al.*[25] who studied the same system via X-ray photoelectron spectroscopy.

3.4.2.2 Stearic acid-TiO₂ dye region @ 514 nm

With the view of further clarifying the N719-TiO₂ binding system, the Raman spectra of the analogous stearic acid-TiO₂ system were examined. The Raman spectra of stearic

acid and its deuterated derivatives in its crystalline solid state have been previously reported [51], thus the assignments are not discussed in any detail (Table 3.4).

Table 3.4 Raman assignment for stearic acid and stearic acid adsorbed TiO₂ film

SA v(cm ⁻¹)	SA-TiO ₂ v(cm ⁻¹)	Assignment	ref
146,162	144	TiO ₂ (E _g)	42,45
		LAM	51,52
	196	TiO ₂ (E _g)	42,45
	396	TiO ₂ (B _{1g})	42,45
	513	TiO ₂ (A _{1g} ,B _{1g})	42,45
	636	TiO ₂ (E _g)	42,45
	795		
893		CH ₃ rocking	51,52
910		v(C-C)	51,52
985			
1060		v _{as} (C-C)	51,52
1104		CH ₂ twist	51,52
1126	1126	v _s (C-C)	51,52
1180		CH ₂ twist	51,52
1293	1299	CH ₂ twist	51,52
1421			
1439	1450	CH ₂ scissoring	51,52
1458			
1468			
2202			
2413			
2581			
2722			
2744			
2885	2879	v _s (CH ₂)	51,52

2925			
2967			
3079	3079	v(OH)	
3593			

Figure 3.10 shows the Raman spectra of stearic acid in the crystalline solid state and that of stearic acid adsorbed onto TiO₂ film substrate (Dyesol only).

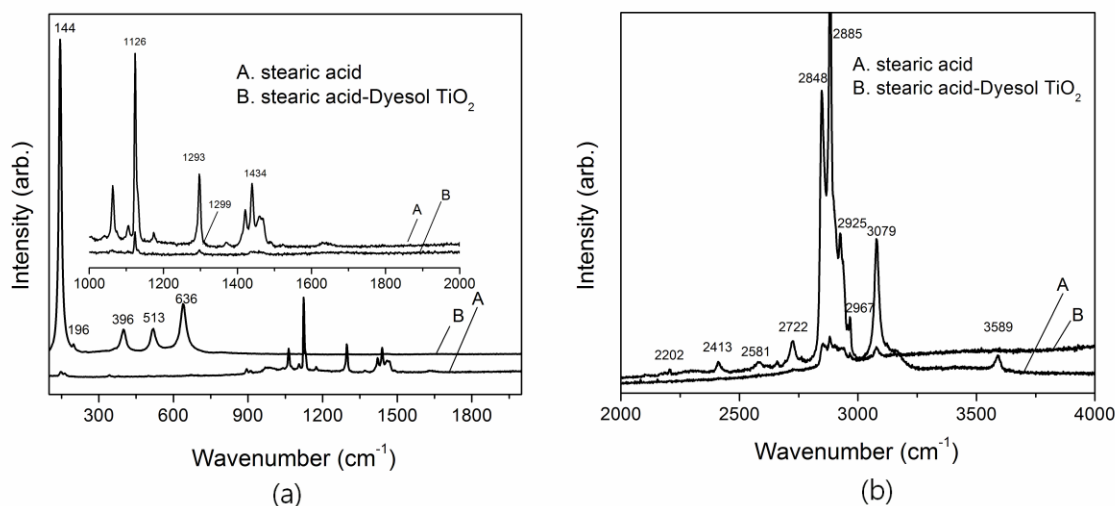


Figure 3.10 Raman spectra of Stearic acid and Stearic acid- TiO₂ in (a) low wave number region and (b) high wave number region

Raman studies of stearic acid on nano-crystalline TiO₂ substrates have not been previously reported; only FTIR measurements are available [34]. From Figure 3.10, it can be observed that there is a significant spectral structural change in the Raman active vibrations (and IR, Fig. 3.5) in the pure state of stearic acid versus that of the adsorbed state. Similar effects to the Raman spectra have been observed in previous works on stearic acid adsorbed onto Al, Au, Ag and Al₂O₃ surfaces [52]. Thus, the adsorption of the N719 dye upon the TiO₂ surface lacks this structural change in the Raman (and IR) spectra, which is clearly present in the stearic acid examples.

3.4.2.3 Confocal Raman Imaging

Raman imaging provides detailed information on the spatial distribution of individual chemical species of interest in samples such as anatase-rich and rutile-rich domains in

P25 [53]. Hence it was decided to apply Confocal Raman imaging to examine the distribution of N719 molecules on the TiO₂ surfaces (Dyesol and Aqueous). To this end, 4 groups of interest in the N719 dye adsorbed TiO₂ films were selected for observation: the anatase band at $\sim 640\text{ cm}^{-1}$ (E_g mode), the $\text{COO}^-_{\text{sym}}$ band at $\sim 1376\text{ cm}^{-1}$, the bipyridine band at 1542 cm^{-1} and the C=O band at $\sim 1725\text{ cm}^{-1}$. Raman images were obtained at two different step sizes in order to obtain information about the distribution of the dye molecular groups over both, large ($70 \times 70\ \mu\text{m}$ using $10\ \mu\text{m}$ step size) (Fig. 3.11) and small ($10 \times 10\ \mu\text{m}$ using $2\ \mu\text{m}$ step size) (Fig. 3.12) area. The large area using a bigger step size shows an overall/bulk view of the samples.

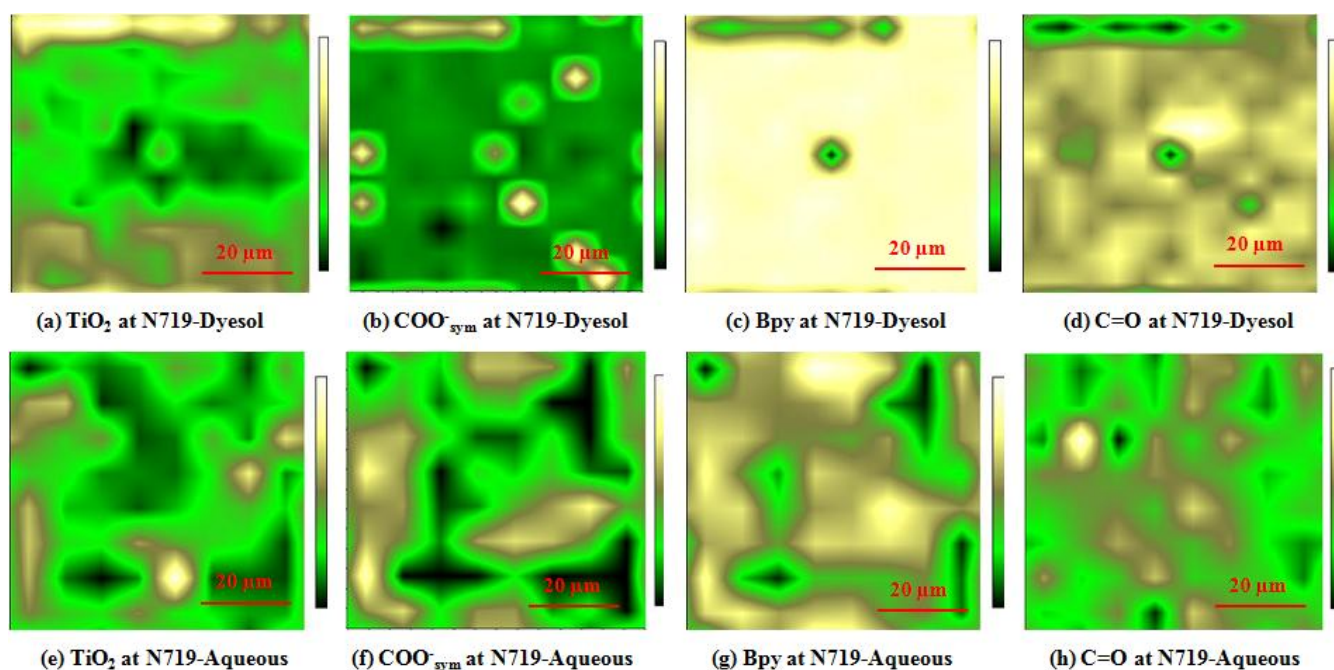


Figure 3.11 Confocal Raman images showing the N719 distribution on TiO₂ film (Dyesol and Aqueous), $70 \times 70\ \mu\text{m}$ wide, $10\ \mu\text{m}$ step size, monitoring the intensity at (a),(e) 640 cm^{-1} , (b),(f) 1376 cm^{-1} (c),(g) 1542 cm^{-1} and (d),(h) 1725 cm^{-1}

The Raman image of E_g mode (at $\sim 640\text{ cm}^{-1}$) represents (Fig. 3.11 and 3.12 (a), (e)) where TiO₂ regions exist in the dye adsorbed TiO₂. The distribution of anatase is partially uneven in both the small and large area, but the anatase covers whole surface. Previous studies [8,54] have reported that the $\text{COO}^-_{\text{sym}}$ Raman band can be used as evidence of the chemisorption of N719 on TiO₂; thus, mapping in $\sim 1376\text{ cm}^{-1}$ ($\text{COO}^-_{\text{sym}}$) should indicate

where the N719 bonding units exist. As shown in Figure 3.11 and 3.12 (b),(f), this covalent bonding is present in both samples. In the small area (Fig. 3.12(b), (f)), however, the occurrence of the covalent bonding sites is more distinctively distributed.

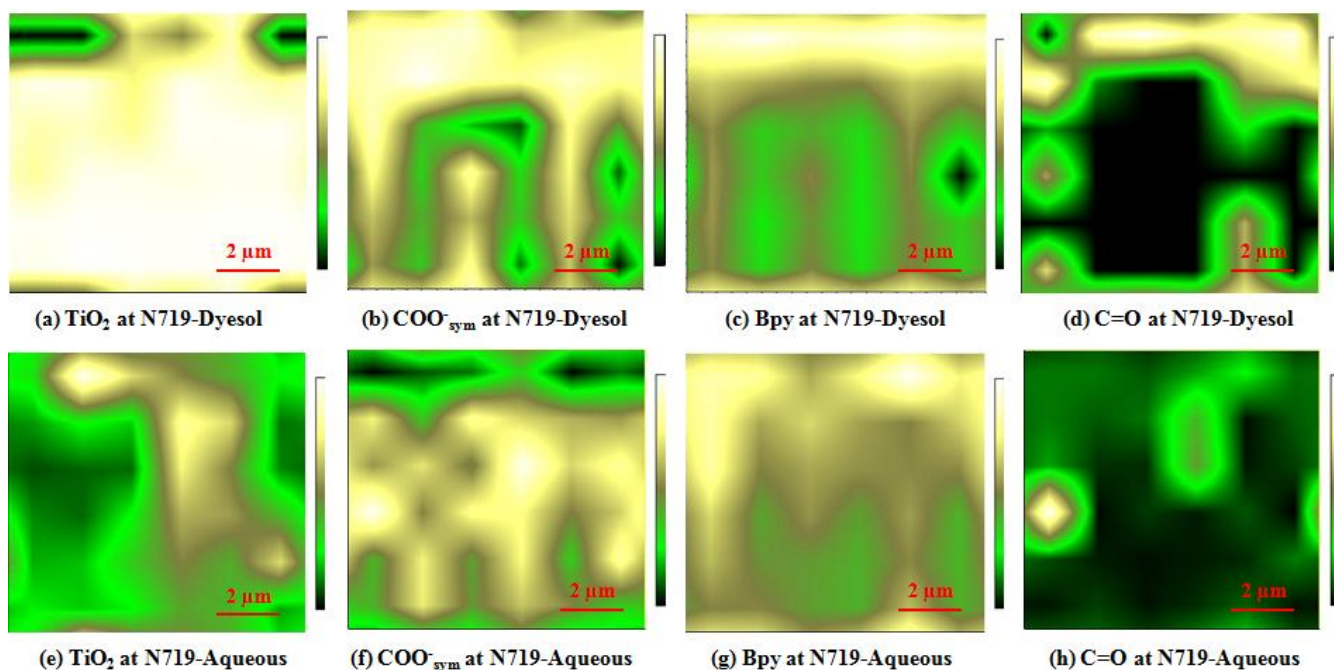


Figure 3.12 Confocal Raman images showing the N719 distribution on TiO₂ film (Dyesol and Aqueous), 10 x 10 μm wide, 2 μm step size, monitoring the intensity at (a),(e) 640 cm⁻¹, (b),(f) 1376 cm⁻¹ (c),(g) 1542 cm⁻¹ and (d),(h) 1725 cm⁻¹

The overall distribution of the N719 dye was observed via the strongest bipyridine ring-stretching mode at ~1545 cm⁻¹ (Fig. 3.11 and 3.12 (c),(g)). In the case of the N719-Dyesol sample (Fig. 3.11(c)), the N719 molecules are distributed fairly well throughout the sample, indicating that essentially all the area of the Dyesol TiO₂ has been occupied by the N719 molecules. For the N719-Aqueous TiO₂ (Fig. 3.11(g)), however, we observe uneven distribution of the dye, which may be attributed to different surface characteristic and favourable surface complex energetics. A closer look (small area images in Fig. 3.12 (c), (g)) reveals that the distribution of bipyridine for both samples is not level; thus, mapping the small area with a small step size may show detailed surface characteristic not observed at the large scale.

The Raman images (obtained at 1725 cm⁻¹) (Fig. 3.11 and 3.12 (d),(h)) provide the distribution of free C=O groups associated with one or more unbound carbonyl groups from the N719 dye molecules on the TiO₂ film surface. The dark regions (Fig. 3.12 (d),(h)) are assumed to represent chemisorbed sites from which free C=O groups have been covalently displaced. On the other hand, the bright regions are considered to indicate high concentration of unbound C=O groups thought involved in electrostatic bonding with the TiO₂ surface.

3.4.2.4 N719-TiO₂ high wave-number region @ 514 nm

Surface Ti-OH/Ti-OH₂ groups on TiO₂: Figure 3.8(b and c) and Table 3.3 present the Raman spectra of the high wavenumber region for the pure TiO₂ films (Dyesol and Aqueous), N719 dye and the N719-TiO₂ samples. Unlike the observations from IR measurements made by Finnie *et al.*[6] in which three sharp stretching bands (~3600 cm⁻¹) were observed in the non-sensitized TiO₂ sample, we observe only bands at lower wavenumber in the range 2884-3100 cm⁻¹ in the Raman spectra. We attribute these bands to surface hydroxyl groups of the Ti-OH/Ti-OH₂ form [38,39], in agreement with those observed in the ATR-FTIR spectra [22]. The observation of these surface groups and their consideration in the N719-TiO₂ binding mechanism is especially important as in previous theoretical computations [10-12], no TiO₂ surface OH/H₂O groups prior to adsorption had been considered and only transfer of protons from dye molecules to unsaturated oxygen of TiO₂ surface had been invoked to create Ti-OH surface groups. As we have shown via IR and now Raman spectroscopy, these Ti-OH/Ti-OH₂ groups are clearly on the surface before adsorption; moreover, as shown with the IR measurements, the C=O modes from COOH appear before and after adsorption which suggests that the invoked previously mechanism of proton transfer from the dye to TiO₂ is unlikely [11,12].

OH in dye-TiO₂ adsorbed films: In the case of the high wavenumber Raman spectra of pure N719, unlike the ATR-FTIR spectra, we saw that it is dominated by large fluorescence using the 514 nm wavelength. Measurements using the 488 and 632 nm wavelength were also conducted but similar results were obtained. However, from a close up, we were able to observe very weak vibrations at ~ 3006 and 3080 cm⁻¹ (Fig. 3.8(c)),

which we tentatively assign to the $\nu(\text{CH})$ from bpy stretches and possibly mixed $\nu(\text{OH})$ from COOH group vibration in agreement with what was observed in the ATR-FTIR spectra of 2,2'-bipyridine and 2,2'-bipyridine-4,4'-dicarboxylic acid. In the case of the adsorbed samples, weak vibrations at ~ 3015 and 3085 cm^{-1} for Dyesol and Aqueous were observed as well similar to those in the neat N719 but slightly shifted to higher energies. Again we tentatively assign these features to CH bpy stretches and possibly $\nu(\text{OH})$ from COOH group vibrations as observed in the ATR-FTIR measurements (Fig. 3.4(b)). It appears in other words that some of the COOH groups remain (as seen by the C=O) intact after adsorption which indicates that they are not all involved in covalent bonding via H transfer/exchange as proposed previously [11,12]. Finally it must be clarified that in the present system, the strong surface Ti-OH/Ti-OH₂ group vibrations observed at $\sim 3300 \text{ cm}^{-1}$ in the ATR-FTIR were not visible in the Raman spectra, not because they were not present but because most likely these features were masked by the large fluorescence at higher energies or were Raman inactive.

3.4.2.5 Stearic acid-TiO₂ high wave-number region @ 514 nm

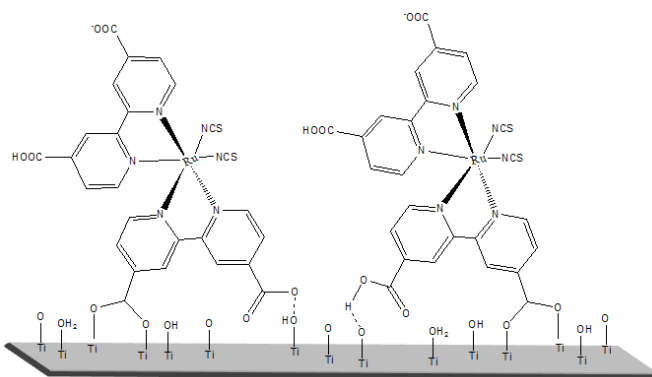
The stearic acid Raman spectra (Fig. 3.10 (b), Table 4.4) consist of the alkyl chain symmetric and asymmetric stretches occurring between $2848\text{-}2967 \text{ cm}^{-1}$ in agreement with previous works [51,52], but in addition, well defined strong vibrations at 3079 and 3593 cm^{-1} which we attribute to come from the OH units of the COOH groups.

From Figure 3.10, it can be observed that upon adsorption of stearic acid onto the TiO₂, there is a significant loss in Raman intensity (but not vibrational structure) of the $\nu(\text{C-H})$ modes, most likely due to lack of order among the alkyl chains in the adsorbed state in comparison to the crystalline stearic acid [52]. More importantly, we observe here that the intensity of the $\nu(\text{OH})$ carboxylic band at 3080 cm^{-1} is reduced to negligible level while the band at 3589 cm^{-1} is removed upon adsorption of the stearic acid. This spectral observation is in agreement with the covalent bonding nature of the binding mechanism (bidentate) by which stearic acid adsorbs on the TiO₂ surface via its COOH groups (hence the loss of the hydroxyl vibrations from the acid groups) as already discussed in reference to all the other collected data via IR and Raman measurements, such as loss of C=O and appearance COO⁻ modes. In comparison, as already described above, the

$\nu(\text{C}=\text{O})$ of the COOH groups in N719 are still present after adsorption onto TiO₂ which implies that at least one of the two COOH groups does not form covalent bonding. Hence the previously proposed binding mechanism involving covalent bonding through both COOH groups via proton transfer (Fig. 3.3 (F)) is unlikely [11,12].

3.4.3 Proposed binding Scheme

On the basis of all spectroscopic and Raman imaging data collected, we propose a modified structure for the binding of N719 dye on TiO₂ (Dyesol and Aqueous) films as shown in Scheme 3.1. In our scheme, the binding of the N719 dye to TiO₂, in departure with previous configurations (Fig. 3.3) is proposed to occur via two neighboring carboxylic acid/carboxylate groups linked on the same bipyridine ligand via a combination of bidentate-bridging and H-bonding. The proposed involvement of only one carboxylic group in the adsorption of N719 via covalent bidentate bridging (or bidentate chelating) has not been considered previously other than by Hirose *et al.*[16]. However, very recent work by Srinivas *et al.*[27] involving the adsorption of sensitizers on TiO₂ carrying malonic and cyanoacrylic acid groups found, in contrast to previous works [55] that the mono carboxylic acid group shows stronger binding affinity and slightly higher IPCE and efficiency than dicarboxylic acid groups [56]. In our proposed binding mechanism the formed surface complex is stabilized via the development of H-bonding with Ti-OH/Ti-OH₂ (Ti-O) and COO-(COOH) groups; however since adsorbed molecular water deteriorates the power generation performance in DSSCs, we propose that it is the surface hydroxyl groups that maybe involved to aid in the higher efficiencies, higher dye adsorption and short circuit current observed in recent reports [16,18,22].



Scheme 3.1 Schematic depicting the adsorption of two N719 carboxylic groups onto TiO₂ via bidentate bridging and H-bonding involving Ti-OH surface groups. The left side (right side) shows the schematic where the carboxylic acid (carboxylate) groups form a bidentate bond while the carboxylate (carboxylic acid) units form H-bonds via the surface Ti-OH (Ti-O) groups respectively.

3.5 Conclusions

In this work, the binding mechanism of N719 dye in sensitized TiO₂ films has been investigated with Micro-Raman, ATR-FTIR spectroscopy and Confocal Raman imaging. A particular focus of the present spectroscopic study is the elucidation of the role surface Ti-OH/Ti-OH₂ groups play in the binding mechanism.

In the dye region of the vibrational spectra, we considered structural changes caused by symmetry changes due to binding, as well as we evaluated carboxylate ($\Delta\nu_{\text{salt}}$ and $\Delta\nu_{\text{Ads}}$) splitting. The dye region of the IR and Raman spectra of N719 adsorbed-TiO₂ was not much different in comparison to that of the neat N719. A small band at 1372 cm⁻¹ was observed in the Raman spectra of N719 adsorbed-TiO₂, which was taken as proof of chemisorption (via bidentate bridging) as in previous works. In the IR spectra, both C=O and COO⁻ groups were observed before and after adsorption and our $\Delta\nu$ values were indicative of bidentate bridging coordination. In the Raman imaging, the distribution of COO⁻_{sym} on TiO₂ gave us an idea of where the covalent bonding exists. For the distribution of carbonyl mode, two regions exist: the dark regions are assumed to be from covalently displaced C=O groups; while, the bright regions are considered to indicate

where the unbound C=O groups exist ATR-FTIR spectroscopy of the high wave number region displayed Ti-OH/Ti-OH₂ bands before and after adsorption indicating the N719 molecules interact via a dual character: electrostatic (H-bonding) and covalently (bidentate-bridging mode). The presence of carbonyl groups was attributed to COOH groups not participating in covalent bonding but more likely involved in H-bonding. Overall, we propose that one carboxylic group (COO⁻ or COOH) binds to TiO₂ using a bidentate bridging for chemisorption rather than two and the other is electrostatically (H-bond attached) via surface Ti-OH/Ti-OH₂ groups.

3.6 Acknowledgements

The project is funded through the strategic research grant program of NSERC (the Natural Sciences and Engineering Research Council of Canada), and sponsored by partners Nanometrix Inc., CIS Scientific Inc. and Process Research Ortech Inc. The authors are grateful to Professors Nahzat and Chromik for the use of the ATR-FTIR and Micro-Raman instruments. We also thank Cecile Charbonneau for the synthesis of the aqueous TiO₂ anatase powder; and Holger Strauss, Benedetto Marelli and Jacqueline Sanchez for their assistance respectively with the Micro-Raman and AFM measurements. Authors also thank Professor Dmitrii F. Perepichka for providing us 2,2'-bipyridine and 2,2'-bipyridine-4,4'-dicarboxylic acid.

3.7 References

- [1] Gratzel, M. *Nature* **2001**, *414*, 338-344
- [2] Robertson, N. *Angew. Chem. Int. Ed.* **2006**, *45*, 2338 – 2345
- [3] Kroon, J. M.; Bakker, N. J.; Smit, H. J. P.; Liska, P.; Thampi, K. R.; Wang, P.; Zakeeruddin, S. M.; Gratzel, M.; Hinsch, A.; Hore, S.; Wurfel, U.; Sastrawan, R.; Durrant, J. R.; Palomares, E.; Pettersson, H.; Gruszecki, T.; Walter, J.; Skupien, K.; Tulloc, G. E. *Prog. Photovolt: Res. Appl.* **2007** *15*, 1–18

- [4] Hara, K.; Nishikawa, T.; Kurashige, M.; Kawauchi, H.; Kashima, T.; Sayama, K.; Aika, K.; Arakawa, H. *Sol. Energy Mater. Sol. Cells* **2005**, *85*, 21–30
- [5] Falaras, P. *Sol. Energy Mater. Sol. Cells* **1998**, *53*, 163-175
- [6] Finnie, K. S.; Bartlett, J. R.; Woolfrey, J. L. *Langmuir* **1998**, *14*, 2744-2849
- [7] Nazeeruddin, Md. K.; Humpry-Baker, R.; Liska, P.; Gratzel, M. *J. Phys. Chem. B* **2003**, *107*, 8981-8987
- [8] Leon, C. P.; Kador, L.; Peng, B.; Thelakkat, M. *J. Phys. Chem. B* **2006**, *110*, 8723-8730
- [9] Kay, A.; Gratzel, M. *Chem. Mater.* **2002**, *14*, 2930-2935
- [10] Shklover, V.; Ovchinnikov, Y. E.; Braginsky, L. S.; Zakeeruddin, S. M.; Gratzel, M. *Chem. Mater.* **1998**, *10*, 2533-2541
- [11] De Angelis, F.; Fantacci, S.; Selloni, A.; Nazeeruddin, Md. K.; Gratzel, M. *J. Am. Chem. Soc.* **2007**, *129*, 14156-14157
- [12] De Angelis, F.; Fantacci, S.; Selloni, A.; Gratzel, M.; Nazeeruddin, Md. K. *Nano Lett.* **2007**, *7*, 3189-3195
- [13] Hagfeldt, A.; Gratzel, M. *Chem. Rev.* **1995**, *95*, 49-68
- [14] Galoppini, E. *Coord. Chem. Rev.* **2004**, *248*, 1283-1297
- [15] Vittadini, A.; Selloni, A.; Rotzinger, F. P.; Gratzel, M. *J. Phys. Chem. B* **2000**, *104*, 1300-1306
- [16] Hirose, F.; Kuribayashi, K.; Suzuki, T.; Narita, Y.; Kimura, Y.; Niwano, M. *Electrochem. Solid-State Lett.* **2008**, *11*, A109-A111
- [17] Kuribayashi, K.; Iwata, H.; Hirose, F. *ECS Trans.* **2007**, *6*, 15-19
- [18] Wang, W.; Lin, Z. *Chem. Mater.* **2010**, *22*, 579–584
- [19] Chang, J.G.; Chen, H.T.; Ju, S.P.; Chen, H.L.; Hwang, C.C. *Langmuir* **2010**, ASAP

- [20] Tilocca, A.; Di Valentin, C.; Selloni, A. *J. Phys. Chem. B* **2005**, *109*, 20963-20967
- [21] He, G.; Zhang, M.; Pan, G. *J. Phys. Chem. C* **2009** *113*, 21679–21686
- [22] Demopoulos, G. P.; Charbonneau, C.; Lee, K.E.; Shan, G.B.; Gomez, M. A.; Gauvin, R. *ECS Trans.* **2009**, *21*, 23-34
- [23] The first film was built using a commercial nanostructured TiO₂ paste (DSL 18NR-T) available from Dyesol. The second film was prepared by using an in-house made hydroxyl-rich TiO₂ powder (Aqueous TiO₂) produced by forced hydrolysis of 0.2 M aqueous TiCl₄ solution at 80 °C for 30 min in a well agitated reactor. The Aqueous TiO₂ powder consists of 5~10 nm sized anatase in comparison to the ~20nm particle size of the Dyesol product[22].
- [24] Ito, S.; Chen, P.; Comte, P.; Nazeeruddin, Md. K.; Liska, P.; Péchy, P.; Grätzel, M. *Prog. Photovolt: Res. Appl.* **2007**, *15*, 603-612
- [25] Johansson, E. M. J.; Hedlund, M.; Siegbahn, H.; Rensmo, H. *J. Phys. Chem. B* **2005**, *109*, 22256-22263
- [26] Li, Q.F.; Lu, K.; Zhou, Q.; Baik, D. H. *J. Mater. Sci.* **2006**, *41*, 8271-8275
- [27] Srinivas, K.; Yesudas, K.; Bhanuprakash, K.; Rao, V. J.; Girbabu, L. *J. Phys. Chem. C* **2009**, *113*, 20117–20126
- [28] Nakamoto, K. *Infrared and Raman Spectra of Inorganic and Coordination Compounds, Part B: Applications in Coordination, Organometallic, and Bioinorganic chemistry*, 5th ed.; Wiley-Interscience : New York, 1997; pp 59-62
- [29] Deacon, G. B.; Phillips, R. J. *Coord. Chem. Rev.* **1980**, *33*, 227-250
- [30] For example, Falaras *et al*[5] reported $\Delta v_{\text{salt}} = 242$ $\Delta v_{\text{ads}} = 235$ and $\Delta v_{\text{salt-ads}} = 7$ cm^{-1} , Nazeeruddine *et al*[7] $\Delta v_{\text{salt}} = 243$ $\Delta v_{\text{ads}} = 227$ and $\Delta v_{\text{salt-ads}} = 16$ cm^{-1} , Leon *et al*[8] $\Delta v_{\text{salt}} = 252$ $\Delta v_{\text{ads}} = 227$ and $\Delta v_{\text{salt-ads}} = 25$ cm^{-1} . Hirose *et al*[16,17] recently reported only $\Delta v_{\text{ads}} = 274$ cm^{-1}

[31] The modest shift in energy observed for the CN group vibrations may be indicative that these groups are involved in the binding interaction of the N719 molecule to TiO₂.

[32] Taratual, O.; Rochford, J.; Piotrowiak, P.; Galoppini, E. *J. Phys. Chem. B* **2006**, *110*, 15734-15741

[33] Tarantula *et al.* showed the disappearance of C=O band (1702 cm⁻¹) and appearance of broad bands in the carboxylate region made them suggest binding as bidentate or monodentate carboxylate bonds onto the TiO₂ surface[32].

[34] Pal, S. K.; Bhattacharaya, S.; Batabyal, S. K.; Pradhan, T. K.; Ganguly, T. *J. Photochem. Photobiol., A* **2007**, *189*, 86-93

[35] The IR spectra of the adsorbed sample also showed substantial spectral changes at ~1290 cm⁻¹, as these broad bands disappear upon adsorption, these spectral changes show that the symmetry of the binding groups is changed for the -COO⁻ modes, causing splitting and significant spectral change in the vibrational modes upon binding.

[36] It should be noted at this point that although Nazeeruddin *et al.* [7] observed this band in their N719 and N3 spectra no assignment to it was made and only its numerical values were reported (3092 cm⁻¹, 3078cm⁻¹). However, this band was not observed in the spectra of the N712 dye in Nazeeruddin *et al.*'s work since this dye has no carboxylic acid groups present further

[37] The groups that have been attributed to these IR vibrations has been due specifically to linear and bridged hydroxyl groups and adsorbed molecular water groups as described by Takeuchi *et al.* and Minella *et al.*[38,39])

[38] Minella, M.; Giulia, M. F.; Maurino,V.; Minero,C.; Pelizzetti,E.; Coluccia, S.; Martra. G. *Langmuir*, **2010**, *26*, 2521-2527

[39] Takeuchi, M.; Bertinetti, L.; Martra, G.; Coluccia, S.; Anpo, M. *Appl. Catal. A*, **2006**, *307*, 13-20

[40] It should be noted at this point that although Nazeeruddin *et al.* observed this band in their N719 and N3 spectra no assignment to it was made and only its numerical values

were reported (3092 cm⁻¹, 3078cm⁻¹)[7] However, this band was not observed in the spectra of the N712 dye in Nazeeruddin *et al.*'s work since this dye has no carboxylic acid groups present further justifying our assignment.

[41] Li, L.; Chen, Y.; Kan, S.; Zhang, X.; Peng, X.; Liu, M.; Li, T. *Thin Solid Films* **1996**, 284-285, 592-295

[42] Arora, A. K.; Rajalakshmi, M.; Ravindran, T. R.; Sivasubramanian, V. *J. Raman Spectrosc.*, **2007**, 38, 604-617

[43] Dote, J. L.; Mowery, R. L. *J. Phys. Chem.* **1988**, 92, 1571-1575

[44] Summary: From the analysis of the high wavenumber region (Figure 3.4(d)), it becomes clear that the hydroxyl from Ti-OH/Ti-OH₂ surface groups still remain after N719 dye adsorption indicating that terminal/isolated OH/H₂O groups and weak H-bonding,[20] remains even after dye adsorption. This suggests that the surface groups of TiO₂ are involved in the binding mechanism via H-bonding as opposed to be completely displaced by the attachment of the dye as previously thought. In addition the $\nu(\text{C}=\text{O})$ band remains indicating that not all the COOH groups are involved in covalent bonding upon dye adsorption to TiO₂. This finding contradicts the assertion by De Angelis *et al.* that both of the carboxylic acid groups in N719 participate in the bonding via proton transfer from the COOH to the TiO₂[11]. The lack of change observed in the hydroxyl vibrations of the N719 dye and surface TiO₂ groups before and after sensitization, it is interpreted on our part as indication that the interaction between surface Ti-OH/Ti-OH₂ groups and at least one of the COOH groups in the N719 molecule is of electrostatic nature (H-bonding).

[45] Ohsaka, T.; Izumi, F.; Fujiki, Y. *J. Raman Spectrosc.* **1978**, 7, 321-324

[46] Greijer, H.; Lindgren, J.; Hagfeldt, *J. Phys. Chem. B.* **2001**, 105, 6314-6320

[47] No significant shifts for the dye-adsorbed Dyesol and Aqueous samples are observed in the region of the intense bipyridine ring-stretching modes nor the ring breathing mode (Fig 3.5(a), Table 3.3), as expected since they don't participate in coordination between the N719

[48] Umopathy, S.; Cartner, A. M.; Parker, A. W.; Hester, R. E. *J. Phys. Chem.* **1990**, *94*, 8880-8885

[49] Another possibility is for the carbonyl groups to belong to excess N719 dye molecules residing on the TiO₂ surface without involving any covalent bonding. However, we do not believe this to be the case here since after adsorption of the dye onto the TiO₂ substrates, the samples were washed thoroughly to ensure that all non adsorbed (i.e. non-bound) molecules were removed.

[50] It should be noted that this shift in energy of the $\nu(\text{CN})$ stretch is also observed in the ATR-FTIR spectra, further indicating that some interactions of the NCS ligands should occur (Fig. 3.3(D))

[51] Sunder, S.; Mendelsohn, R.; Bernstein, H. J. *Chem. Phys. Lipids*, **1976**, *17*, 456-465

[52] Thompson, W. R.; Pemberton, J. E. *Langmuir* **1995**, *11*, 1720-1725

[53] Minella, M.; Faga, M. G.; Maurino, V.; Minero, C.; Pelizzetti, E.; Coluccia, S.; Martra, G. *Langmuir*, **2009**, *25*, 11269-11271

[54] Shoute, L. C. T.; Loppnow, G. R. *J. Am. Chem. Soc.* **2003**, *125*, 15636-15646

[55] Schmidt-Mende, L.; Campbell, W. M.; Wang, Q.; Jolley, K.W.; Officer, D.L.; Naseeruddin, M.K.; Gratzel, M. *ChemPhysChem*. **2005**, *6*, 1253-1258

[56] In the case of malonic dicarboxylic acid, the possibility of both carboxylic acid groups binding to the TiO₂ surface was deemed impossible due to highly strained binding mode and ATR-FTIR spectroscopic evidence, which indicated that one acid group is free and the other acid group binds to TiO₂ in a bidentate-bridging mode

[57] Robinson, S. D.; Uttley, M. F. *J. Chem. Soc., Dalton Trans.* **1973**, 1912 - 1920

[58] Suss-Fink, G.; Herrmann, G.; Morys, P.; Ellermann, J.; Veit, A. *J. Organomet. Chem.* **1985**, *284*, 263-273

[59] Kutsumizu, S.; Kimura, H.; Mohri, F.; Hara, H.; Tachino, H.; Hirasawa, E.; Yano, S. *Macromolecules* **1996**, *29*, 4324-4330

Chapter 4. Vibrational Spectroscopic Imaging of N719-TiO₂ Films in the High Wavenumber Region Coupled to EIS Analysis

In Chapter 3, we reported on Raman mapping of bipyridine, COO⁻_{sym} and C=O bands by focusing on the low wavenumber region where the distribution of dye molecules on TiO₂ surface can be characterized. The same study provided IR evidence of the involvement of hydroxyl groups in the binding mechanism via H-bond bridging. In order to further probe the involvement of TiO₂ surface groups (Ti-OH/Ti-OH₂) in the dye-TiO₂ adsorption process further spectroscopic work was undertaken reported in this chapter. In particular, naked and dye-adsorbed TiO₂ films were investigated in the high wavenumber region (3000 ~ 4000 cm⁻¹) via the use of Raman and IR imaging techniques to investigate the effect of surface TiO₂ groups upon binding mechanism. Again, we used two types of TiO₂ (commercial and aqueous-synthesized varieties) in this regard and we focused on the TiO₂ substrate upon dye adsorption in order to study the reason for the completely distinct distribution of vibrational groups of interest (Bpy, COO⁻_{sym} and C=O) between the two types of TiO₂ observed in Chapter 3. In addition to the spectroscopic work photoanodes built from the commercial and aqueous-synthetic TiO₂ were used to fabricate DSSCs and the cells were evaluated by I-V (photocurrent-voltage) measurement and electrochemical impedance spectroscopy (EIS).

4.1 Abstract

In this study, vibrational (IR and Raman) imaging of two naked and dye-coated TiO₂ films (one built from a commercial paste “Dyesol” and one built from an in-house aqueous synthesized anatase variety “Aqueous”) is investigated in the high wavenumber region (3000 ~ 4000 cm⁻¹). Raman and IR imaging showed the distribution of surface Ti-OH/Ti-OH₂ groups in Aqueous TiO₂ to be qualitatively richer than in Dyesol TiO₂. After dye adsorption, the Ti-OH/Ti-OH₂ surface group intensity was observed to decrease but still to remain, which provides further supporting evidence that not all surface groups are consumed upon the binding of the dye on the TiO₂ surface. The reduced surface group intensity upon adsorption is attributed to regions where bidentate bridging bonding occurs while the remaining Ti-OH/Ti-OH₂ groups are proposed to be involved in electrostatic/H-bonding interaction with neighboring carboxylic groups as reported in our previous studies. However, photocurrent-voltage measurements of DSSCs prepared with the two different TiO₂ varieties did not produce improved conversion efficiency (η) for Aqueous (4.00 vs. 5.33%). Based on electrochemical impedance spectroscopy analysis of the two different DSSCs, the lack of improvement for the Aqueous TiO₂ was traced to extra charge transfer resistance in the photoanode film probably arising from particle aggregation and inefficient electrolyte diffusion (small pore size).

4.2 Introduction

The dye-sensitized solar cell based on anatase TiO₂, which was invented by Gratzel's group [1], has become a highly active field of research [2-5]. Electron injection from the dye to the semiconductor is affected by the governing dye binding modes on TiO₂ [6] thus, the TiO₂ semiconductor/Ru complex interface has been studied to understand the binding mechanism using vibrational spectroscopy [7-10], XPS [11] and computational modeling [12,13]. Vibrational spectroscopy has been widely used to investigate the interaction of N719 molecules with the TiO₂ surface in terms of the characteristic vibrational signals of the dye molecules (1000-2200 cm⁻¹). However, most studies have only focused in the low wavenumber region (1000-2200 cm⁻¹). Hirose *et al.*[14] were the first to correlate the surface hydroxyl groups on TiO₂ to the binding mechanism between N719 and TiO₂ by showing the IR spectrum in the range of 1000-4000 cm⁻¹. In their

study, they radiated the TiO₂ films with UV and this produced an increased efficiency in terms of cell current density. They suggested that after UV radiation, more surface hydroxyl sites are generated which allowed easier binding of the dye molecule [14].

Interestingly, the TiO₂ surface has been well known to be composed of surface hydroxyl groups and adsorbed molecular water due to dissociative adsorption of waters on its defect sites [15]. For this reason, we recently reported new data about the binding mechanism (Scheme 3.1) of N719 onto TiO₂ using ATR-FTIR and Raman spectroscopy by looking at Ti-OH/Ti-OH₂ groups in the high wavenumber region [16]. In our study, Confocal Raman imaging was also performed but in the low wavenumber region in order to show how the bonding and nonbonding groups of the dye molecules are distributed on the dye coated TiO₂ sample. A schematic showing Raman configuration used in this study is shown in Figure 4.1.

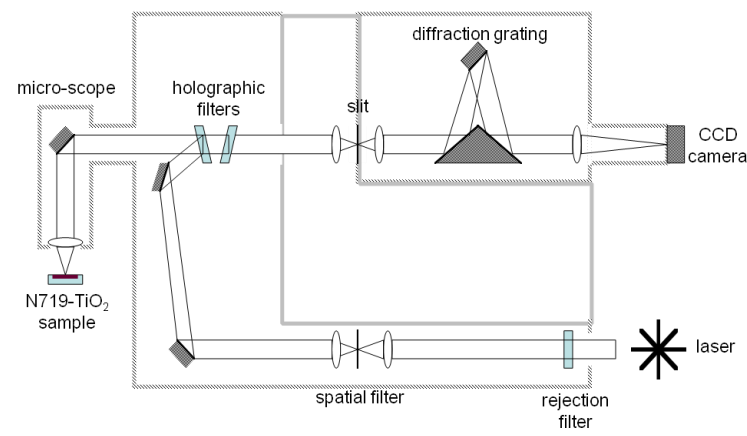


Figure 4.1 Schematic of Raman instrumentation

Raman imaging provides detailed information on the spatial distribution of individual chemical species of interest in the samples. We used the single point method for mapping of the pure TiO₂ films and N719 adsorbed TiO₂ as it offers advantages such as high sensitivity, high spectral resolution and true confocality [17]. A particular focus of our previous spectroscopic study was the elucidation of the role surface Ti-OH/Ti-OH₂ groups play in the binding mechanism. Based on our investigation from Micro-Raman, ATR-FTIR spectroscopy and Confocal Raman imaging in the low wavenumber region, we proposed that one carboxylic group (COO⁻ or COOH) in N719 molecules binds to TiO₂ by a dual

bonding mechanism involving bidentate bridging (chemisorptions) plus electrostatic coupling (H-bonding) via the surface Ti-OH/Ti-OH₂ groups (Scheme 3.1) [16].

In DSSC, several charge-transfer processes are involved in energy conversion- electron injection (from dyes to TiO₂), recombination (from TiO₂ to dyes), re-reduction (from electrolyte to dyes) and dark current (recombination between injected electrons and tri-iodide ions) [18] and they interact with each other in a complicated manner. To improve the conversion efficiency, it is important to comprehend these charge transfer processes and the internal resistances of the cells [19]. Recently, electrochemical impedance spectroscopy (EIS) has become a major tool for investigating the properties and quality of dye sensitized solar cell (DSSC) devices [20]. It has been used to analyze internal resistance and wide range of electrochemical processes in DSSC[21]. EIS is a steady state method measuring the current response to the application of an ac voltage as a function of the frequency [22].

In this paper, we focus on the hydroxyl vibrations (high wavenumber region) of TiO₂ surface groups (before and after sensitization), and their relation to the type of bonding mechanism [16] that occurs upon adsorption using Confocal Raman imaging and *micro* ATR-IR imaging.

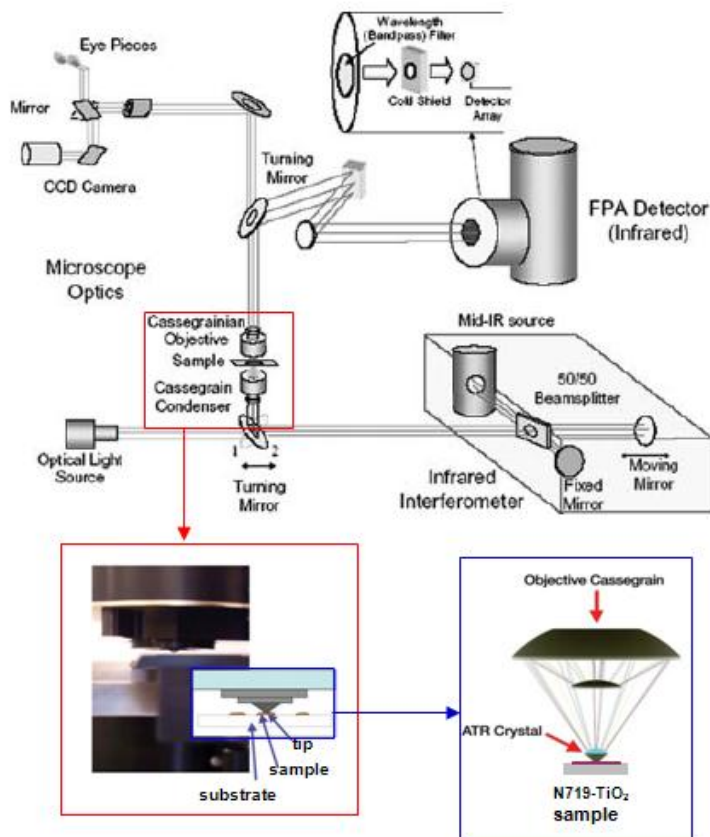


Figure 4.2 Schematic of micro-ATR-FTIR instrumentation* and geometries of IR beam

This is done to reveal the role of surface groups before and after adsorption of two different TiO₂ films; one is a commercial product (“Dyesol”) and one made from a hydroxyl-rich anatase variety (“Aqueous”) synthesized in our laboratory [23,24]. Figure 4.3 shows the optical images of Aqueous and Dyesol TiO₂ films.

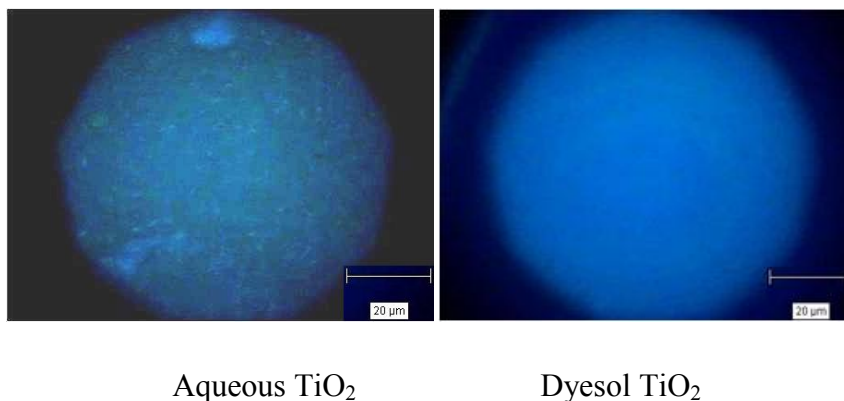


Figure 4.3 Real microscope images of Aqueous (left) and Dyesol (right) TiO₂ films

The influence of these surface binding features on the photovoltaic performance of DSSC devices prepared with the two different TiO₂ electrodes is also discussed on the basis of electrochemical impedance spectroscopic analysis and I-V curve measurements.

4.3 Experimental

4.3.1 TiO₂ film preparation and cell fabrication

The Ru complex (N719: (bis(tetrabutylammonium)[cis-di(thiocyanato)-bis(2,2'-bipyridyl-4-carboxylate-4'-carboxylic acid)-ruthenium(II)]) was obtained from Dyesol. The TiO₂ pastes were prepared using two kinds of TiO₂ (both anatase; one commercial-Dyesol (DSL 18NR-T) and our aqueous produced variety-Aqueous[23,24]). TiO₂ electrodes were prepared by screen printing on FTO conductive glass substrates (Nippon Sheet Glass with a sheet resistance of 10 Ω per square). The TiO₂ paste was spread out onto a FTO glass and sintered at 450°C in air for 30 min yielding a 9~10 μm thick film for Dyesol and a 8~9 μm thick film for Aqueous, measured by a Dektak 3 surface profile measuring system. The dye coated TiO₂ films were prepared by immersion into the dye solution for 24 h at room temperature [25]. The coated TiO₂ was rinsed several times with ethanol to remove excess physisorbed N719 dye molecules and was left to dry in air. A sandwich-type cell was assembled to measure the I-V curves and impedance spectroscopy. As a counter electrode, a Pt layer was prepared by spreading one drop of 5 mM H₂PtCl₆ solution (*iso*-propanol), air dry, and then heat at 380°C for 30 min. A 30 μm thick thermoplastic film (Surlyn®-30, Dyesol) was employed to seal the two electrodes and a commercial electrolyte solution (EL-HPE, Dyesol) was filled through the hole on the Pt electrode.

4.3.2 Raman imaging

Confocal Raman images were collected with a polarized ion Ar laser operating at 514 nm by moving the sample with a piezo-motorized stage at a step size of 10 μm using a 100x short distance objective. The beam size from the x100 objective is about 1 μm and its penetration depth is 2 μm. The area of the mapping images collected was 70 μm x 70 μm. A schematic showing Raman configuration used in this study is shown in Figure 4.1. The

laser radiation at the microscope exit was 3 mW. The data processing procedure is mentioned in detail elsewhere [16].

4.3.3 ATR-FTIR imaging

Micro-ATR-FTIR imaging was performed using a Varian FTIR microscope consisting of a FTS 7000e FTIR spectrometer coupled to a Varian model 600 UMA microscope. A schematic of the IR beam and sample configuration can be found in Figure 4.2 [26]. The FTIR images were acquired using a liquid nitrogen-cooled FPA detector. The FPA detector consisted of 1024 pixels (size 5.5 μm x 5.5 μm each), arranged in a 32 x 32 array format, giving an IR image over a 176 μm x 176 μm area of the specimen and a typical spatial resolution of 5.5 μm . The area of the IR mapping images collected is 35 μm x 35 μm . In the micro-ATR configuration, a Varian slide-on ATR accessory with germanium crystal (Refractive Index = 4; Numerical Aperture = 2.4) was attached to a 15 \times Cassegrainian objective mounted on the IR microscope. The penetration depth is expected to be 0.65 μm at 2000 cm^{-1} .

4.3.3.1. Data preprocessing and map generation on IR imaging

The use of a germanium crystal allows a better spatial resolution of about 1.1 μm to be achieved in the fingerprint region of the mid-infrared spectrum, hence giving an IR image over a 35 μm x 35 μm area of the sample. Accurate positioning and focus adjustment of the ATR accessory were performed before each series of measurements. An FTIR image was obtained by simultaneous acquisition of 1024 spectra from the pixels of the FPA detector. Each pixel measures an IR absorption spectrum at a specific location of 1.1 μm x 1.1 μm within the sample. The spectra were acquired in continuous scan mode over the range 4000–900 cm^{-1} at 4 cm^{-1} resolution by co-addition of 256 interferograms. A background FTIR image was collected prior to each measurement in the absence of the sample using a clean micro-ATR crystal. Varian Resolution Pro 4.1 software was used for the acquisition and processing of spectral datasets. No ATR correction was applied to the measured FTIR spectra before analysis. Each generated FTIR image is a hyper spectral data cube comprising two spatial dimensions and one spectral dimension given by the absorbance scale. The chemical images were created by attributing a color to each

pixel according to the absorbance intensity of a spectral feature characteristic of a specific chemical compound or functional group vibration.

4.3.4 Photo-electrochemical measurements

The current-voltage curves were measured using a small area solar simulator (PV measurements Inc., Model SASS). A tungsten lamp was used to provide uniform light approximating the AM 1.5 Global reference spectrum to a 1 cm diameter test region. The light intensity was adjusted with a Si reference cell. Duplicate measurements with each type of DSSC (Dyesol and Aqueous) were made to ensure reproducible results. The electrochemical impedance spectra were measured by using a VSP instrument (BioLogic) and analyzed with the EC-lab software. The impedance measurements were carried out under 100 mW/cm² illumination and applied open circuit voltage (OCV) and were recorded over a frequency range of 0.01 to 100 kHz with ac amplitude of 10 mV.

4.4 Results and Discussion

4.4.1 Confocal Raman imaging

In our previous work [16], 4 groups of interest in the N719 dye adsorbed TiO₂ films were selected for observation (Figure 4.4(a)): the anatase band at ~640 cm⁻¹ (E_g mode), the COO⁻_{sym} band at ~1376 cm⁻¹, the bipyridine band at 1542 cm⁻¹ and the C=O band at ~1725 cm⁻¹.

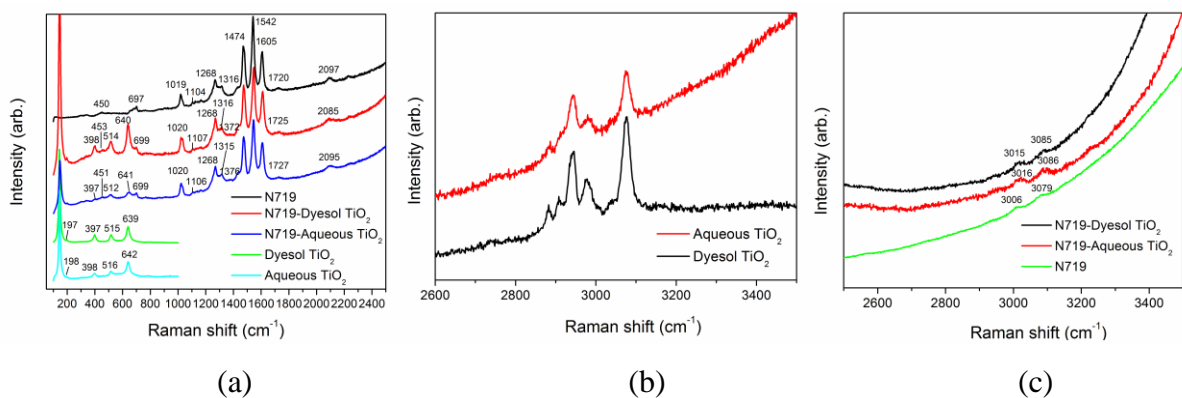


Figure 4.4_Raman spectra of (a) TiO₂, N719 and N719 –TiO₂ in low wave number region, (b) TiO₂ film in high wave number region and (c) N719 and N719-TiO₂ in high wave number region (adopted from Figure 3.8)

The Raman image of E_g mode (at ~640 cm⁻¹) was used to represent where TiO₂ regions exist in the dye adsorbed TiO₂. For the COO⁻_{sym} band at 1376 cm⁻¹, previous studies [16] have reported that the COO⁻_{sym} Raman band can be used as evidence of the chemisorption of N719 on TiO₂; thus, mapping in ~1376 cm⁻¹ (COO⁻_{sym}) energy should then indicate where the N719 bonding units reside. The overall distribution of the N719 dye was observed via the strongest bipyridine ring-stretching mode at ~1545 cm⁻¹. The Raman images obtained at 1725 cm⁻¹ provided us with the distribution of free C=O groups associated with one or more unbound carbonyl groups from the N719 dye molecules on the TiO₂ film surface.

For Raman imaging, the sample is mounted on the stage which moves to x and y direction (no z direction in our case), and the spectra are collected from different spots (10 μm step size) controlled by the stage. The beam size from the x100 objective is about 1 μm and its penetration depth is 2 μm. Both Aqueous and Dyesol TiO₂ show nano meter scale roughness (Figure 4.5), and both are in the range of the depth of resolution.

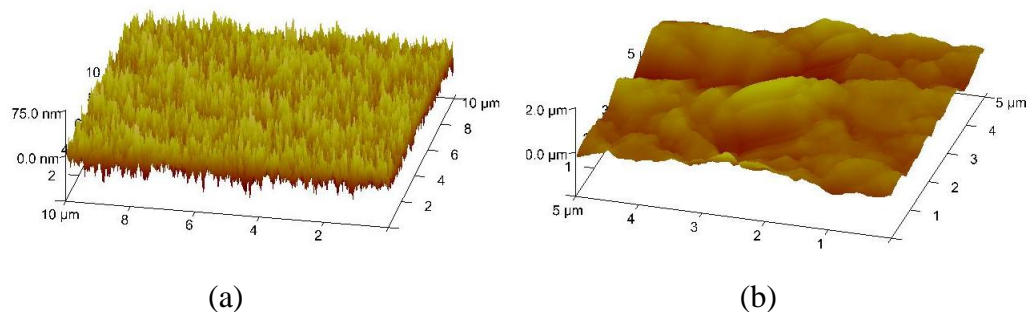


Figure 4.5 AFM images of Dyesol (a) and Aqueous TiO₂ (b)

For Dyesol, the roughness factor (Rq) is 13 nm and Rq of Aqueous sample is from 50 nm to 250 nm. Consequently, there is no relation in our case between surface roughness and Raman imaging because the Raman scattering is not originated nor affected by the topographic character as mentioned above, but rather from groups of interest. Therefore the images in our studies come from the entire surface throughout the TiO₂ film and the intensities observed are not affected by surface topography (roughness).

Anatase has six Raman active modes (A_{1g} + 2B_{1g} + 3E_g), which appear, according to our previous study (Figure 4.4(a)), at 145(146), 197(198), 398(397), 515(516) and 639(642) and which can be assigned as the E_g (1), E_g (2), B_{1g}, A_{1g} or B_{1g}, and E_g (3) modes, for the

Dyesol and in house-made Aqueous phase, respectively [16]. The band position and line-broadening of the E_g (144 and 639 cm⁻¹) Raman active modes show a distinctive peak and this peak can be used to estimate the relative crystallite size [28]. Figure 4.3 shows optical images of TiO₂ films which were used for the imaging. The distribution of anatase throughout the films was observed by curve fitting the E_g (640 and 641 cm⁻¹) modes for the naked TiO₂ (Dyesol and Aqueous).

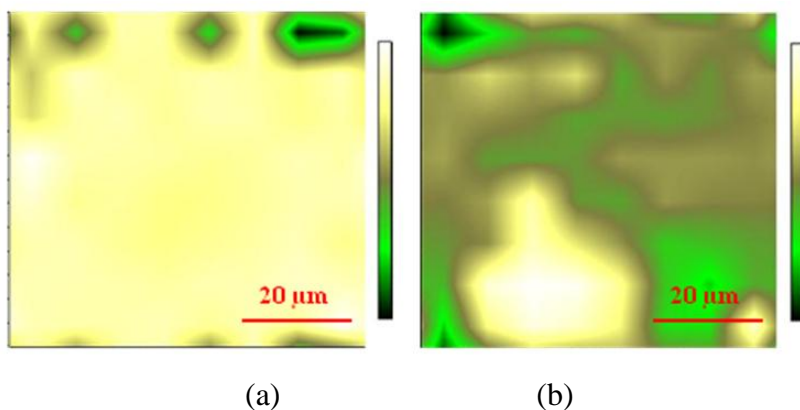


Figure 4.6 Confocal Raman images of the naked TiO₂ film at 640 cm⁻¹ (a) Dyesol TiO₂ (b) Aqueous TiO₂

As shown in Figure 4.6, we selected use of the E_g mode at 640 cm⁻¹ rather than the E_g mode at 144 cm⁻¹ despite the fact that the E_g mode at 144 cm⁻¹ is the most distinctive band among Raman active modes. This was done because the E_g mode at 144 cm⁻¹ is located near the cut off filter (~100 cm⁻¹) of our Raman system; thus, the signal could be dropped significantly if the cut off filter hits the 144 cm⁻¹ band. In the case of the commercial (Dyesol) TiO₂, it is observed (Figure 4.6 (a)) that the distribution is very homogeneous throughout the sample. For our in-house made Aqueous TiO₂ (Figure 4.6 (b)), we observe that although the E_g (640 cm⁻¹) mode is active and distributed throughout the sample, some variation in intensity of this mode is present. This may be due to different surface characteristics and favourable surface complex energetic [16].

The Raman spectroscopic characterization of TiO₂ in high wavenumber region has not been well known or reported unlike its IR counterpart [8-10]. In our studies, the assignment of the higher wave number modes in Raman IR spectra was based on our previous work [16] and that of Minella *et al.* [27]. Between 2500-3500 cm⁻¹ ν_{OH} vibration

of linear and/or bridged H-bonded hydroxyl groups exist; also adsorbed molecular water hydroxyl vibrations occur in this same energy region. Therefore, it is nearly impossible to assign which type of OH (linear or bridge) or H₂O molecule occurs in our Raman (and IR) measurements. All we can say is that the bands we observe at 3000-3200 cm⁻¹ are due to surface Ti-OH (linear and/or bridged) and Ti-OH₂ groups. The water groups can be seen in our IR spectra for both TiO₂ films in the range of ~1600 cm⁻¹ (Figure 4.7).

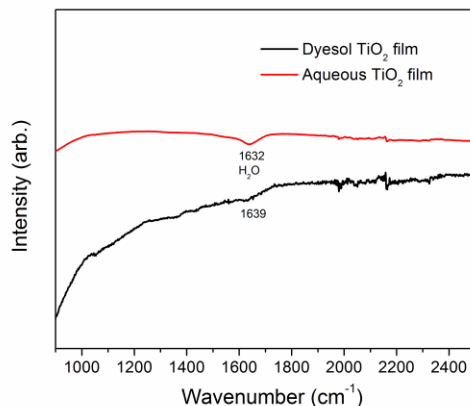


Figure 4.7 IR spectra of the naked TiO₂ films showing the water groups ~1600 cm⁻¹ (adopted from Figure 3.6)

In our previous study [16], we observed a sharp peak at 3080 cm⁻¹ interpreted as Ti-OH/Ti-OH₂ groups in our Raman spectrum (Figure 4.4(b)). Figure 4.8 shows the contrasting Raman images of the naked TiO₂ (Dyesol and Aqueous) obtained by curve fitting the 3076 cm⁻¹ bands to show the distribution of the Ti-OH/Ti-OH₂ surface groups in our samples.

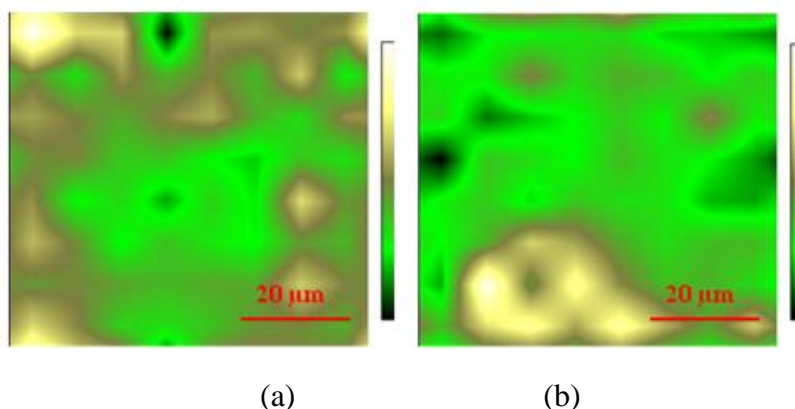


Figure 4.8 Confocal Raman images for the naked TiO₂ films showing surface OH/OH₂ groups at 3076 cm⁻¹ (a) Dyesol and (b) Aqueous

In the case of the Dyesol TiO₂ sample, the hydroxyl density/intensity seems to be distributed throughout the sample more or less homogeneously; but some localization (hot spots) of Ti-OH/Ti-OH₂ sites is evident. For our Aqueous TiO₂, we observe that the occurrence of hydroxyl bonding hot spots is localized. Another thing that should be noted from these images is that when we compare the hydroxyl Raman spectra of our in-house made Aqueous TiO₂ material with the commercial Dyesol product, both exhibit similar hydroxyl stretching modes [16]. However, we can observe the Ti-OH/Ti-OH₂ groups and in particular, the distribution of hot spots to be qualitatively richer and localized in our in-house versus the commercial TiO₂ products. This qualitatively higher surface (OH/H₂O) group content in our Aqueous TiO₂ may be attributed to the method of synthesis (Aqueous solution) and the large surface area our product exhibits [23] which may adsorb more surface groups (OH/H₂O). Higher content of surface groups (OH/H₂O) may translate to better dye binding and hence sensitization, if the results from Hirose *et al.* are considered [14].

To further explore how the hydroxyl surface groups detected in the non-adsorbed TiO₂ samples (Dyesol and Aqueous) changed after adsorption of the N719 dye onto TiO₂ (Dyesol and Aqueous), Raman and ATR-IR contrasting images were collected by curve fitting the features occurring at 3086 cm⁻¹ (Figure 4.9).

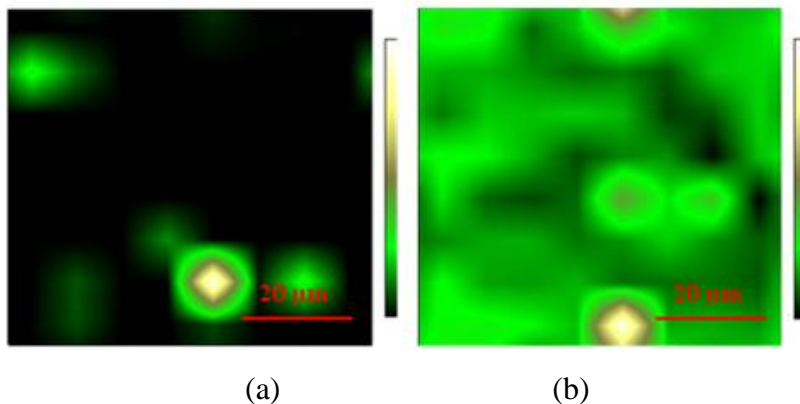


Figure 4.9 Confocal Raman images for the N719 adsorbed TiO₂ showing surface OH/OH₂ groups at 3086 cm⁻¹ (a) Dyesol and (b) Aqueous

In the case of our in-house made Aqueous TiO₂ film, it was mentioned that Ti-OH/Ti-OH₂ groups were distributed throughout the sample and fairly evenly distributed (but at lower density/intensity) at 3076 cm⁻¹ mode (Figure 4.8). It should be noted that there are areas where the hydroxyl “density” is low for the 3076 cm⁻¹ mode, likely indicating that not all these groups will participate in the binding of the N719 molecules. For the mode at 3085 cm⁻¹, the N719-Aqueous TiO₂ sample is not much changed after adsorption; however, it is observed that the local hot spots observed in the non-adsorbed sample (Figure 4.8) are removed upon adsorption (Figure 4.9). For the N719-Dyesol sample, a somewhat similar situation is observed as in our Aqueous TiO₂. However, for the 3085 cm⁻¹ mode we observe that almost all hydroxyl groups have been removed upon adsorption (Figure 4.9(a) vs, Figure 4.9(b)), which is in contrast to what we observed for the N719-Aqueous TiO₂ sample. This difference between the two TiO₂ samples may reflect the different amount of surface groups (OH/H₂O) available before and after sensitization.

4.4.2 Micro ATR-IR imaging

IR imaging was combined with Confocal Raman imaging to spatially resolve Ti-OH/Ti-OH₂ groups on the TiO₂ surface and investigate their role at the micron level. Typical spectra of the neat TiO₂ and N719-TiO₂ are shown in Figure 8 and detailed assignment maybe found in our previous work [16].

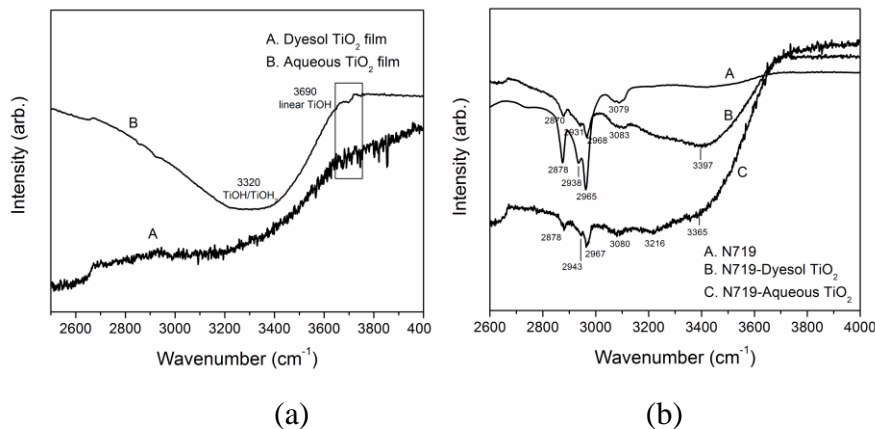


Figure 4.10 ATR-FTIR spectra of naked TiO₂ and N719 adsorbed TiO₂ in the range of 2600-4000 cm⁻¹ (adopted from Figure 3.6(b) and Figure 3.4(b), respectively)

Again, it should be noted that the IR image produced of Ti-OH/Ti-OH₂ groups comes from the entire TiO₂ surface and the intensity of signal observed is not related to surface topography in the IR imaging. The IR images of the naked TiO₂ (Dyesol and Aqueous) obtained by curve fitting the broad 3220 cm⁻¹ bands is represented in Figure 4.11 to show the distribution of the Ti-OH/Ti-OH₂ surface groups in our samples.

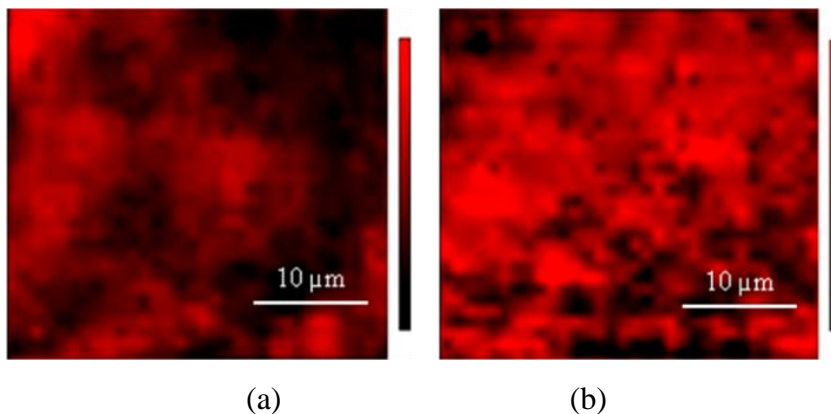


Figure 4.11 ATR-IR images for the naked TiO₂ showing surface OH/H₂O groups at ~3200 cm⁻¹ (a) Dyesol and (b) Aqueous

For the Dyesol TiO₂ sample (Figure 4.11(a)), the hydroxyl density seems to be distributed throughout the sample less homogeneously; but some bright part shows Ti-OH/Ti-OH₂ sites evidently. In the case of our Aqueous TiO₂ (Figure 4.11(b)), we observe the hydroxyl bonding sites (the bright contrast) more clearly than Dyesol TiO₂. IR

imaging shows similar trends with Confocal Raman imaging after dye adsorption on TiO₂ surface as evident in Figure 4.12.

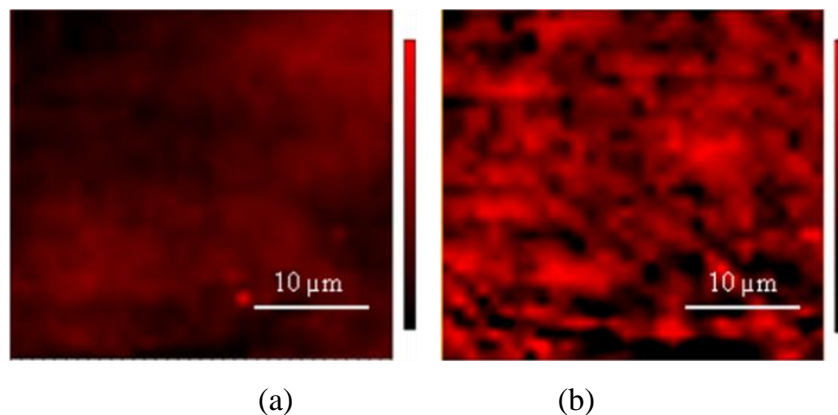


Figure 4.12 ATR-IR images for the N719 adsorbed TiO₂ showing surface OH/H₂O groups at $\sim 3100\text{ cm}^{-1}$ (a) Dyesol and (b) Aqueous

The local hot spots observed in the non-adsorbed sample (Figure 4.11) are somewhat removed upon adsorption (Figure 4.12). However, as mentioned in the Raman imaging section, not all Ti-OH/Ti-OH₂ groups are removed upon dye adsorption. For the dye coated Dyesol TiO₂, we can barely observe the local hot spots, while, in case of the dye coated Aqueous TiO₂, the distribution of bright spots is reduced but the local hot spots still remain. This difference between the two TiO₂ samples possibly reflects the different amount of surface groups (OH/H₂O) that exists in the two substrates (before and after sensitization) but also shows how different surface characteristics (Dyesol vs. Aqueous) of anatase substrates affect the distribution of these groups.

4.4.3. Electrochemical impedance spectroscopy

Electrochemical impedance spectroscopy was conducted to analyze the cell performance of the DSSCs fabricated with the two different TiO₂ electrodes. Impedance spectroscopy is an effective method to investigate physical properties of multi-component electrochemical systems so that individual resistances can be extracted from different sections of the spectra, which are frequency dependent [21]. Key resistances relevant to the DSSC performance are the iodide species diffusion in the electrolyte, the FTO/electrolyte interface, the recombination of electrons in the TiO₂/dye/electrolyte

interface, and the charge transfer at the working (FTO/TiO₂) or Pt counter electrodes [20-22]. The obtained EIS spectra usually consist of Bode phase plots and Nyquist plots. The typical impedance spectra of DSSC exhibit three semicircles, which have been assigned to (a) the electrochemical reaction at the Pt counter electrode and/or electrical contact between conductive substrate/TiO₂ or TiO₂ particles (R_1) in the high-frequency region (1~100 kHz) [29-31]; (b) to electron recombination at the TiO₂/dye/electrode interface (R_2) in the middle-frequency region (1~1000 Hz); and (c) to the Nernst diffusion process of I⁻/I₃⁻ in the electrolyte (R_3) in the low-frequency region (0.01~1 Hz) [20-22,32]. The overall series resistance of the cell (R_s) is the resistance measured when electrons are transported through the device in the high-frequency range exceeding 100 kHz [33]. In addition, the recombination phenomenon (charge transfer resistance, R_2) can be characterized by the electron life time (τ_R) obtained from the EIS plot [34].

The EIS spectra under illumination and open-circuit condition are illustrated in Figure 4.13. Also, the I-V characteristics and impedance data of the DSSCs fabricated with the two different TiO₂ electrodes are listed in Table 4.1.

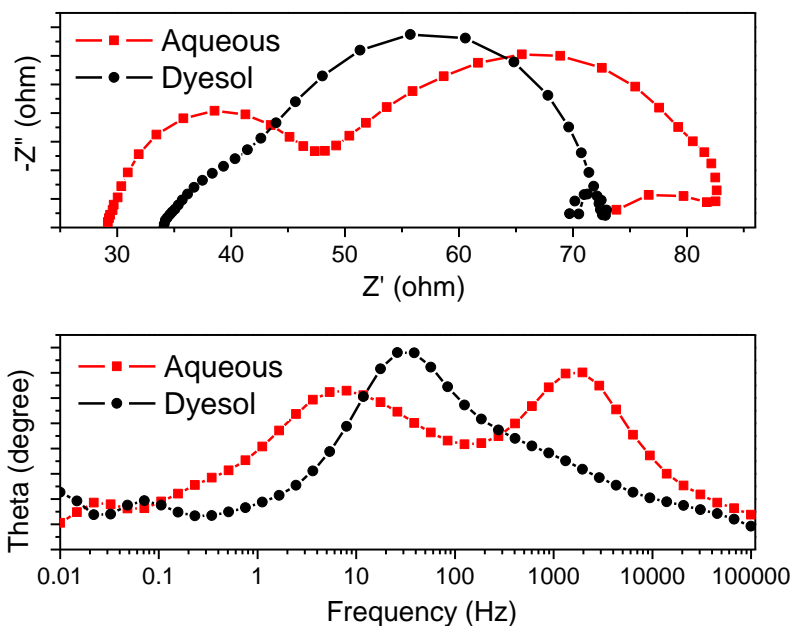


Figure 4.13 Electrochemical impedance spectra of the DSSCs based on two different TiO₂ films (Dyesol and Aqueous) measured at open circuit voltage under 100 mW/cm² (top) Nyquist plot (bottom) Bode phase plot

Table 4.1 Photovoltaic performance and impedance data of the DSSCs fabricated with two different TiO₂ electrodes

Device	R _s (Ω)	R ₂ (Ω) ^a	PF ^b (Hz)	J _{sc} (mA/cm ²)	V _{oc} (V)	FF	η (%)
Dyesol	34.0	32	31.0	14.6	0.58	0.64	5.33
Aqueous	29.2	37	7.22	9.31	0.63	0.68	4.00

^a The values R₂ are obtained from the diameter of the center arc in the Nyquist plot.

^b PF: the peak frequency in the middle range of the Nyquist plot

In our Nyquist plot (Figure 4.13 (top)), the overall series resistance (R_s) for Dyesol and Aqueous made electrodes are 34.0 Ω and 29.2 Ω, respectively. This indicates that the Aqueous TiO₂ made electrode film shows slightly higher conductivity than the Dyesol counterpart resulting in smaller R_s value. However, in terms of the size of R₁ in the Nyquist plot, the Aqueous sample shows a bigger semicircle than the Dyesol sample, implying that there is more charge transfer resistance at the counter electrode and/or

electrical contact between conductive substrate/TiO₂ or TiO₂ particles in the Aqueous DSSC. The higher resistance at the Pt electrode in Aqueous DSSC can be excluded in this case, since we made the counter electrodes in the same way for both DSSCs. Thus, R₁ is most likely the resistance derived from electrical contact between FTO/TiO₂ or TiO₂ particles. The bigger size of R₁ in the Aqueous sample is probably due to the aggregation of the Aqueous TiO₂ particles in the photo-anode. This can be seen from the roughness factor of AFM analysis (50~250 nm for Aqueous TiO₂ and 13.5 nm for Dyesol TiO₂, Figure 4.5). Similarly, Sawatsuk *et al.* observed the effect of aggregation on the electrical impedance of dye-sensitized solar cells based on TiO₂-MWCNTs (multi wall carbon nanotubes) composite electrodes [35]. In their study, they found a degradation of the DSSC performance with increasing concentration of MWCTs incorporated into TiO₂ film. They concluded that this result is from aggregation of MWCNT in the composite electrode.

Meanwhile, the values of the recombination resistance at the TiO₂/dye/electrolyte interface (R₂) of both samples are similar, but the Aqueous sample has a bit bigger R₂. However, it should be noted that we estimated the diameter of center arc (R₂) from the Nyquist plot because the border line between R₁ and R₂ semicircles in the case of Dyesol DSSC was not clear.

According to the EIS theory, the characteristic frequency in the middle range of the Bode phase plots (Figure 4.13(bottom)) can be related to the inverse of recombination life time (τ_r) in TiO₂ films ($\omega_R=1/\tau_R$) [32,36]. In the Bode phase plot of Figure 4.13(bottom), the characteristic middle frequency peak moves from 20.5 Hz for the Dyesol sample to 11.5 Hz for the Aqueous sample. This indicates that the electron recombination times are 0.048 s and 0.087 s in the Dyesol and Aqueous sample, respectively. The higher value of R₂ and increased recombination lifetime may indicate that the Aqueous DSSC is better to block the electron recombination at the TiO₂/electrolyte interface than the Dyesol DSSC.

The third semicircle (R₃) apparently is overlapped with the second semicircle (R₂), which is different from typical impedance spectra [32]. Wang *et al.* also observed this overlapping phenomenon in their EIS spectra of DSSC made with the black dye [37]. In terms of size of the third semicircle, it is observed that the Aqueous sample has bigger resistance than the Dyesol sample. This can be due to the smaller pore size of the

Aqueous TiO₂ made film owing to its smaller nanocrystallite size (5~10 nm) in comparison to the Dyesol TiO₂ made film (20 nm). The small pore size obviously affects the flow of electrolyte into the pores as well ion diffusion hence producing extra resistance.

Although the Aqueous TiO₂ film may accommodate more dye adsorbed molecules due to its higher BET surface area [23,24] and surface hydroxylation, it showed lower conversion efficiency (4 %) in comparison to the Dyesol TiO₂ made film (5.35 %). This can be explained by our EIS results on the basis of increased resistance at the TiO₂ particles (R_1) and pore electrolyte diffusion (R_3), the former derived from particle aggregation and the latter from small pore size. The advantage of higher value of R_2 and increased recombination lifetime for the Aqueous sample may have not been adequate enough to compensate for the resistances due to small pore size and particle aggregation of Aqueous TiO₂ hence the net drop in conversion efficiency. Therefore, based on this analysis, further optimization work is planned to improve the properties of the Aqueous TiO₂-made mesoporous film by modifying the particle dispersion and increasing the pore size hence allowing for the benefits of improved dye binding via surface hydroxylation to be materialized.

4.5 Conclusions

Contrasting Raman images and *micro* IR imaging of the naked anatase TiO₂ (Dyesol and Aqueous) films obtained showed the distribution of surface Ti-OH/Ti-OH₂ groups to be distinct qualitatively richer in our in-house versus the commercial TiO₂ products. Upon dye adsorption the Ti-OH/Ti-OH₂ surface group intensity was observed to decrease but still to be present. These findings provide further supporting evidence that not all surface OH/H₂O groups are consumed upon the binding of the dye on the TiO₂ surface. The reduced hydroxyl group intensity upon adsorption is attributed to bidentate bridging binding of one of the carboxylic groups while the remaining Ti-OH/Ti-OH₂ groups are proposed to be involved in electrostatic/H-bonding interaction with a neighboring carboxylic group as reported in our previous study.¹⁶ However, photo-electrical performance measurements of DSSC devices built with the two different TiO₂ varieties did not yield improved conversion efficiency (η) in the case of our material (4.00 vs.

5.33%). Based on electrochemical impedance spectroscopy analysis of the two different devices, the lack of improvement for the Aqueous TiO₂ was traced to extra charge transfer resistance in the photoanode film most probably arising from particle aggregation and inadequate electrolyte diffusion (small pore size). Higher efficiencies are expected to be achieved with the hydroxyl-rich Aqueous TiO₂ material upon altering its particle properties to allow for optimization of its pore size distribution and film thickness.

4.6 Acknowledgements

The project is funded through the strategic research grant program of NSERC (the Natural Sciences and Engineering Research Council of Canada). The authors thank Cecile Charbonneau for the synthesis of the aqueous TiO₂ anatase powder.

4.7 References

- [1] Gratzel, M. *Nature*, **2001**, *414*, 338
- [2] Li, B.; Wang, L.; Kang, B.; Wang, P.; Qiu, Y. *Sol. Energy Mater. Sol. Cells* **2006**, *90*, 549
- [3] Kroon, J. M.; Bakker, N. J.; Smit, H. I. P.; Liska, P.; Thampi, K. R.; Wang, P.; Zakeeruddin, S. M.; Gratzel, M.; Hinsch, A.; Hore, S.; Wurfel, U.; Sastrawan, R.; Durrant, J. R.; Palomares, E.; Pettersson, H.; Gruszecki, T.; Walter, J.; Skupien, K.; Tulloch, G. E. *Prog. PhotoVoltaics* **2007**, *15*, 1
- [4] Nazeeruddin, M. K.; Klein, C.; Liska, P.; Gratzel, M. *Coord. Chem. Rev.* **2005**, *249*, 1460
- [5] Hagfeldt, A.; Boschloo, G.; Sun, L.; Kloo, L.; Pettersson, H. *Chem. Rev.* **2010**, *110*, 6595
- [6] Hagfeldt, A.; Gratzel, M. *Chem. Rev.* **1995**, *95*, 49
- [7] Falaras, P. *Sol. Energy Mater. Sol. Cells*, **1998**, *53*, 163
- [8] Finnie, K. S.; Bartlett J. R.; Woolfrey, J. L. *Langmuir*, **1998**, *14*, 2744
- [9] Nazeeruddin, Md. K.; Humpry-Baker, R.; Liska, P.; Gratzel, M. *J. Phys. Chem. B*, **2003**, *107*, 8981
- [10] Leon, C. P.; Kador, L.; Peng, B.; Thelakkat. M. *J. Phys. Chem. B*, **2006**, *110*, 8723

- [11] Johansson, E. M. J.; Hedlund, M.; Siegbahn, H.; Rensmo, H. *J. Phys. Chem. B.* **2005**, *109*, 22256
- [12] Shklover, V.; Ovchinnikov, Y. E.; Braginsky, L. S.; Zakeeruddine, S. M.; Gratzel, M. *Chem. Mater.* **1998**, *10*, 2533
- [13] De Angelis, F.; Fantacci, S.; Selloni, A.; Nazeeruddin, Md. K.; Gratzel, M. *J. Am. Chem. Soc.* **2007**, *129*, 14156
- [14] Hirose, F.; Kuribayashi, K.; Suzuki, T.; Narita, Y.; Kimura, Y.; Niwano, M. *Electrochem. Solid-State Lett.* **2008**, *11*, A109
- [15] Gong, X.; Selloni, A.; Batzill, M.; Diebold, U. *Nat. Mater.* **2006**, *5*, 665
- [16] Lee, K. E.; Gomez, M. A.; Elouatik, S.; Demopoulos, G. P. *Langmuir*, **2010**, *26*, 9575
- [17] Lee, E. *Proc. of SPIE.* **2007**, 6765, 67650E
- [18] Hara, K.; Arakawa, H. in *Handbook of Photovoltaic Science and Engineering*. A. Luque and S. Hegedus, Editor. Chapter 15, John Wiley & Sons, New York (2003)
- [19] Hoshikawa, T.; Yamada, M.; Kikuchi, R.; Eguchi, K. *J. Electrochem. Soc.*, **2005**, *152*, E68
- [20] Kalyanasundaram, K. in *Dye-sensitized Solar Cells*, Chapter 12, CRC Press, (2010).
- [21] Bisquert, J. *J. Phys. Chem. B.* **2002**, *106*, 325
- [22] Ross, M. J.; William, K. R. in *Impedance Spectroscopy: Emphasizing Solid Materials and Systems*; John Wiley & Sons, New York (1987).
- [23] Charbonneau, C.; Lee, K. E.; Shan, G. B.; Gomez, M. A.; Gauvin, R.; Demopoulos, G. P. *Electrochem. Solid-State Lett.*, **2010**, *13*, 8, H257
- [24] Charbonneau, C.; Gauvin, R.; Demopoulos, G. P. *J. Electrochem. Soc.* **2011**, *158*, H224
- [25] Ito, S.; Chen, P.; Comte, P.; Nazeeruddin, M. K.; Liska, P.; Pechy, P.; Gratzel, M. *Prog. Photovolt: Res. Appl.* **2007**, *15*, 603
- [26] Levin, I. W.; Bhargava, R. *Annu. Rev. Phys. Chem.*, **2005**, *56*, 429
- [27] Minella, M.; Faga, M. G.; Maurino, V.; Minero, C.; Pelizzetti, E.; Coluccia, S.; Martra, G. *Langmuir*, **2010**, *26*, 2521
- [28] Arora, A. L.; Rajalakshmi, M.; Ravindran, T. R.; Sivasubramanian, V. *J. Raman Spectrosc.*, **2007**, *38*, 604

- [29] Han, L.; Koide, N.; Chiba, Y.; Mitate, T. *Appl. Phys. Lett.*, **2004**, *84*, 2433
- [30] Kern, R.; Sastrawan, R.; Ferber, J.; Stangl, R.; Luther, J. *Electrochim. Acta*, **2002**, *47*, 4213
- [31] Park, J. H.; Jun, Y.; Lee, H. Y. S.; Kang, M. G. *J. Electrochem. Soc.* **2008**, *155*, F145
- [32] Wang, Q.; Moser, J. E.; Gratzel, M. *J. Phys. Chem. B*, **2005**, *109*, 14945
- [33] Lee, K. M.; Hu, C. W.; Chen, H. W.; Ho, K. C. *Sol. Energy Mater. Sol. Cells* **2008**, *92*, 1628
- [34] Adachi, M.; Sakamoto, M.; Jiu, J.; Ogata, Y.; Isoda, S. *J. Phys. Chem. B* **2006**, *110*, 13872
- [35] Sawatsuk, T.; Chindaduang, A.; Sae-kung, C.; Pratontep, S.; Tumcharern, G. *Diamond Relat. Mater.* **2009**, *18*, 524
- [36] van de Lagemaat, J.; Park, N. G.; Frank, A. J. *J. Phys. Chem. B* **2000**, *104*, 2044
- [37] Wang, Z.; Yamaguchi, T.; Sugihara, H.; Arakawa, H. *Langmuir* **2005**, *21*, 4272

Chapter 5. Electronic Interactions between N719 Sensitizer and Anatase TiO₂ Films: A Combined XAS and XPS study

Having shed light in Chapters 3 and 4 on the manner by which dye molecular groups bind on the nanocrystalline TiO₂ surface next the electronic structure and interactions at the dye-TiO₂ interface were investigated and the results are reported in this Chapter. Towards this end XAS (X-ray absorption spectroscopy) and XPS (X-ray photoelectron spectroscopy) techniques were employed to study two nanocrystalline TiO₂ (commercial and our aqueous synthetic) and their dye-coated counter parts. The electronic structure and interaction of dye-TiO₂ gave complementary information to our previous vibrational spectroscopic studies in chapter 3 and 4. The experimental Ti L,K-edge and O K-edge were employed to monitor the coordination effect and verify the previously reported study. The C K-edge and N K-edge XANES spectra were employed to observe interactions on the electronic structure of N719 on two different TiO₂ with regard to the aspect of dye molecule upon adsorption, which was firstly focused in this field. XPS was further employed for better surface sensitivity to monitor the surface interactions between the two different anatase substrates and their sensitized counter parts. Finally, DSSCs fabricated with two TiO₂ photoanodes were evaluated by I-V (photocurrent-voltage) measurement.

5.1 Abstract

In this study, the electronic properties of N719 adsorbed onto anatase were comparably investigated by using XAS and XPS techniques. Sensitized TiO₂ films made from two different nanocrystalline anatase powders were investigated: a commercial one (Solaronix) and our synthetic variety produced through aqueous synthesis. This was done to investigate how our aqueous produced nanocrystalline anatase substrates compared with commercial products and to observe if both nanocrystalline anatase anodes behaved in a similar manner in terms of their bonding and electronic interactions. Surface coordination changes to Ti-O groups previously reported using Ti K-edge EXAFS data (using transmission or FY) between the pure TiO₂ and the adsorbed state were not observed in our measurements via the Ti L or K XANES (nor EXAFS) data for both substrates using a surface sensitive detection technique (TEY). This is likely due to the probing depth of TEY mode (5~10 nm), in which the coordination changes that occur to the surface groups which should in turn affect the XANES spectrum are not observed at Ti K or L edge XANES spectrum. The C and N K-edge XANES spectra of the N719 adsorbed onto two TiO₂ films were for the first time evaluated in this work. From the C K-edge XANES data, the spectral changes revealed that additional electronic states occur between dye molecules and TiO₂ surface. The C K-edge XANES spectra allowed us to propose that electronic interactions do not only occur through the covalent bonding of the anchoring groups but also through the aromatic electron density of the bipyridine groups and the d states found in TiO₂. This was further confirmed via the XPS analysis by monitoring the N bipyridine groups before and after sensitization. XPS used in combination with XAS (in TEY mode) provided complementary information owing to its higher surface sensitivity. The Ti 2p and O 1s XPS spectra showed that the adsorption of the dye on TiO₂ leads to a change of the surface dipole and/or a change in the Fermi level position in the band gap, which shifts all the core levels of TiO₂. These are not equal for both TiO₂ substrates in spite of them being nanocrystalline anatase. This effect was found to be greater for the N719-Aqueous TiO₂ system than the respective Solaronix one. For the N 1s and S 2p XPS, the shift toward higher energy indicated that there exists

additional H-bonding interaction of the NCS ligand of the dye molecule with the TiO₂ surface groups (OH/H₂O).

5.2 Introduction

Dye sensitized solar cell (DSSC) has become an active field of research since it holds a lot of promise because of the use of an abundant and benign semiconductor material TiO₂ [1]. Binding of the dye to the TiO₂ substrate plays a key role in the efficiency of DSSC because electron transfer depends on the binding mode [2]. A question that also remains of interest is if all nanocrystalline anatase substrates behave in the same manner chemically and electronically. For example, polycrystalline titania nanotubes were thought to offer advantages of directed electron transport and higher electron mobility [3,4] compared to sintered TiO₂ nanoparticle films, yet macroscopic measurements have shown their electron mobility to be as low as that of nanoparticle thin films. Recent studies by Richter and Schmuttenmaer [5] have proposed this lack of electron mobility to exciton-like trap states. Thus, our aqueous produced TiO₂ material has motivated us to investigate how the bonding, electronic interactions and electrical performances may vary in nanocrystalline anatase films. Our previous study using vibrational spectroscopy and Confocal Raman imaging, demonstrated that indeed different surface bonding properties (covalent and H-bonding) and distributions for two differently synthesized nanocrystalline anatase substrates were observed [6,7]. As a result a subsequent study to investigate how the electronic interaction in our aqueous and commercial products compared is presented in this manuscript via the use of core level surface sensitive spectroscopies (XAS and XPS).

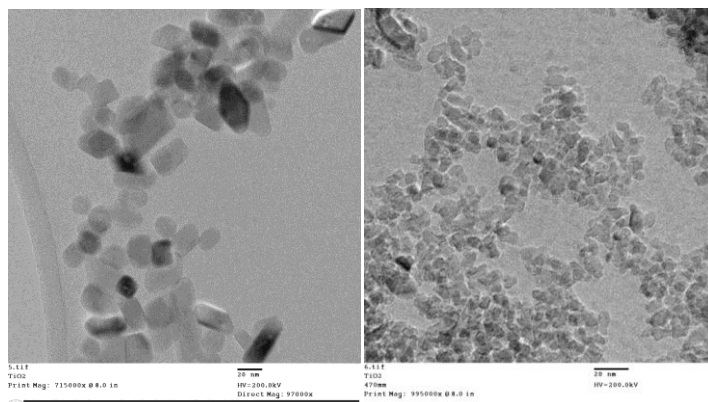
X-ray Absorption Spectroscopy (XAS) is a perfect probe to investigate coordination changes that occur around an element of interest in both the X-ray Absorption Near Edge Structure (XANES) and the Extended X-ray Absorption Fine Structure (EXAFS) region. XANES in particular can be used to investigate the local coordination chemistry (octahedral, tetrahedral), molecular orbitals interactions (p-d hybridization,), band structure (the density of unoccupied electronic states) and spin state (high or low spin) of materials at the bulk and interfaces [8-10]. More specifically, XANES at the L_{2,3}-edge of

transition metal cations (such as $3d^0$ ions as Ti⁴⁺ or Ca²⁺) are dominated by exchange interactions, spin-orbit splitting and crystal field effects which makes it a perfect probing tool to study coordination states [11-14]. Therefore, the L_{2,3}-edge XANES probes the electronic structure and crystal field details within the first coordination sphere (e.g. surface) and bulk depending upon which decay channel is used for detection (TEY-surface (5~10 nm), FY- bulk (≥ 50 nm)). In addition to the L-edge XANES, the K-edge XANES spectra of transition metals also offer the advantages of sensitivity to coordination states as shown extensively in the literature [15-19].

Several groups have studied the interface properties of dye/TiO₂ using X-ray absorption spectroscopy to elucidate electron transfer mechanism. Ju *et al.* reported an XAS study on the Ti K-edge of TiO₂ nanoparticles of 10-20 nm with and without an assembly of N3 dye [20]. They suggested that the coordination numbers for the TiO₂/N3 interface was 2.7 ($N_{\text{Ti-O}}$) and 2.2 ($N_{\text{Ti-Ti}}$) in comparison to the coordination number of the isolated TiO₂ nanoparticles (4.0 for $N_{\text{Ti-O}}$ and 1.6 for $N_{\text{Ti-Ti}}$) as derived from their fitted EXAFS data, which was measured in transmission mode. These findings were interpreted as a result of the reconstruction of Ti local structure upon adsorption of the N3 dye on the TiO₂ surface. However, it should be noted that their XAS spectra at the Ti K-edge were measured in transmission mode, which is not surface sensitive. Similarly, Zubavichus *et al.*[21] characterized Ru complexes (N719 and black dye) adsorbed anatase TiO₂ using Ti K-edge XAS (XANES and EXAFS) in combination with out-of-plane XRD and XPS analysis. In their Ti K-edge XANES spectrum, the uniform enhancement of the pre-edge peaks was suggested to correspond to higher distortions of a local Ti coordination in the coated samples as this is forbidden in the centrosymmetric octahedral environment. The EXAFS data measured via fluorescence yield supported their interpretation of the XANES spectrum. The coordination numbers $N_{\text{Ti-O}}$ and $N_{\text{Ti-Ti}}$ were drastically diminished (2.8 and 1.4) in comparison with those for the uncoated sample (4.6 and 2.7), because coating with the dyes lead to a stronger distortion of the local environment of Ti atoms in anatase nanoparticles[21]. Their calculated coordination numbers are different than those suggested by Ju *et al.*[20]. Furthermore, it may be noted that FLY at Ti K-edge detects mostly the bulk, unless the dye coating is very thick, i.e. this approach is not interface sensitive.

In terms of XPS studies, the adsorption orientation and electronic coupling of N3 onto TiO₂ have been studied in a number of publications [22-24]. Rensmo *et al.* conducted XPS studies of Ru-polypyridine complexes for solar cell application, in which they reported the C 1s, O 1s, N 1s and S 2p spectra to support the general picture of bonding via the carboxyl groups of a single bi-isonicotinic acid ligand of the complex. For the measurement of N3 with TiO₂, they concluded that the –NCS ligand to TiO₂ interaction was small [22]. Later on, Johansson *et al.* compared the electronic and molecular structure of the dyes (black dye, N3 and N719) adsorbed onto nanostructured TiO₂ using PES (photo electron spectroscopy). In their study, they proposed that a fraction of the –NCS groups interacts with the TiO₂ surface through the sulfur atoms based on their S 2p spectra. From the O 1s spectrum of N719 on TiO₂, they deduced the –OH units in carboxylic acid groups to be at a larger distance from the TiO₂ surface than carboxylated oxygen, indicating that N719 is anchored to the TiO₂ surface through carboxylated groups, partly having TBA⁺ (tetrabutyl ammonium ion) as counter ions. Moreover, from the N 1s spectrum, the TBA⁺ counter ions were found to be at the surface, although the amounts were clearly smaller than expected from the molecular formula [23]. Similarly, Mayor *et al.* reported an experimental study of the bonding geometry and electronic coupling of the N3 dye adsorbed on rutile TiO₂, via the (110) plane along with supporting theoretical calculations. In their study, the carboxylic groups of one bi-isonicotinic acid ligand de-protonated so that its O atoms bonded to the Ti atoms of the substrate and one of the thiocyanate groups bonds via a S atom to an O atom of the Ti substrate. Their DFT calculations supported that this geometry was energetically more favorable than the bonding of one carboxylic group from each bi-isonicotinic acid ligand [24].

In this paper, two nanocrystalline TiO₂ (commercial and our aqueous synthetic - Figure 5.1) and their dye-coated counter parts have been studied via XAS (X-ray absorption spectroscopy) and XPS (X-ray photoelectron spectroscopy) techniques.



(a) Solaronix (b) Aqueous

Figure 5.1 TEM image of TiO₂ particulate

The experimental Ti L,K-edge, O K-edge, C K-edge and N K-edge XANES spectra were employed to monitor the bonding (coordination) effects and interactions on the electronic structure of N719 ((bis(tetrabutylammonium)[cis-di(thiocyanato)-bis(2,2'-bipyridyl-4-carboxylate-4'-carboxylic acid)-ruthenium(II)]) on two distinct anatase TiO₂ films. All XAS measurements were conducted in TEY mode for improved surface/interface sensitivity.

XPS was further employed for better surface sensitivity to monitor the surface interactions between the two different anatase substrates and their sensitized counter parts. The O 1s XPS data was used to estimate the amount of OH groups on the surface of pure TiO₂ (Solaronix and Aqueous) substrate. The N 1s and S 2p XPS data was used to monitor the chemical interactions occurring between these groups and the TiO₂ surfaces. Finally, the C1s data is used to observe surface contamination before dye adsorption.

5.3 Experimental Section

5.3.1 Sample preparation

The N719 (bis(tetrabutylammonium)[cis-di(thiocyanato)-bis(2,2'-bipyridyl-4-carboxylate-4'-carboxylic acid)-ruthenium(II)]) used in this work was obtained from Dyesol. The electronic study of the N719 involved two nanostructured TiO₂ (both anatase; one commercial-Solaronix (Ti-Nanoxide T20) and one synthesized in our laboratory-Aqueous [25]) films prepared by paste deposition, annealing and sensitization. The commercially available Solaronix TiO₂ (15~20 nm) was produced by hydrothermal

reaction and our synthetic variety (5~10 nm) was produced through aqueous synthesis (TEM image in Figure 5.1). The preparation of the Aqueous TiO₂ paste followed Ito *et al.*'s procedure [26]. TiO₂ electrodes were prepared by screen printing on FTO glass substrates (Nippon Sheet Glass with a sheet resistance of 10 Ω per square). The TiO₂ paste was spread out onto a FTO glass and sintered at 450°C in air for 30 min yielding a 5~8 μm thick nanostructured anatase film, measured by a Dektak 3 surface profile measuring system. The dye adsorption was performed by immersing the TiO₂ electrodes for 24 h in a 0.3 mM solution of N719 at room temperature. The coated TiO₂ was rinsed thoroughly with ethanol to remove physisorbed dye molecules.

In the case of sample preparation of neat dye for XANES measurement, 5 mg of dye was dissolved in 0.25 ml of ethanol, stirred and put in ultrasonic bath for 30s. Approximately 0.01 ml was dropped onto a 5x5 mm gold coated Si wafer (unpolished). The ethanol was allowed to evaporate, leaving a layer of sample that was estimated to be 100 μm thick or more. For XPS measurement, the neat dye was prepared similarly to one in XANES measurement.

5.3.2 XANES

XANES spectra were obtained at the Canadian Light Source (CLS) on the spherical grating monochromator (SGM) beamline ($\Delta E/E$: $\sim 10^{-4}$) for the Ti L-edge, O K-edge, N K-edge and C K-edge. XANES spectra were recorded in the surface sensitive total electron yield (TEY) using specimen current and bulk sensitive fluorescence yield (FY) using a multi-channel plate detector under high vacuum (5 e^{-8} Torr). For the C K edge measurements a 100 nm Ti filter was placed in the beamline to reduce the contribution of the O K edge excited by second order light [27]. C K edge spectra were normalized to the incident photon flux as recorded by a photodiode (AXUV100). All other spectra were normalized to the incident flux recorded using a Au mesh (85% transmission). The energy calibration at the Ti L_{3,2}-edge and the O K-edge were conducted based on the TiO₂ anatase powder and literature values [28,29]. Carbon K-edge and nitrogen K-edge were calibrated using CO and N₂ gas, respectively. Ti K-edge was conducted at the SXRMB beam line using a step size of 0.3 eV and in TEY mode.

5.3.3 XPS

X-ray photoelectron spectroscopy (XPS) measurements were conducted in a Thermo Scientific K-Alpha, using a Al K α X-ray source at 1486.6 eV. The base pressure was $\sim 10^{-10}$ Torr. High-resolution spectra were obtained at a perpendicular takeoff angle, using a pass energy of 20 eV and steps of 0.05 eV. Spectral peaks were separated using the VG Avantage program, and the Shirley background was subtracted. The scale of the binding energy was calibrated against Au (4f_{7/2}). No effects due to charging or X-ray damage were observed during the experiment.

5.3.4 Cell fabrication and photovoltaic measurements

A sandwich-type cell was assembled to measure the IV curves. As a counter electrode, a Pt layer was prepared by spreading one drop of 5 mM H₂PtCl₆ solution (*i*-propanol), air dry, and then heat at 380° for 30 min. For the photoanode, the TiCl₄ pre-treatment was applied before screen printing TiO₂ paste on the FTO glass[26]. The thickness of photoanodes is ~ 10 -12 μ m for both TiO₂ without using scattering layer. A 60 μ m thick thermoplastic film (Meltonix 1170-60 Series, Solaronix) was employed to seal the two electrodes and a commercial electrolyte solution (EL-HPE, Dyesol) filled through the hole on the Pt electrode. The current-voltage curves were measured using a small area solar simulator (PV measurements Inc., Model SASS). The replicate tests of IV measurements were performed for better accuracy. A tungsten lamp was used to provide uniform light approximating the AM 1.5 Global reference spectrum to a 1 cm diameter test region. The light intensity was adjusted with a Si reference cell.

5.4 Results and Discussion

5.4.1 XANES

5.4.1.1 Ti L-edge

Previous EXAFS studies via the Ti K edge [20,21] have indicated that the coordination of Ti-O is changed when the COOH group of the dye molecules is adsorbed onto TiO₂, as described in the introduction. This in turn should modify significantly the crystal field of the surface interacting TiO₂ nanoparticles as a result of the coordination change that occurs from the pure state to the adsorbed state in which bidentate bonding occurs

between the dye molecule and TiO₂. Such coordination changes should then be clearly observed at the Ti L or K-edge XANES spectra [11,15,16,30]. Thus, the motivation of our XAS study using the surface sensitive TEY mode at the Ti L,K-edge and O K-edge XANES is to observe and verify these coordination changes for the dye-coated TiO₂ in comparison to the pure TiO₂, and to observe if any differences occur between the two distinct anatase nanocrystalline substrates (our aqueous and commercial).

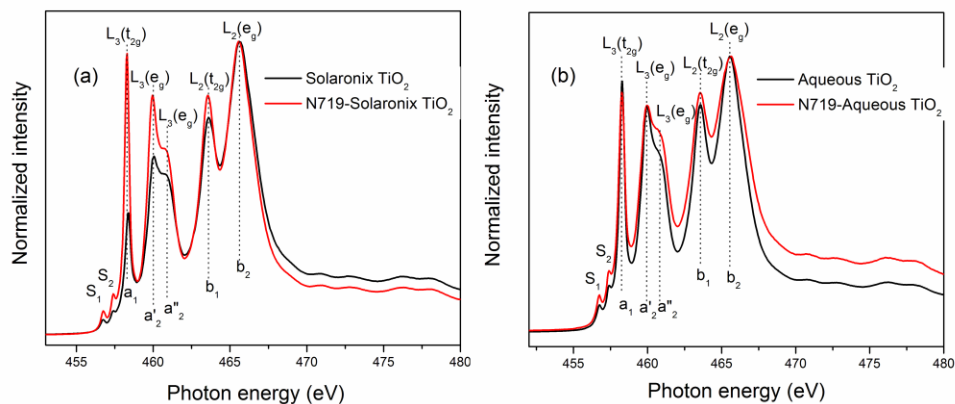


Figure 5.2 Titanium L-edge XANES spectra of the TiO₂ and N719-adsorbed TiO₂ film

Figure 5.2 shows the Ti L-edge XANES spectra of the pure TiO₂ and N719 dye-coated TiO₂ for the commercial Solaronix and our lab-based Aqueous anatase. In the pure TiO₂, the XANES spectra contain weak pre-edge peaks, denoted S₁ and S₂ [27]. The spectra also consist of the usual sets of peaks, denoted L₃ and L₂ in the higher photon energy. The L₃ features (a₁ and a₂) results from the dipole allowed transition of the 2p_{3/2} to the final state of Ti 3d_{5/2} and the L₂ peaks (b₁ and b₂) are derived from 2p_{1/2} to the final state of Ti 3d_{3/2} (($\Delta l = \pm 1$, $\Delta j = 0, \pm 1$); the character of these states is modified by the combined spin-orbit and crystal field interactions [27-29]. According to the work of de Groot, the peaks of L₂ are broader due to the shorter lifetime of its excited state, since L₂ has extra decay channels, compared to L₃ [30]. As the crystal field splits the 3d state of Ti into two levels, t_{2g} and e_g, each L peak represents two contributions a'₁ (b₁) and a'₂ (b₂), respectively. Furthermore, the e_g peak of the L₃ edge has an asymmetry or an additional splitting (a''₂) that is the XANES finger print for the crystallographic phases of anatase. The reason for different relative intensities between a₂ (a''₂) and b₁ (b₂) peaks has been discussed by a number of publications [30-33]. It has been known that the additional splitting is due to distortions from octahedral symmetry [30,31]. However, current work by Kruger has

mentioned that the distortion of the TiO₆ octahedra is not a sufficient condition to describe the L₃(e_g) peak splitting since there is not splitting for an isolated (distorted) TiO₆ octahedron. Also, his analysis showed that the distortion is not even a necessary condition since ideal rutile made from undistorted octahedral also shows a L₃(e_g) peak splitting of about the same width as real rutile. Kruger's analysis using the first-principles multichannel multiple-scattering method with a particle-hole wave function, clearly shows that the L₃(e_g) peak splitting is not a local effect. Therefore it can neither be explained with atomic crystal field theory nor TiO₆ charge transfer models. Instead it is a non-local effect that requires a quite precise description of the Ti-3d band structure which is possible only using k-space band structure or large cluster calculations [32,33].

Now as can be seen from Figure 5.2, the dye-coated TiO₂ Ti 2p XANES spectrum is virtually identical to that of anatase without dye in terms of splitting and symmetry of peaks, but their intensity differs. At this point, it is worth to remind the reader that in XAS, the core electron is excited to a bound state, i.e. we probe the empty density of states (empty orbitals in chemical terms) and as such transitions ("peaks") are only observed if these states are unoccupied. Moreover, the intensity of the XAS peaks can also be qualitatively used to estimate the density of unoccupied states for the particular transitions as observed in literature work [34,35]. In spite of the fact that both Solaronix and our synthetic substrate are nanocrystalline anatase films, the density of states (as indicated from the intensity of the XANES spectra) for the L₃ (t_{2g} and e_g) orbital varies significantly once the dye molecule is adsorbed in both anatase substrates. For example, in the case of the dye-adsorbed Solaronix TiO₂, the intensity of the L₃ (t_{2g}) orbital is much higher than the pure TiO₂, indicating that once the N719 bonds to the surface, the density of states of these lower energy electronic states in TiO₂ become free (unoccupied) and as such may be the ones that are filled later once the injection process occurs. For our Aqueous TiO₂ substrate, we observe a completely different behavior than that observed in the Solaronix, namely, the density of states for the L₃ (t_{2g} and e_g) remains the same before and after dye adsorption. In the case of Aqueous TiO₂, the splitting of L₃ (e_g)/L₃'(e_g) peak in the dyed TiO₂ is less sharp than the one in the pure TiO₂ or the Solaronix case. The peaks in the range of 465 eV are also broadened, which is likely attributed to some degree of local structure change in TiO₂ nanoparticles. However, most

of the spectral structural change that is observed for the TiO₂ XANES before and after dye adsorption is little to none in both anatase substrates. This was rather unexpected since the XANES spectrum at the L -edge is a very sensitive probe to coordination of transition metals such as Ti⁴⁺ systems [11,13] and as that reported in previous studies for the K-edge [20,21]. The simplest interpretation for that is that most of the XANES TEY signal comes from the Ti atoms far from the dye - TiO₂ interface; in other words even the use of the TEY mode (which can probe 5-10 nm [36]) is not sufficiently surface sensitive to monitor the interface coordination changes in two distinct nanocrystalline anatase substrates. This then raises questions about the EXAFS data reported by Ju *et al.*[20] and Zubavichus *et al.*[21] in which they reported to have detected surface coordination changes to the Ti-O bonds of the pure and adsorbed state using less sensitive detection techniques (transmission and FY). However, as shown by our XANES Ti L-edge (and later K-edge) data in TEY detection mode, the pure and adsorbed states gave rise to the same XANES spectrum indicating that no changes to their crystal field (and therefore their coordination of the surface groups) could be observed upon dye adsorption, in spite of the fact we used even more surface sensitive techniques than Ju *et al.*[20] and Zubavichus *et al.*[21]. If this is not the case (i.e. surface sensitivity), then it would mean that the Ti L-edge spectrum of the interface Ti atoms is not influenced by the dye adsorption. However, the latter case is unlikely, and it is the lack of sensitivity of the TEY mode of the Ti L-edge which does not allow us to see the coordination changes to the surface TiO₂ group upon dye adsorption. Auger Electron Yield (AEY) or Partial Electron Yield (PEY) maybe sensitive enough to detect these changes in coordination states but this is out of the scope of the present study.

Another reason that we may not see a difference in the Ti L-edge XANES signals from the coated versus that of the uncoated samples, is that a very small amount of the Ti signal actually comes from the TiO₂ that is interacting with the dye. Even though the surface area in our nanocrystalline anatase is high, the TiO₂ that is interacting with the dye only makes up a small fraction of the total TiO₂ that is giving us the signal. Thus one is looking for a very small effect on top of a large background in the present study and those of previous works [20,21].

With reference to the point of sensitivity, it is well known that total electron yield (TEY) is more surface sensitive than fluorescence yield (FY) because the sampling depth of the TEY is ~5-10 nanometers [8,34], while that of FY is obtained from deep inside the bulk ($\geq 50\text{nm}$) [8,34] of the TiO₂. Thus, the intensity of FY is always higher than TEY's because the signal collected for titanium atoms from the FY is always expected to be much stronger than the one from TEY.

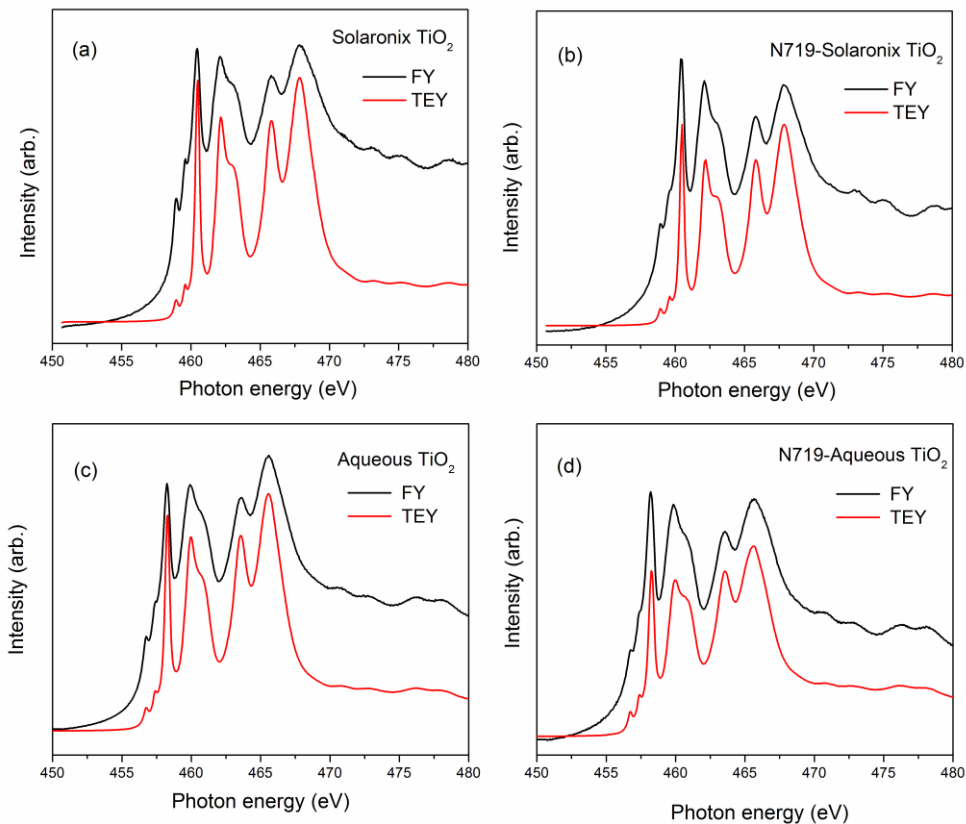


Figure 5.3 Ti L-edge of TEY and FY for the pure TiO₂ (a) (c) and N719-TiO₂ (b) (d)

Figure 5.3 shows the Ti 2p XANES of TEY in comparison to FY. It is observed that FY shows a higher background and signal as expected, since more TiO₆ atoms contribute to the Ti L-edge XANES spectra as a result of the greater probing depth. Upon comparison of the TEY with the FY mode for the pure and sensitized TiO₂ samples, it can be observed that the L_{2,3} and pre-edge features are much more well defined; this is especially observed for the characteristic L₃(e_g)/L₃'(e_g) features. The other peaks are suppressed due to self-absorption.

At this point, it is worth noting that all the XANES measurements conducted on our TiO₂ films were dipped in the dye solution for 24 hrs, similar to the procedure used by Ju *et al.*[20] and for longer times than that of Zubavichus *et al.*[21] who only used 12-15 hrs retention time. Thus, the amount of dye loading (i.e. thickness of dye coverage on TiO₂) in our experiment and that of Ju *et al.*[20] and Zubavichus *et al.*[21] should ideally be the same or very similar and so we can rule out major experimental differences between the works. So it may be inferred that the results reported by Ju *et al.*[20] using Ti K-edge EXAFS measurements which report change in coordination of the surface TiO₂ groups are not possible, since the transmission mode cannot give the surface sensitivity required to observe these coordination changes that occur at the surface of the TiO₂ nanoparticles. Similarly, the work by Zubavichus *et al.*[21] showed a significant coordination (Ti-O) change using the FY mode at the Ti K-edge but as previously discussed, these two types of detection modes are more bulk than using electron yield. In our studies, via the Ti L-edge XANES in surface sensitive TEY mode, coordination changes to the TiO₂ surface groups of both substrates could not be observed in spite of the fact that the L-edge XANES is a perfect probe to measure these coordination changes around Ti atoms [9,11,13].

Therefore, to clarify the above point, we decided to further conduct Ti K-edge measurements using the electron yield mode, which should in theory be more surface sensitive than the FY and transmission measurement to further verify our L-edge findings. XPS measurements were also applied to investigate these interactions of dye-TiO₂ in both substrates with the advantage of giving even greater surface sensitivity than TEY mode; this is later discussed in the manuscript.

5.4.1.2 Ti K-edge

As mentioned previously, to clarify and verify if the coordination changes previously reported by Ju *et al.*[20] Zubavichus *et al.*[21] could be observed for both systems, we decided to conduct Ti K-edge analysis using the surface sensitive TEY mode.

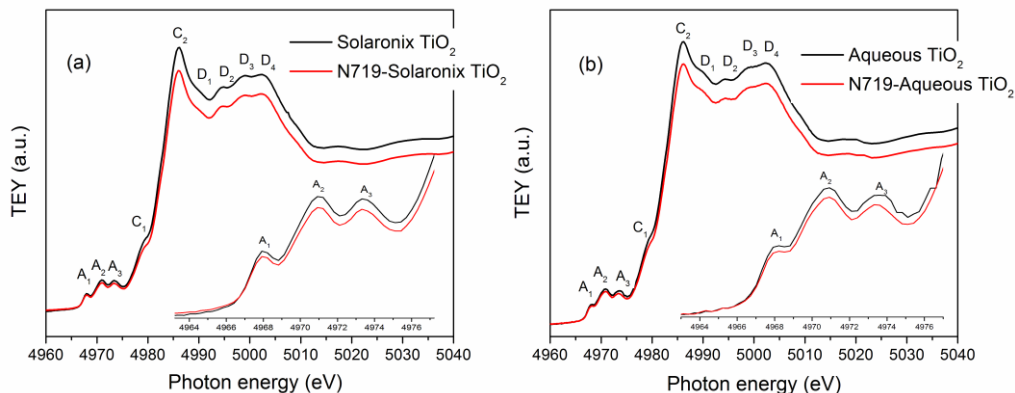


Figure 5.4 Ti K-edge XANES of TiO₂ and N719-TiO₂ (a) Solaronix and (b) Aqueous

Figure 5.4 presents the Ti K-edge of the pure anatase (Solaronix and Aqueous) films as well as that of the sensitized substrates. The spectra of our unsensitized TiO₂ (Solaronix and Aqueous) show the typical near-edge feature (A₁, A₂ and A₃) as well as the middle edge feature (B) and the white line feature (C) of anatase [15,37-39]. Previous works have interpreted these pre-edge features to arise from mixing of the p orbital of absorbing Ti atom with the d orbital of the neighboring Ti atoms. Wu *et al.* suggested that the first and second features (A₁ and A₂) arise from dipolar transitions from the Ti 1s to the t_{2g} and e_g levels, while the third feature (A₃) represents a transition from the 1s → 4p states of the absorbing atoms [40]. Others [41-44] have suggested A₁ to arise from quad polar transition to the t_{2g} states of TiO₆; A₂, A₃ are largely to 1s → 3d dipolar transition to the t_{2g} and e_g orbital of neighboring octahedral. Zubavichus *et al.* based on previous works [45,46] attributed these pre-edge triplets to quadrupole (A₁) and dipole (A₂, A₃) 1s → 3d transitions due to distortions of the centrosymmetric O_h environment with participation of the valence p states of the titanium and oxygen atoms; while feature B and C were attributed to a 1s → 4p transition and promotion of a photo electron to higher vacant np states of Ti and Ti-O anti-bonding states in the coordination environment of Ti [45-49]. Furthermore, in this study [21] a weak but clear splitting of the A₂ feature was observed by looking at the derivative (dμ/dE) of XANES spectra, this was attributed to penta coordinated surface Ti atoms as it corresponded to their fitted EXAFS coordination numbers.

In our case, if we consider the Ti K-edge XANES spectrum (Figure 5.4), then we observe substantial damping of the white line and post edge features in the sensitized

sample in comparison to the pure TiO₂ substrates, as that observed by Zubavichus *et al.*[21] but we do not observe the enhancement of the pre-edge features in the sensitized samples (rather the opposite occurs). Similar observations with ours (damping of white line and post edge features) have also been observed by Chen *et al.*[38] for ascorbic acid onto TiO₂ nanocrystalline; these enhancement of pre-edge features were correlated to the higher distortions of the local Ti coordination in the sensitized samples.

The derivative of our Ti K-edge XANES data (Figure 5.5) shows no splitting of the A₂ feature as that in the work of Zubavichus *et al.*[21] for either of our anatase substrate.

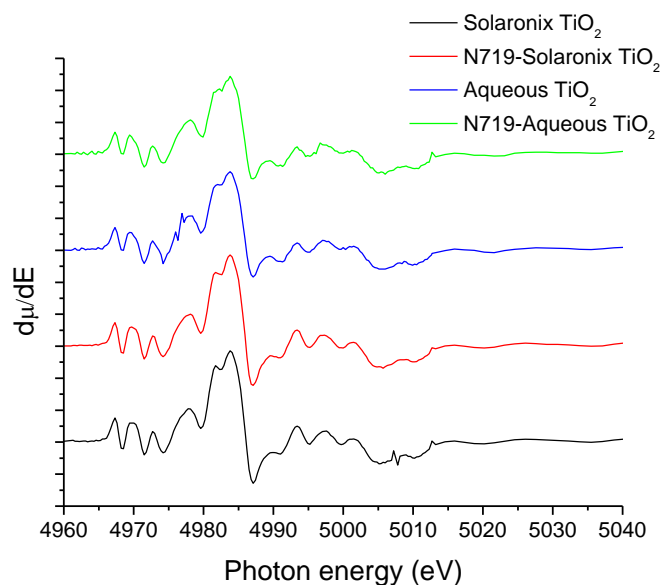


Figure 5.5 Derivatives of Ti K-edge XANES for TiO₂ and N719-TiO₂

With this in mind, we decided to further investigate the EXAFS region of our Ti K-edge data for our coated and uncoated TiO₂ substrates as shown in Figure 5.7. As it can be observed from the k space data (which was collected up to k~15), when one compares the sensitized versus the unsensitized EXAFS data for both anatase substrates, we can safely say that they are exactly identical (Figure 5.6).

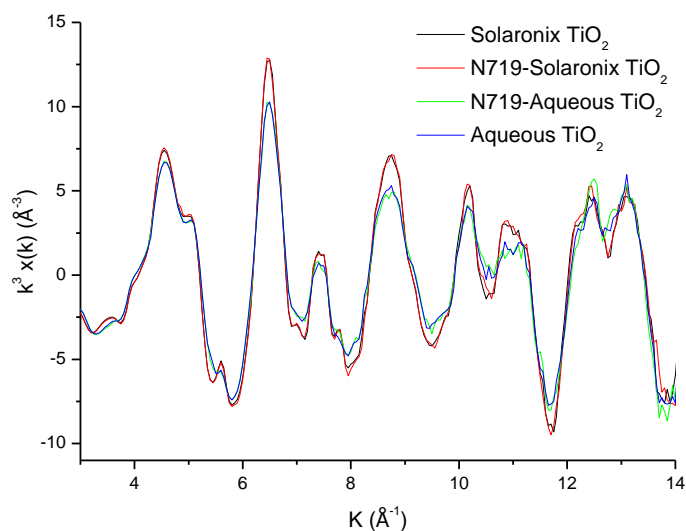


Figure 5.6 EXAFS spectra of TiO₂ and N719-TiO₂

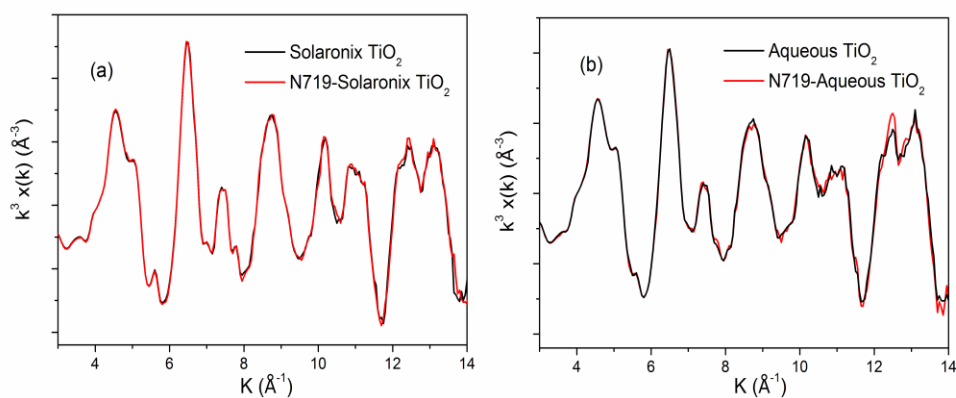


Figure 5.7 EXAFS spectra of TiO₂ and N719-TiO₂ (a) Solaronix and (b) Aqueous

Moreover, it is worth to point out that at the Ti K-edge, when coordination changes occur, these are clearly observed not only in the XANES region but also in the EXAFS region (in k space) as demonstrated very nicely in TiO₂ colloids where the Ti-O coordination changes [50]. All of this suggests that no coordination change has been detected to the surface TiO₂ groups upon dye adsorption to either anatase nanocrystalline substrates (using TEY) in our measurements as that reported in previous studies [20,21]. Previous investigators have reported the coordination of the Ti-O shell to change up to 2 units from the pure to adsorbed states. Now such a huge coordination change (~ 2 unit) if

indeed occurs should be clearly observed in the Ti K-edge EXAFS or in the XANES data, as many studies have demonstrated [15,47,50] or at least be observed at the Ti L-edge [11,13] which is more sensitive to crystal field (coordination) changes.

Finally, it is interesting to note that the spectral structures of the pure and adsorbed state of the Ti K and L-edge XANES data are similar. In spite of this, there are small differences between the anatase substrates that are observed as evident from the EXAFS features occurring at 5.8 \AA^{-1} and 7.8 \AA^{-1} (indicated by the arrows in Figure 5.7) and from the intensity of the t_{2g} and e_g states of the Ti L-edge XANES spectra. Therefore, the Ti K-edge showed little difference in the spectrum between the pure and adsorbed state (Figure 5.4) at Ti K-edge in the XANES or EXAFS region as in previous reports [20,21]. However, it should be pointed out that these coordination changes may not be observable at the Ti K-edge even with a more surface sensitive technique than FY as TEY. Since the probing depth is usually hundreds of nanometers at the K-edge and in our case (in addition to Zubavichus *et al.*[21] and certainly not Ju *et al.*[20]), we may not be sensitive enough to detect these changes in coordination state (and therefore crystal field changes) which only occur to the surface groups of the anatase nanoparticles [37].

5.4.1.3 O K-edge

The oxygen 1s XANES spectra of TiO₂ reflect the density of unoccupied electronic states of the 2p type. Because the O 2p orbitals are hybridized with the Ti 3d and 4sp orbitals, they also account for these metal states [27]. In Figure 5.8, we can distinguish two energy regions; one is the region from 530 to 535 eV and another is the region from 537 to 550 eV.

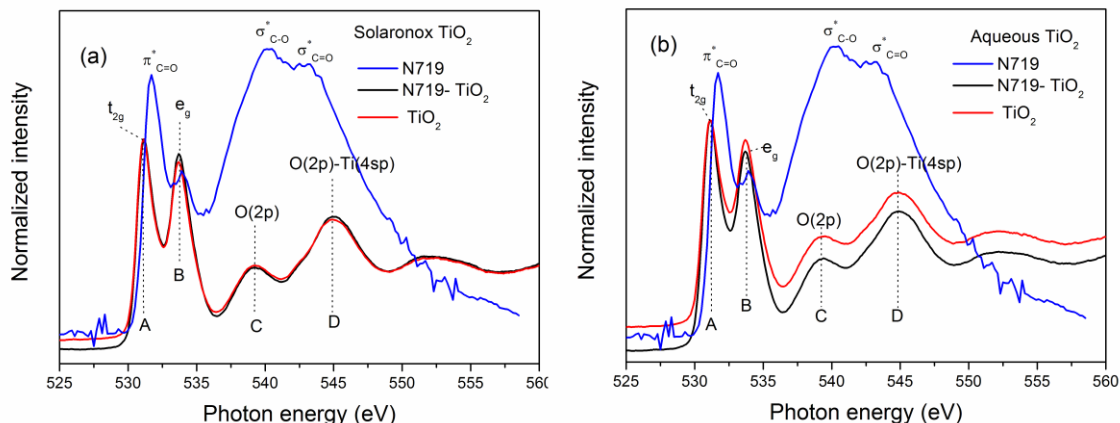


Figure 5.8 Oxygen K-edge XANES spectra of the TiO₂, neat N719 and N719-adsorbed TiO₂ films (a) Solaronox (b) Aqueous

The features in the range of 530-535 eV are associated with transitions to the O (2p)-Ti (3d) band. As the crystal field splits the 3d levels into t_{2g} and e_g orbitals this gives rise to two contributions labeled A and B, respectively. The higher energy region in the 537 to 555 eV includes transitions to the O 2p antibonding state (peak C) and O (2p)-Ti (4sp) band (peak D) [29]. For the TiO₂ it can be observed from the O K-edge that the samples are indeed composed of only anatase as only two higher energy features are observed [30], in agreement with our XRD and Raman data [25]. In the case of the N719 pure dye, the O K-edge has never been reported and as such the features can be described only in terms of the functional groups that contain oxygen atoms, namely the carboxylic acid and carboxylate groups. In general, the O K-edge XANES of carboxylic acid has three components, all due to the carboxylic acid groups. These are attributed to the $\pi^*_{C=O}$ at 531.7eV, the σ^*_{C-O} resonance at 540.3 eV and the $\sigma^*_{C=O}$ resonance at 542.9 eV. The latter two features are generally not well resolved in carboxylic acids such as formic acid [42], but in the case of N719 as can be observed in Figure 5.8 these are indeed well resolved, this is likely due to the high resolution power at the SGM. The feature at 533.9 eV is well pronounced and resolved but does not generally appear in the XANES spectra of carboxylic acid, so we can only qualitatively attribute this to a $\pi^*_{COO^-}$ type of feature from the carboxyl groups that form part of the N719 molecule. In the case of dye-adsorbed TiO₂ samples, the O K-edge is almost identical with the pure TiO₂; moreover the N719 character of the COOH and COO⁻ groups has completely disappeared. Thus, it

may be inferred that the O K-edge is insensitive to show any structural change before and after dye adsorption. As result of this, further investigation on the oxygen edge via XPS was conducted and will be discussed in the later sections.

Since the O K-edge was found to be dominated by TiO₂ contributions, we decided to investigate the changes occurring to the dye molecules after adsorption by looking at carbon and nitrogen K-edge XAS spectra.

5.4.1.4 C K-edge

As can be seen in Figure 5.9, the carbon K-edge XANES spectra for the neat dye and dye-coated TiO₂ (Solaronix and Aqueous) are completely different in structures. Although some uncertainty may be introduced by the normalization [51], it cannot account for these significant spectral changes.

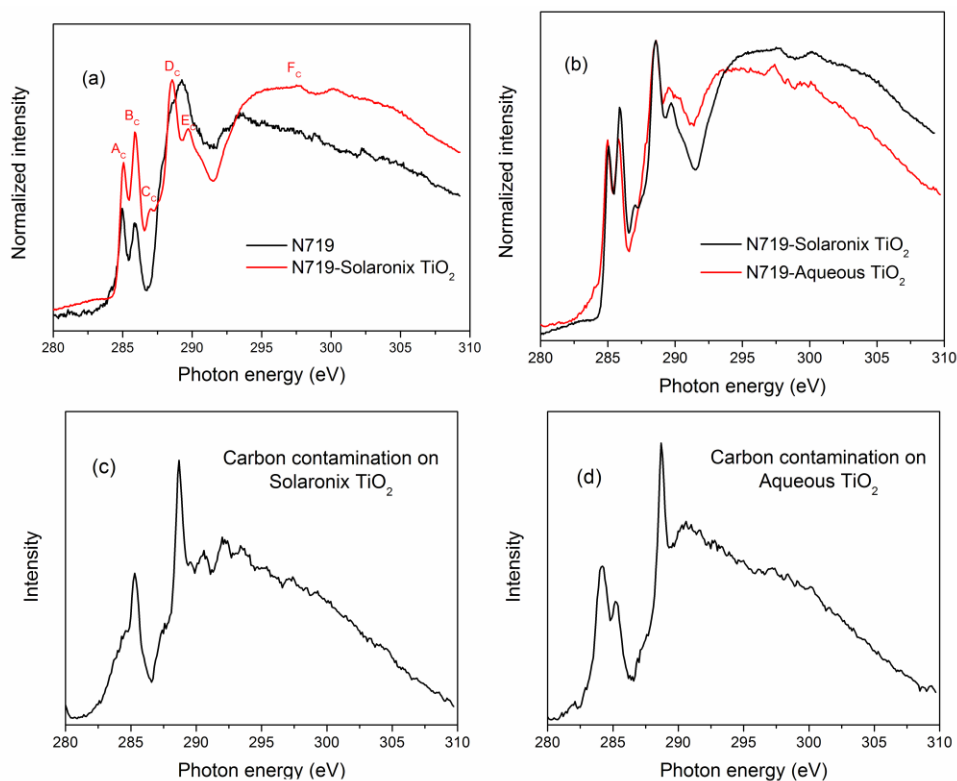


Figure 5.9 Carbon K-edge XANES spectra of (a) neat N719 and N719-Solaronix TiO₂ (b) comparison of N719-adsorbed Solaronix and Aqueous; and naked TiO₂ film (c) Solaronix (d) Aqueous

The C K-edge spectra from the neat TiO₂ films are shown in Figure 5.9 (c) and (d). As expected a small amount of organic contamination are present in the bare films (as evident from the C K-edge XANES and later quantified in the C 1s in the XPS section (~ 6 %)). However, when the TiO₂ films are dipped into the dye solution during cell fabrication, most of the organic contaminant molecules should be displaced by the dye molecules (otherwise no adsorption of dye would occur) and therefore contributions from organic contaminant to the C K-edge XANES spectra of the sensitized TiO₂ films is not expected to significantly contribute to the C K-edge XANES spectra of the sensitized samples. The C K-edge XANES in Solaronix and Aqueous TiO₂ shows the organic contamination from the air.

As can be seen, the C K-edge XANES spectra for the pure TiO₂ (Solaronix and Aqueous) shows the carbon contamination on our neat TiO₂ films (Figure 5.9 (c) (d)). Interestingly, the C K-edge spectra are different for Solaronix and Aqueous TiO₂ implying that each sample may contain different types of carbon contamination. The peak around 285 eV may indicate to π - π^* transition of C=C in aromatic ring and/or amorphous carbon. The sharp peak at 288 eV corresponds to σ^* -resonances of the C=O in CO₂. Interestingly, it is worthy to note that these features from the organic contaminants are in slightly different energy region in comparison to the C K-edge spectrum of dye coated TiO₂. All C K-edge data presented in this paper were energy calibrated using CO. For clear comparison, we overlaid the C K-edge spectra of the pure TiO₂ and dye coated TiO₂ sample (Figure 5.10).

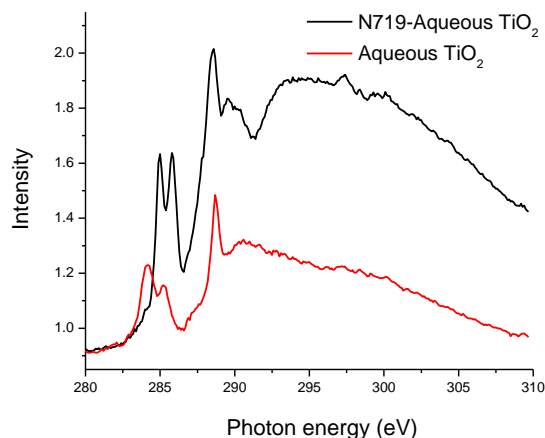


Figure 5.10 C K-edge XANES of the bare aqueous TiO₂ (organic contaminant) and the dyed adsorbed TiO₂

As can be seen, the carbon contamination from the neat TiO₂ does not appear to give a significant contribution to the C K-edge XANES spectrum in the dye coated TiO₂ surface.

In this work, the C K-edge assignment of dye and dye-coated TiO₂ is based on previous XANES studies for bi-isonicotinic acid which is the binding ligand of N719 [51,52]. For the neat N719 dye, the strong narrow peak at ~285 eV arises from transitions to the ring π^* state, the peak at 288 eV is from C 1s $\rightarrow \pi^*$ resonance of C=O the group and the broad peak above 295 eV corresponds to C 1s $\rightarrow \sigma^*$ transitions. Generally, peaks A_C and B_C can be assigned to signals arising from the inequivalent C atoms in the pyridyl rings and/or the carboxyl side groups. However, these two peak transitions are assumed to occur solely from ring C 1s $\rightarrow \pi^*$ resonances as determined by computation conducted by Thomas *et al.*[52]. A small peak at 287 eV (C_C) observed in the adsorbed sample is a new feature, which is not observed in the neat N719 and may be assigned to C 1s $\rightarrow \pi^*$ transition in the range of pyridine rings, indicating that there are additional electronic states between dye molecules and TiO₂ surface in comparison to the neat dye. The clear feature at 288.5 eV (peak D_C) arises from C 1s $\rightarrow \pi^*$ resonance in pyridine and the peak at 289.7 eV, peak E_C is believed to be a C 1s $\rightarrow \pi^*$ transition arising from the carbon in

COOH/COO⁻ groups. We also observe the typical broad peaks from C 1s to σ^* transitions above 295 eV (E_C) which are analogous to the peaks seen in pyridine [51-53].

In addition to the π^* changes, there are other differences in the σ^* region in the spectra, that again indicate slight modification of the electronic structure around the pyridine structures once the dye molecules are adsorbed onto TiO₂. From these spectral changes to the XANES spectrum, it seems reasonable to propose that the aromatic electronic density from pyridine should interact with TiO₂ electron density once the N719 molecule is adsorbed, a feature that has not been considered by any previous electronic studies on this system [54]. Interestingly, according to the study by Kaneko *et al.*, on ruthenium complexes without binding groups (COOH or COO⁻) such as tris(2,2'-bipyridine) ruthenium dichloride (Ru(bpy)₃) and tris(bipyrimidine) ruthenium(II), there were found to also generate photocurrent; which indicates that electrostatic interactions of adsorption onto the TiO₂ also contribute to producing current. These electronic interactions may be generated between π - π orbital interaction in pyridines and the d states found in TiO₂ [55]. Thus, we can assume that in the N719-TiO₂ system, electronic interactions occur not only through the covalent bonding of the anchoring groups but also through the aromatic electron density of the bipyridine groups.

Furthermore, it is interesting to compare the electronic interactions that occur between the N719 molecule and two anatase substrates, namely Solaronix and our aqueous product. From Figure 5.9(b), it can be observed that when the dye is adsorbed onto Solaronix and Aqueous TiO₂, the C K-edge spectra show no real substantial spectral differences. Both of the dyed samples show exhibit sp^2 and sp^3 character with similar peak features but with some shift, in energies to the E_C and the broad σ^* features.

To gain more information on the adsorption geometry of N719 molecules on the Solaronix TiO₂ surface, XANES spectroscopy at normal and grazing incidence (30°) was carried out (Figure 5.11).

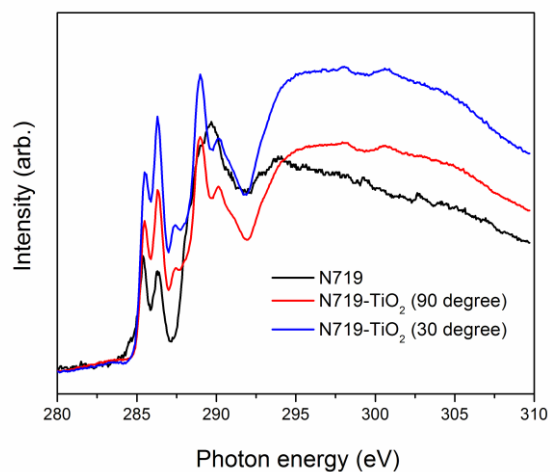


Figure 5.11 C K-edge spectra recorded at normal (90°) and grazing photon incidence angle (30°) for neat N719 and N719-Solaronix samples

It can be observed that when the polarization of the synchrotron beam is perpendicular to the sample (90 degrees) and at grazing incidence (30 degrees), there is no significant change in intensity for any particular π^* and σ^* feature for the adsorbed sample as it is often observed for other organic adsorbed molecules [56]. Rather we observe that at grazing incidence all the π^* and σ^* features increase in intensity versus those of 90 degrees. This phenomenon was rather unexpected but it may be attributed to the fact that since many carbon atoms exist in the dye molecule, each carbon in the dye molecule is oriented in different angle, thus, changes in the σ^* and π^* features due to orientation effects are not detected.

5.4.1.5 N K-edge

Figure 5.12(a) shows the N K-edge XANES spectra of the neat N719 and the adsorbed samples, while Figure 5.12(b) displays the nitrogen K-edge XANES spectra for N719 and dye-coated TiO₂ (Solaronix and Aqueous) with the surface normal and at grazing incidence. The N K-edge XANES spectra of N719 [57] and similar molecules [58] have been previously reported and our spectral assignments have been based on these works. However, the N K-edge XANES of the adsorbed state are for the first time evaluated here for two distinct nanocrystalline anatase substrates (Figure 5.12).

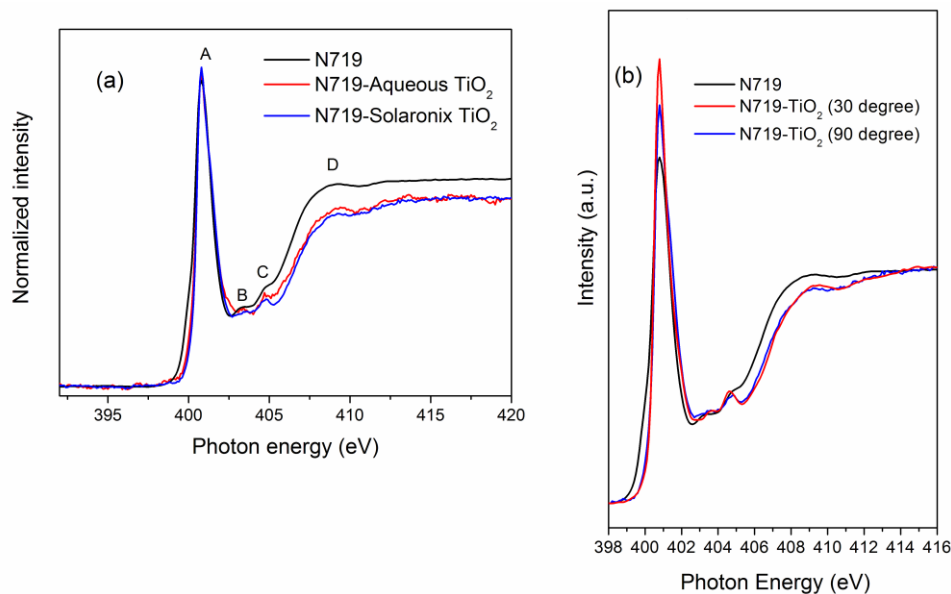


Figure 5.12 Nitrogen K-edge XANES spectra of (a) the neat N719 and N719-adsorbed TiO₂ films (Solaronix and Aqueous) at normal incidence and (b) the neat N719 and N719-TiO₂ (Solaronix) at normal (90°) incidence and 30 degree

In the case of the neat dye, four main features are observed: the N 1s \rightarrow π^* resonance peak (A) at photon energy of 400.8 eV, weak shoulders N 1s \rightarrow π^* peak at 403.4 eV and 404.85 eV (C and D, respectively) and broad σ^* resonances at 409.3(D). It has been reported in previous studies [59] that the N K-edge of materials and films which show transitions centered at 402 and 404 eV can be attributed to sp^2 and sp^3 types of environment. In the case of the N719 neat, it can be observed that the N K-edge spectrum of the N719 is largely dominated by the single transition at 402 eV attributed to a sp^2 conjugated π bond type of environment. The dye-adsorbed TiO₂ spectra for both TiO₂ (Solaronix and Aqueous) show exactly the same N environment with the dye molecule, indicating that the bipyridine groups retain their sp^2 conjugated π bond character after adsorption onto both distinct TiO₂ surfaces. This is unlike the carbon environment observed via the C K-edge in which we observed the Solaronix and Aqueous TiO₂ give rise to different sp hybridizations [60]. Looking at the orientation measurements in Figure 5.12(b), it is observed that when the dye-coated TiO₂ is measured with grazing incidence (incident light angle of 30° from the surface), the intensity for the N 1s \rightarrow π^* resonance peak is increased. This may indicate that the sp^2 conjugated π bond in the bipyridine

groups are more aligned with the TiO₂ substrate at grazing incidence than normal to the surface. If this is indeed the case then the geometry would favor the electronic aromatic interaction between the TiO₂ surface and the N719 molecule as stated in the C K-edge section and in accordance with the work by Kaneko *et al.* which showed that photocurrent could be generated via π - π orbital interaction of pyridines and TiO₂ [55]. The broad σ^* resonances at 409 eV also have some slight differences but nothing substantial. XPS analysis via N 1s edge later presented further supports this analysis.

5.4.2 XPS

An XPS spectrum displays the number of collected electrons as a function of binding energy. The electron binding energies are element-specific and also specific for each particular level inside an atom and as such they can be used to distinguish between different chemically inequivalent states of the same atom. Although core electrons do not participate in chemical bonds, any change in the electron charge distribution of the valence levels in either the ground or excited state will affect the core level binding energies giving rise to the so-called chemical shifts in the photoemission spectra [61]. Furthermore, XPS is a very surface sensitive technique. This is due to the short mean free path of the electrons in the material. The radiation penetrates several hundreds of Ångström into the material, but the electron elastic escape depth is very small [62]. Another characteristic for XPS, is that Ti 2p shows no further splitting (as in the XAS spectra) since we do not probe the empty density of states which are the ones that sensitive to coordination states via the crystal field. Therefore, the XPS spectrum is simpler than XAS spectrum and only atomic like states are observed [9]. For these reasons, XPS analysis of Ti 2p edge and O 1s edge are used to provide complementary data to our synchrotron XAS analysis to monitor the electronic changes and interactions of our two TiO₂ substrates before and after dye adsorption; something that our TEY XANES analysis could not clearly capture as a result of surface sensitivity.

5.4.2.1 Ti 2p

Figure 5.13 shows the Ti 2p XPS high resolution spectra for the pure TiO₂ films and dye-coated TiO₂. For the uncoated TiO₂ films, the usual splitting due to spin-orbit coupling is observed; the peak at 459.4 eV for Solaronix TiO₂ (459.5 eV for Aqueous TiO₂) is attributed to the Ti⁴⁺2p_{3/2} state while the peak at 465.1 eV for Solaronix TiO₂ (465.2 eV for Aqueous TiO₂) corresponds to Ti⁴⁺ 2p_{1/2}.

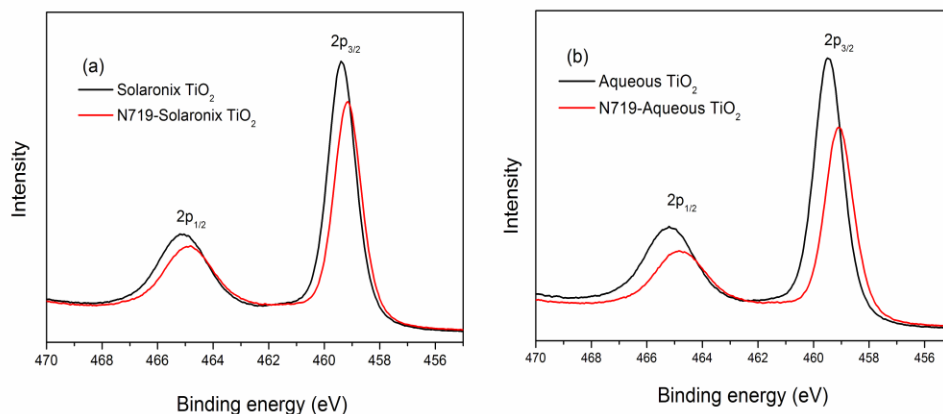


Figure 5.13 Ti 2p XPS spectra of TiO₂ and dye-adsorbed TiO₂; (a) Solaronix (b) Aqueous TiO₂

The Ti 2p peaks of the TiO₂ films show that the surface oxide consists mainly of titanium (IV) dioxide, indicating that suboxides such as TiO, Ti₂O₃ and Ti₃O₅ are not present on the oxide surface [63-65]. For the dye-coated TiO₂, the Ti 2p spectrum is slightly shifted to lower binding energy compared to the uncoated TiO₂; moreover, there is a decrease in intensity with the coverage of the dye for both samples. The intensity decrease is likely attributed to the absorbed dye layer that scatters the emitted electrons. The shift to lower energy upon dye adsorption can be due to a change of the dipole of the surface or a change in the Fermi level position in the band gap, which shifts all the core states of TiO₂ to lower energy in our case.

Interestingly, the dye-adsorbed Aqueous TiO₂ is shifted -0.4 eV for Ti 2p_{3/2} and -0.35 eV for Ti 2p_{1/2} while dye-coated Solaronix TiO₂ is shifted -0.25 eV for Ti 2p_{3/2} and -0.2 eV for Ti 2p_{1/2} in comparison to the peaks in the pure TiO₂ substrates. These types of shifts to the Ti 2p XPS spectra (and changes to the work function) have also been observed for other studies [66,68-71] where the TiO₂ interactions were also monitored in

addition to the adsorbate molecule interaction. Thus, we may infer that the change in the surface dipole and/or shift to the Fermi level between our Aqueous TiO₂ substrate and the N719 molecule are qualitatively greater than those found in the dye-Solaronix TiO₂ system. This larger shift for the aqueous substrate (vs. Solaronix) may be attributed to the greater occurrence of excess surface groups (OH/H₂O) which may further contribute to the change in the surface dipole (and/or E_f) that occurs to the TiO₂ upon the adsorption of the N719 molecule. Certainly several studies have indeed shown that adsorption of water to the TiO₂ surface induces the formation of a dipole layer which locally changes the work function [69,71], which in our case we were able to qualitatively observe via the XPS measurements.

5.4.2.2 O 1s

Figure 5.14 shows the O 1s XPS spectra for the TiO₂ film and dye-coated TiO₂. Similarly to the Ti 2p spectra, these results show that the dye-coated O 1s entire spectrum is shifted to lower energy in comparison to the pure TiO₂ film accompanied by a decrease in intensity. These results indicate that there is contribution to the O 1s spectra from the dye molecules and that a change in surface dipole or shift of the E_f (Fermi level energy) occurs in both TiO₂ substrates once the N719 is adsorbed. The dye-adsorbed Aqueous TiO₂ is shifted by -0.4 eV, while that of the dye-adsorbed Solaronix TiO₂ shifted by -0.3 eV. This difference is in agreement with our Ti 2p XPS findings where a greater change was observed in the aqueous sample than those in the Solaronix sample.

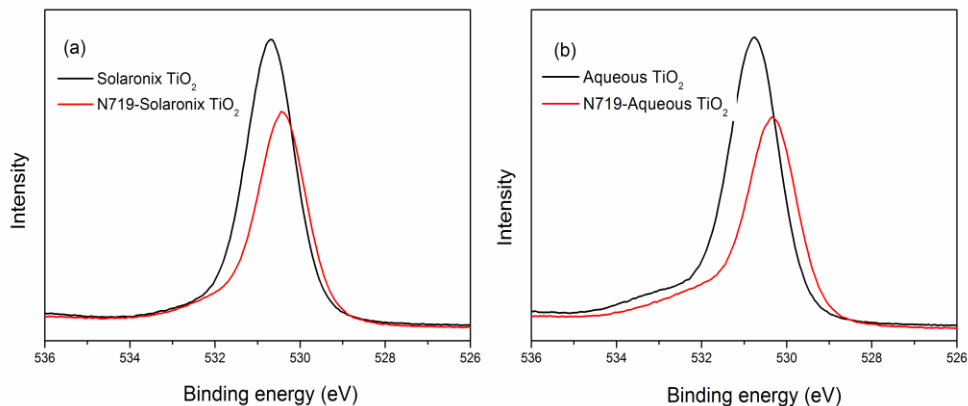


Figure 5.14 O 1s XPS spectra of TiO₂ and dye-adsorbed TiO₂; (a) Solaronix (b) Aqueous TiO₂

As it can be further observed, the O 1s XPS spectra for the dye-coated TiO₂ show an asymmetrical broadening toward the higher binding energy side of the major peak, which indicates the presence of other molecular species on the surface, namely Ti-OH/OH₂ and adsorbed organic components as observed in the C 1s XPS. The role of these molecular surface species on TiO₂ upon the binding mechanism between the N719 and TiO₂ interface has been the topic of our previous work and others [6, 72]. The spectra shown in Figure 5.14 include O 1s contributions from both the dye and the TiO₂ substrate surface groups as well as small amounts of organic contamination, with the dominant feature arising from the substrate signal. The tailing of the emission line toward higher binding energies contains also the signals due to carboxylic and carboxylic oxygens of the dye. Johansson *et al.* reported that the tailing peak could be attributed to three molecular contributions, namely the -COO⁻TBA⁺, O=C and COO-Ti groups [23].

This asymmetrical feature can be better analyzed with the Peak fitting data presented in Figure 5.15. It has been known that Ti-OH/Ti-OH₂ groups exist on the TiO₂ surface due to dissociative adsorption of water [6,73]. In several publications, Gaussian model peaks for the TiO₂ were fitted to the spectra in order to identify the asymmetrical broadening toward the higher binding energy. Furthermore, it has been proposed that the presence and concentration of surface hydroxyls on oxidized metal surfaces can be determined directly via X-ray photoelectron spectroscopy.

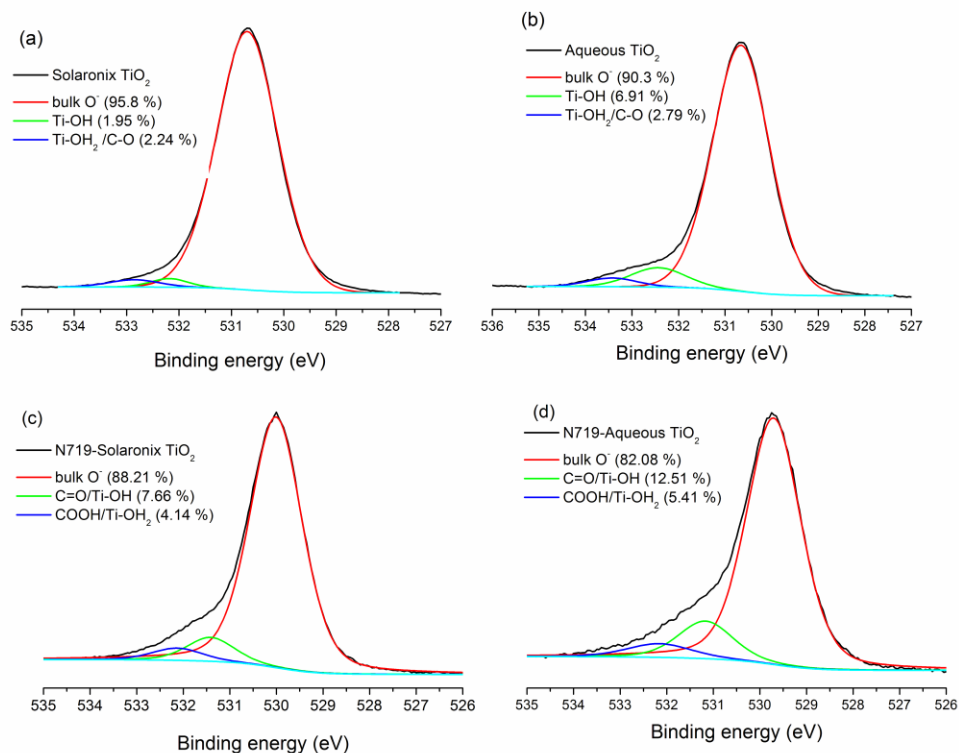


Figure 5.15 Peak fitting of the O 1s XPS spectra for pure (a) Solaronix and (b) Aqueous TiO₂; and dye-coated (c) Solaronix and (d) Aqueous N719-TiO₂ systems

Simmons and Beard [74] reported via curve fitting that their O 1s XPS spectrum of TiO₂ shows at least three resolved peaks at 529.9, 531.5, and 532.8 eV. In their study, the most intense peak at 529.9 eV was attributed to the oxygen in the TiO₂ bulk, the lower intensity peak at 531.5 eV was believed to be the oxygen in surface hydroxyl groups, and the relatively small peak at 532.8 eV could be attributed to adsorbed molecular water and/or to the oxygen present due to organic contamination. On the other hand, Erdem *et al.*[75] only observed two peaks at 530.64 and 531.86 eV in TiO₂ and these were assigned to bulk oxide (O²⁻) and hydroxyl (OH) species, respectively. In our studies, we were able to de-convolute the O 1s spectrum into three components as in the work of Simmons and Beardt [74]. Therefore for our bare TiO₂ substrates, the bulk oxygen was observed at 530.7 eV for Solaronix TiO₂ (530.65 eV for Aqueous TiO₂), the surface Ti-OH groups at 532.2 eV for Solaronix TiO₂ (532.5 eV for Aqueous TiO₂), adsorbed water and/or organic contaminants at 532.9 eV for Solaronix TiO₂ (533.45 eV for Aqueous TiO₂) [76,77]. As each peak area is proportional to the quantity of each component, we

can estimate the quantity of surface groups (OH/H₂O) on the commercial and synthesized TiO₂ surface (Figure 5.15). Our synthesized Aqueous TiO₂ showed a more asymmetric feature, which was attributed to having more surface hydroxyl (6.91 %) and water/organic (2.79 %) contents than those found in the commercial TiO₂ (Ti-OH 1.95 % and Ti-OH₂/organic 2.24 %). These occurrences of the differences of the surface hydroxyl/water groups on our aqueous synthesized TiO₂ compared to commercial TiO₂ similar to the Solaronix product were qualitatively observed via vibrational spectroscopy in our previous work [6].

For the dye-adsorbed TiO₂, our deconvolution analysis showed that the asymmetric broadening is increased qualitatively after dye adsorption for the pure TiO₂ substrate. This is due to the contribution of COOH groups present in the dye molecules and likely a small contribution due to some remaining organic contaminant. Considering the surface groups on TiO₂, the O 1s XPS features for the dye-coated TiO₂ can be assigned as followed: the peak at 530 eV for N719-Solaronix TiO₂ (529.7 eV for N719-Aqueous TiO₂) is attributed to O⁻ from TiO₂ surface and the peak at 531.45 eV for N719-Solaronix TiO₂ (531.2 eV for N719-Aqueous TiO₂) is attributed to C=O from the dye and OH from the TiO₂ surface. Finally, the peak at 532.15 eV for N719-Solaronix TiO₂ (532.2 eV for N719-Aqueous TiO₂) can be attributed to several contributions, from the OH groups of the dye's COOH groups, H₂O from the TiO₂ surface and/or from the small amount of organic contamination. At this point, it is worth to note that although small amounts of organic contamination to the bare TiO₂ is natural under ambient conditions (which are the fabrication and working conditions of DSSC's) when these are placed into the dye solution most of the organic contaminant found in the bare TiO₂ are expected to be largely displaced by the adsorption of the dye molecules. Therefore in the sensitized samples, contributions from these organic contaminants to the XPS spectra (O 1s and C 1s) are not assumed to be significant as in other XPS studies on this or similar systems [58].

5.4.2.3 N 1s

The N 1s spectra of the N719 and dye-coated TiO₂ are shown in Figure 5.16. The spectrum of N719 is composed of three peaks; the peak at lowest binding energy (398.13

eV) corresponds to the nitrogen in the NCS groups, the middle peak at 399.95 eV is attributed to the nitrogen in the bipyridine ligands, and the peak at the highest binding energy (402.23 eV) corresponds to the nitrogen in TBA⁺ (tetra butyl ammonium) cations.

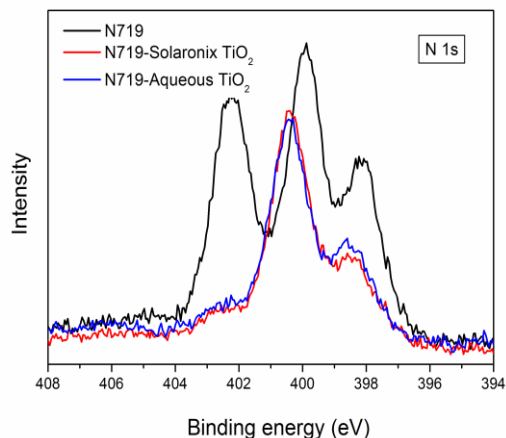


Figure 5.16 N 1s XPS spectra of N719 and N719-adsorbed TiO₂; (a) Solaronix and (b) Aqueous TiO₂

The assignment of these peaks and their contribution in the N 1s XPS spectra are based on the work of Johansson *et al.*[23] and Rensmo *et al.*[22] In their work, a series of selectively substituted Ru-complexes were evaluated to separate all group (NCS, TBA⁺, bipy) contributions to the N1s XPS spectra. In our N1s spectra, the intensity of TBA⁺ is distinctively reduced after dye adsorption, but as can be observed from our deconvolution analysis (Figure 5.17) not all the TBA⁺ is completely consumed. This implies that not all of the TBA⁺ counter ions are exchanged upon adsorption of the dye molecule on the TiO₂ surface, an observation that is consistent with previous results obtained for the N719-TiO₂ system using vibrational spectroscopy [6,23].

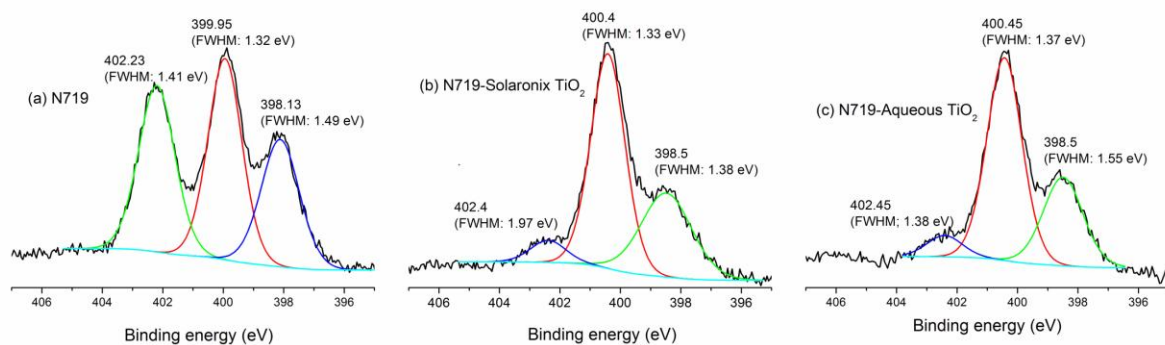


Figure 5.17 Peak fitting of N 1s XPS spectra for (a) N719 and dye-adsorbed TiO₂; (b) Solaronix and (c) Aqueous TiO₂

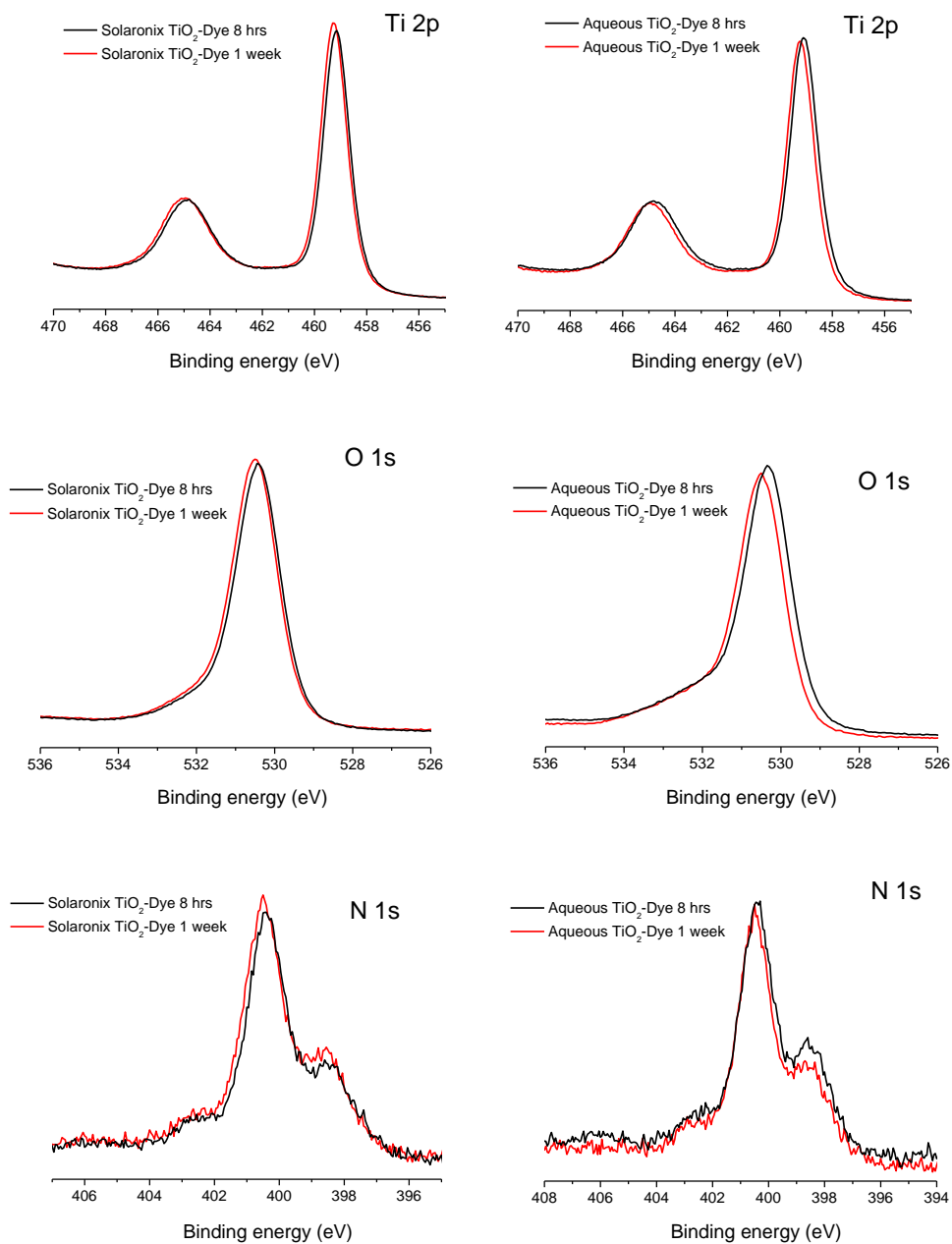
More strikingly, the NCS peak of dye-coated TiO₂ shows a shift (0.25 eV) toward higher energy and an increase in FWHM compared to neat N719, indicating that there is some kind of interaction (H-bonding) for the NCS ligand with the TiO₂ surface, something that we have postulated in our previous work involving vibrational spectroscopy [6]. Similar effects (increase of FWHM and shifts to higher binding energy) have been reported by O'shea *et al.*[78,79] for H-bonding systems. Furthermore, the bipyridine peak is also found to be shifted by 0.45 eV for dye-Solaronix TiO₂ and 0.5 eV for dye-Aqueous TiO₂ to a higher energy relative to the neat N719, which further supports our C and N K-edge XANES results that the aromatic π electron density in the pyridine rings should interact with the TiO₂ surfaces. This interaction between the bipyridine groups and the TiO₂ surface is something, which has not been previously reported and which may be important in the electron transfer from the dye to TiO₂ in addition to the ones occurring via the covalent bonds.

The intensities of the N 1s peaks relative to each other are shown in Table 5.1 for the dye and dye-coated TiO₂ films sensitized at different absorption times (8 hrs and 1 week). These experiments were conducted to determine if there are significant spectral changes for samples with different adsorption time due to production of multi layers as reported in the XPS work of Mayor *et al.*[24]. It is noted first that the intensity ratio (intensity ratio = intensity of NCS or TBA⁺ peaks compared to the intensity of the bipyridine peak) of NCS and TBA⁺ for 1 week sample is almost the same as the 8 hrs sample.

Table 5.1 N 1s Intensity Ratios

Sample	N 1s peaks		
	TBA ⁺	Bipyridine	NCS
N719	0.88	1	0.71
N719- Solaronix TiO ₂ (8 hrs)	0.11	1	0.57
N719- Solaronix TiO ₂ (1 week)	0.10	1	0.53
N719-Aqueous TiO ₂ (8 hrs)	0.11	1	0.49
N719-Aqueous TiO ₂ (1 week)	0.13	1	0.48

This can be explained by Langmuir adsorption/desorption equilibrium for dye molecules deposited on TiO₂ surface [80], thus the 1week dye coated sample does not suggest multilayer dye adsorption on TiO₂ as found in the spectra of dye-coated TiO₂ using an electrospray method in previous studies [24]. Interestingly, our results in Figure 5.18 show that the spectra between 8 hrs and 1 week do not present any significant spectral difference or increase of intensity.



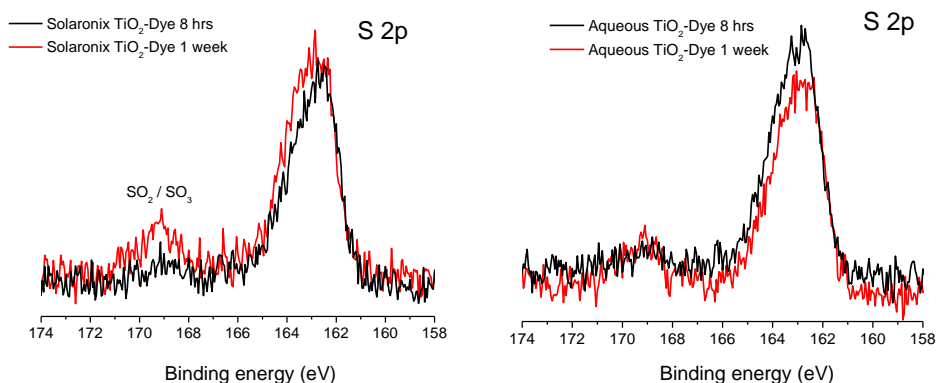


Figure 5.18 XPS spectra for comparison of 8hrs and 1week sample for N719-TiO₂

This indicates that at least in our case there is equilibrium for the dye loading onto the TiO₂ surfaces; thus, the spectrum is expected to be similar even if the deposition time is longer. Interestingly, we can observe oxidized sulfur (SO₂ or SO₃) in the S 1s XPS for the 1 week sample, implying that the NCS ligands are oxidized due to longer time duration. Several publications have mentioned that there is spectral difference between monolayer and multilayer coverage of the dye on TiO₂ surface (i.e. the multilayer spectrum shows totally different features with the monolayer spectrum) [24]. However, in their case, the dye molecule was deposited by *in situ* UHV electrospray deposition under an applied pressure, while in our case the dye coated TiO₂ film were made by dip coating method, which is used most commonly in this system.

5.4.2.4 S 2p

The S 2p spectra of neat N719 and dye-coated TiO₂ for both Solaronix and Aqueous anatase films are shown in Figure 5.19.

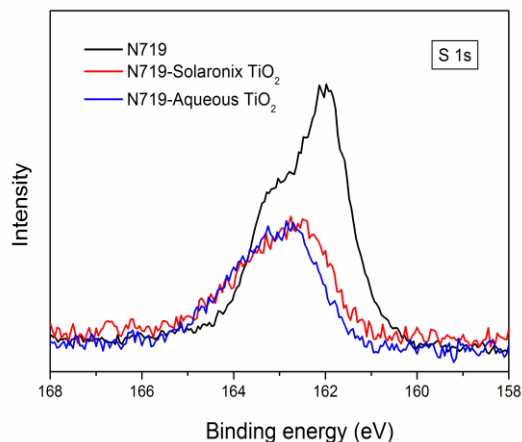


Figure 5.19 S 2p XPS spectra of N719 and N719-adsorbed TiO₂; (a) Solaronix and (b) Aqueous TiO₂

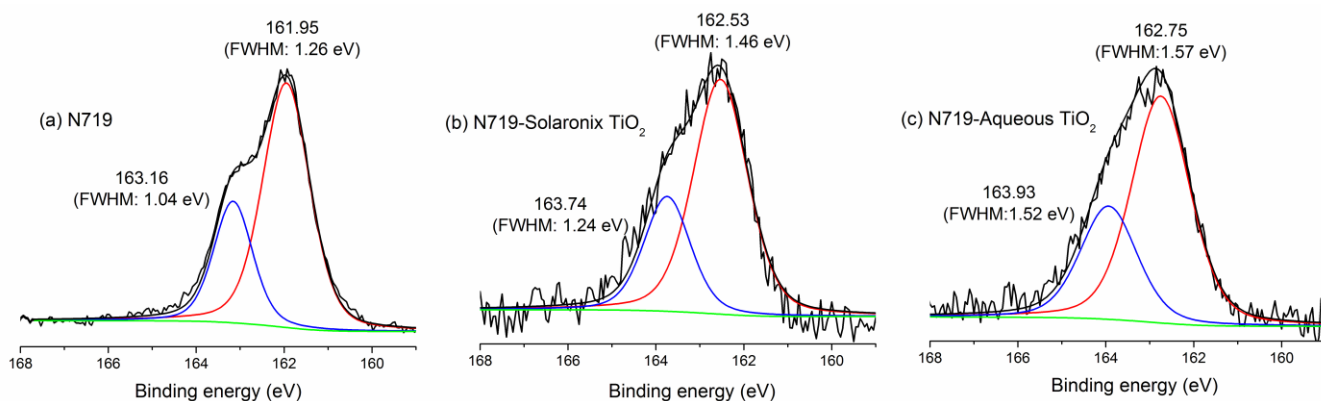


Figure 5.20 Peak fitting of S 1s XPS spectra for (a) N719 and dye-adsorbed TiO₂; (b) Solaronix and (c) Aqueous TiO₂

The S 2p spectra of the neat dye were de-convoluted (Figure 5.20) with the spin-orbit split doublet originating from the sulfur in the NCS ligands, which means that the chemical states of the NCS groups within neat dye are very similar [23]. The de-convoluted peaks for both samples are shifted by 0.58 eV and 0.8 eV toward higher binding energies for the Solaronix and Aqueous adsorbed samples, relative to the neat N719. The intensity relation between S2p_{3/2} and S2p_{1/2} is close to 1:2 and the energy difference between them is about 1.2 eV. It is noted at this point that in our S 2p spectra there is an additional component that could not be confidently added as in the work of Johansson *et al.*[23]. This is because in our case, the probing energy was fixed (lab

source) and therefore, the lower photon energies needed to observe this extra contribution could not be confidently attained to fit into our deconvolution analysis. This additional contribution to the S 2p spectra of the adsorbed state in Johansson *et al.*'s work [23] was attributed to surface interactions of the NCS groups with the TiO₂ surface, further supporting our findings for our two anatase substrates. Therefore, it may be concluded that a fraction of the molecules adsorbed onto TiO₂ interact (likely through H-bonding) with the substrate through at least one of the NCS groups, in agreement with our N 1s XPS results above and those from our previous vibrational work.⁶ and that of Johansson *et al.*'s work [23].

5.4.2.5 C1s/Ru 3d

Figure 5.21 shows the C 1s spectrum of the pure TiO₂ substrates. As can be observed from the XPS analysis, there exist organic contaminants (air) in the surface of our bare TiO₂ films in both cases.

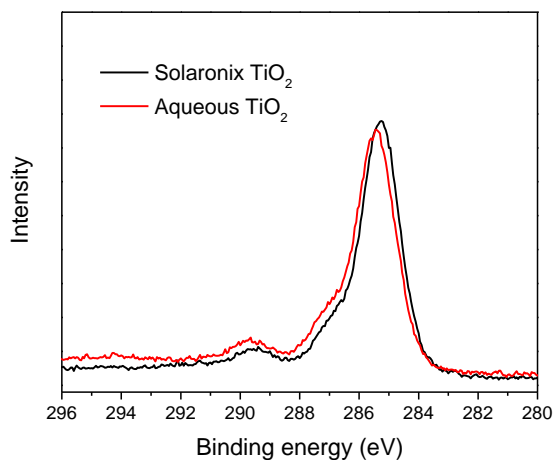


Figure 5.21 C 1s XPS of the bare TiO₂ (organic contaminant) for Solaronix and Aqueous TiO₂

The quantity was calculated from XPS analysis. Each uncoated TiO₂ substrate was found to contain ~6 % C, which is similar value with the previous work of Johansson *et al.*'s where ~5% C was reported [58]. The major peaks around 286 eV and 289 eV in the pure TiO₂ substrates indicate the presence of C-O and C=O species respectively. Figure

5.22 shows the C 1s/Ru 3d spectrum of the N719 and the adsorbed samples which are dominated by four peaks. The two main peaks at the lower binding energy originate from C 1s and Ru 3d_{5/2}. However, it should be noted that the peak for the Ru 3d_{3/2} is hidden under the major C1s peak (~285 eV) [68] and this Ru 3d_{3/2} is shifted 4.3 eV from the Ru 3d_{5/2} [22]. The XPS studies of pyridine [81] and pyridine-carboxylic acid monomers (isonicotinic acid, nicotinic acid, and picolinic acid) on rutile TiO₂ [82] show that the peak position of the C 1s pyridine ring peaks at around 284 eV and the carboxylic C 1s occurs around 289 eV [83].

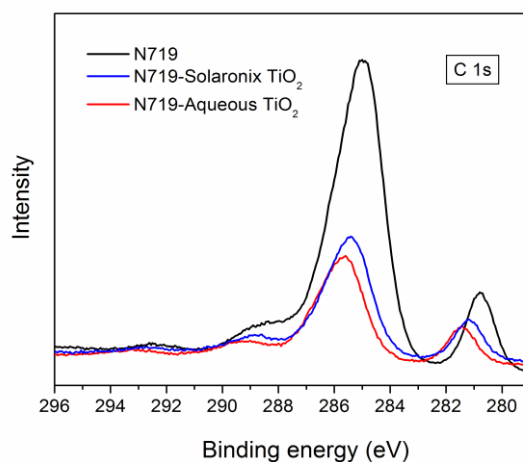


Figure 5.22 C 1s XPS spectra of N719 and N719-adsorbed TiO₂; (a) Solaronix and (b) Aqueous TiO₂

For our C 1s XPS spectra, the spectral features are similar with the pyridine-carboxylic acid monomers. However, in our case, the main peak at ~285 eV in N719 and N719-TiO₂ spectra (for both TiO₂ samples) contain not only pyridine contributions but also NCS and TBA⁺ ions group contributions. Thus, the broad peak around 285 eV is contributed by C=C, C-C, C=N, C-O and Ru_{3/2}. Furthermore, as some TBA⁺ ions still remain on the dye coated TiO₂ after dye adsorption [6] they also contribute to the C 1s spectral features. Therefore, the deconvolution process for the C 1s XPS was not performed due to the fact that large contributions from many groups under in one broad peak bring uncertainty to the C 1s curve fitting. The peak at 288 eV are also attributed to O-C=O and C=O from COOH/COO⁻ groups [82]. While the peak at around 292 eV is derived from CO₂ adsorption [84].

It is worthy to note that in spite of the complexity of all the components which make up the C 1s spectrum, there is noticeable shift to the higher energy from the neat N719 to the adsorbed N719-TiO₂ (for both samples). This shift is also observed for the Ru 3d_{5/2}, and the peak due to COO-/COOH located at 288 eV are shifted to higher energy (0.4 eV for Solaronix and 0.6 eV for Aqueous), indicating that their chemical environment has changed from their pure N719 state upon adsorption to the TiO₂ surfaces as expected but in a distinct manner depending upon the anatase substrate used.

5.4.3 Photovoltaic characteristics

To further evaluate how these electronic interactions may vary in the two distinct anatase nanocrystalline substrates, photovoltaic IV curves were measured as shown in Figure 5.23. The short circuit photocurrent densities (J_{sc}) obtained with Solaronix and Aqueous [25] DSSC were 16.2 and 13.1 mA/cm², respectively. For Solaronix DSSC, the photovoltaic performance of 7.30 % (open circuit voltage V_{oc} = 0.718 V and fill factor FF = 62.8 %) was achieved for the sample of 0.168 cm² cell area.

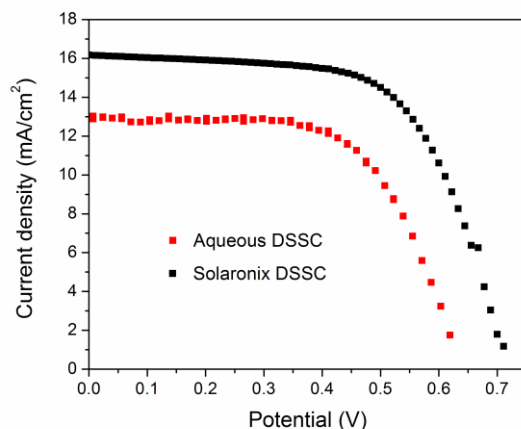


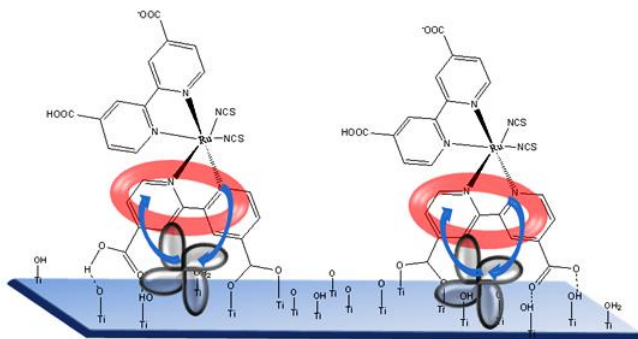
Figure 5.23 I-V curves of DSSCs fabricated with two different TiO₂ electrodes

In the case of Aqueous DSSC, the efficiency was 5.02 % with V_{oc} = 0.63 V and FF = 64.1 % for the sample of 0.175 cm² cell area. These IV measurement show that indeed the electrical performances vary in these two nanocrystalline anatase films produced from different synthetic methods. There are many factors that influence the electronic performance of the DSSC [85]; in our studies we observed a difference in surface charge

interactions that may also contribute to their different electrical performances. Although H-bonding may aid in stabilizing the dye molecules as reported in our previous work [6], the creation of excess H-bonding sites or excess surface Ti-OH₂ sites (as in our aqueous product) may result in excess positive charge sites that contribute to the lower mobility of electrons [86].

5.4.4 Proposed binding scheme

On the basis of all previous vibrational spectroscopic results, imaging data and electron spectroscopy, we proposed a modified structure for the binding of N719 dye on TiO₂ films as shown in Scheme 5.1. In our scheme, it was proposed that electronic interactions of the N719 dye to TiO₂ occur not only through the covalent bonding of the anchoring groups (as previously reported, Chapter 3) but also through the aromatic electron density of the bipyridine groups and the d states found in TiO₂.



Scheme 5.1, Schematic describing the adsorption and electronic interactions of the N719 onto TiO₂ surface.

5.5 Conclusion

The electronic properties of N719 adsorbed-anatase films (one commercial-Solaronix and our aqueous-synthesized variety) were comparably investigated by using XAS and XPS techniques. Here are the major findings:

- (1) Our Ti L-edge and O K-edge XANES data, in contrast to previous reports by Ju *et al.* and Zubavichus *et al.*, did not show any structural changes in terms of crystal field (i.e. coordination) modification after dye adsorption to the surface TiO₂ groups of either

substrate. This was attributed to the fact that most of the XANES signal comes from Ti atoms and O atoms far from the dye–TiO₂ interface and as such detecting such coordination changes to surface groups was not feasible even with this surface sensitive TEY mode. Ti K-edge XANES and EXAFS data support our Ti L-edge data that the coordination changes from the pure to the adsorbed state cannot be observed because of the probing depth of Ti K-edge in TEY mode and as such observing these changes in transmission or FY yield are not possible.

- (2) The C K-edge XANES spectral changes revealed that there are additional electronic states (not observed in the neat N719) that occur between dye molecules and TiO₂ surface once adsorption occurs. Furthermore, the π^* and σ^* regions in the spectra indicate slight modification of the electronic structure around the pyridine structures after dye adsorption. These spectral changes to the XANES spectrum allow us to propose that the aromatic electronic density from pyridine interacts with TiO₂ electron density. Thus, we can postulate that in the N719-TiO₂ system, electronic interactions occur not only through the covalent bonding of the anchoring groups but also through the aromatic electron density of the bipyridine groups and the d states found in TiO₂. The orientation experiment conducted showed that the adsorbed sample at normal incidence (90°) and at grazing incidence (30°) exhibits no intensity change for the π^* or σ^* states; this was rationalized as result of each carbon in the dye molecule being oriented differently in space and as such no angle dependency was observed. The N K-edge in contrast to the C K-edge showed no additional electronic states; once adsorption occurred most of the neat N719 character remained intact. On the other hand, the orientation measurements in the N K-edge showed that the intensity for the N 1s \rightarrow π^* resonance peak increased at 30°, indicating that the sp² conjugated π bond in the bipyridine groups is more aligned with the TiO₂ substrate at 30° than 90° to the surface. Further suggesting that this type of geometry favors electronic aromatic interaction between the TiO₂ surface and the N719 molecules.
- (3) Ti 2p and O 1s XPS showed a shift to lower energy in the dye-coated TiO₂ compared to the pure TiO₂ for both substrates. The shift in energy may be due to a change of the

dipole of the surface or a change in the Fermi level position was distinct for each nanocrystalline anatase substrate. Interestingly, the N719-Aqueous TiO₂ sample was consistently shifted to lower energies in comparison to the N719-Solaronix sample for both the Ti 2p and O 1s XPS results. Thus, we may conclude that the changes to the surface dipole and/or E_f between our Aqueous TiO₂ substrate and the N719 molecule are greater than those found for the Solaronix TiO₂. This is likely due to higher occurrence of surface OH/H₂O groups in our aqueous product which may further contribute to the change in the surface dipole (and/or E_f) that occurs upon dye adsorption to the TiO₂ substrate.

- (4) In the N 1s XPS spectrum, the NCS peak of dye-coated TiO₂ shows a shift toward higher energy and an increase in FWHM compared to neat N719, indicating that there are interactions (likely H-bonding) between the NCS ligand and the TiO₂ surfaces. Furthermore, the bi-pyridine peak was also found to shift to higher energy for the dye-coated TiO₂ relative to the neat N719, which further supports our C and N K-edge XANES result that the aromatic π electron density in the pyridine rings interacts with the electronic TiO₂ surface density. In the case of S 2p XPS, the de-convoluted peaks for both samples are shifted to higher binding energies for the adsorbed samples compared to the neat N719. Therefore, it may be concluded that a fraction of the molecules adsorbed onto TiO₂ interacts (likely through H-bonding) with the substrate through at least one of the NCS groups, in agreement with our N 1s XPS results.

- (5) Although the two nanocrystalline anatase (our aqueous and commercial) substrates showed a similar type of bonding environment around the TiO₂ (in pure and adsorbed states) as observed via our XAS data, the TiO₂ surface interactions upon dye adsorption (monitored via binding energy shifts in XPS) were found to be distinct in the two substrates, indicating that not all anatase nanocrystalline substrates behave in the same way once the N719 is adsorbed in terms of electronic interactions (surface dipole or shift to the Fermi level) and as a result may contribute to the distinct manner they perform in the DSSC.

5.6 Acknowledgements

The project is funded through the strategic research grant program of NSERC (the Natural Sciences and Engineering Research Council of Canada). All XAS measurements were performed at Canadian Light Source. The authors are grateful to Prof. Kruger and de Groot for useful discussion. We also thank Prof. Cerruti for the use of XPS instrument; Slawomir Poplawski for his aid of XPS data collection.

5.7 References

- [1] Gratzel, M, *Nature* **2001**, *414*, 338-344
- [2] Hagfeldt, A.; Grätzel, M. *Chem. Rev.* **1995**, *95*, 49-68
- [3] Kopidakis, N.; Benkstein, K. D.; van de Lagemaat, J.; Frank, A. J. *Phys. Rev. B* **2006**, *73*, 045326
- [4] Varghese, O. K.; Paulose, M.; Grimes, C. A. *Nat. Nanotechnol.* **2009**, *4*, 592–597
- [5] Richter, C.; Schmittenmaer, C. A. *Nat. Nanotechnol* **2010**, *5*, 769-772
- [6] Lee, K. E.; Gomez, M. A.; Samir Elouatik, S.; Demopoulos, G. P. *Langmuir* **2010**, *26*, 9575–9583
- [7] Lee, K. E.; Gomez, M. A.; Elouatik, S.; Demopoulos, G. P. *ECS Trans.* **2010** *28*, 1-7
- [8] Stóhr, J. *NEXAFS Spectroscopy*; Springer: Berlin, 1992
- [9] Nilsson, A. *J. Electron. Spectrosc. Relat. Phenom.* **2002**, *126*, 3–42
- [10] Ade, H.; Stoll, H. *Nat.Mat.* **2009**, *8*, 281-290
- [11] Handerson, G. S.; Liu, X.; Fleet, M. E. *Phys Chem Mineral* **2002**, *29*, 32-42
- [12] Fleet, M. E.; Liu, X. *Am. Mineral.*,**2009**, *94*, 1235–1241
- [13] de Groot, F. *Coord. Chem. Rev.***2005**, *249*, 31-63

- [14] Gomez, M. A.; Becze, L.; Blyth, R. I. R.; Cutler, J. N.; Demopoulos, G. P. *Geochim. Cosmochim. Acta* **2010**, *74*, 5835-5851
- [15] Farges, F.; Brown, G. E.; Rehr, J. J. *Phys. Rev. B* **1997**, *56*, 1809
- [16] Wilke, M.; Farges, F.; Petit, P. -E.; Brown Jr. G. E.; Martin, F. *Am. Mineral.* **2001**, *86*, 714-730
- [17] Westre, T. E.; Kennepohl, P.; DeWitt, J. G.; Hedman, B.; Hodgson, K. O.; Solomon, E. I. *J. Am. Chem. Soc.* **1997**, *119*, 6297-6314
- [18] Bare, S. R.; Mitchell, G. E.; Maj, J. J.; Vrieland, G. E.; Gland, J. L. *J. Phys. Chem.*, **1993**, *97*, 6048-6053
- [19] Rentería, M.; Traverse, A.; Anunziata, O. A.; Lede, E. J.; Pierella, L.; Requejo F. G. *J. Synchrotron Rad.* **2001** *8*, 631-633
- [20] Ju, X.; Wu, K. W.; Hou, Y. J.; Xie, P. H.; Zhang, B. W. *Surf. Interface. Anal.* **2001**, *32*, 95-97
- [21] Zubavichus, Y. V.; Slovokhotov, Yu. L.; Nazeeruddin, M. K.; Zakeeruddin, S. M.; Gra tzel, M.; Shklover, V. *Chem. Mater.* **2002**, *14*, 3556-3563
- [22] Rensmo, H.; Westermark, K.; Sodergren, S.; Kohle, O.; Persson, P.; Lunell, S.; Siegbahn, H. *J. Chem. Phys.* **1999**, *111*, 2744-2750
- [23] Johansson, E. M. J.; Hedlund, M.; Siegbahn, H.; Rensmo, H. *J. Phys. Chem. B* **2005**, *109*, 22256-22263
- [24] Mayor, L. C.; Taylor, J. B.; Magnano, G.; Rienzo, A.; Satterley, C. J.; O'Shea, J. N.; Schnadt, J. *J. Chem. Phys.* **2008**, *129*, 114701-114709
- [25] Charbonneau, C.; Lee, K. E.; Shan, G. B.; Gomez, M. A.; Gauvin, R.; Demopoulos, G. P. *Electrochem. Solid-State Lett.* **2010**, *13*, H257-H260
- [26] Ito, S.; Chen, P.; Comte, P.; Nazeeruddin, Md. K.; Liska, P.; Péchy, P.; Grätzel, M. *Prog. Photovolt: Res. Appl.* **2007**, *15*, 603-612

- [27] Zhou, J. G. ; Fang, H. T. ; Maley, J. M. ; Murphy, M. W. ; Ko, J. Y. P.; Cutler, J. N.; Sammynaiken, R.; Sham, T. K.; Liue, M.; Lie, F. *J. Mater. Chem.*, **2009**, *19*, 6804–6809
- [28] Kucheyev, S. O.; van Buuren, T.; Baumann, T. F.; Satcher, J. H.; Willey, T. M.; Meulenbergh, R. W.; Felter, T. E.; Poco, J. F.; Cammon, S. A., Terminello, L. J. *Phys. Rev. B*. **2004**, *69*, 245102
- [29] Stewart, S. J.; Fernandez-Garcia, M.; Belver, C.; Mun, B. S.; Requejo, F. G. *J. Phys. Chem. B* **2006**, *110*, 16482-16486
- [30] de Groot, F. M. F.; Fuggle, J. C.; Thole, B. T.; Sawatzky, G. A. *Phys. Rev. B*. **1990**, *41*, 928
- [31] de Groot, F. M. F.; Figueiredo, M. J.; Basto, M.; Abbate, H.; Petersen, H.; Fuggle, J. C. *Phys. Chem. Miner.* **1992**, *19*, 140-147
- [32] Kruger, P. *J. Phys. Conf. Ser.* **2009**, *190*, 012006
- [33] Kruger, P. *Phys. Rev. B*. **2010**, *81*, 12512
- [34] Chakhalian, J.; Freeland, J. W.; Habermeier, H. U.; Cristiani, G.; Khaliullin, G.; van Veenendaal, M.; Keimer, B. *Science* **2007**, *318*, 1114-1117
- [35] Sham, T. K. *Chem. Phys. Lett.*, **1983**, *101*, 567-572
- [36] Yu, P.; Lee, J.-S.; Okamoto, S., Rossell, M. D.; Huijben, M.; Yang, C.-H.; He, Q.; Zhang, J. X.; Yang, S. Y.; Lee, M. J.; Ramasse, Q. M.; Erni, R.; Chu, Y.-H.; Arena, D. A.; Kao, C.-C.; Martin, L. W.; Ramesh, R. *Phys. Rev. Lett.* **2010**, *105*, 027201
- [37] Luca, V.; Djajanti, S.; Howe, R. F. *J. Phys. Chem. B* **1998**, *102*, 10650.
- [38] Chen, L. X.; Raih, T.; Jager, W.; Nedeljkovic, J.; Thurnauer, M. *J. Synchrotron Radiat.* **1999**, *6*, 445
- [39] Raih, T.; Nedeljkovic, J. M.; Chen, L. X.; Poluektov, O.; Thurnauer, M. C. *J. Phys. Chem.* **1999**, *103*, 3515

- [40] Wu, Z. Y.; Ouvrard, G.; Gressier, P.; Natoli, C. R. *Phys. Rev. B* **1997**, *55*, 10382–10391
- [41] Uozumi, T.; Okada, K.; Kotani, A.; Durmeyer, O.; Kappler, J. P.; Beaupair, E.; Parleb, J. C. *Europhys. Lett.* **1992**, *18*, 85-90
- [42] Khan, M. A.; Kotani, A.; Parlebas, J.-C. *J. Phys. Condens. Matter* **1991**, *3*, 1763
- [43] K. Okada and A. Kotani, *J. Electron Spectrosc. Relat. Phenom.* **1993**, *62*, 131
- [44]. Brouder, C. *J. Phys. Condens. Matter* **1990**, *2*, 701
- [45] Parlebas, J. C.; Khan, M. A.; Uozumi, T.; Okada, K.; Kotani, A. *J. Electron Spectrosc. Relat. Phenom.* **1995**, *71*, 117
- [46] Wang, L.-Q.; Ferris, K. F.; Shultz, A. N.; Baer, D. R.; Engelhard, M. H. *Surf. Sci.* **1997**, *380*, 352
- [47] Farges, F.; Brown, G. E., Jr.; Rehr, J. J. *Geochim. Cosmochim. Acta* **1996**, *60*, 3023
- [48] Wu, Z. Y.; Ouvrard, G.; Gressier, P.; Natoli, C. R. *Phys. Rev. B* **1997**, *55*, 10382
- [49] Joly, Y.; Cabaret, D.; Renevier, H.; Natoli, C. R. *Phys. Rev. Lett.* **1999**, *82*, 2398
- [50] Chen, L. X.; Rajh, T.; Wang, Z.; Thurnauer, M. C. *J. Phys. Chem. B* **1997**, *101*, 10688-10697
- [51] Hocking, R. K.; George, S. D.; Gross, Z.; Walker, F. A.; Hodgson, K. O.; Hedman, B.; Solomon, E. I. *Inorg. Chem.*, **2009**, *48*, 1678–1688
- [52] Thomas, A. G.; Flavell, W.R.; Chatwin, C.P.; Kumarasinghe, A.R.; Rayner, S.M.; Kirkham, P.F.; Tsoutsou, D.; Johal, T.K.; Patel, S. *Surf. Sci.* **2007**, *601*, 3828–3832
- [53] As shown in Figure 7, there is a slight shift toward higher energies [0.1 eV] in the first π^* peak [A_C] when the dye is adsorbed onto TiO₂ and a definite change in the intensity ratio of these two peaks [A_C and B_C]. It is worth to note at this point, that in our studies, computations of the C K-edge were not attempted due to the complexity of the N719 molecule which contains numerous amounts of carbon atoms in various electronic

states and thus assigning each spectral feature and contribution to each of these carbon atoms is unlikely.

[54] Richard, G.; Cros, A.; Mathey, Y.; Tourillon, G.; Laffon, C.; Parent, Y. *J. Phys. IV* **1993**, 3, 789-792

[55] Kaneko, M.; Moroi, T.; Shiriishi, H. *Macromol. Symp.* **2002**, 186, 177-185

[56] Outka, D. A.; Storhr, J.; Madix, R. J.; Rotermund, H. H.; Hermsmeier, B.; Solomon, J. *Surf. Sci.* **1987**, 185, 53-74

[57] Johansson, E. M. J.; Hedlund, M.; Odelius, M.; Siegbahn H.; and Rensmo, H. *J. Chem. Phys.* **2007**, 126, 244303 _

[58] Johansson, E. M. J.; Odelius, M.; Plogmaker, S.; Gorgoi, M.; Svensson, S.; Siegbahn H.; Rensmo, H. *J. Phys. Chem. C*, **2010**, 114, 10314–10322

[59] Metson, J. B.; Trodahl, B. J.; Ruck, B. J.; Lanke, U. D.; Bittar, A. *Surf. Interface. Anal.* **2003**, 35, 719-722

[60] Thomas, A. G.; Flavell, W. R.; Chatwin, C.; Rayner, S.; Tsoutsou, D.; Kumarasinhe, A. R.; Brete, D.; Johal, T. K.; Patel, S.; Purton, J. *Surf. Sci.* **2005**, 592, 159-168

[61] Isvoranu, C. Metal-Organic Complexes at Surfaces, PhD dissertation, Lund University, 2010

[62] Johansson, E. Interfaces in Dye-Sensitized Oxide / Hole-Conductor Heterojunctions for Solar Cell Applications, PhD dissertation, Uppsala University, 2006

[63] Gouttebaron, R.; Cornelissen, D.; Snyders, R.; Dauchot, J. P.; Wautelet, M.; Hecq, M. *Surf. Interface. Anal.* **2000**, 30, 527-530

[64] Shirkhazadeh, M. *J. Mater. Sci.- Mater. Med*, **1995**, 6, 206-210

[65] Kim, Y.; Yoon, C.; Kim, K.; Lee, Y. *J. Vac. Sci. Technol.* **2007**, A25, 1219-1225

[66] Liu, G.; Jaegermann, W.; He, J.; Sundstrm, V.; Sun, L. *J. Phys. Chem. B*, **2002**, 106, 5814-5819

- [67] Bard, A. J. *J. Phys. Chem.* **1982**, *86*, 172
- [68] Liu, G.; Klein, A.; Thissen, A.; Jaegermann, W. *Surf. Sci.* **2003**, *539*, 37-48
- [69] Onda, K.; Li, B.; Petek, H. *Phys. Rev. B.* **2004**, *70*, 045415
- [70] Marques, H. P.; Canario, A. P.; Moutinho, A. M. C.; Teodoro, O. M. N. D.; *Vacuum*, **2008**, *82*, 1425-1427
- [71] Bundaleski, N.; Silva, A. G.; Schroder, U.; Moutinho, A. M. C.; Teodoro, O. M. N. D.; *JPCS*, **2010**, *257*, 012008
- [72] Hirose, F.; Kuribayashi, K.; Suzuki, T.; Narita, Y.; Kimura, Y.; Niwano, M. *Electrochem. Solid-State Lett.* **2008**, *11*, A109–A111
- [73] Selloni, A. *Nat. Mater.* **2008**, *7*, 613-615
- [74] Simmons, G. W.; Beardt, B. C. *J. Phys. Chem.* **1987**, *91*, 1143-1148
- [75] Erdem, B.; Hunsicker, R. A.; Simmons, G. W.; Sudol, E. D.; Dimonie, V. L.; El-Aasser, M. S. *Langmuir* **2001**, *17*, 2664-2669
- [76] Huang, N. K.; Wang, D. Z.; Lu, Z.; Lin, L. B. *Surf. Coat. Technol.* **1994**, *70*, 69-71
- [77] Lopez, S.; Dunlop, H. M.; Benmalek, M.; Tourillon, G.; Wong, M. S.; Sproul, W. D. *Surf. Interface Anal.* **1997**, *25*, 827–835
- [78] O'Shea, J. N.; Schnadt, J.; Brühwiler, P. A.; Hillesheimer, H.; Mårtensson, N. *J. Phys. Chem. B*, **2001**, *105*, 1917–1920
- [79] O'Shea, J. N.; Luo, Y.; Schnadt, J.; Patthey, L.; Hillesheimer, H.; Krempasky, J.; Nordlund, D.; Nagasono, M.; Brühwiler, P. A.; Mårtensson, N. *Surface Science*, **2001**, *486*, 157-166
- [80] Wen, P.; Itoh, H.; Tang, W.; Feng, Q. *Microporous Mesoporous Mater.* **2008**, *116*, 147-156

- [81] Schnadt, J.; Schiessling, J.; O'Shea, J. N.; Gray, S. M.; Patthey, L.; Johansson, M. K.-J.; Shi, M.; Krempaský, J.; Åhlund, J.; Karlsson, P. G.; Persson, P.; Mårtensson, N.; Brühwiler, P. A. *Surf. Sci.* **2003**, *540*, 39-54
- [82] Guo, Q.; Cocks, I.; Williams, E. M. *Surf. Sci.* **1997**, *393*, 1-11
- [83] Schnadt, J.; O'Shea, J. N.; Patthey, L.; Schiessling, J.; Krempasky, J.; Shi, M.; Martensson, N.; Brühwiler, P.A. *Surf. Sci.* **2003**, *544*, 74-86
- [84] Cueto, L. F.; Hirata, G. A.; Sánchez, E. M. *J Sol-Gel Sci Techn.* **2006**, *37*, 105-109
- [85] Hagfeldt, A.; Boschloo, G.; Sun, L.; Kloo, L.; Pettersson, H. *Chem. Rev.* **2010**, *110*, 6595-6663
- [86] Pal, S.; Manna, A. K.; Pati, S.K. *J. Chem. Phys.* **2008**, *129*, 204301

Chapter 6. Enhanced surface hydroxylation of nanocrystalline anatase films improves photocurrent output and electron lifetime in DSSC photoanodes

As clearly revealed in the previous chapters, TiO₂ surface groups are involved in the mechanism by which the N719 dye molecules adsorb on the semiconductor surface. In the meantime, I-V measurements done by others in literature had shown that DSSC devices whose photoanodes were made with OH-rich TiO₂ exhibited improved performance. In this last Chapter the author sets as goal to link these two separate observations by undertaking a systematic comparison of three equivalents in thickness and interfacial area photoanode films that differ only in the amount of surface hydroxylation. The study described here incorporates comprehensive characterization of the physical properties of the three mesoporous thin TiO₂ films as well as cell I-V performance and electrochemical analysis via impedance spectroscopy and open circuit voltage decay techniques. The films were built by screen printing pastes made with three type of anatase nanocrystallites (single layer deposition), namely two commercial ones (“Alfa Aesar 5 nm” and “Alfa Aesar 10 nm”) and our aqueous synthetic one (“Aqueous TiO₂”).

6. 1 Abstract

Anatase TiO₂ nanocrystalline films were prepared from commercial (Alfa Aesar 5 nm and 10 nm) and aqueous-solution synthesized precursors (Aqueous TiO₂) by screen printing with the purpose of elucidating the influence of surface hydroxylation on DSSC performance. These two commercial TiO₂ sources were selected as they possessed similar nanocrystallite size and mesoporous film interfacial surface area with our in-house variety. In this way it was possible to distinguish the effect of surface hydroxylation on DSSC photocurrent output and electron life time from other film surface properties. Their morphological features were characterized in terms of particle size, shape, BET surface area, topography and their surface hydroxyl groups quantified using TGA and XPS analysis. The electrochemical properties of the DSSCs composed of the Aqueous TiO₂, Alfa Aesar 5 nm and 10 nm photoelectrodes were probed via impedance spectroscopy (EIS) and open circuit voltage decay (OCVD). The combined EIS and OCVD results showed that photoelectrodes composed of surface hydroxyl-rich TiO₂ nanocrystalline material exhibits longer electron lifetime attributed to enhanced surface-dye binding that suppresses interfacial recombination. As a result of the stabilized surface hydroxyl-dye (N719) binding, the photocurrent output from the OH-rich anatase photoanodes (Aqueous and Alfa Aesar 5 nm TiO₂,) was a remarkable 85-108% higher than that of the OH-poor film (Alfa Aesar 10 nm) despite their equivalent surface area and porosity.

6.2 Introduction

The dye sensitized solar cell (DSSC) is currently a very active research area with the imminent promise of commercial breakthrough [[1]. Key components of the DSSC are the TiO₂ photoanode, the sensitizer, and the electrolyte. Development of anatase TiO₂ mesoporous photoelectrodes with enhanced light harvesting, electron generation and transport properties attracts a lot of attention as this can lead to DSSCs with enhanced solar energy conversion efficiency [2-4]. Many studies have focused on the relation between nanocrystalline TiO₂ (nc-TiO₂) structure and power conversion efficiency [5-7]. It is known that a large surface area, high crystallinity, and good connectivity improve J_{sc} values [8]. The overall performance of DSSC strongly depends on the surface area of the

TiO₂ photoelectrode, as it is directly correlated to the amount of dye loading[9]. But in addition to increasing dye loading, and hence cell performance by increasing the nc-TiO₂ surface area, other surface properties such as an increase in the surface roughness factor [9] or the surface hydroxyl groups are known to also boost cell performance. Recognition that dye loading can be enhanced via TiO₂ surface alteration has led to several surface treatments to be developed such as acid pretreatment of TiO₂ films prior to dye sensitization [10], and UV radiation or plasma treatments [11,12]. Although the formation of surface hydroxyl groups was invoked in some of these previous works to explain the positive effect the surface treatment had on dye loading and photocurrent output, no direct evidence to this effect was presented nor definitive electrochemical interpretation was presented. The only exception was the work of Hirose et al., who correlated the surface hydroxyl groups on TiO₂ to the binding mechanism between N719 and TiO₂ by showing the IR spectrum in the range of 1000-4000 cm⁻¹ [13].

We recently reported a new type of binding mechanism of N719 onto TiO₂ using ATR-FTIR and Raman spectroscopy by investigating the Ti-OH/Ti-OH₂ groups in the high wavenumber region [14]. A particular focus of our previous spectroscopic study was the elucidation of the role that surface Ti-OH/Ti-OH₂ groups play in the binding mechanism. Based on our investigation from Micro-Raman, ATR-FTIR spectroscopy and Confocal Raman imaging in the low wavenumber region, we proposed that one carboxylic group (COO⁻ or COOH) in N719 molecules binds to TiO₂ by a dual bonding mechanism involving bidentate bridging (chemisorptions) plus electrostatic coupling (H-bonding) via the surface Ti-OH/Ti-OH₂ groups [14]. This H-bonding feature, not identified previously was proposed to help stabilize the N719 dye molecule on the substrate surface while at the same time have an effect of the surface charges as observed via our core level electron spectroscopic (XANES and XPS) studie [15]. Later on, we further focused on the hydroxyl vibrations (high wavenumber region) of TiO₂ surface groups (before and after sensitization), and their relation to the type of bonding mechanism [14] that occurs upon adsorption using confocal Raman imaging and micro ATR-FTIR imaging [16]. This was done to reveal the role of surface groups (Ti-OH/Ti-OH₂) before and after adsorption of two different TiO₂ films; one was a commercial product (“Dyesol”) and one made from

our anatase variety (“Aqueous”) synthesized in our laboratory [16,17]. However, in our previous works the average nanocrystallite size of the commercial TiO₂ anatase films (Dyesol or Solaronix TiO₂) was 20 nm, hence complicating direct comparison with Aqueous TiO₂ (5~10 nm) as far it concerns the contribution of the surface hydroxyl groups.

In order to unequivocally clarify the role of surface hydroxylation on DSC performance we chose in the present work to compare “head-to-head” our synthesized Aqueous TiO₂ with two commercial TiO₂ products (Alfa Aesar 5 nm and Alfa Aesar 10 nm) that have equivalent BET surface area as well as crystallite size but varying in the level of surface hydroxylation.

The characterization of photoanodes made from the three different nanocrystalline anatase TiO₂ varieties was evaluated by transmission electron microscopy (TEM), atomic force microscopy (AFM), Brunauer–Emmett–Teller analysis (BET), thermogravimetric analysis (TGA) and X-ray photoelectron spectroscopy (XPS). But in addition, we employed electrochemical impedance spectroscopy (EIS) [16] and open circuit voltage decay (OCVD) analysis in order to probe the interface electron process and electron life time (denoted as τ), respectively [18-19]; and as such shed light on the manner by which surface hydroxylation leads to improved photocurrent output. As pointed out recently by Bisquert et al.[20], the electrochemical understanding of the kinetic barriers that impede interfacial recombination is one of the keys for improving the performance of DSSC. EIS is a powerful method of investigating internal resistances and charge transfer processes in electrochemical systems. Wide range of electrochemical processes and internal resistances that govern the performance of DSSC can be analyzed by this method. The open-circuit voltage decay (OCVD) technique on the other hand allows for straightforward carrier lifetime determination and very good correlation with real electrical device parameters [21]. The current–voltage characteristics (I–V characterization) was also investigated in relation to the TiO₂ film physical properties. It is the primary purpose of this report to demonstrate the connection between surface hydroxylation and enhanced cell performance as a result of suppression of interfacial recombination arising from the fully stabilized dye layer on the TiO₂ surface. As

secondary objective, the inherent advantage of aqueous synthesis as a facile and low cost route towards production of hydroxyl-rich anatase nanocrystallites is pursued and further optimization opportunities in terms of mesoporous film structure development are identified.

6.3 Experimental

6.3.1 TiO₂ film preparation and cell fabrication

The Ru complex (N719: (bis(tetrabutylammonium)[cis-di(thiocyanato)-bis(2,2'-bipyridyl-4-carboxylate-4'-carboxylic acid)-ruthenium(II)]) was obtained from Dyesol. The TiO₂ pastes were prepared using three kinds of TiO₂ (anatase; two commercial-Alfa Aesar 5 nm and Alfa Aesar 10 nm (CAS #: 1317-70-0 for both) and our aqueous produced variety through “A synthesis route” -Aqueous [17,22]). TiO₂ electrodes were prepared by screen printing on FTO conductive glass substrates (Nippon Sheet Glass with a sheet resistance of 10 Ω per square). The TiO₂ paste was spread out onto a FTO glass and sintered at 450°C in air for 30 min yielding a 12~14 μm thick films, measured by a Dektak 3 surface profile measuring system. Dye coated TiO₂ films were prepared by immersion into the dye solution for 24 h at room temperature [23]. The coated TiO₂ was rinsed several times with ethanol to remove excess physisorbed N719 dye molecules and was left to dry in air. Photoelectrodes were achieved without the use of any anti-reflection coating, back-scattering layer, or TiCl₄ post treatment. As our focus was the clarification of the effect of surface hydroxylation on photoelectrode performance we opted for single and equivalent in thickness and surface area films without employing TiCl₄ post treatment [24] or back-scattering layer [25]. A sandwich-type cell was assembled to measure the I-V curves, impedance spectroscopy and open-circuit voltage decay (OCVD). As a counter electrode, a Pt layer was prepared by spreading one drop of 5 mM H₂PtCl₆ solution (*iso*-propanol), air dry, and then heating at 380°C for 30 min. A 30 μm thick thermoplastic film (Surllyn®-30, Dyesol) was employed to assemble and seal the two electrodes and a commercial electrolyte solution (composition: I₃⁻/I, organic iodide salt, pyridine derivative, acetonitrile & valeronitrile; EL-HPE; Dyesol) was filled through the hole on the Pt electrode.

6.3.2 TiO₂ films characterization

The surface area and film porosity data were obtained with Brunauer Emmett–Teller (BET) surface area analysis performed on a Micromeritics TriStar 3000 nitrogen adsorption–desorption apparatus. A multiple point specific surface area type of analysis was carried out. Each sample weighed approximately 200 mg and had been degassed for 4 h at 80°C prior to nitrogen physisorption. The thickness and surface roughness of the films were studied using a Dektak 3 surface profiler (1 cm scan length, 30 mg load). AFM images were acquired from these samples using a Digital Instruments 3000, Nanoscope III, AFM to investigate the surface morphology.

The chemical properties of the films, namely the amounts of surface adsorbed and structural hydroxyl/water molecules were investigated by combining TGA (thermogravimetric analysis) and XPS (X-ray photoelectron spectroscopy). TGA analyses were performed on the films with a TA Instruments Q500 TGA, starting at ambient temperature up to 600°C with a heating rate of 10°C/min under N₂ atmosphere. X-ray photoelectron spectroscopy (XPS) measurements were conducted in a Thermo Scientific K-Alpha, using a Al K α X-ray source at 1486.6 eV. High-resolution spectra were obtained at a perpendicular takeoff angle, using a pass energy of 20 eV and steps of 0.1 eV. Spectral peaks were separated using the VG Advantage program, and the Shirley background was subtracted. The scale of the binding energy was calibrated against Au (4f_{7/2}) located at 84 eV.

In order to determine the dye loading on the sensitized TiO₂ films the latter were immersed in 4 mL of NaOH solution (0.1 M) for 1 min [26]. This caused desorption of the dye from TiO₂ into the solution while keeping the TiO₂ layer intact. The supernatant solution was introduced into a cuvette, and the spectrum of dye in the basic solution was measured by Varian Cary 300 UV-Vis spectrometer.

6.3.3 Photo-electrochemical measurements

The current-voltage curves were measured using a small area solar simulator (PV measurements Inc., Model SASS). A tungsten lamp was used to provide uniform light

approximating the AM 1.5 Global reference spectrum to a 1 cm diameter test region. The light intensity was adjusted with a Si reference cell. Duplicate measurements with each type of DSSC (Alfa Aesar 5 nm, 10 nm and Aqueous) were made to ensure reproducible results. The impedance measurements were carried out under 100 mW/cm^2 illumination and applied open circuit voltage (OCV) and were recorded over a frequency range of 0.01 to 100 kHz with ac amplitude of 10 mV. For the photoinduced open circuit voltage decay (OCVD) measurements, the illumination was turned off using a shutter after the cell was first illuminated to a steady voltage, and then the OCVD curve was recorded. The above two measurements were carried out on a VSP instrument (BioLogic) and analyzed with the EC-lab software.

6.4 Results and discussion

6.4.1 TiO_2 films properties

TEM images in Figure 6.1 show the crystallite size and morphology of three TiO_2 (Aqueous TiO_2 , Alfa Aesar 5 nm and 10 nm substrates). In the TEM images, the average crystallite size of Aqueous TiO_2 ranged in 5~10 nm and the two commercial TiO_2 particles represent ~5 nm and ~10 nm, respectively.

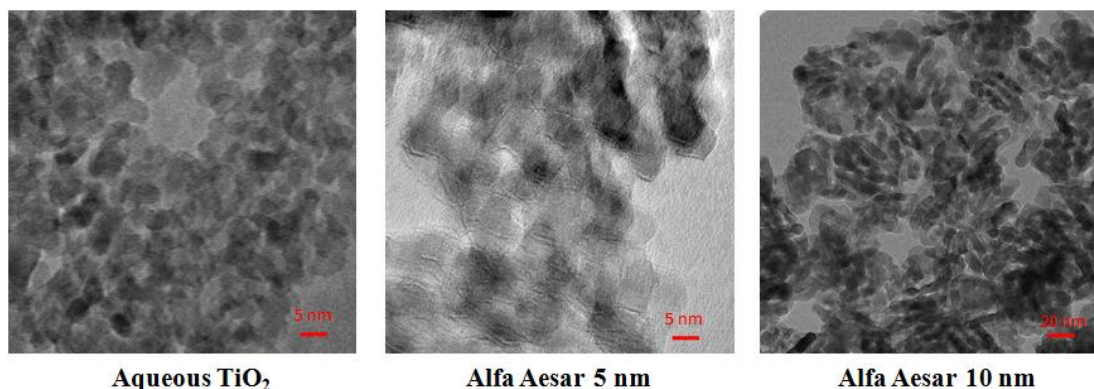


Figure 6.1 TEM images of TiO_2 anatase nanocrystallites (a) Aqueous (b) Alfa Aesar 5 nm (c) Alfa Aesar 10 nm

The structural phases of all three films are anatase as confirmed by Raman spectroscopy (Figure 6.2). The Raman lines at 144, 197, 399, 515 and 639 can be assigned as the E_g (1), E_g (2), B_{1g} , A_{1g} or B_{1g} , and E_g (3) modes of the anatase phase, respectively [27]. The inset shows the Raman spectrum at 144 cm^{-1} . We chose to further look at the peak position and

line-broadening of the E_g (144 cm^{-1}) Raman band in order to estimate the relative crystallite size[28]. As the crystallite size decreases, the frequency and line-width of the E_g Raman peak blue-shifts and increases, respectively as a result of the phonon confinement effect. The Raman spectrum at 144 cm^{-1} shows that Alfa Aesar 5 nm and Aqueous shifted further to higher energy than Alfa Aesar 10 nm, indicating the size of Aqueous TiO_2 is similar with Alfa Aesar 5 nm and rather smaller than Alfa Aesar 10 nm, although Aqueous TiO_2 is composed of 5~10 nm particulates.

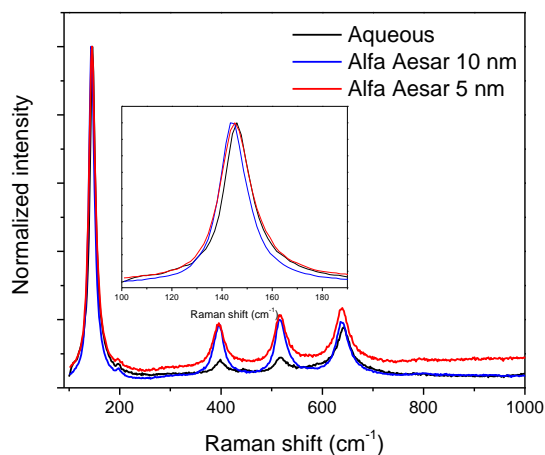


Figure 6.2 Raman spectra of TiO_2 films

The topography and roughness factor of each film were analyzed by AFM as shown in Figure 6.3. The roughness of Aqueous TiO_2 was slightly higher than that of two commercial TiO_2 films.

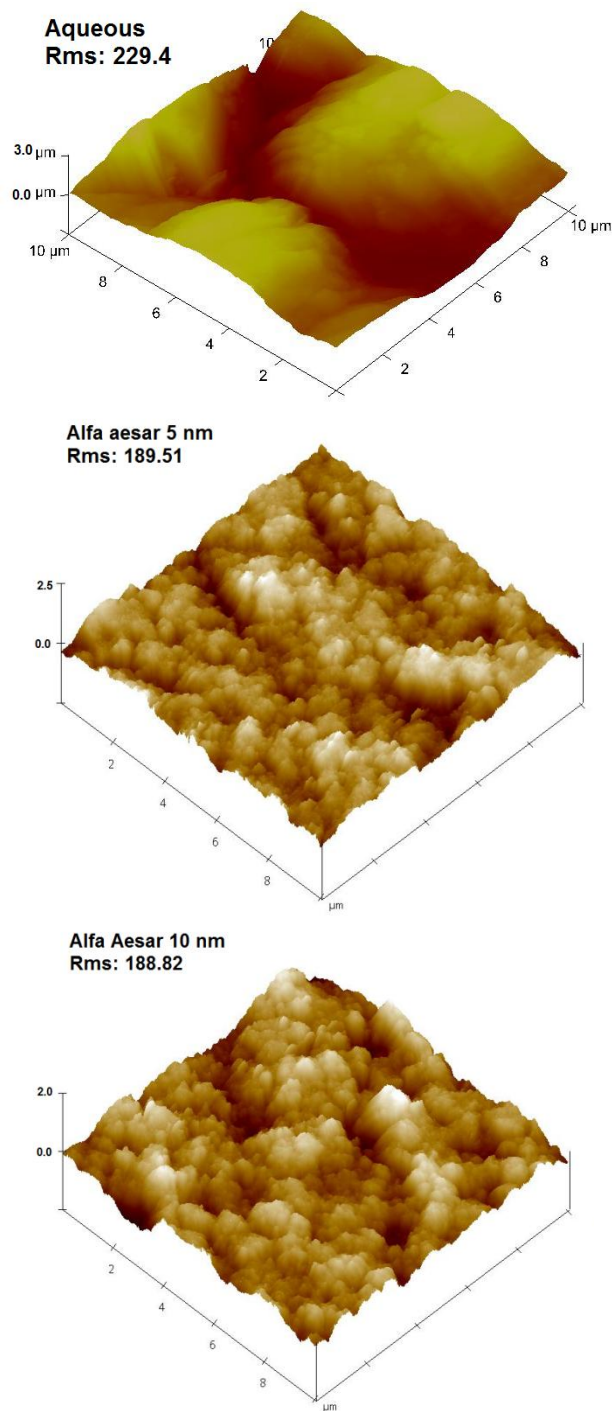


Figure 6.3 Tapping mode AFM three-dimensional height images of TiO₂ films

In our Raman characterization, we could estimate that the Aqueous TiO₂ crystallites were of similar size as the Alfa Aesar 5 nm and as such exhibited a similar phonon confinement effect. However, we can observe in Figure 6.3 that the roughness factor for

Aqueous TiO₂ films was higher than that of Alfa Aesar 5 nm, indicating that Aqueous TiO₂ particles in the film are more aggregated than in the case of Alfa Aesar 5 nm. This is further confirmed by our surface profiling results. The surface profiling technique has been widely used not only to measure the thickness of films without damages but also to observe the degree of surface roughness[23].

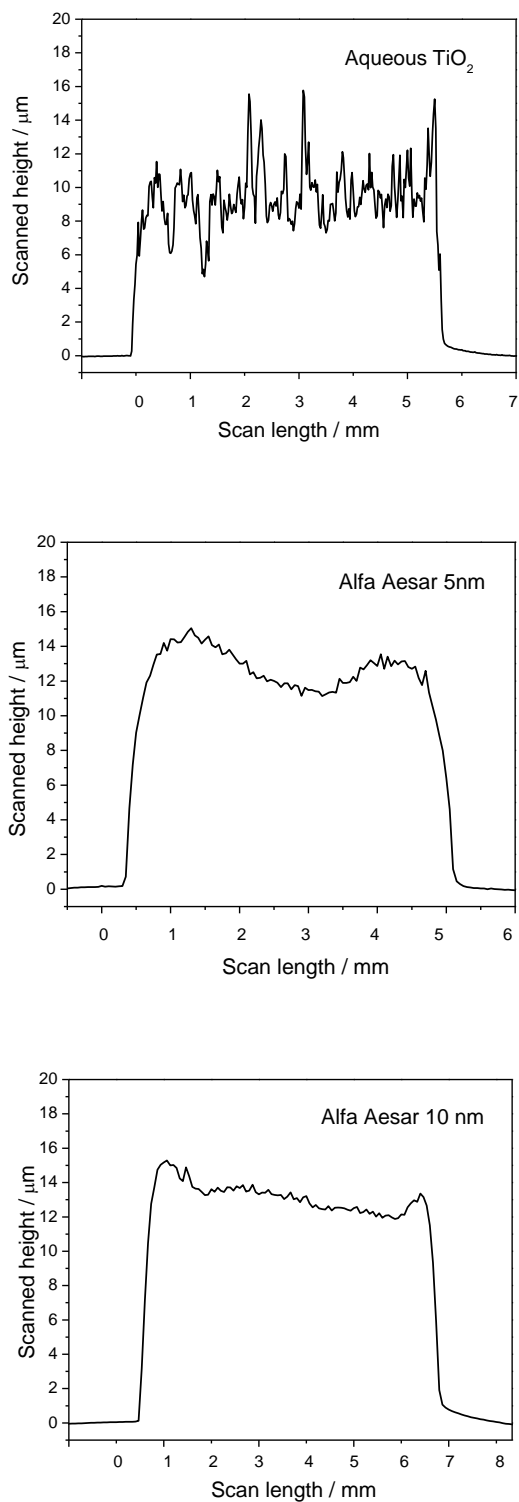


Figure 6.4 Surface profiles of TiO₂ films

As can be seen in Figure 6.4, the profile of Aqueous TiO₂ surface was significantly noisier in comparison to two commercial films indicating a greater roughness in the former. Otherwise all films were prepared with similar thickness (12~14 μm). Next the films were dye loaded to establish how much dye molecules were adsorbed. After dye adsorption, the dye coated films were bleached using 0.1 M NaOH solutions and the concentration of dye per the film area was calculated using Beer-Lambert law ($A = \epsilon bc$) by measuring the extracted solution using UV-Vis spectroscopy, where, ϵ (extinction coefficient) of N719 dye is 13,500 M⁻¹cm⁻¹ at 535 nm [29] As it can be observed from Table 6.1, the Aqueous TiO₂ films absorbed the largest amount of dye molecules in comparison to the commercial substrates as a consequence of the greater surface roughness observed in the former, the latter fact could be advantageous for the cell efficiency.

Table 6.1 Dye adsorption on TiO₂ films

	Alfa Aesar 5 nm	Alfa Aesar 10 nm	Aqueous TiO ₂
Adsorbed dye on films (μmol/cm ²)	0.0745	0.0517	0.0967

In order to assess possible differences of interparticle network construction among the three films, we decided to look at the pore size distribution and surface area of each film using BET. The pore size distribution of the three nanostructured films is depicted in Figure 6.5. High TiO₂ film porosity is a crucial characteristic for good photovoltaic performance by the DSSC device since the pores allow for the electrolyte to penetrate and diffuse without hindrance. It becomes evident that if the pore size in the film is small, then we can anticipate that the flow of electrolyte and dye regeneration would be adversely affected. For this reason, smaller nanoparticles are not always beneficial in spite of their large surface area to accommodate more dye molecules [30]. As can be seen in Table 6.2, the surface areas of the three films do not significantly vary: 69.3, 77.4 and 72.2 m²/g for Alfa Aesar 10 nm, Alfa Aesar 5 nm and Aqueous TiO₂, respectively. However, the pore size distribution of these similar size and surface area films varies from 146 Å and 119 Å for Alfa Aesar 10 nm, and Alfa Aesar 5 nm to only 72 Å for the

Aqueous TiO₂ (Table 6.2). These differences arise from the packing behavior of the different nanoparticles. The relatively low pore size of the Aqueous TiO₂ material in comparison to its isometric counterpart Alfa Aesar 5 nm may be indicative of aggregation by the former, which needs to be optimized in the future.

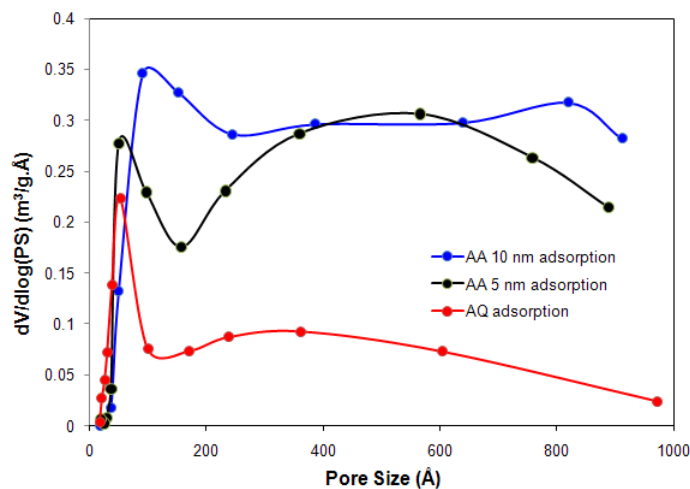


Figure 6.5 Pore size distribution of TiO₂ films

Table 6.2 Properties of TiO₂ films determined from adsorption-desorption curves

TiO ₂ film	Crystallite size (nm)	BET surface area (m ² /g)	Pore size (Å)
Alfa Aesar 10 nm	10	69.3	146
Alfa Aesar 5 nm	5	77.4	119
Aqueous TiO ₂	5~10	72.2	72

In our previous publications, we have shown that the surface TiO₂ groups play an important role in the binding of dye molecules via the dual covalent and electrostatic mechanism [13-16]. In this study, we estimated the amount of surface TiO₂ groups (Ti-OH/Ti-OH₂) using TGA and XPS analysis in order to correlate it to photocurrent output measured by J-V characterization of assembled cells.

X-ray photoelectron spectroscopy has been used to probe the presence and concentration of surface hydroxyls on oxidized metal surfaces because of its surface sensitivity. In our

studies, we were able to de-convolute the O 1s spectrum into three components as in the work of Simmons and Beardt [31]. Therefore for our TiO₂ substrates, the bulk oxygen was observed at ~530.7 eV, the surface Ti-OH groups at ~532.2 eV, adsorbed water and/or organic contaminants at ~532.9 eV [32,33]. As each peak area is proportional to the quantity of each component, we can estimate the quantity of surface groups (OH/H₂O) on the commercial and our synthetic TiO₂ surface (Figure 6.6).

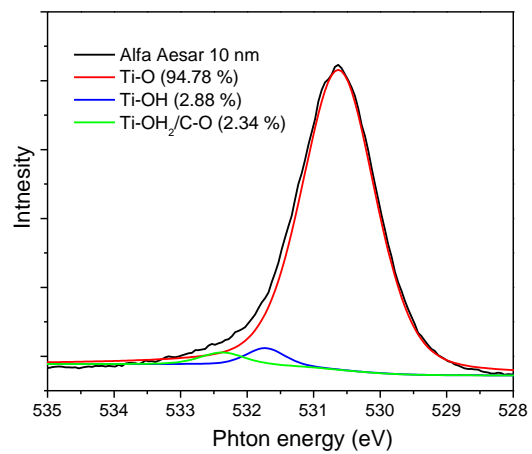
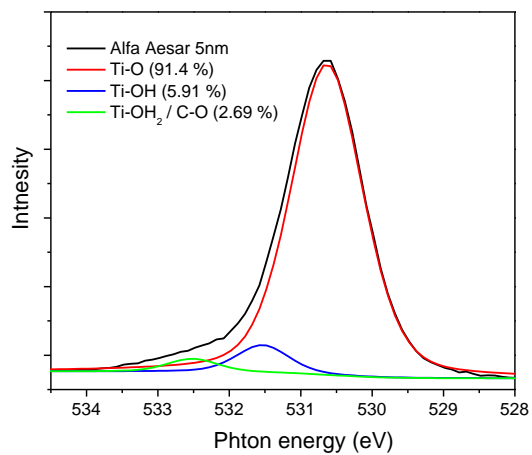
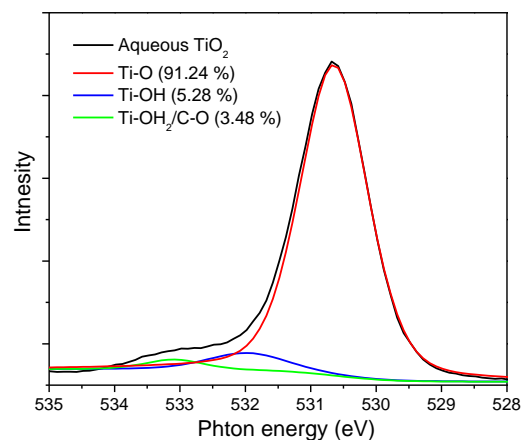


Figure 6.6 O 1s XPS spectra of TiO₂ films

The XPS analysis of our Aqueous TiO₂ film showed more water/organic groups (3.48 %) than the two commercial TiO₂ films (2.69 % and 2.34 % for Alfa Aesar 5 nm and 10 nm, respectively) in agreement with our previous results [16]. As water is known to be undesirable from a cell stability point of view due to risk of degradation of the liquid iodide/triiodide electrolyte [34] long-term accelerated ageing data will need to be collected to verify if this type of surface water imposes such risk. Meanwhile, the amount of Ti-OH surface groups in the Aqueous TiO₂ and Alfa Aesar 5 nm films is twice as much (5.3-5.9 %) to that for Alfa Aesar 10 nm material (2.9 %). As mentioned previously, the importance of surface hydroxyl groups is that they enhance and stabilize the anchoring of the N719 dye molecules on the TiO₂ surface via the H-bond bridges [13-16]. The TGA analysis provided further validation of the presence of these surface groups. As it can be seen in Figure 6.7 all three TiO₂ films show two temperature regions as follows: below and above 100-120 °C. In the first region (< 100-120 °C), the weight loss is a result of weakly adsorbed water removal from the surface of TiO₂ film, while higher temperatures (100-600 °C) correspond to the weight loss from removal of covalent bonded surface hydroxyl groups mainly and to lesser degree chemically bound water. The amount of surface groups (Ti-OH/Ti-OH₂) of Aqueous TiO₂ and Alfa Aesar 5 nm was similar, but in the case of Alfa Aesar 10nm, it was almost half of the corresponding content of the other two films (Aqueous and Alfa Aesar 5 nm) in agreement with our O 1s XPS data.

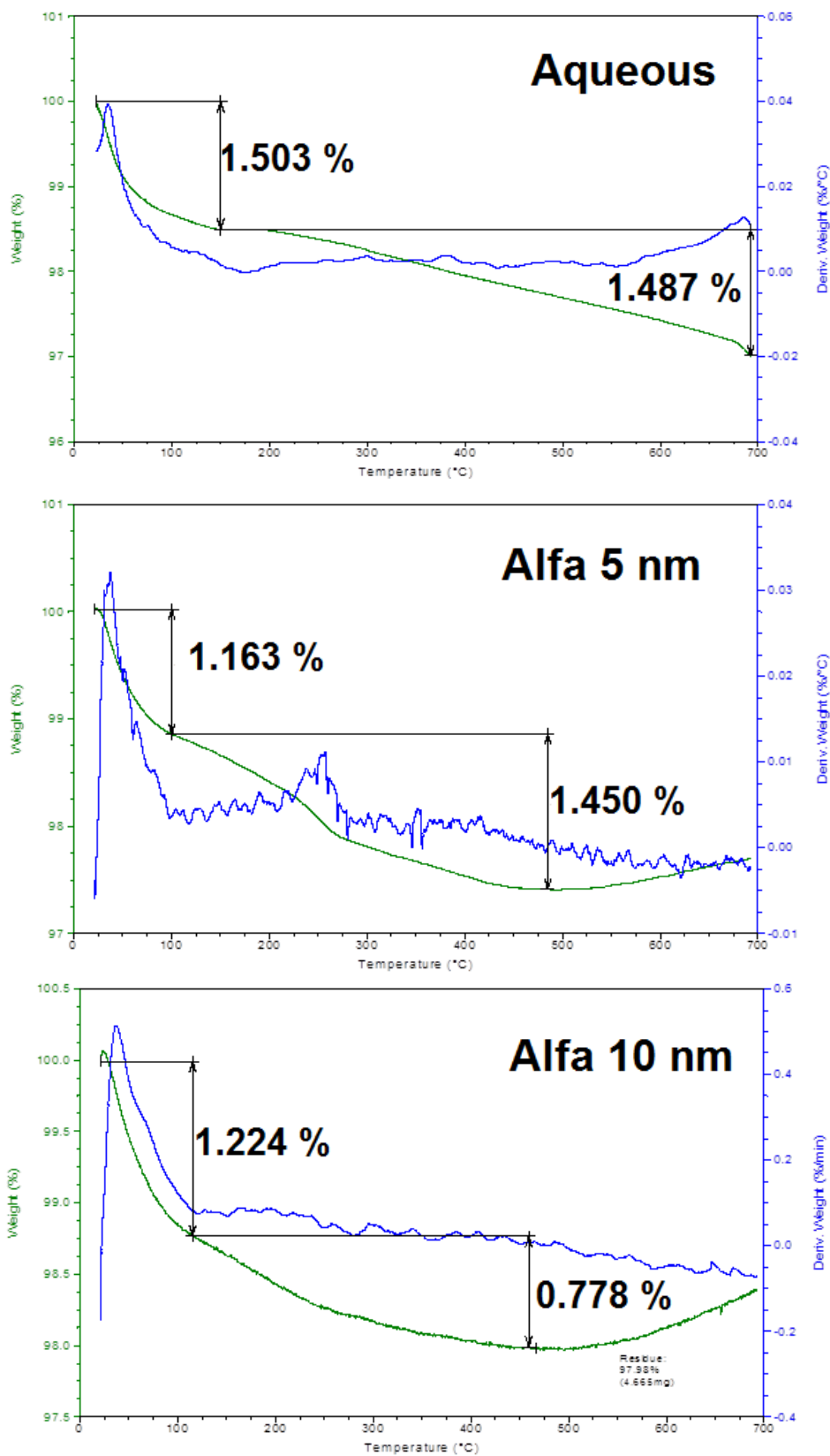


Figure 6.7 TGA results of TiO₂ films

I-V measurements made on cells built from the three films (as a reminder of similar surface area all) showed the higher hydroxyl-content films (Aqueous and Alfa Aesar 5nm) to produce almost double short circuit current density and conversion efficiency (an increase between 85 and 110 % was realized; see data in Table 6.3) in direct correspondence to their Ti-OH content. This is a remarkable improvement much higher than previously reported results as are those for example of Park and Dhayal [12] who reported 40 % improvement following plasma treatment of the TiO₂ film. At the same time the open circuit voltages were found to be almost the same for all films, confirmed by several I-V measurements. We anticipated some V_{oc} changes for each DSSC electrode because of the different amount of surface groups (Ti-OH/Ti-OH₂). In our previous electron spectroscopic study, we observed a greater shift for the Aqueous TiO₂ after sensitization in comparison to Solaronix TiO₂ at the Ti 2p and O 1s XPS spectra due to its excess surface groups [15]. In order to understand the observed I-V performance data the built devices were subjected to EIS and OCVD analysis.

6.4.2 EIS and OCVD

Electrochemical impedance spectroscopy (EIS) was used to analyze the internal resistance and a wide range of electrochemical processes that operate in the various DSSC devices fabricated with the three different TiO₂ electrodes. We further probed our systems via the use of open circuit voltage decay (OCVD) in order to comprehend the nature of recombination within our cells. Figure 6.8 shows EIS spectra composed of the Nyquist plot and Bode phase plots.

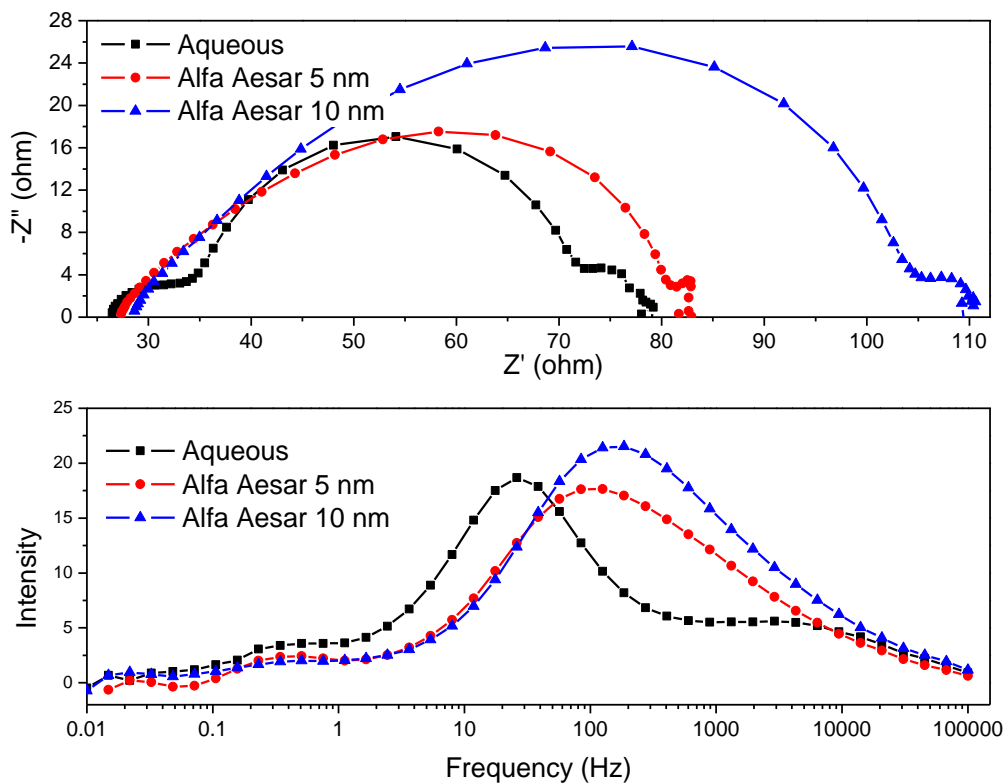


Figure 6.8 Nyquist plot (above) and Bode phase plot (below)

Table 6.3 I-V characteristics of DSSCs fabricated with Aqueous, Alfa Aesar 5 nm and 10 nm TiO₂ films

	V _{oc} (V)	J _{sc} (mA/cm ²)	$\frac{\Delta J_{sc}}{J_{sc}}$ (% J _{sc} increase)	FF	η (%)
Alfa Aesar 10 nm	0.72	4.42	-	0.63	2.00
Alfa Aesar 5 nm	0.75	9.19	107.9%	0.73	5.03
Aqueous TiO ₂	0.72	8.21	85.7%	0.71	4.20

The three semicircles in Nyquist plot represent key resistances relevant to the DSSC performance: the charge transfer at the working (FTO/TiO₂) and/or Pt counter electrodes

(R_1), the recombination of electrons in the $\text{TiO}_2/\text{dye}/\text{electrolyte}$ interface (R_2) and the iodide species diffusion in the electrolyte (R_3) [20, 35-37].

In terms of the size of R_1 in the Nyquist plot, the Aqueous TiO_2 film shows a bigger semicircle than the two commercial material-made films, implying that there is more charge transfer resistance at the Pt counter electrode and/or electrical contact between conductive substrate/ TiO_2 or TiO_2 particles in the Aqueous DSSC. The likelihood of higher resistance at the Pt electrode of the Aqueous DSSC was rejected because the counter electrodes for all three devices were prepared in the same way. Thus, R_1 is most likely the resistance derived from electrical contact between FTO/ TiO_2 or TiO_2 particles. For the Aqueous TiO_2 photoanode, the bigger size of R_1 can be rationalized to stem from aggregation of the Aqueous TiO_2 nanocrystallites as evident from the small pore size and large surface roughness results described in the previous section.

On the other hand, the size (diameter) of the second semicircle (R_2) of the Aqueous and Alfa Aesar 5nm TiO_2 -based devices is considerably smaller (with the Aqueous device exhibiting the smallest R_2) than that of the Alfa Aesar 10 nm device. The diameter of the semicircle in the middle frequency (R_2) is known [36,38] to relate to the charge recombination of I_3^- with the electrons on the photoelectrode. Hence it is deduced that the OH-rich TiO_2 made photoelectrodes are associated with lower recombination thus explaining their higher photocurrent generation (see data in Table 6.3).

In the Bode phase plot of Figure 6.8 (bottom), the characteristic middle frequency peak is located at 26.1 Hz for the Aqueous TiO_2 electrode and this peak moves to higher frequency for both Alfa Aesar 5 nm and 10 nm electrodes. Since the characteristic frequency in the middle range of the Bode phase plots (Figure 6.8 (bottom)) can be related to the inverse of recombination life time (τ_R) in TiO_2 films ($\omega_R=1/\tau_R$) [39], these results indicate that the electron recombination time (“lifetime”) of Aqueous TiO_2 built DSSC is longer than the other two commercial material made devices. This interpretation is further supported by the OCVD results discussed below.

Referring now to the size of the third semicircle of the Nyquist plots in Figure 6.8, it is observed that the Aqueous TiO_2 film has bigger resistance than that of the Alfa Aesar 5 nm film, an observation that can be attributed to its smaller pore size (see data in Table 6.2). The small pore size can obviously affect the flow of electrolyte into the pores as well as affect ion diffusion, hence producing extra resistance. Although our Aqueous TiO_2 film showed a relatively big size third semicircle in comparison to the 5 nm and 10 nm Alfa Aesar films, it was nevertheless significantly improved vis-à-vis our previous EIS results [16] probably due to repeated particle dispersion conducted during the TiO_2 pastes preparation stage.

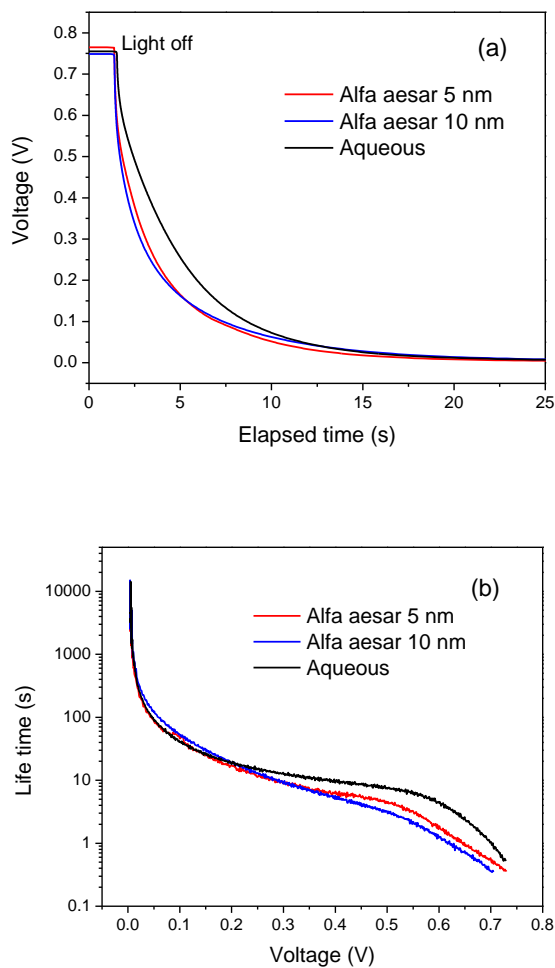


Figure 6.9 Open circuit voltage decay (a) and life time (b)

The OCVD technique has been employed as a powerful tool to study the electron lifetime in DSSC devices as a measure of recombination kinetics[20]. In order to conduct the OCVD measurement, simulated solar light is illuminated at DSSC and a steady-state voltage is obtained. Then, the potentiostat monitors the decay of photovoltage (V_{oc}) after interrupting illumination. The decay of the photovoltage reflects the decrease of the electron concentration at the FTO surface, which is mainly caused by charge recombination. In other words, the recombination rate is proportional to the response of the OCVD[40]. Figure 6.9 (a) shows the open-circuit voltage-decay curves for the commercial (Alfa aesar 5 nm and 10 nm) and our in-house Aqueous TiO_2 DSSCs after the light was turned off. The response time τ (Figure 6.9(b)) can be deduced from the derivative of the V_{oc} decay curve using the equation[39]:

$$\tau = -\frac{k_B T}{e} \left(\frac{dV_{oc}}{dt} \right)^{-1} \quad \text{eq. 6.1}$$

where k_B is the Boltzmann's constant, e is the elementary charge and T is the temperature. The calculated response times τ as a function of V_{oc} for the three types of DSSCs are displayed in Figure 6.9(b). From the above measurements, it is obvious that the decay rates of Alfa Aesar 5nm and 10 nm substrates are faster than that of the Aqueous TiO_2 system in agreement with the EIS results [41].

The question that arises is via which mechanism the surface hydroxyl groups help extend electron lifetime. As mentioned, based on presented data here and elsewhere [13-16] the surface hydroxyl groups help stabilize the N719 molecules on the surface of TiO_2 . As such a higher dye loading per unit area can be accommodated (see data of Table 6.1) effectively providing complete dye coverage/coating of the TiO_2 surface. Such effective dye coating by extension can be thought to act as an organic passivating layer that impedes recombination of triiodide species in the electrolyte and the photogenerated electrons collected by the TiO_2 semiconductor [20]:



The passivating role of the well anchored on the TiO_2 surface dye molecules can be paralleled to that of co-adsorbing non-dye molecules as is a phosphinate amphiphile described by Gratzel and co-workers [42] or the commonly used 4-tert-butyl pyridine (TBP) electrolyte additive [18]. In the present case though it is the active dye molecules

themselves that provide protection against recombination as was also noted recently by Bazzan et al.[4]. While in the latter case the researchers had to resort to a desorption/adsorption cycling process repeated multiple times until saturation was reached or by others to co-adsorbing ions that essentially compete with the dye lowering its loading the aqueous synthesized anatase nanocrystallites are endowed with rich surface hydroxyl groups achieving equivalent if not better results in a more straight forward manner.

While the Aqueous TiO₂ built electrode showed a higher recombination resistance than the DSSCs made from the two commercial TiO₂ substrates, its conversion efficiency was slightly lower than that of the Alfa Aesar 5nm built device despite otherwise similar if not better surface dye loading features. This loss in efficiency is thought to relate to the smaller pore distribution in the Aqueous TiO₂ film that likely generates increased resistance at the TiO₂ particles (R₁) and pore electrolyte diffusion (R₃), respectively. Thus, based on this analysis, further optimization work is planned to improve the properties of the Aqueous TiO₂ mesoporous film structure via the employment of blends of aqueous-synthesized TiO₂ particles of different sizes.

6.5 Conclusion

A “head-to-head” analytical comparison and performance evaluation of three anatase TiO₂ nanocrystalline building materials for DSSC mesoporous electrode construction revealed that surface hydroxylation is a critical surface property greatly influencing the type of dye binding regime and cell performance. The three materials tested (two commercial ones. “Alfa Aesar 5 nm and 10 nm” and one home-made variety, “Aqueous TiO₂”) were selected to have similar crystallite size (5-10nm) and film BET surface area (~73 m²/g) but differ in their surface hydroxyl content. Thus enhanced surface hydroxylation that can easily be endowed to the anatase material via our aqueous-solution synthesis protocol (“Aqueous TiO₂”) is shown to lead to well anchored stabilized dye molecular coverage of the semiconductor surface providing a kinetic barrier (“passivating organic layer”) against recombination at the TiO₂/dye/electrolyte interface.

The surface profile and AFM analysis showed that our Aqueous TiO₂ exhibited a rougher surface, which allowed it to adsorb more dye molecules. UV spectroscopic results of bleached films further confirmed that the dye loading onto Aqueous TiO₂ surface was the highest among the three films made with a similar thickness. For the pore size distribution, Aqueous TiO₂ showed the smallest pore probably due to particle aggregation, a characteristic that needs to be further optimized. XPS and TGA results showed that the Aqueous TiO₂ and Alfa Aesar 5 nm made films contain a similar amount of surface hydroxyl groups, double of that contained in Alfa Aesar 10 nm film. There was a striking correlation between surface hydroxyl group content and current density, J_{sc}, generated by the devices with the OH-rich photoelectrodes delivering 85-110 % higher output than the low OH content photoelectrode. EIS and OCVD measurements on the three devices showed the enhanced photocurrent output to correlate nicely with slower recombination rate at the TiO₂/dye/electrolyte interface as evident by a longer electron lifetime.

Referring specifically to the performance of our Aqueous TiO₂-built photoanode, we observe that although it possessed similar content of surface hydroxyl groups as did the Alfa Aesar 5 nm built photoanode, its power conversion efficiency was slightly lower (4.20 %) than its counterpart (5.03 %). This lower efficiency and particular EIS behavior observed maybe rationalized on the basis of its smaller pore size and higher aggregation already mentioned earlier. Nevertheless, our OCVD results showed that such a photoelectrode with the surface characteristics of the Aqueous TiO₂ possess longer lifetime for efficient electron transport. Therefore, higher efficiencies are expected to be achieved with our Aqueous TiO₂ material upon altering its particle properties to allow for optimization of its pore size distribution, which will be a topic of future work.

6.6 References

- [1] Hagfeldt, A.; Boschloo, G.; Sun, L.; Kloo, L.; Pettersson, H. *Chem. Rev.* **2010**, *110*, 6595
- [2] Yu, J.; Li, Q.; Shu, Z. *Electrochim. Acta* **2011**, *56*, 6293

- [3] Liao, J.; Lei, B.; Kuang, D.; Su, C. *Energy Environ. Sci.* **2011**, DOI: 10.1039/c1ee01574e
- [4] Bazzan, G.; Deneault, J. R.; Kang, T.; Taylor, B. E.; Durstock, M. F. *Adv. Funct. Mater.* **2011**, *21*, 3268
- [5] de Freitas, J. N.; Nogueira, A.F.; De Paoli, M. A. *J. Mater. Chem.* **2009**, *19*, 5279
- [6] Han, H. W.; Liu, W.; Zhang, J.; Zhao, X. Z. *Adv. Funct. Mater.* **2005**, *15*, 1940
- [7] Baek, I. C.; Vithal, M.; Chang, J. A.; Yum, J.; Nazeeruddin, Md. K.; Gratzel, M.; Chung, Y.; Seok, S. I. *Electrochem. Commun.* **2009**, *11*, 909
- [8] Park, J. T.; Roh, D. K.; Patel, R.; Kim, E.; Ryu, D. Y.; Kim, J. H. *J. Mater. Chem.* **2010**, *20*, 8521
- [9] Yang, W.; Wan, F.; Chen, Q.; Li, J.; Xu, D. *J. Mater. Chem.* **2010**, *20*, 2870
- [10] Wang, Z.; Yamaguchi, T.; Sugihara, H.; Arakawa, H. *Langmuir* **2005**, *21*, 4272
- [11] Wang, J.; Lin, Z. *Chem. Mater.* **2010**, *22*, 579
- [12] Park, K.; Dhayal, M. *Electrochem Comm.* **2009**, *11*, 75
- [13] Hirose, F.; Kuribayashi, K.; Suzuki, T.; Narita, Y.; Kimura, Y.; Niwano, M. *Electrochem. Solid-State Lett.* **2008**, *11*, A109
- [14] Lee, K. E.; Gomez, M. A.; Elouatik, S.; Demopoulos, G. P. *Langmuir* **2010**, *26*, 9575
- [15] Lee, K. E.; Gomez, M. A.; Regier, T.; Hu, Y.; Demopoulos, G. P. *J. Phys. Chem. C* **2011**, *115*, 5692
- [16] Lee, K. E.; Gomez, M. A.; Elouatik, S.; Shan, G. B.; Demopoulos, G. P. *J. Electrochem. Soc.* **2011**, *158*, H708
- [17] Charbonneau, C.; Gauvin, R.; Demopoulos, G. P. *J. Electrochem. Soc.* **2011**, *158*, H224

- [18] Itagaki, M.; Nakano, Y.; Shitanda, I.; Watanabe, K. *Electrochim. Acta* **2011**, *56*, 7975
- [19] Fabregat-Santiago, F.; García-Cañadas, J.; Palomares, E.; Clifford, J. N.; Haque, S. A.; Durrant, J. R.; Garcia-Belmonte, G.; Bisquert, J. *J. Appl. Phys.* **2004**, *96*, 6903
- [20] Bisquert, J.; Fabregat-Santiago, F.; Mora-Seró, I.; Garcia-Belmonte, G.; Giménez, S. *J. Phys. Chem. C* **2009**, *113*, 17278
- [21] Zaban, A.; Greenshtein, M.; Bisquert, J. *ChemPhysChem*. **2003**, *4*, 859
- [22] Charbonneau, C.; Lee, K. E.; Shan, G. B.; Gomez, M. A.; Gauvin, R.; Demopoulos, G. P. *Electrochem. Solid-State Lett.* **2010**, *13*, H257
- [23] Ito, S.; Chen, P.; Comte, P.; Nazeeruddin, M. K.; Liska, P.; Péchy, P.; Gratzel, M. *Prog. Photovolt: Res. Appl.* **2007**, *15*, 603
- [24] Sommeling, P. M.; O'Regan, B. C.; Haswell, R. R.; Smit, H. J. P.; Bakker, N. J.; Smits, J. J. T.; Kroon, J. M.; van Roosmalen, J. A, M. *J. Phys. Chem. B* **2006**, *110*, 19191
- [25] S. Horea, C. Vetterb, R. Kerna, H. Smitc, A. Hinscha, *Sol. Energy Mater. Sol. Cells* **90** (2006) 1176
- [26] Watson, T.; Holliman, P.; Worsley, D. *J. Mater. Chem.* **2011**, *21*, 4321
- [27] Akhilesh, K.; Arora, M.; Rajalakshmi, T.; Ravindran, R.; Sivasubramanian, V. *J. Raman Spectrosc.* **2007**, *38*, 604
- [28] Porto, S. P. S.; Fleury, P. A.; Damen, T. C. *Phys. Rev.* **1967**, *154*, 522
- [29] Nazeeruddin, M. K.; De Angelis, F.; Fantacci, S.; Selloni, A.; Viscardi, G.; Liska, P.; Ito, S.; Takeru, B.; Gratzel, M. *J. Am. chem. Soc.* **2005**, *127*, 16835
- [30] Kaczmarski, K.; Bellot, J. C. *Acta Chromatogr.* **2003**, *13*, 22
- [31] Simmons, G. W.; Beard, B. C. *J. Phys. Chem.* **1987**, *91*, 1143
- [32] Huang, N. K.; Wang, D. Z.; Lu, Z.; Lin, L. B. *Surf. Coat. Technol.* **1994**, *70*, 69

- [33] Lopez, S.; Dunlop, H. M.; Benmalek, M.; Tourillon, G.; Wong, M. S.; Sproul, W. D. *Surf. Interface Anal.* **1997**, *25*, 827835
- [34] Kern, R.; Van der Burg, N.; Chmiel, G.; Ferber, J.; Hasenhindl, G.; Hinsch, A.; Kinderman, R.; Kroon, J.; Meyer, A.; Meyer, T.; Niepmann, R.; van Roosmalen, J.; Schill, C.; Sommerling, P.; Spath, M.; Uhlandore, I. *Opto-Electron. Rev.* **2000**, *8*, 284
- [35] Kalyanasundaram, K. *Dye-sensitized Solar Cells*, 1st ed. Chapter 12, EPFL Press, Lausanne, Switzerland, 2010.
- [36] Bisquert, J. *J. Phys. Chem. B* **2002**, *106*, 325
- [37] Ross, M. J.; William, K. R. *Impedance Spectroscopy: Emphasizing Solid Materials and Systems*, John Wiley & Sons, New York, 1987.
- [38] Kern, R.; Sastrawan, R.; Ferber, J.; Stangl, R.; Luther, J. *Electrochim. Acta* **2002**, *47*, 4213
- [39] Bisquert, J.; Zaban, A.; Greenshtein, M.; Mora-Sero, I. *J. Am. Chem. Soc.* **2004**, *126*, 13550
- [40] Yua, H.; Zhanga, S.; Zhaoa, H.; Willb, G.; Liua, P. *Electrochim. Acta* **2009**, *54*, 1319
- [41] Hu, X.; Huang, K.; Fang, D.; Liu, S. *Mater. Sci. Eng. B* **2011**, *176*, 431
- [42] Wang, M.; Li, X.; Lin, H.; Pechy, P.; Zakeeruddin, S. M.; Gratzel, M. *Dalton Trans.* **2009**, 10015

Chapter 7. Global conclusions and claims to originality

In this work, we studied the binding mechanism at the surface of dye-sensitized semiconductor films. The obtained results provide several new findings that allow for a better understanding of the parameters governing the nature of Dye (N719) -TiO₂ (anatase) bonding which is important for electron transfer. These results are particularly relevant for the development of new dyes and surface engineering of dye sensitized solar cell (DSSC). Chapter 7 outlines general conclusions based on the whole body of the results presented and discussed through Chapters 3 to 6, as well as the contributions to original knowledge.

7.1 Global conclusions

In the vibrational spectra of the dye region (1000~2500 cm⁻¹), we considered structural changes caused by symmetry changes due to binding, as well as we evaluated carboxylate vibrations (Δv_{salt} and Δv_{Ads}) via the splitting method; this was followed by contrasting Raman imaging and *micro* IR imaging to show the distribution of surface Ti-OH/Ti-OH₂ groups before and after sensitization (for commercial and aqueous-synthesized anatase) as well as the dye distribution on the substrates; as a result of these combined studies we arrived to the following findings:

- The dye region of the IR and Raman spectra of N719 adsorbed-TiO₂ was not much different in comparison to that of the neat N719. A small band at 1372 cm⁻¹ was observed in the Raman spectra of N719 adsorbed-TiO₂, which was taken as proof of chemisorption (via bidentate bridging) as in previous works. In the IR spectra, both C=O and COO⁻ groups were observed before and after adsorption and our Δv values were indicative of bidentate bridging coordination. ATR-FTIR spectroscopy of the high wave number region displayed Ti-OH/Ti-OH₂ bands before and after adsorption indicating that not all surface groups had been displaced upon the dye binding. This fact along with the presence of leftover binding ligands (C=O and COO⁻) indicated that the N719 molecules interact via a dual character: electrostatically (H-bonding) and covalently (bidentate-

bridging mode) with the TiO_2 substrates regardless of their method of production (commercial vs. synthetic). Based on this spectroscopic data (and other relevant literature works), we proposed one carboxylic group (COO^- or COOH) binds to TiO_2 using a bidentate bridging for chemisorption rather than two and the other is electrostatically (H-bond attached) bound via surface $\text{Ti-OH}/\text{Ti-OH}_2$ groups.

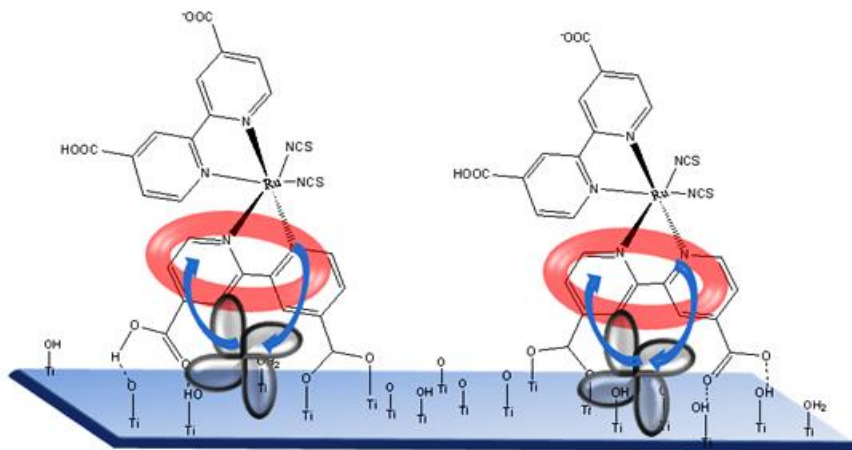
The electron spectroscopic study gave complimentary information to our vibrational spectroscopic results but also provided us new sights into the electronic interactions of the substrates and dye molecules:

- The C K-edge XANES spectral changes revealed that there are additional electronic states (not observed in the neat N719) that occur between dye molecules and TiO_2 surface once adsorption occurs. Furthermore, the π^* and σ^* regions in the spectra indicate modification and extra states that occur in the electronic structure around the pyridine structure after dye adsorption. These spectral changes to the XANES spectrum allowed us to propose that the aromatic electronic density from pyridine interacts with TiO_2 electron density. Thus, we can postulate that in the N719- TiO_2 system, electronic interactions occur not only through the covalent bonding of the anchoring groups but also through the aromatic electron density of the bipyridine groups and the d states found in TiO_2 . This effect remarkably was later proved by computation by De Angelis and collaborators via DFT [1].
- Orientation experiments that were conducted showed the adsorbed sample at normal incidence (90°) and at grazing incidence (30°) to exhibit no intensity change for the π^* or σ^* states of the C K-edge; this was rationalized as a result of each carbon in the dye molecule being oriented differently in space and as such no angle dependency was observed. The N K-edge in contrast to the C K-edge showed no additional electronic states; once adsorption occurred and most of the neat N719 character remained intact. Interestingly, the orientation measurements in the N K-edge showed that the intensity for the $\text{N } 1s \rightarrow \pi^*$ resonance peak increased at 30° , indicating that the sp^2 conjugated π bond in the bipyridine groups is more aligned with the TiO_2 substrate at 30° than 90° to the

surface. This further suggests that this type of geometry favors electronic aromatic interaction between the TiO_2 surface and the N719 molecules.

- Although the two nanocrystalline anatase (our aqueous-synthesized and commercial) substrates showed a similar type of bonding environment around the TiO_2 (in pure and adsorbed states) as observed via our XAS data, the TiO_2 surface interactions upon dye adsorption monitored via binding energy shifts in XPS were found to be distinct in the two substrates indicating that not all anatase nanocrystalline substrates behave in the same way once the N719 is adsorbed in terms of electronic interactions (surface dipole or shift to the Fermi level). As a result, this may contribute to the distinct manner which they perform electronically in the DSSC.

From the vibrational and electronic spectroscopic results, a new binding mechanism, pictorially shown below, was developed to outline the electronic and bonding components never before reported.



After studying the dye- TiO_2 binding mechanism, we prepared different photoanodes with commercial and aqueous-synthesized anatase nanocrystallites and assembled complete solar cells in order to investigate and characterize their electrochemical properties and performance. The TiO_2 materials tested were selected to have similar surface area but differ in their surface hydroxylation content in order to shed light on the effect of the

latter. All films tested were furthermore built to have the same thickness and they were not subjected to TiCl_4 post-treatment. Here are the major findings:

- In our work, we observed a relationship between surface hydroxyl groups and current density exhibited in the I-V curves. The OH-poor material (“Alfa Aesar 10 nm”) showed almost half of J_{sc} (mA/cm^2 , current density) value in comparison to the “Alfa Aesar 5 nm” and “Aqueous TiO_2 ” materials that contained twice as much surface OH content. This beneficial effect of surface hydroxyl groups on DSSC performance was shown to arise from higher dye loading on TiO_2 surface facilitated by the dual electrostatic/bidentate bridging binding mechanism elaborated above. Combined EIS and OCVD measurements revealed further that the photoelectrodes composed of surface hydroxyl-rich TiO_2 nanocrystalline material exhibit longer electron lifetime attributed to enhanced surface-dye binding that suppresses interfacial recombination. Therefore, higher performance is expected to be achieved with aqueous-synthesized TiO_2 material due to its inherent higher surface hydroxyl content. For this to materialize, however, the aqueous-synthesized material needs first to be optimized in terms of particle properties and pore size distribution since EIS showed otherwise relatively elevated electrolyte diffusion resistance.

7.2 Claims to originality

Most parts of this thesis can be considered as contributions to original knowledge and understanding of the system as can be observed from the quality of journals where this material was published. Here below, we outline the most important:

A. Chemical bonding:

- The Δv method that has been used in the past to infer coordination bonding information was found not to be reliable in the present system questioning the findings of several previous dye- TiO_2 investigations.
- We showed spectroscopically and visually (via ATR-FTIR and Raman imaging) for the first time, the distribution of the surface Ti-OH/Ti-OH₂ substrate groups and how these are affected after N719 dye adsorption. Most importantly, it was shown for the first time that the distribution of these groups was not equal in otherwise similar nanocrystalline

anatase substrates with nanometer scale roughness and that not all these surface groups were consumed upon binding of the N719 in contrast to previous models.

- Also the presence of free ligand groups (C=O and COO⁻) after adsorption on both anatase substrates is a new discovery.
- A new binding mechanism involving covalent and H-bonding components was introduced based on the spectroscopic, imaging data, and combination of theories taking into account previous research work. This new mechanism has now been accepted as one of the main modes of binding by all the leading experts in the DSSC field around the world as maybe seen from the citations of our work.

B. Electronic interactions

- Despite what was claimed in previous literature works, we showed that the use of Ti K-edge EXAFS data (with fluorescence yield or transmission yield) cannot detect coordination changes involving Ti-O surface groups reacting with N719 dye molecules.
- The use of electronic spectroscopy (XAS and XPS) showed for the first time that: (1) the electronic interactions between the N719 and TiO₂ substrate not only occur via covalent bonding of the ligand groups (COOH and COO⁻) but also through the non-bonded aromatic electron density and d-states of TiO₂. This is important as it provides further explanation for the ultrafast electron injection mechanism/pathways that occur after light absorption in the N719-TiO₂ system. This type of concept was confirmed independently via Density Function Theory computations (published around the same time with us).
- The adsorption of dye on the TiO₂ substrate leads to a change into surface dipole and/or E_f position of TiO₂. This effect is not equal for all nanocrystalline anatase substrates and was found to be greater for substrates with higher surface OH/H₂O groups; the latter fact was likely a result of change to work function of the substrate that is observed when a different distribution (e.g. localization of hot spots) of surface dipoles occurs in the surface.

- It was demonstrated that although two nanocrystalline anatase substrates (aqueous-synthesized and commercial) showed a similar type of molecular bonding (XAS and vibrational), the surface charge interactions (XPS) were not equivalent in all substrates. This indicates that electron transport and mobility at the surface of nanocrystalline anatase substrates may not be only a function of their physical properties but also their surface group (Ti-OH) content and method of production.

C. Electrochemical properties

- Combined EIS and OCVD analysis of photoelectrode films built with similar physical properties but differing only in their Ti-OH content demonstrated for the first time that those rich in surface hydroxylation exhibit longer electron lifetime, i.e. less interfacial charge recombination. This was attributed to enhanced surface-dye binding that apparently leads to formation of a protective passivating organic film. This opens the avenue for further optimization of the dye-TiO₂ interface and construction of devices with higher conversion efficiencies.

7.3 Suggestions to future work

- Chapter 6 reports the physical properties of TiO₂ photoanodes (commercial and synthetic-Aqueous TiO₂) and the electrochemical properties of complete solar cells using TiO₂ photoanodes very well characterized. We have used Aqueous TiO₂ as 100 % anatase form for DSSC and observed disadvantages such as small pore size and particle aggregation. Thus, further development of Aqueous TiO₂ pastes mixed with anatase and rutile is suggested that may greatly contribute to increased pore size distribution (i.e. minimized electrolyte diffusion resistance) while at the same time taking advantage of rutile's scattering effect.

7.4 References

- [1] Pastore, M.; De Angelis, F. *J. Phys. Chem. Lett.* **2011**, 2, 1261–1267

Appendix - Experimental details

A.1 Materials and Reagents

A.1.1 Conductive glass

Coated glass with highly F-doped transparent conducting oxide (TCO) usually serves as a support for the dye-sensitized oxide. It allows light transmission while providing good conductivity for current collection. TCO should establish a good mechanical and electrical contact with the dye-sensitized oxide in order to increase electron injection from the latter to the outer circuit. In this work, FTO was purchased from Nippon Sheet Glass with a sheet resistance of 10 Ω per square.

A.1.2 Preparation of mesoporous TiO₂ pastes

In this work two types of pastes were used: those obtained ready from commercial suppliers, namely Dyesol and Solaronix and those prepared in the laboratory. Of the latter the one used in all parts of the work was prepared from anatase TiO₂ nanopowder obtained from the Aqueous synthesis method introduced in Charbonneau *et al.*'s publications [1,2]. Also, pastes were prepared with commercial anatase nanopowders, namely: Alfa Aesar 5nm and Alfa Aesar 10 nm TiO₂.

The fabrication scheme for TiO₂ pastes is described in Figure A.1 First the nano titania particles are manually ground after mixing them with acetic acid, water and ethanol. After grinding the TiO₂ slurry is transferred with excess of ethanol to a beaker where is magnetically stirred initially and then homogenized using a Ti-horn-equipped sonicator. This is filled with the addition of a mixture of anhydrous terpineol and a mixture of ethyl cellulose and ethanol by stirring and sonication again. Finally the contents are concentrated by evaporation [3].

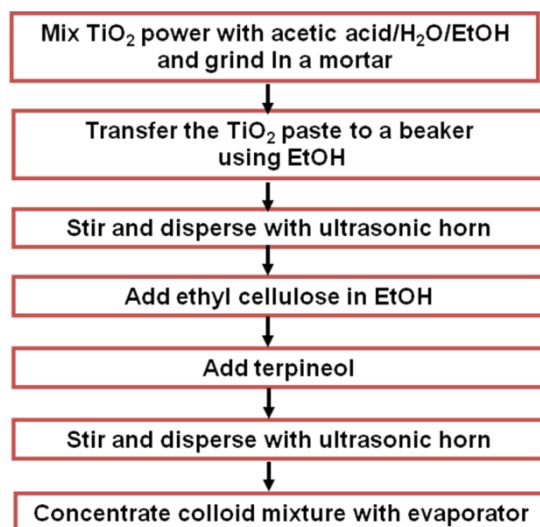


Figure A.1 Preparation protocol for TiO₂ paste (adapted from [3])

At each step, liquids were added drop by drop into a mortar. The diameter of the mortar was ca. 20 cm. The condition was in the ambient air at room temperature. The TiO₂ powders stuck on the inside of the mortar was removed by a plastic spatula in order to grind large aggregates. The TiO₂ dispersions in the mortar were transferred with excess of ethanol (100 ml) to a tall beaker and stirred with a 4 cm long magnet tip at 300 rpm. The ultrasonic homogenization was performed with using a Ti-horn-equipped sonicator (Ultrasonic processor, Cole Palmer). Anhydrous terpineol (Aldrich) and ethyl cellulose (Aldrich) in ethanol were added, followed by stirring and sonication. The contents in dispersion were concentrated by evaporator at 50°C using an evaporator.

A.1.3 Preparation of mesoscopic TiO₂ electrodes

To prepare the DSC working electrodes, the FTO glass was first cleaned in a detergent solution using an ultrasonic bath for 15 min, and then rinsed with water and ethanol. After treatment in a UV-O₃ system (PSD Series Digital UV-Ozone system, Novascan) for 15 min, the FTO glass plates were pre-treated by being immersed into a 50 mM aqueous TiCl₄ solution at 70°C for 30 min and washed with water and ethanol. A layer of paste was coated on the FTO glass plates by screen-printing and then dried for 6 min at 125°C.

The temperature profile used in the sintering process has a great impact on the quality of the film. Figure A.2 is a typical TiO₂ sintering profile reported by Lewis et al[4].

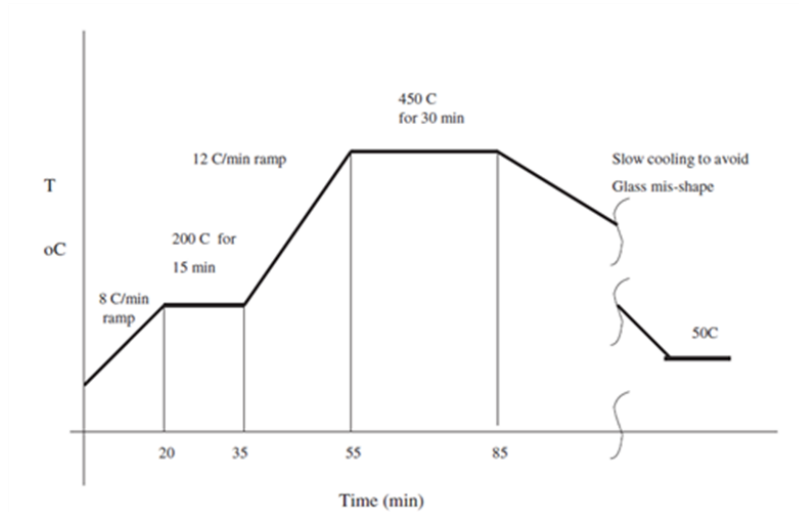


Figure A.2 Typical sintering profile of TiO₂ film (adapted from Lewis et al.[4])

The maximum temperature should not exceed 550 °C, because the phase transition from anatase to rutile starts in this temperature region, along with grain coarsening resulting in loss of nano structure [5]. The heating rate should be very slow. In the temperature interval 200 °C < T < 350 °C, organic materials such as dispersants and organic solvents used during the TiO₂ film deposition stage decompose. The decomposition process induces mechanical stress into the TiO₂-layer. If the heating is done too fast, the adhesion to the FTO-substrate is not firm. Consequently, cracks form within the layer, and the film becomes brittle. The cooling rate of the sintered TiO₂-electrode also needs to be slow in order to minimize the stress within the TiO₂-layer [6]. In general, except in Chapter 6, following annealing the films after cooling were post-treated [7] by immersion into a 0.2 M TiCl₄ solution at 60 °C for 30 min and then annealed once more before they were sensitized.

A.1.4 Sensitizers

N719 dye adsorption on nanocrystalline TiO₂ films was obtained by immersion of electrodes, heated beforehand under air at 450 °C for 30 min and let cooled to 80 °C, in

pure ethanolic (0.5 mM) sensitizer solutions. The TiO₂ films were dipped in the dye solution for about 24 hours in the dark at ambient temperature.

A.1.5 Counter electrode

To prepare the counter electrode, a hole was drilled in the FTO glass by sand blasting. The perforated sheet was washed with detergent solution in ultrasound for 20 min and rinsed by distilled water and ethanol. After drying, the Pt catalyst was deposited on the FTO glass by coating with a drop of H₂PtCl₆ solution (5 mM) and repeating the heat treatment at 380°C for 20 min.

A.1.6 Device assembly

All cells were carefully sealed before photoelectrochemical measurement. The sensitized photoanodes and the counter electrode were separated by a 25- μ m-thick Surlyn® and sealed by heating. The internal space was filled with electrolyte through a hole made by a sandblasting drill on the counter electrode glass substrate. The electrolyte introduction hole was subsequently sealed with a Bynel sheet (obtained from Dyesol) under a thin glass cover by heating. The whole fabrication process is illustrated in Figure 3.3.

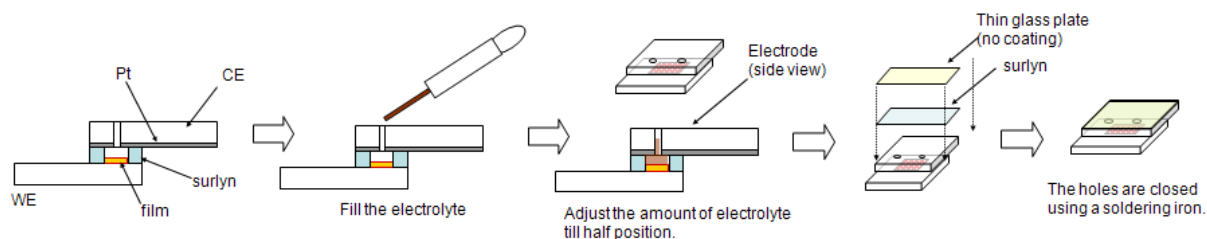


Figure A.3 Schematic of DSSC device assembly procedure

A.2 Current-Voltage curves

A current-voltage (I-V) curve shows the possible combinations of current and voltage output of a photovoltaic (PV) device. A PV device, such as a solar module, produces its maximum current when there is no resistance in the circuit, i.e., when there is a short circuit between its positive and negative terminals. This maximum current is known as the short circuit current and is abbreviated I_{sc}. When the module is shorted, the voltage in the circuit is zero. Conversely, the maximum voltage occurs when there is a break in the

circuit. This is called the open circuit voltage (V_{oc}). Under this condition the resistance is infinitely high and there is no current, since the circuit is open.

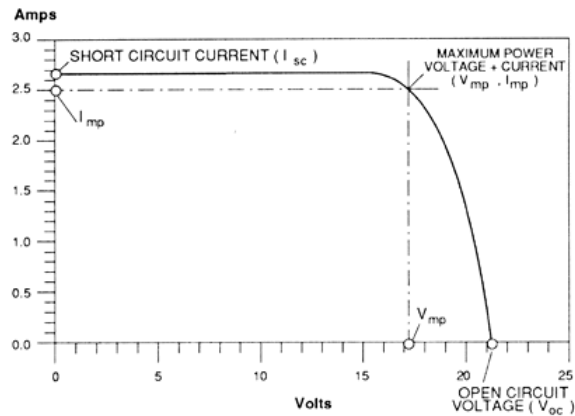


Figure A.4 I-V curve of photovoltaic cells [8]

These two extremes in load resistance, and the whole range of conditions in between them, are depicted on the I-V curve (see Figure A.4). Current, expressed in Amps, is on the (vertical) y-axis. Voltage, in Volts, is on the (horizontal) x-axis. The power available from a photovoltaic device at any point along the curve is just the product of current and voltage at that point and is expressed in Watts. At the short circuit current point, the power output is zero, since the voltage is zero. At the open circuit voltage point, the power output is also zero, but this time it is because the current is zero.

There is a point on the knee of the curve where the maximum power output is located. This maximum power point on our example curve is where the voltage is 17 volts, and the current is 2.5 amps. Therefore the maximum power in Watts is 17 Volts times 2.5 Amps, or 42.5 Watts.

The I-V of a PV device curve is based on the device being under standard conditions of sunlight and device temperature. It assumes there is no shading on the device. Standard sunlight conditions on a clear day are assumed to be 1,000 Watts of solar energy per square meter (1000 W/m^2 or 1 kW/m^2). This is sometimes called one sun, or a peak sun. Less than one sun will reduce the current output of the PV device by a proportional

amount. For example, if only one-half sun (500 W/m^2) is available, the amount of output current is roughly cut in half.

A.3 References

- [1] Charbonneau, C.; Lee, K. E.; Shan, G. B.; Gomez, M. A.; Gauvin, R.; Demopoulos, G. P. *Electrochem. Solid-State Lett.* **2010**, *13*, 8, H257
- [2] Charbonneau, C.; Gauvin, R.; Demopoulos, G. P. *J. Electrochem. Soc.* **2011**, *158*, H224
- [3] Ito, S.; Chen, P.; Comte, P.; Nazeeruddin, M. K.; Liska, P.; Pechy, P.; Gratzel, M. *Prog. Photovolt: Res. Appl.* **2007**, *15*, 603
- [4] Lewis, L. N.; Spivack, J. L.; Gasaway, S.; Williams, E. D.; Gui, J. Y.; Manivannan, V.; Siclován, O. P. *Sol. Energy Mater. Sol. Cells*, **2006**, *90*, 1041-1051
- [5] Li, Y.; Demopoulos, G. P. *Hydrometallurgy*, **2008**, *90*, pp. 26–33
- [6] M. Junghänel, “Novel Aqueous Electrolyte Films for Hole Conduction in Dye Sensitized Solar Cells and Development of an Electron Transport Model” PhD dissertation, Ecole Polytechnique Federale de Lausanne Institute des Sciences et Ingenierie Chimiques, 2007
- [7] Sommeling, P. M.; O’Regan, B. C.; Haswell, R. R.; Smit, H. J. P.; NBakker, N. J.; Smits, J. J. T.; Kroon, J. M.; van Roosmalen, J. A. M. *J. Phys. Chem. B* **2006**, *110*, 19191
- [8] http://www.daviddarling.info/encyclopedia/I/AE_I-V_curve.html